RICE UNIVERSITY

Rashba Spin-Orbit Coupled Quantum Gases

by

Ramachandhran Balasubramanian

A Thesis Submitted
in Partial Fulfillment of the
Requirements for the Degree

Doctor of Philosophy

Approved, Thesis Committee:

Han Pu, Chair
Associate Professor of Physics

Randall G. Hulet
Favez Sarofim Professor of Phvsics

Junichiro Kono
Professor - Dept. of Electrical &
Computer Engineering,
Dept. of Physics & Astronomy, and
Dept. of Materials Science &
NanoEngineering

Houston, Texas

March, 2014

ABSTRACT

Rashba Spin-Orbit Coupled Quantum Gases

by

Ramachandhran Balasubramanian

Spin-orbit (SO) coupling* leads to many fundamental phenomena in a wide range of quantum systems from nuclear physics, condensed matter physics to atomic physics. For instance, in electronic condensed matter systems, SO coupling can lead to quantum spin Hall states or topological insulators, which have potential applications in quantum devices. Recently, SO coupling has been *artificially* induced in quantum gases – ultracold dilute atomic Bose and Fermi gases – by the so-called *synthetic gauge fields*. Combined with unprecedented controllability of interactions and geometry in ultracold atoms, this manipulation of SO coupling opens an entirely new paradigm for studying strong correlations of quantum many-body systems under Abelian and non-Abelian gauge fields. In the major portion of this thesis, we theoretically investigate the ground state and collective excitations of a two-component Bose gas in a two-dimensional harmonic trap, subject to Rashba SO coupling. Our work represents an important extension into the regime of non-Abelian gauge field in which the spin degrees of freedom play an essential role.

*This abstract and the thesis are primarily based on our publications in Refs. [1–3]. The discussion in Appendices is primarily based on our publications in Refs. [4, 5].

LIST OF PUBLICATIONS

The following journal publications are reproduced extensively in this thesis*. Reprinted with permission from the American Physical Society. Copyright (2014) by the American Physical Society.

[1] H. Hu, **B. Ramachandhran**, H. Pu, and X.-J. Liu, "Spin-orbit coupled weakly interacting Bose-Einstein condensates in harmonic traps," Phys. Rev. Lett., vol. 108, p. 010402, Jan 2012.

[2] **B. Ramachandhran**, B. Opanchuk, X.-J. Liu, H. Pu, P. D. Drummond, and H. Hu, "Half-quantum vortex state in a spin-orbit-coupled Bose-Einstein condensate," Phys. Rev. A, vol. 85, p. 023606, Feb 2012.

[3] **B. Ramachandhran**, H. Hu, and H. Pu, "Emergence of topological and strongly correlated ground states in trapped Rashba spin-orbit-coupled Bose gases," Phys. Rev. A, vol. 87, p. 033627, Mar 2013.

[4] **B. Ramachandhran**, S. G. Bhongale, and H. Pu, "Finite-temperature study of Bose-Fermi superfluid mixtures," Phys. Rev. A, vol. 83, p. 033607, Mar 2011.

[5] M. Yan, B. J. DeSalvo, **B. Ramachandhran**, H. Pu, and T. C. Killian, "Controlling condensate collapse and expansion with an optical Feshbach resonance," Phys. Rev. Lett., vol. 110, p. 123201, Mar 2013.

---

*The author's name in legal documents is listed as *Ramachandhran Balasubramanian*. In journal publications and in documents prior to year 2003, the author's name is listed as *B. Ramachandhran*.

Acknowledgments

In the past 6 years, I have enjoyed learning physics and doing research at Rice University. Through this time, I have received support and guidance from several people. I take this opportunity to thank them here.

I would like to thank my beloved parents, Mr. Balasubramanian and Mrs. Sampurna. Their continuous support and trust have been critical to all my scientific and personal pursuits in life. I know I can't thank them enough! Of course, there are no words to thank my lovely wife, Mahalakshmi, for all the support and confidence I have received from her. She has been a wonderful companion in all my challenges, in all my successes, and in all my memorable moments. I have received tremendous support from my mother-in-law, Mrs. Saraswathy, and my grandmother-in-law, Mrs. Gomathy. I have had the pleasure of receiving constant support from my brother, Sivaramakrishnan and my sister-in-law, Shilpa. Through this time, I have always received words of encouragement from all my family members. I know that I am extremely lucky to have them all!

I have had the pleasure of having a wonderful research advisor in Prof. Han Pu. He has offered tremendous support and guidance all through my journey at Rice University. He has taught me to choose the right problems, to ask the right questions, and to systematically solve problems to gain confidence in the solutions. All through my graduate program, he has offered me enviable freedom to pursue my scientific interests and career goals. What more can a physics graduate student ask for! I would like to thank Prof. Hui Hu for his support during several research collaborations that

significantly contribute to this thesis. His hard work and dedication have always been inspirational.

I especially thank my colleague and friend, Dr. Satyan Bhongale, for continuing to be a mentor in my scientific pursuits. It has always been fun (and thought-provoking) to discuss science and several aspects of life with him. I thank Prof. Andriy Nevidomskyy for his guidance and encouragement during my research on topological phases of matter. I would like to thank Prof. Randy Hulet for being a source of inspiration all through my graduate program. It has been my pleasure to have him on both my advisory committee and defense committee. I thank Prof. Junichiro Kono for encouraging participation as part of my defense committee and for substantial feedback on my thesis. I thank Prof. Edison Liang for several discussions during the advisory committee meetings. I thank Prof. Tom Killian for the opportunity to collaborate with him. I thank Dr. Leslie Baksmaty for several motivating discussions. I thank my colleague and collaborator Lin Dong for his continuous support and encouragement through several research projects.

My life at Rice University and Houston has brought tremendous joy to me – thanks to all the staff and friends! The staff in Physics department have been awesome! Special thanks to Bridgitt Ayers (now at Office of Graduate and Postdoctoral Studies), Barbara Braun, Rose Berridge, Umbe Cantu, Rosa Almendarez, and Lanie Anderson. Office of International Students and Scholars (OISS) has been a source of great support for me and my wife. OISS staff - you have been great! I would like to thank my friends at Rice, Houston, Austin, and all those scattered elsewhere in the world!

Contents

*Chapter 3 taken largely from our publications in Refs. [1, 2].

*Chapter 4 taken largely from our publication in Ref. [2].

†Chapter 5 taken largely from our publication in Ref. [3].

*Appendix A taken largely from our publication in Ref. [4].

†Appendix B taken largely from our publication in Ref. [5]. Associated experiments were performed by M. Yan, B. J. DeSalvo, and T. C. Killian.

List of Figures

Chapter 1

Introduction

1.1 Quantum mechanics: wave-particle duality

In his Physics Nobel prize acceptance speech in 1913, Prof. Heike Kamerlingh Onnes said "(Progress in cryogenics) can contribute towards lifting the veil which thermal motion at normal temperature spreads over the inner world of atoms and electrons" [6]. The cartoon depiction in Fig. 1.1 illustrates the fundamental change in atomic behavior at lower temperatures. As shown in Fig. 1.1(a), the behavior of a gas of atoms at room temperature is typically dominated by their random thermal motion and billiard-ball like particle behavior [7]. Averaged over time, we can characterize this ensemble of atoms in terms of thermodynamic variables like temperature and pressure [8].

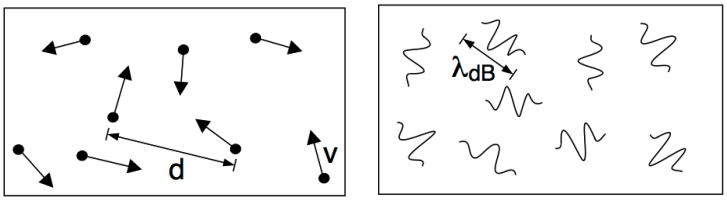

Figure 1.1 : (a): left, At high temperature, thermal motion dictates behavior with arrows indicating the random instantaneous velocity **v**. The average inter-particle spacing d determines the density n of the gas as d^{-3}. (b): right, At sufficiently lower temperatures, quantum mechanics dominates behavior. In a simplified description, the atoms can be regarded as wavepackets with an extension λ_{dB} (see text). Image and caption adapted from the seminal review article by Ketterle *et al.*, Ref. [7].

The energy of an atomic ensemble is related to the (average) speed (v) and mo-

mentum (p) by $E \propto mv^2 \propto p^2/m$, with m being the mass of the particle. The mean thermal energy is given by $E \propto k_B T$, where k_B is the Boltzmann constant and T is the equilibrium temperature. Thus at thermal equilibrium, the momentum is related to equilibrium temperature by $p \simeq \sqrt{mk_B T}$. It is evident that as the temperature is lowered, the particle's thermal motion is reduced. However, atoms do not come to a complete stop even at zero temperature. Quantum mechanics helps us understand this non-intuitive behavior by ascribing wave-like attributes to the particle and thereby, associating a finite uncertainty in simultaneously specifying momentum and position of the particle. When such a description proves appropriate, the particle's wavelength λ (manifesting wave-nature) and momentum p (manifesting particle-nature) are intimately related. First proposed by Louis de Broglie, the relation takes the form: $\lambda = h/p \simeq h/\sqrt{mk_B T}$, where h is the Planck constant that accounts for the quantum mechanical description. This wavelength is typically referred to as the thermal de Broglie wavelength λ_{dB}.

Let us now determine the criteria for quantum mechanical effects to become important in an atomic ensemble, largely following Leggett's elegant description in Ref. [9]. We understand from classical optics that a wave will behave very much like a stream of particles, if the wavelength λ is small compared to the characteristic dimension d of whatever is obstructing it: an example of this fact is that 'one cannot see around doors' [9]. Therefore, when λ_{dB}, due to lowering of temperature, becomes a substantial fraction of d, we expect that quantum mechanical effects start to become important. Another important aspect of quantum mechanics is the identical nature of quantum particles that results in their indistinguishability. As λ_{dB} further increases at lower temperatures, the atomic wavepackets begin to overlap. In such a scenario, indistinguishability of particles becomes important to the extent that it begins to

affect their macroscopic statistical distribution.

1.2 Quantum statistics: Bosons and Fermions

To further understand the significance of achieving low temperatures, it is important that we highlight the fundamental nature of atoms and their statistical distribution in thermal equilibrium.

Atoms exhibiting classical behavior: For a system of non-interacting distinguishable particles, Maxwell-Boltzmann (M-B) statistics describes their average distribution over various energy states in thermal equilibrium. M-B statistics is applicable when the temperature is high enough or the particle density is low enough to render quantum effects negligible [10]. The expected number of particles $\langle N_i \rangle$ with energy ε_i in state i is

$$\text{Maxwell-Boltzmann statistics}: \quad \langle N_i \rangle = \frac{g_i}{e^{(\varepsilon_i - \mu)/k_B T}}. \tag{1.1}$$

Here, ε_i is the energy of the i^{th} state and g_i is the degeneracy of energy level i, i.e. number of states with energy ε_i. The chemical potential μ is obtained from the normalization condition that $\sum_i \langle N_i \rangle = N$, where N is the total number of particles. In Fig. 1.2(a), we illustrate Equation (1.1) with the occupation distribution at different temperatures as a function of state energy (with respect to μ). As the temperature is continuously lowered, it is evident that an increasing number of atoms tend to occupy states with smaller energy (as an exponentially decreasing function of $(\varepsilon_i - \mu)/k_B T$).

When particles are further cooled to lower temperatures, they no longer obey M-B statistics. As described in Sec. 1.1, below a certain critical temperature, quantum mechanical nature of particles becomes dominant, and a description in terms

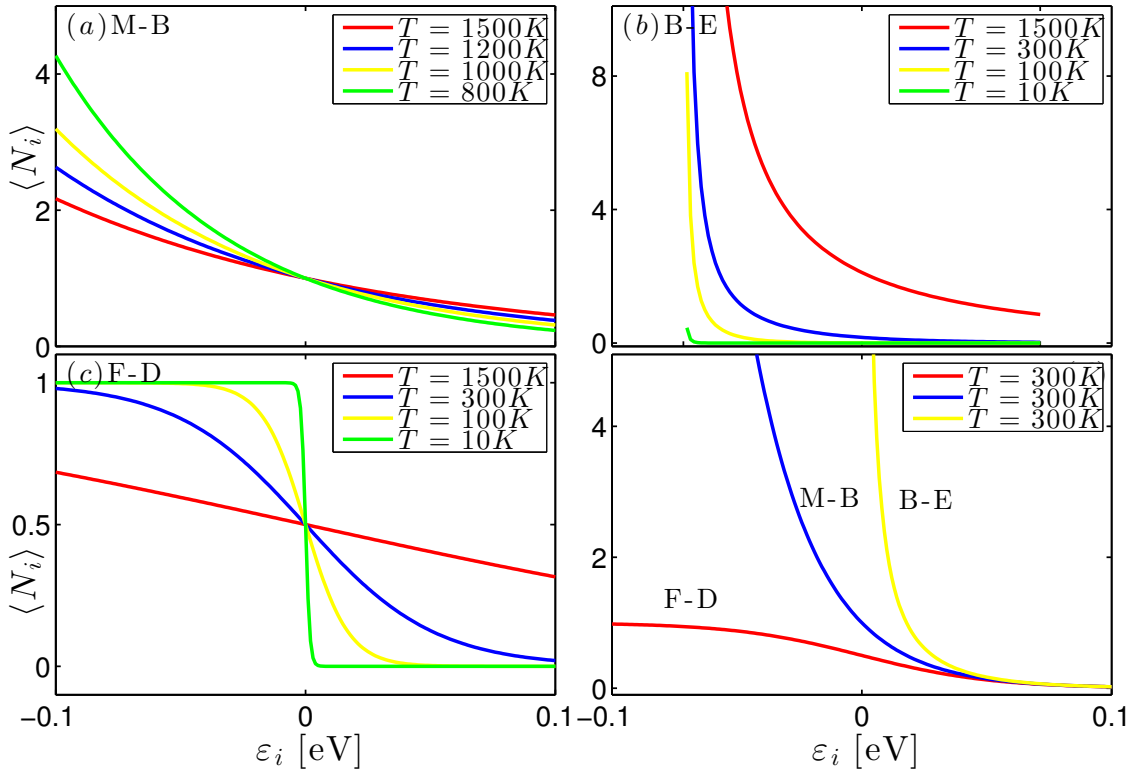

Figure 1.2 : Occupation distribution at different temperatures as a function of state energy ε_i (with respect to μ): (a) Maxwell-Boltzmann statistics (b) Bose-Einstein statistics (c) Fermi-Dirac statistics (d) A comparison of different statistical functions (at a fixed temperature) clearly illustrates the macroscopic manifestation of quantum statistics. The degeneracy of energy level g_i is assumed to be unity in all plots, and in the accompanying discussion*.

of atomic wavepackets becomes appropriate. As atomic wavepackets begin to overlap, the atomic ensemble may be classified into two distinct classes based on their quantum statistics - Bosons and Fermions.

Fermionic atoms: Fundamental particles such as electrons, protons, and neutrons are identical quantum particles, each with an intrinsic half-integer quantum spin.

*At first sight, distributions at a temperature of $T = 300K$ may seem too high to display macroscopic quantum statistical effects. As elaborated in Sec. 1.5, what matters is not an absolute temperature scale, but rather the temperature relative to other energy scales in the system.

They are grouped in a generic class as fermions and obey the Pauli-exclusion principle that includes the condition that no two identical particles occupy the same state. An atom with a cumulative odd integer sum of these fundamental particles will have a net half-integer spin, and hence acts as a composite fermion. For example, ^{6}Li atom is a composite fermion since it has 3 electrons, 3 protons, and 3 neutrons.

If an ensemble of fermionic atoms is assumed to have negligible mutual interaction, the many-particle system may be described in terms of single-particle energy states. Even in such a simple setup, the Pauli-exclusion principle has a considerable effect on the properties of the system at low temperatures. The result is the Fermi-Dirac (F-D) distribution of fermionic atoms in thermodynamic equilibrium, where the expected number of particles $\langle N_i \rangle$ with energy ε_i is

$$\text{Fermi-Dirac statistics}: \quad \langle N_i \rangle = \frac{g_i}{e^{(\varepsilon_i - \mu)/kT} + 1}. \tag{1.2}$$

While the parameters have similar roles as described in Eqn. (1.1)*, $\mu(T = 0) = E_f$ is typically called the Fermi level. The F-D distribution is only valid if the number of fermions in the system is large enough so that adding one more fermion to the system has negligible effect on μ [11]. Since the F-D distribution is derived using the Pauli exclusion principle, which allows at most one electron to occupy each possible state, the result is that $0 < \langle N_i \rangle < 1$ (assuming $g_i = 1$). In Fig. 1.2(c), we show the distribution of identical fermions over single-particle energy states at different temperatures. As temperature is continuously lowered, the F-D distribution tends towards a unique transition†: at zero temperature, all states that satisfy the condition $(\varepsilon_i - \mu) < 0$ are occupied by one fermion ($\langle N_i \rangle = 1$) and rest of the states are not

*In the function's denominator, '+1' statistically accounts for the identical nature of fermions.

†Experimental signatures in proximity of this transition are discussed in Sec. 1.3.2.

occupied ($\langle N_i \rangle = 0$).

Bosonic atoms: An atom with a cumulative even integer sum of half-integer spin fundamental particles will have a net integer spin, and hence acts as a composite boson. For example, ^{7}Li is a composite boson, since it has 3 electrons, 3 protons, and 4 neutrons. Similar to their fermionic counterpart, a many-body system of bosons with negligible mutual interaction may be described in terms of single-particle energy states. Bosons are identical quantum particles that are statistically allowed to occupy the same energy state, which has a considerable effect on the properties of the system. The result is the Bose-Einstein (B-E) distribution of these quantum particles in thermodynamic equilibrium, and the expected number of particles $\langle N_i \rangle$ with energy ε_i is

$$\text{Bose-Einstein statistics}: \quad \langle N_i \rangle = \frac{g_i}{e^{(\varepsilon_i - \mu)/kT} - 1} \text{ with } \mu < 0, \tag{1.3}$$

where the parameters have the same definitions as in Eqn. (1.1)*. In Fig. 1.2(b), we show the distribution of identical bosons over single-particle energy states at different temperatures. At low temperatures, bosons behave very differently from fermions because a macroscopic (in principle, unlimited) number of bosons can occupy the same low-energy state, a phenomenon called condensation (Sec. 1.3.2).

1.3 Quantum gases: ultracold dilute atomic gases

Largely inspired by Leggett's definition of quantum liquids, a quantum gas is defined to be a many-particle system in the gaseous phase in whose behavior not only the effects of quantum mechanics, but also those of quantum statistics, are important [9]. Based on the considerations in Sec. 1.1 and Sec. 1.2, we see that for a quantum gas

*Condition $\mu < 0$ ensures that the function converges; '-1' in the denominator statistically accounts for the identical nature of bosons.

to manifest itself, the atoms must be cooled until the thermal de Broglie wavelength is on the order of the spacing between atoms, $\lambda_{dB} \simeq d$ [7, 9]. In this scenario, the atomic wavepackets begin to become degenerate and indistinguishability starts to play a critical role. The densities required to achieve degeneracy in a three-dimensional atomic gas is determined by the condition $\lambda_{dB}^3 n \simeq 1$. Therefore, we find that the criterion for a quantum gas to appear is

$$k_B T^* \lesssim n^{2/3} \hbar^2 / m, \tag{1.4}$$

where $\hbar = h/2\pi$. The temperature, T^*, at which this degenerate quantum state appears is typically referred to as the quantum degeneracy temperature. With the advent of innovative cooling techniques, physicists now prepare novel quantum gases: atomic clouds of various species, which are in a metastable gaseous phase at ultra-low temperatures for a long enough time [7].

1.3.1 Trapping and cooling

To achieve the quantum degeneracy temperature or lower, atoms are trapped with magnetic fields or with laser light inside ultrahigh vacuum chambers [12, 13]. As stated by Ketterle *et al.*, such a setting allows atoms to be thermally isolated from all material walls [7]. Such traps can store atoms for seconds or even minutes, which is enough time to cool them. The number of atoms typically ranges between a few thousands to several millions [7]. Thus, trapping of atomic gases is of paramount importance to confine atoms and achieve cooling. In the words of Ketterle *et al.*, pre-cooling is a prerequisite for trapping because conservative atom traps can only confine neutral atoms with a maximum energy of one Kelvin at best (and in many

cases the trap depth is just a few milli-Kelvin) [7]. While pre-cooling is usually done by laser cooling, the final cooling is done by evaporative cooling methods. Several useful resources exist that illustrate the fundamental physical processes governing these cooling techniques, as can be found, for example, in Refs. [14–16].

Let us now briefly review the atomic species of interest to ultracold atomic physics before presening an overview of the frontiers in low-temperature physics research. Alkali atoms have a simple electronic structure and low-lying excited states, and hence are ideal systems for cooling and trapping [7]. Among alkali atoms, the two stable fermionic isotopes, ^{6}Li and ^{40}K, have become the main workhorses in the field [17–19]. Bosonic atomic species of interest are ^{7}Li, ^{87}Rb, and ^{23}Na [20–22]. Recently, there has been tremendous experimental progress in achieving quantum degeneracy in alkaline earth metal atoms. In this class, atomic species of interest to ultracold temperature physics are ^{173}Yb, ^{87}Sr (fermions), and ^{88}Sr (boson) [23–25]. It is important to note that a given trap configuration confines only certain atomic states, depending upon their response to the electromagnetic fields. In general, cooling of atomic gases to ultracold temperatures is very much a species-specific and state-specific technique.

Frontiers of low-temperature physics research: Trapping and cooling of atomic gases, specifically those of alkali atoms, have played an essential role in achieving ultra-low temperatures in the recent past. Several of the developments either led to cooling atoms to new limits or cooling of new species. Since Onnes's remarkable technological achievement in liquefying helium (^{4}He) in 1908, we have witnessed phenomenal progress towards reaching lower temperatures in the last 100 years. Large-scale cryogenic equipment and dilution refrigerators were predominantly used in achieving low temperatures (in the milli-Kelvin range) in the major part of the 20$^{\text{th}}$ century. This led to remarkable discoveries that included liquefaction of N_2 and ^{4}He, and observa-

tion of superfluidity in ^{4}He and ^{3}He. With the discovery of laser cooling of atomic gases in the 1970'-s, researchers embarked on a route to using atomic species-specific techniques, as compared to generic cryogenic techniques used earlier. Within the realm of laser cooling, Doppler and Sisyphus cooling techniques enabled researchers to slow atoms down and achieve temperatures that were hitherto impossible to reach (micro-Kelvin range) [12, 13]. With the innovative application of evaporative cooling techniques in the 1990'-s, trapped atomic gases are now routinely cooled down to ultra-low temperatures (nano-Kelvin range). We emphasize that these achievements mark the coldest temperatures ever achieved in experiments, nearly 11 orders of magnitude below room temperature [7, 12]. Furthermore, scientists continue to make commendable strides to achieve even lower temperatures and lower entropies, and to theoretically understand the intriguing, and often non-intuitive, physical phenomena that determine the behavior of atoms and electrons at low temperatures.

1.3.2 Quantum degeneracy and condensation

At high temperatures or at low concentrations, all atoms behave classically with no apparent distinction between bosons and fermions. In this section, we discuss the manifestation of quantum degeneracy and condensation in fermionic and bosonic atoms at ultracold temperatures through a cartoon depiction in Fig. 1.3, and through experimental measurements in Fig. 1.4.

Let us assume that a gas of alkali atoms is trapped in an isotropic harmonic potential. The atoms distribute themselves in discrete energy levels, whose energy spacing is determined by the curvature (frequency) of the harmonic trapping potential, as shown in Fig. 1.3. At temperatures much higher than the quantum degeneracy temperature, T^*, the classical nature of atoms still dominates their motion and statis-

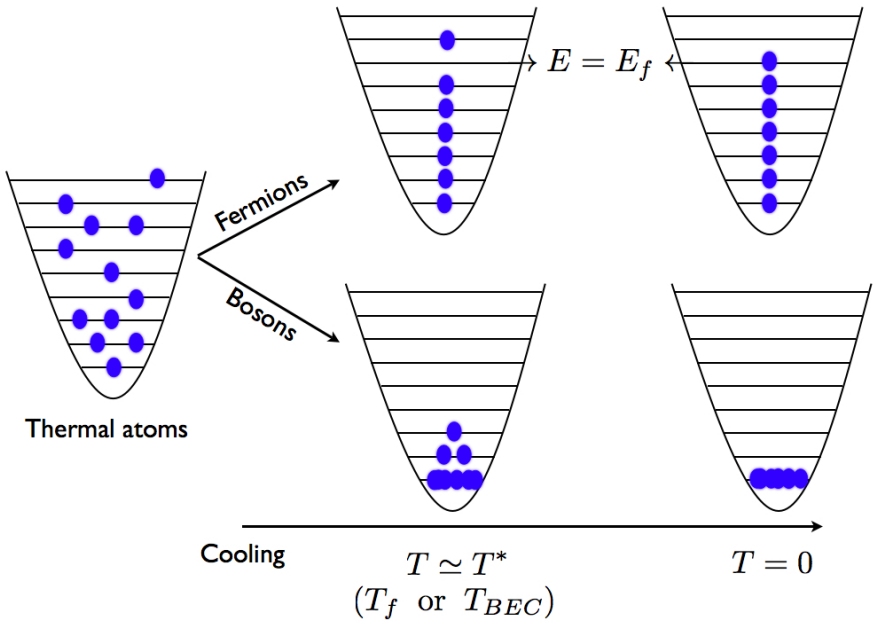

Figure 1.3 : Illustrating quantum degeneracy and condensation phenomena in ultra-cold fermionic and bosonic gases upon cooling.

tical distribution. In the vicinity of $T \simeq T^*$, quantum statistical properties begin to become dominant, and a distinction between fermionic and bosonic atoms emerges.

Bose-Einstein condensation: In a gas of bosonic atoms, we observe a striking manifestation of the B-E statistics as illustrated in the bottom panel of Fig. 1.3. B-E distribution allows multiple atomic occupation of energy levels, and hence atoms begin to predominantly occupy lower energy levels at temperatures in the proximity of T^*. When bosonic atoms are cooled further to reach a threshold transition temperature, (essentially) all bosonic atoms condense to occupy the lowest energy level, a distribution referred to as Bose-Einstein condensation. The transition temperature to this condensed state is referred to as Bose-Einstein condensate (BEC) transition temperature, T_{BEC}. At zero temperature, all atoms occupy the lowest energy level

forming a pure BEC.

Table 1.1 : Multi-stage cooling to BEC in the MIT experiment. Through a combination of optical and evaporative cooling, the temperature of a gas is reduced by a factor of 10^9, while the density at the BEC transition is similar to the initial density in the atomic oven (all numbers are approximate). Courtesy: Ketterle *et al.* in Ref. [7].

Stage	Temperature	Density (cm^{-3})	Phase-space density
Oven	500 K	10^{14}	10^{-13}
Laser cooling	50 μK	10^{11}	10^{-6}
Evaporative cooling	500 nK	10^{14}	1
BEC			10^{7}

In order to create a BEC, the atomic gas must be cooled and compressed in a trap to reach quantum degeneracy. As an illustration of this process in real experiments, Table. 1.1 shows a typical example of how these cooling techniques together reduce the temperature of the atoms by a factor of a billion. As stated by Ketterle *et al.* in Ref. [7], Bose-Einstein condensation can be regarded as 'free cooling', as it increases the quantum occupancy by another factor of about a million without any extra effort. This reflects one important aspect of the BEC: the fractional population of the ground state is no longer inversely proportional to the number of states with energies smaller than k_BT, but quickly approaches unity when the sample is cooled below the transition temperature [7]. As expected, we observe this behavior in the illustrative statistical distribution plots in Fig. 1.2(b). Furthermore, it is important to understand the 'window' in density for achieving bosonic degeneracy. Citing Ketterle *et al.* in Ref. [7], at densities below 10^{11} cm^{-3}, thermalization is extremely slow, and evaporative cooling can no longer compete with (technical) sources of heating and loss. At densities above 10^{15} cm^{-3}, losses due to three-particle collisional losses usually become dominant [7].

Table 1.2 : Various stages towards a quantum degenerate Fermi sea in the MIT experiment. Through a combination of laser cooling and sympathetic cooling, the temperature is reduced by 9 orders of magnitude. Courtesy: Inguscio *et al.* in Ref. [17].

Stage	Temperature	Density	T/T_F
Oven	720 K	$10^{14}\,\mathrm{cm}^{-3}$	10^8
Laser cooling (*Zeeman slower* & *MOT*)	1 mK	$10^{10}\,\mathrm{cm}^{-3}$	10^4
Sympathetic cooling (*Magnetic trap*)	1 μK	$10^{13}\,\mathrm{cm}^{-3}$	0.3

Quantum degenerate Fermi sea: When a gas of fermionic atoms is cooled towards the degeneracy temperature, the quantum statistical nature of the F-D distribution begins to emerge as illustrated by the cartoon in the top panel of Fig. 1.3. We observe a striking manifestation of the Pauli-exclusion principle. At temperatures in the proximity of $T \simeq T^* = T_f$, nearly all energy levels below the Fermi energy ($E = E_f$) are occupied by one atom each and nearly all levels above E_f are empty. Fluctuations in the occupation distribution typically occur close to the Fermi energy level E_f. As the temperature decreases further below T_f and eventually to $T = 0$, only energy levels up to E_f are occupied by one atom each. Thus, fermionic atoms reach degeneracy in this non-intuitive fashion, referred to as the Fermi sea. The 'window' in density and temperature for achieving fermionic degeneracy is similar to the BEC window. In this density window, fermionic degeneracy is typically achieved at temperatures between 100 nK and 5 μK [17]. The cooling and trapping techniques to reach such low temperatures are similar to those that have been developed for BEC. A crucial difference is the inclusion of fermions (or bosons) of other state or species to cool the fermions under study, a mechanism rightly termed as sympathetic cooling. Due to the Pauli-exclusion principle, identical fermions are unable to undergo the collisions

necessary to rethermalize the gas during evaporation and therefore unable to undergo evaporative cooling by themselves. In Table. 1.2, we show a typical example of the different cooling stages to reach a quantum degenerate Fermi sea with alkali atoms in the MIT experiment [17].

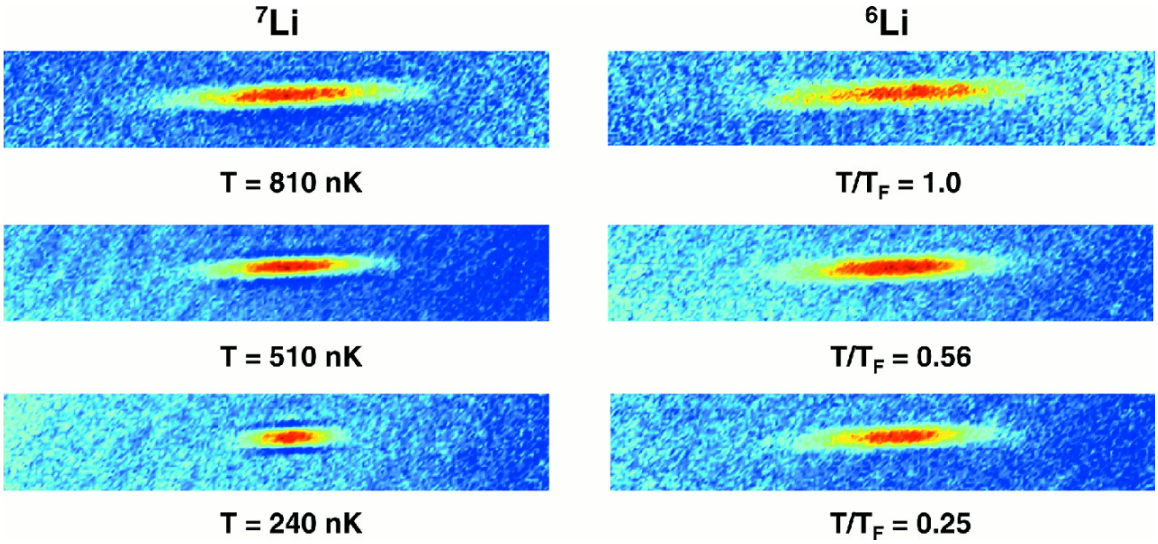

Figure 1.4 : Two-dimensional false-color images of both ^{7}Li and ^{6}Li clouds. At $T/T_f = 1.0$, the two clouds are approximately the same size, but as the atoms are cooled further, to $T/T_f = 0.56$, the Bose gas contracts, whereas the Fermi gas exhibits only subtle changes in size. At $T/T_f = 0.25$, the size difference between the two gases is clearly discernible. Figure reprinted with permission from AAAS: Truscott et al., Science 291, 2570 (2001) in Ref. [19]. Copyright License Number: 3330250950101.

In a pioneering experiment, Hulet's group at Rice University illustrated the simultaneous condensation of bosonic atoms to a BEC and fermionic atoms to a quantum degenerate Fermi sea [19]. In Fig. 1.4, we reproduce these seminal results showing exotic manifestations of macroscopic quantum statistical properties in a mixture containing bosonic ^{7}Li atoms and fermionic ^{6}Li atoms. An important aspect of trapped atomic gases is their inhomogeneity, which leads to several important consequences, especially to atomic Bose gases. As illustrated above, BEC shows up not only in

momentum space, but also in coordinate space, i.e., the BEC may be considered to be a macroscopic object physically present in the center of the trap, as well as a macroscopic occupation of atoms in the zero-momentum state in momentum (energy) space [26]. This double possibility of investigating the effects of condensation is very interesting from both the theoretical and experimental viewpoints. For instance, this provides novel methods for investigation of frequencies of collective excitations [26].

1.4 Experimental control and tunability

Ultracold trapped-atom experiments offer the unique possibility to understand many-body physics beyond what can be explored in typical condensed matter settings [27]. Essentially, they provide clean many-body systems in which attributes like trap dimensionality, atomic states, density, and interactions, may be controlled with commendable precision [7, 17, 28]. In this section, we briefly review the techniques and opportunities to manipulate some of these attributes in experiments.

1.4.1 Trap geometry and dimensionality

In most experimental scenarios, the confining traps are well approximated by harmonic potentials. The confining trapping potential in 3-dimensions takes the generic quadratic form: $V_{\rm ext}(\mathbf{r}) = (M/2)(\omega_x^2 x^2 + \omega_y^2 y^2 + \omega_z^2 z^2)$, where M is the mass of atom and $\omega_{x,y,z}$ represent frequencies in different directions. It is typical to use frequency ω_{ho} to represent the geometric mean of trapping frequencies in different directions. Parameter ω_{ho} also provides a characteristic length scale for the system, $a_{ho} = \sqrt{\hbar/(M\,\omega_{ho})}$, of the order of a few microns.

The harmonic potential $V_{\rm ext}(\mathbf{r})$ holds for generic three-dimensional (3D) trapping geometries. If experiments are set up such that $\omega_x = \omega_y = \omega_z$, an isotropic 3D

spherical harmonic potential is achieved [7]. Furthermore, two-dimensionality can be readily realized by imposing a strong harmonic potential $V(z) = M\omega_z^2 z^2/2$ along axial direction, in such a way that $\mu, k_B T \ll \hbar\omega_z$ [29]. In the bulk of this thesis, we consider atomic Bose gases confined in two-dimensional (2D) trap geometries. A variety of interesting many-body quantum phenomena may be explored in such experimental settings [27]. If the trap geometry is further deformed such that the confinement in two orthogonal directions is made much tighter compared to that in the third, the system can be effectively considered to be 1-dimension. In such a case, the trapping frequency in the tight directions is such that $\mu, k_B T \ll \hbar\,\omega_{\rm tight}$. The ability to simulate the behavior of atomic gases in one-dimensional (1D) geometries opens the possibility to study exotic correlations that exclusively occur in 1-dimension [27, 30].

In addition to modifying the dimensionality of the trapping potential, there are other attributes related to trap geometry that can be controlled in experiments. For example, the tightness of the trap may be controlled by modifying the trapping frequency. This becomes specifically important in multiple-species experiments, where either species could be confined in tighter traps. Such a consideration is completely justified as the trapping potential for each species can be independently controlled [17]. Another example of engineering trapping potentials is the creation of double-well traps. In this case, trapping potential has a finite barrier near the center: $V(\mathbf{r}) = (1/2)\,M\,\omega_\perp(x^2+y^2) + (1/2)\,M\,\omega_z z^2 + V_0\exp(-z^2/2\sigma^2)$. Here, $\omega_\perp$ (ω_z) is the trap frequency in the transverse (longitudinal) direction to the Gaussian beam creating the trapping potential, and V_0 and σ define the barrier peak and beam-width, respectively. In Appendix A, we illustrate several of these interesting possibilities in realistic experimental settings and study the behavior of a mixture of Bose and Fermi superfluids.

1.4.2 Interaction strengths

Ultracold trapped atomic gases are typically very dilute in nature. For instance, the average distance between atoms is more than ten times the range of interatomic forces [26]. As stated by Dalfovo *et al.* in Ref. [26], despite the inhomogeneity present in these systems due to trapping potential, which makes the solution of the many-body problem nontrivial, the dilute nature of the gas allows one to describe the effects of the interaction in a rather fundamental way. Interestingly, a single parameter that describes the two-body contact interaction, the s-wave scattering length, is sufficient to obtain an accurate description of Bose gases [26]. In single-component Fermi gases, the Pauli-exclusion principle obviates the possibility of s-wave contact interaction, but a higher order p-wave scattering length is sometimes used in relevant scenarios* (for example, see Ref. [31]).

In addition to the inherent interatomic forces present in alkali gases, Feshbach resonances act as an important tool to control and tune the interaction between ultracold atoms. In Fig. 1.5, we briefly review the physical origin and the elementary properties of a Feshbach resonance. The key features of a magnetically-tuned Feshbach resonance can be captured by a simple expression†, for the s-wave scattering length a as a function of the magnetic field B:

$$a(B) = a_{\rm bg}\left(1 - \frac{\Delta}{B - B_0}\right) . \tag{1.5}$$

*s-wave contact interaction is allowed in two-component Fermi gases (being non-identical). In Appendix A, we discuss this scenario and the possible emergence of interaction-driven s-wave superfluidity.

†We note that this simple expression in Eqn. (1.5) applies to resonances without inelastic two-body channels. Some Feshbach resonances, especially the optical ones, feature inelastic decay processes and a more general discussion is given in Appendix B.

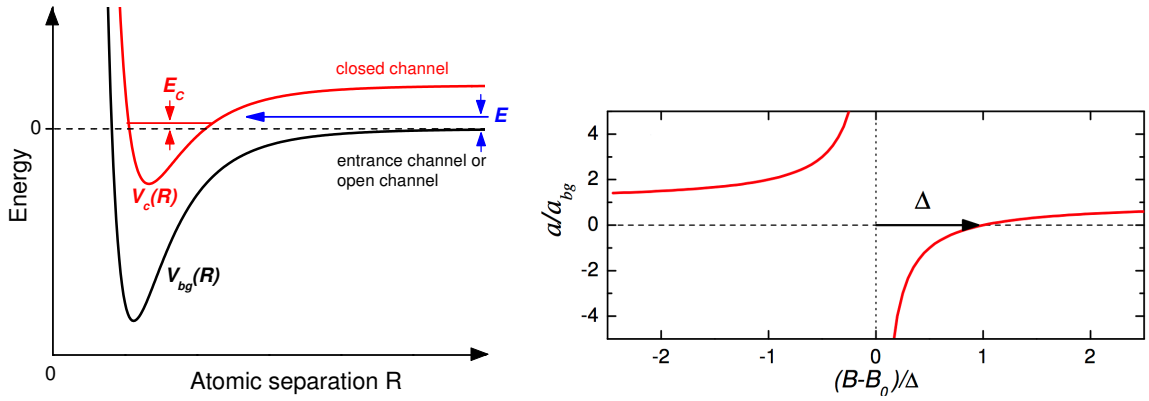

Figure 1.5 : (a): left, Feshbach resonance occurs when two atoms colliding at energy E in the entrance channel resonantly couple to a molecular bound state with energy E_c supported by the closed channel potential. In the ultracold domain, collisions take place near zero-energy, $E \to 0$. Resonant coupling is then conveniently realized by magnetically tuning E_c near 0, if the magnetic moments of the closed and open channels differ. (b): right, s-wave scattering length a near a magnetically tuned Feshbach resonance. Image adapted and reprinted with permission from "Feshbach resonances in ultracold gases": Cheng Chin, Rudolf Grimm, Paul Julienne, and Eite Tiesinga, Rev. Mod. Phys. 82, 1225-1286 (2010). Copyright (2014) by the American Physical Society.

Figure 1.5(b) illustrates this resonance expression. Parameters $a_{\rm bg}$, B_0, and Δ represent the background scattering length, resonance position, and the resonance width respectively.

1.5 Applications with ultracold atomic gases

We have seen enormous progress in cooling atomic gases to ultracold temperatures, where quantum degeneracy and condensation sets in. As Onnes had rightly predicted [6], theoretical and experimental progress in reaching ultracold temperatures continue to help us unearth fundamental aspects about the behavior of matter when thermal motion is made insignificant. It would be natural to wonder about potential applications with ultracold atomic gases. It is important to remember that only

nearly thirty years from the invention of lasers that we started using it in our daily lives [32]. With similar optimistic projections, we will probably see ultracold atomic gases finding innovative applications in the near future. That said, several proposals, prototypes, and benchmark results already exist for practical applications. We shall review some of these exciting prospects in this section.

Quantum metrology: Quantum metrology is the study of making high-resolution and highly sensitive physical measurements using principles based on quantum theory [33]. For example, ultracold gases have exciting potential applications towards precision measurement of fundamental constants. This in-turn has innovative possibilities to improve navigation, mining, and oil exploration, to name a few. Another possibility is gravimetry, the measurement of the strength of a gravitational field. An interesting prospect in gravimetry is gravity gradient sensing, which is defined as a measure of how gravity changes with height. An accurate measurement of gravity gradients is attractive to, for example, operators in oil and natural gas exploration and mining, in that it being a passive technology. Atom interferometry, based on the fact that atoms have wave-like attributes at low temperatures, has some exciting features that promise to overcome current limitations in gravity gradient sensing. In Fig. 1.6, we illustrate the basic idea of atom interferometric gravity gradient sensors. The article by Bongs in Ref. [34] and Midlands ultracold atom research centre (MUARC) webpage in Ref. [35] provide excellent motivations on this prospect.

Furthermore, phenomenal prospects exist for gravimetry applications in space. Inspirational work is being performed by the Stanford research group of Kasevich, as elaborated in Refs. [37–41]. Atom interferometers have the potential to make sensitive gravitational wave detectors which would reinforce our fundamental understanding of gravity and provide a new means of observing the universe [37]. While techniques

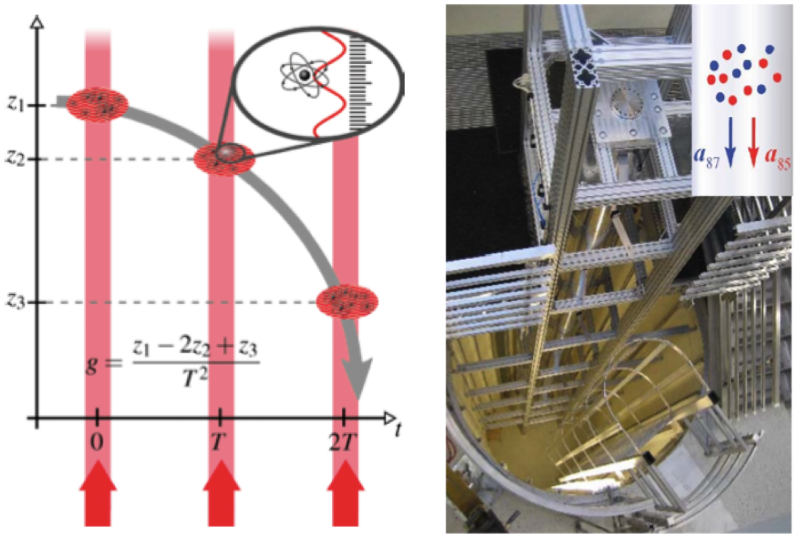

Figure 1.6 : (a): left, Basic idea of atom interferometric gravity gradient sensors is simple: they measure the trajectories of two vertically separated ensembles of atoms under the influence of gravity using a laser ruler. The gravity gradient will show up in tiny differences in how the two ensembles drop: a density anomaly in the ground will attract the lower ensemble more than the higher one, leading to the lower ensemble to drop faster. Image and Caption adapted from Bongs in Ref. [34]. (b): right, 10-m drop tower: Atom interferometry for high precision quantum metrology. Image courtesy: Nasa webpage in Ref. [36] and Kasevich group in Ref. [37].

relevant to an atomic gravitational wave interferometric sensor (AGIS) are being investigated at the Stanford 10-m drop tower – Fig. 1.6(b) – to help in precise detection of terrestrial gravity waves, corresponding AGIS modules are also being designed for space gravity wave detection using atom interferometry in space with degenerate quantum gases. Similarly, several programs are aiming to develop the use of cold atoms in microgravity measurements and space-based atomic clocks [36, 42–44].

Quantum information: As stated by Stajic in Ref. [45] and as illustrated in Fig. 1.7, quantum information processing (QIP) uses qubits as its basic information units. QIP has many facets, from quantum simulation, to cryptography, to quantum computation, which is expected to solve problems more complex than those within the

capabilities of conventional computers. Examples of systems that are engineered to implement quantum computing include – trapped ions and neutral atomic gases at ultracold temperatures – and they play a tremendous role in advancing many facets of QIP.

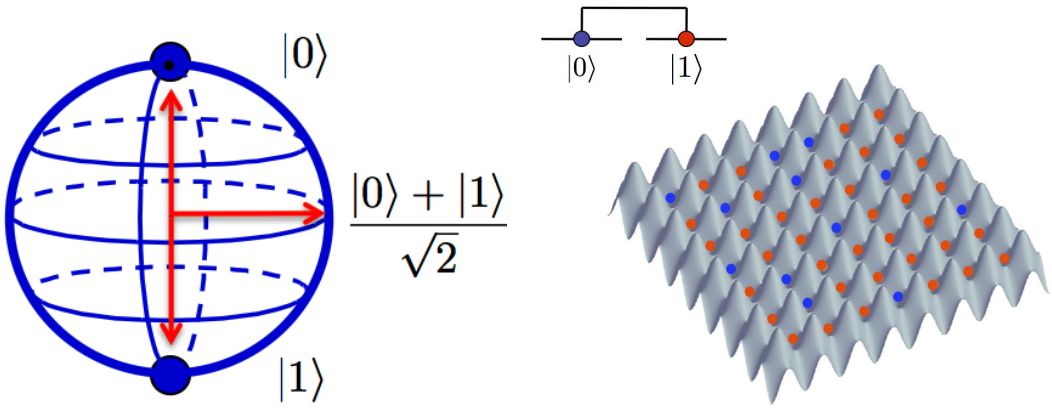

Figure 1.7 : (a): left, Qubit: A traditional BIT has two states: 0 or 1. Qubit, the quantum version of a bit, has many more possible states. The states can be represented by an arrow pointing at a location on a Bloch sphere. The north could be made equivalent to state $|0\rangle$, the south pole to state $|1\rangle$. The other locations are quantum superpositions of states $|0\rangle$ and $|1\rangle$. Caption and image adapted from Refs. [46, 47]. (b): right, Quantum register in an optical lattice: An optical lattice is formed by the interference of counter-propagating laser beams, creating a spatially periodic polarization pattern. Atoms are cooled and congregate in the locations of potential minima. The resulting arrangement of trapped atoms resembles a crystal lattice [48]. Here, we see the potential realization of a quantum register encoded on long-lived internal states of cold neutral atoms in an optical lattice potential. Image and caption adapted from University of Pittsburgh webpage in Ref. [47].

Quantum simulation: Richard Feynman, during his seminal lecture 'Simulating Physics with Computers' in 1981, memorably said: 'Nature isn't classical, dammit, and if you want to make a simulation of nature, you'd better make it quantum mechanical, and by golly it's a wonderful problem, because it doesn't look so easy' [49, 50]. Ultracold quantum gases in optical lattice potentials offer a unique setting for quantum simulation of interacting many-body systems. As stated by Bloch *et al.* in

Table 1.3 : Transition temperatures, Fermi temperatures and their ratio T_C/T_F for a variety of fermionic superfluids or superconductors. Table adapted from Inguscio *et al.* in Ref. [17].

System	T_C	T_F	T_C/T_F
Metallic Li at ambient pressure [52]	0.4 mK	55000 K	10^{-8}
Metallic superconductors (typical)	$1 \sim 10$K	$50000 \sim 150000$K	$10^{-4\cdots-5}$
^{3}He	2.6 mK	5 K	$5 \cdot 10^{-4}$
MgB_2	39 K	6000 K	10^{-2}
High-T_C superconductors	$35 \sim 140$ K	$2000 \sim 5000$ K	$1 \sim 5 \cdot 10^{-2}$
Neutron stars	10^{10} K	10^{11} K	10^{-1}
Strongly interacting atomic Fermi gases	200 nK	1 μK	0.2

Ref. [51], the high degree of controllability, the novel detection possibilities, and the extreme physical parameter regimes that can be reached in these 'artificial solids' provide an exciting complementary set-up compared with natural condensed-matter systems, much in the spirit of Feynman's vision of a quantum simulator. At first sight, it may sound ironic then that we could simulate quantum many-body systems using ultracold atoms at nano-Kelvin temperatures. These nominally low temperatures are often deceiving, because what matters is not an absolute temperature scale, but rather the temperature relative to other energy scales in the system (for example, the Fermi energy), and from this perspective, ultracold atom systems are often not that cold (Table. 1.3). Furthermore, ultracold atomic systems are among the simplest and most controllable of quantum many-body systems.

As stated by Galitski *et al.* in Ref. [53], in contrast to solid-state systems, in which we do not control or even know with certainty all details of the complicated material structure, ultracold atoms are remarkable in that most aspects of their environment can be engineered in the laboratory. Also, their tunable interactions and their single-

particle potentials are both well characterized: the full atomic Hamiltonian is indeed known [53]. This provides a level of control unprecedented in condensed matter and allows one to address basic physics questions at the intersection of material science and many-body theory. "To study material systems, theorists create 'spherical-cow' models of real materials, whereas in cold atom physics experimentalists can actually make spherical cows" [53]. For instance, phenomenal experimental progress has been achieved with atomic gases loaded in optical lattices to emulate traditionally condensed-matter Hamiltonians and associated phenomena [17, 27, 54]. For example, in a recent effort, physicists at ETH Zurich developed a quantum simulator that allows arranging atoms in a way such that they mimic the behavior of electrons in magnetic materials. The experiment opens up the possibility of systematically studying poorly understood properties of novel materials [55].

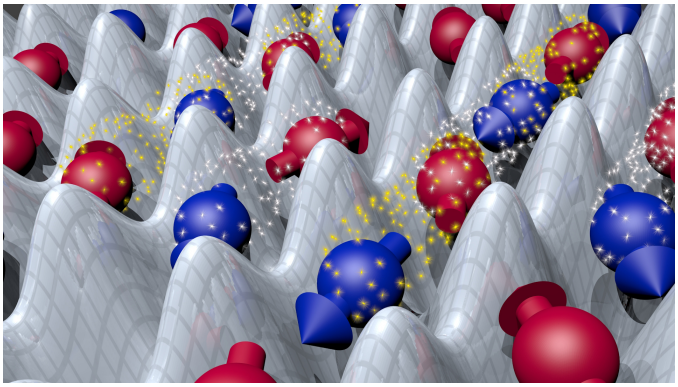

Figure 1.8 : In a magnetic material, electrons interact with each other. In this cartoon depiction of a quantum simulator, atoms (red and blue) may take the role of electrons. They are depicted to be embedded in a "crystal" (grey) made of interfering laser beams. Image and caption adapted from ETH Zurich webpage in Ref. [56].

Due to the neutral nature of atomic gases, however, most experimental systems were limited to exploring quantum phenomena that would occur in the absence of electromagnetic fields. Recently, even this limitation was overcome, when laser fields

were used to successfully generate *effective* magnetic and electric fields in neutral atoms [57, 58]. Such a manipulation of neutral atoms to experience 'synthetic' electromagnetic fields opens an entirely new paradigm for studying quantum many-body systems in experiments with ultracold atomic gases. Spin-orbit (SO) coupling is one such phenomenon that can be simulated with ultracold atoms [59–61]. SO coupling leads to many fundamental phenomena in a wide range of quantum systems from nuclear physics, condensed matter physics to atomic physics. In electronic condensed matter systems, SO coupling can lead to quantum spin Hall states or topological insulators [62], which have potential applications in quantum devices and are expected to retain their quantum nature up to room temperature. In the bulk of this thesis, we discuss in detail the underlying physics of SO coupled ultracold trapped atomic Bose gases. We sincerely believe that our work would further the fundamental understanding and play a significant role in the quantum simulation of this fascinating field of study.

1.6 Outline of Thesis

We begin Chapter 2 with the discussion of the basics of SO coupling in conventional systems in Sec. 2.1 and the realization of SO coupling in ultracold atomic gases in Sec. 2.2. Beginning with Sec. 2.3, we exclusively focus on Rashba SO coupling in atomic gases. We introduce the system under study in Sec. 2.3.1. In Sec. 2.3.2, we discuss the effect of inclusion of Rashba SO coupling in a homogeneous system and present its key attributes. In Sec. 2.3.3, we discuss the effects of including a harmonic trapping potential. This represents a significant scenario, since in a real experiment a confining trapping potential is necessarily present to prevent the atoms from escaping. In addition to being an experimental necessity, the confining trapping

potential allows for the emergence of novel physics in ultracold atomic systems. We derive single-particle solutions at small and large SO coupling strengths to illustrate that the nature of solutions is fundamentally different in these two limits [1, 2].

In Chapter 3, we present a detailed discussion of ground state phases at parameters that correspond to the weakly correlated regime. Mean-field theory provides a suitable approach to analyze this scenario. In Sec. 3.1, we present the system under study – an interacting many-body system of two-component Bose gases confined in a 2D isotropic harmonic trapping potential with Rashba SO coupling. In Sec. 3.2, we present a detailed discussion of the phase diagram of interacting gases at small SO coupling strengths in the weakly correlated regime. We show that in the presence of trap, bosons condense into a half-quantum vortex state and qualitatively show that it occupies a large part of the phase space at small SO coupling strengths. Subsequently in Sec. 3.3, we present an analogous discussion at large SO coupling strengths and present the phase diagram of weakly correlated ground state phases [1, 2].

In Chapter 4, we systematically explore the parameter space for the half-quantum vortex state and analyze its stability. We present the phase diagram as a function of SO coupling and interatomic interaction strengths. We do this by solving the Bogoliubov equations and computing the collective excitation spectrum, since they constitute one of the main sources of information for understanding the physics of many-body systems. Upon introducing this computational procedure in detail in Sec. 4.1, we present a discussion of its solutions in Sec. 4.2. In Sec. 4.3, we analyze the stability of the half-quantum vortex state by monitoring the softening of collective mode frequencies and by comparing the energy with that of competing states. We also investigate the dynamical properties of the half-quantum vortex state by directly simulating the real-time propagation of the mean-field ground state under perturba-

tions in Sec. 4.4. The collective excitation spectrum obtained from the Bogoliubov equations is then compared to the results from direct simulation. Finally, the stability of the half-quantum vortex state against both trap anisotropy and anisotropy in the SO coupling term is examined [2].

The results discussed in Chapter 3 are only valid for weak correlations with large number of bosons. Strongly correlated states would emerge with a small number of bosons and we address this possibility using the exact diagonalization (ED) scheme in Chapter 5. In Sec. 5.1, we begin by re-iterating the model Rashba SO coupling Hamiltonian introduced in Sec. 2.3.1 and discuss various symmetries. We proceed to discuss the implementation of the ED scheme to obtain the low-energy eigenstates of the interacting Hamiltonian in the regime of large SO coupling strengths. Then, we introduce various analysis techniques namely, energy spectrum, density distribution, single-particle density matrix, pair-correlation function, reduced wavefunction, entanglement spectrum, and entanglement entropy. Each technique would offer its unique perspective to the overall understanding of the ground state properties. In Sec. 5.2, we discuss the phase diagram and analyze the ground state properties of the interacting Hamiltonian at different particle numbers N, and at varied inter-atomic interaction strengths. At small particle numbers with $N = 2$, we illustrate the unique topological and symmetry properties of ground states. In the relatively large particle number scenario with $N = 8$, we observe that the ground states fall into two distinct regimes: (a) at weak interaction strengths (mean-field-like regime), we observe ground states with topological and symmetry properties that are also obtained via mean-field theory computations; (b) at intermediate to strong interaction strengths (strongly correlated regime), we report the emergence of strongly correlated ground states. We proceed to illustrate the topological, symmetry and strong correlation

properties of these ground states [3]. Finally in Chapter 6, we summarize and present concluding remarks.

Chapter 2

Rashba spin-orbit (SO) coupling

Ultracold atomic gases offer an exceptional platform to explore many-body quantum phenomena due to outstanding experimental control over interatomic interactions, system geometry, density, and purity [27, 54]. Numerous research groups have, for example, successfully demonstrated the manifestation of few-body bound states and superfluid states in Bose and Fermi gases in trapped atom experiments [63–66]. Furthermore, phenomenal experimental progress has been achieved with atomic gases loaded in optical lattices to emulate traditionally condensed-matter phenomena like superfluid-insulator transition, anti-ferromagnetism, and frustrated many-body systems [67–71]. Until recently, most experimental systems were limited to exploring quantum phenomena that would occur in the absence of electromagnetic fields. For instance, condensation of ultracold Bose and Fermi gases (Sec. 1.3.2) occurs despite the charge neutrality of atoms.

In two seminal publications, Spielman's group at Joint Quantum Institute generated *synthetic* electric and magnetic fields in ultracold Bose gases [57, 58]. To understand the significance of these realizations, let us consider the simple scenario of a particle with charge q in a magnetic field $\mathbf{B}$. In the classical electromagnetism formulation, the Lorentz force for a particle is $\mathbf{v} \times q\mathbf{B}$, where v is the velocity of the particle in the magnetic field. In an equivalent quantum Hamiltonian formalism, we may write the single-particle Hamiltonian as $\mathcal{H} = \hbar^2(\mathbf{k} - q\mathbf{A}/\hbar)^2/2M$, where M is the mass and $\hbar\mathbf{k}$ is the canonical momentum [57]. In the latter formalism, potentials

play defining roles as compared to fields. The vector potential $\mathbf{A}$ gives rise to a magnetic field, as $\mathbf{B} = \nabla \times \mathbf{A}$. As shown in the experimental realization in Ref. [57], the authors engineer a Hamiltonian with a spatially dependent vector potential $\mathbf{A}'$ that produces an artificial magnetic field for neutral atoms: $\mathbf{B}' = \nabla \times \mathbf{A}'$. Similarly in the experimental realization in Ref. [58], the authors engineer a Hamiltonian with a time-dependent vector potential $\mathbf{A}'$ that produces an artificial electric field for neutral atoms: $\mathbf{E}' = -\partial \mathbf{A}'/\partial t$. This ability to generate synthetic electric and magnetic fields in neutral atoms has opened an entirely new paradigm for studying quantum many-body systems in experiments with ultracold atomic gases.

2.1 Basics of SO coupling

The* angular momentum of a classical spinning top can take on any arbitrary continuous value [53]. In contrast, for example, the electron's spin angular momentum along a given direction is discrete and can take only two values: $\pm\hbar/2$. The two spin states are commonly referred to as spin-up or spin-down states, and are represented by $|\uparrow\rangle$ or $|\downarrow\rangle$ respectively. In general, the spin of a quantum particle is its intrinsic quantum mechanical attribute with no classical counterpart, and is quantized. In contrast, a quantum particle's velocity or momentum (linear or orbital momentum) is directly related to classical particle's counterpart [53]. An interesting scenario would then be to consider the coupling of particle's spin with its momentum, and study its consequences. Such a scenario is termed as spin-orbit (SO) coupling and this mechanism has the potential to bring quantum mechanics to the forefront [53]. In materials, this essentially means that the quantum effects could possibly be re-

*The following introduction is largely inspired by the seminal review article in Ref. [53]: "Spin-orbit coupling in quantum gases": Victor Galitski, and Ian B. Spielman, Nature 494, 49 (2013).

tained up to room temperature and contribute to exotic phenomena with potentially spectacular applications [62, 72].

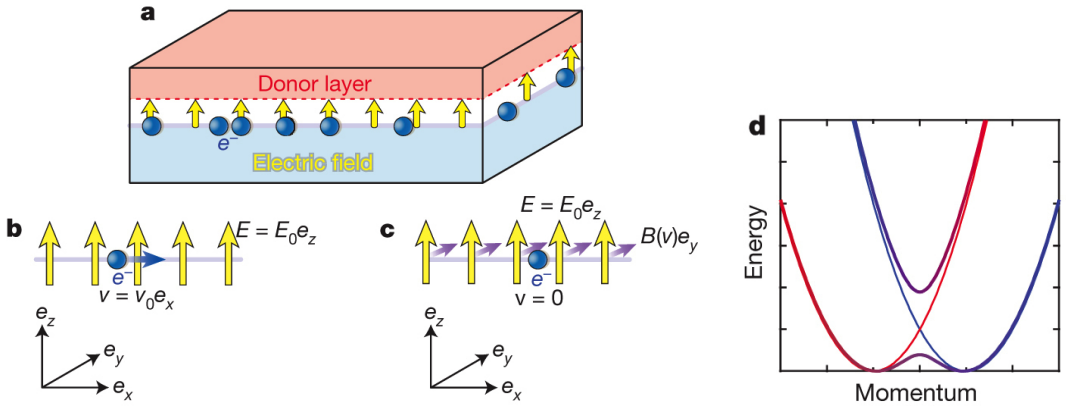

Figure 2.1 : (a), In materials, SO coupling requires a broken spatial symmetry. For example, the growth profile of 2D GaAs electron (or hole) systems can create an intrinsic electric field, thereby breaking inversion symmetry. (b), Model system in laboratory frame. The effective model system consists of an electron confined in the $e_x - e_y$ plane (in this example moving along e_x) in the presence of an electric field along e_z, $\mathbf{E} = E_0\, e_z$. (c), Model system in electron's frame. In the rest frame of the electron, the Lorentz-transformed electric field generates a magnetic field along e_y (yielding a Zeeman shift) that depends linearly on the electron's velocity. The generated spin-orbit magnetic field $\mathbf{B}_{SO} = (E_0\,\hbar/Mc^2) \times (k_x e_y - k_y e_x)$ in the frame of an object moving with momentum $\hbar k$, where c is the speed of light in vacuum and M is the particle's mass. The resulting momentum-dependent Zeeman interaction $-\mu \cdot \mathbf{B}_{SO} \approx \hat{\sigma}_x k_y - \hat{\sigma}_y k_x$, with spin-magnetic moment μ written in terms of Pauli spin matrices $\hat{\sigma}$, is known as Rashba SO coupling [73]. (d), Dispersion of resulting Rashba SO coupling. For such systems the SO coupling is linear, and the usual free-particle $mv^2/2 = p^2/2m$ dispersion relation is altered in a spin-dependent way. In this case, pure Rashba SO coupling shifts the free-particle dispersion relations for each spin state away from zero (red and blue curves). Image and caption adapted with permission from Macmillan Publishers Ltd: [Nature] "Spin-orbit coupling in quantum gases": Victor Galitski, and Ian B. Spielman, Nature 494, 49 (2013). Copyright License Number: 3327120846161. Copyright (2014).

The presence of SO coupling in conventional atomic physics systems generates atomic fine-structure splitting. It is from this context that the phenomenon acquires its name, as a coupling between an electron's spin and its orbital angular momentum

about the atom's nucleus [53]. The charged nucleus produces an electric field in the stationary laboratory frame. On the other hand, an orbiting electron experiences a magnetic field in its co-moving frame of reference. In this reference frame, if the particle possesses a magnetic moment μ parallel to the spin, a Zeeman interaction energy term is present in the form $-\mu \cdot \mathbf{B}$. Therefore, the Zeeman interaction energy term represents the simplest way to understand SO coupling [53]. Generalizing this scenario, we can argue that SO coupling requires symmetry breaking, as the velocity is measured in a preferred reference frame of the particle. In materials, these usually originate either from a lack of mirror symmetry in 2D systems leading to the Rashba SO coupling, or from a lack of inversion symmetry in bulk crystals leading to linear Dresselhaus SO coupling. For example, Fig. 2.1 illustrates a possible manifestation of SO coupling in conventional electronic materials.

2.2 SO coupling in ultracold atomic gases

One of the noteworthy aspects of the ability to generate effective vector potentials in ultracold neutral atomic gases is the possibility to simulate SO coupling. Let us briefly review the mechanism of generation of SO coupling in ultracold gases using two-photon Raman transitions*. The Raman transition is driven by a pair of laser beams, each with wavelength λ. The two-photon Raman process corresponds to the absorption of a single photon from one laser beam and the stimulated re-emission of a photon into the second counter-propagating laser beam [53]. Each photon carries a recoil momentum p_R with magnitude h/λ. If we consider the atom-laser setup to be a closed system, the momentum-conservation principle requires that the atom absorbs

*The following introduction is largely inspired by the seminal review article in Ref. [53]: "Spin-orbit coupling in quantum gases": Victor Galitski, and Ian B. Spielman, Nature 494, 49 (2013).

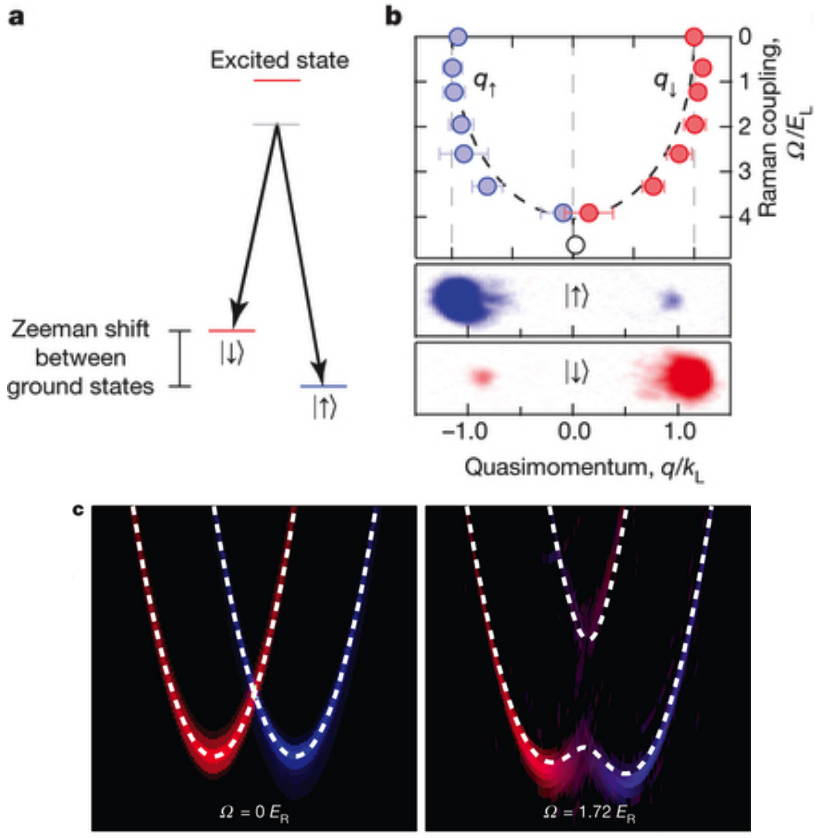

Figure 2.2 : (a), Typical level diagram. A pair of lasers – often counter-propagating – couple together a selected pair of atomic states labelled by $|\uparrow\rangle$ and $|\downarrow\rangle$ that together comprise the atomic 'spin'. These lasers are arranged in a two-photon Raman configuration that uses an off-resonant intermediate state (grey). These lasers link atomic motion along the x direction to the atom's spin creating a characteristic spin-orbit coupled energy-momentum dispersion relation. (b), Minima location. Measured location of energy minimum or minima, where as a function of laser intensity the characteristic double minima of SO coupling dispersion move together and finally merge. The uncertainties reflect the standard deviation of about 10 measurements. (c), Dispersion measured in ^{6}Li. Complete dispersion before and after laser coupling measured in a ^{6}Li Fermi gas (data for figure reproduced from Ref. [61]), compared with the predicted dispersion (white dashed curves), showing the typical spin-orbit dispersion relations depicted in Fig. 2.1(d). Image and caption adapted with permission from Macmillan Publishers Ltd: [Nature] "Spin-orbit coupling in quantum gases": Victor Galitski, and Ian B. Spielman, Nature 494, 49 (2013). Copyright License Number: 3327120846161. Copyright (2014).

the momentum difference of $2\,p_R$. Even though the absolute magnitude of recoil momentum may seem quite small, the low energies of ultracold atomic gases ensures that the recoil momenta play a significant role in determining macroscopic properties of atoms [53]. Thus, as first put forward by Higbie and Stamper-Kurn in Ref. [74], Raman transitions can provide the required velocity-dependent link between the spin and momentum in ultracold neutral atoms.

Fig. 2.2 illustrates a currently implemented technique for creating SO coupling in ultracold neutral atoms. As shown in Fig. 2.2(a), the first step is in the selection of two states, from the many available internal states of an atom [53]. Here, they are represented by pseudo-spin states $|\uparrow\rangle$ and $|\downarrow\rangle$ that form the atomic spin. Following up with the afore-mentioned description, the two counter-propagating laser beams with net recoil momenta $2\,p_R$ couple the pseudo-spin states $|\uparrow\rangle$ and $|\downarrow\rangle$. Hence, a coupling between the atomic spin and the momentum is generated and the atom's energy-momentum dispersion is altered, as shown in Fig. 2.1(d).

Several configurations of SO couplings can be created, with additional lasers linking together additional internal states [75]. Figure 2.3 shows a realistic example in which three internal atomic states can be coupled, eventually helping to produce a tunable combination of Rashba and Dresselhaus SO coupling. However, major technological challenges remain in experimental realization of such configurations. A serious challenge is the heating caused by Raman laser beams, which limit achieving ultracold temperatures required to allow for the manifestation of condensed phases of matter that are of paramount interest. However, we are optimistic that these tough experimental challenges would be overcome in the near future [76]. In the rest of this thesis, we discuss in detail the interesting physics of a system of ultracold bosonic atoms trapped in a 2D trap with pure Rashba SO coupling.

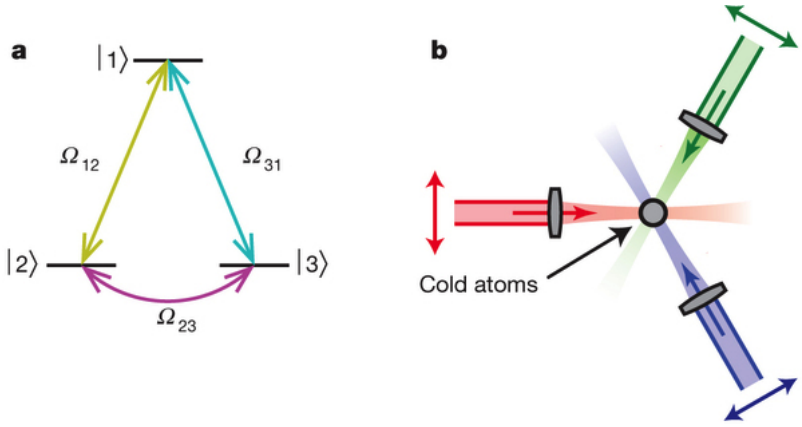

Figure 2.3 : Going beyond current experiments, more complicated forms of SO coupling may be created. These require both more laser beams and more internal states. (a), Coupling scheme. Each state is coupled by a two-photon Raman transition, each produced by a pair of the beams shown in (b). The configuration depicted in (a) and (b) could realize a tunable combination of Rashba and Dresselhaus SO coupling in alkali atoms [75]. Image and caption adapted with permission from Macmillan Publishers Ltd: [Nature] "Spin-orbit coupling in quantum gases": Victor Galitski, and Ian B. Spielman, Nature 494, 49 (2013). Copyright License Number: 3327120846161. Copyright (2014).

2.3 Rashba SO coupling in Bose gases

2.3.1 System under study

We* consider a two-component Bose gas confined by a 2D isotropic harmonic trapping potential $V(\rho) = M\omega_\perp^2(x^2+y^2)/2 = M\omega_\perp^2\rho^2/2$, with a Rashba SO coupling $\mathcal{V}_{SO} = -i\lambda_R(\hat{\sigma}_x\partial_y - \hat{\sigma}_y\partial_x)$. Here, λ_R is the Rashba SO coupling strength and $\hat{\sigma}_x$, $\hat{\sigma}_y$, and $\hat{\sigma}_z$ are the 2×2 Pauli matrices. Our study is motivated by the real experiment, where a harmonic trap is necessary to prevent the atoms from escaping. In addition to being an experimental necessity, the confining trapping potential allows for the emergence of novel physics in ultracold atomic systems. For example, a homogeneous system

*The following section 2.3.1 is taken largely from our publication in Ref. [2].

of 2D bosons does not condense and form a BEC. However, the trapping potential allows for the emergence of BEC [77]. Along similar lines, we shall observe that the SO coupled Bose gas confined by a 2D harmonic trapping potential allows for the emergence of novel ground state phases.

The model Hamiltonian is given by,

$$\begin{aligned} \mathcal{H} &= \int d\mathbf{r}\,[\mathcal{H}_0 + \mathcal{H}_{\rm int}], \\ \mathcal{H}_0 &= \Psi^\dagger \left[-\frac{\hbar^2\nabla^2}{2M} + V(\rho) + \mathcal{V}_{SO} - \mu \right] \Psi, \\ \mathcal{H}_{\rm int} &= (g/2) \sum_{\sigma=\uparrow,\downarrow} \Psi^\dagger_\sigma \Psi^\dagger_\sigma \Psi_\sigma \Psi_\sigma + g_{\uparrow\downarrow} \Psi^\dagger_\uparrow \Psi_\uparrow \Psi^\dagger_\downarrow \Psi_\downarrow. \end{aligned} \tag{2.1}$$

Here, $\mathbf{r} = (x, y)$ and $\Psi = [\Psi_\uparrow(\mathbf{r}), \Psi_\downarrow(\mathbf{r})]^T$ denotes the spinor Bose field operators for the atomic states $|\uparrow\rangle$ and $|\downarrow\rangle$ that create the synthetic spin-half system. In a recent experiment reported by the Spielman group, a spinor (spin-1) Bose gas of ^{87}Rb atoms with $F = 1$ ground electronic manifold is used. However, to create SO coupling, two internal 'spin' states have been selected from the $F = 1$ manifold and have been labeled as pseudo-spin-up and pseudo-spin-down [59]. This gives an effective spin-1/2 Bose gas. In experiments, the 2D geometry can be realized by imposing a strong harmonic potential $V(z) = M\omega_z^2 z^2/2$ along the axial direction, in such a way that $\mu, k_B T \ll \hbar\omega_z$ [29].

The term $\mathcal{H}_0$ in Eqn.(2.1) represents the Hamiltonian for the non-interacting atomic gas with arbitrary SO coupling, and the term $\mathcal{H}_{\rm int}$ accounts for the inter-atomic interactions in the SO-coupled atomic gas. The chemical potential μ is to be determined by the total number of bosons N, i.e., $\int d\mathbf{r}\Psi^\dagger\Psi = N$. For simplicity, we have assumed equal intra-species interaction strength, so that $g_{\uparrow\uparrow} = g_{\downarrow\downarrow} = g$. The inter-species interaction strength is represented by $g_{\uparrow\downarrow}$. The Hamiltonian in Eqn.(2.1)

harbors interesting phases of matter and offers an exceptionally rich playground to study many-body physics in the presence of Rashba SO coupling. The main purpose of the remainder of this thesis is to discuss these attributes of this Hamiltonian in detail. To begin with, let us discuss the simplified scenario in the absence of interatomic interactions and external trapping potential.

2.3.2 Homogeneous non-interacting gas with arbitrary SO coupling

The main ingredient of SO coupled atomic Bose gases is the laser-dressed bosonic states $|\uparrow\rangle$ and $|\downarrow\rangle$ that create a synthetic spin-half system. As stated by Galitski *et al.* in Ref. [53], because the Pauli spin-statistics theorem prohibits the existence of bosons with real spin-half, this is already a weird and interesting entity. Furthermore, when many such entities are brought together in a SO coupled system, the weirdness increases further [53]. As the temperature is lowered, the bosons tend to condense, but in contrast to the conventional BEC, where the zero-momentum state is the unique state with lowest energy, spin-orbit bosons can have energy-momentum dispersion with several lowest-energy states (the ground state is degenerate).

Let us discuss a simple, but important, limiting case of the Hamiltonian in Eqn.(2.1), when the trapping potential and interatomic interactions are assumed to be absent. Hence, this corresponds to the scenario of a homogeneous non-interacting spinor Bose gas with arbitrary strength of Rashba SO coupling. The Hamiltonian in Eqn.(2.1) then takes the simple form:

$$H_{\rm hom} = \frac{\hbar^2 \mathbf{k}^2}{2M} + \lambda_R \left(k_y \hat{\sigma}_x - k_x \hat{\sigma}_y \right) \tag{2.2}$$

In the absence of Rashba SO coupling ($\lambda_R = 0$), the energy-momentum relation is

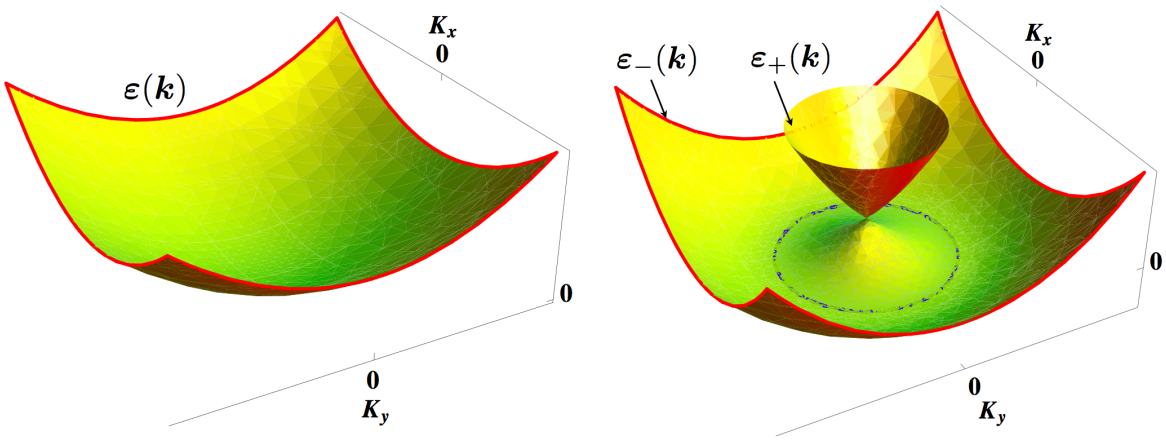

Figure 2.4 : (a): left, Energy dispersion curves in the absence of Rashba SO coupling. (b): right, In the presence of Rashba SO coupling, we notice a (blue) ring of states that represent the minima in momentum space, typically referred to as Rashba ring.

a simple free-particle parabolic dispersion, as shown in Fig. 2.4(a). In the presence of SO coupling, this limiting scenario allows us to explore single-particle physics in momentum space for a system that preserves translational invariance. With finite λ_R, the pseudo-spin index is no longer a good quantum number, as it starts to precess about the direction of momentum. As shown in Fig. 2.4(b), the eigenspectrum of the Hamiltonian in Eqn.(2.2) now has upper and lower branches:

$$\varepsilon_{\pm}(\mathbf{k}) = \frac{\hbar^2 k_{\perp}^2}{2M} \pm \lambda_R k_{\perp}, \text{ with } k_{\perp} = \sqrt{k_x^2 + k_y^2}. \tag{2.3}$$

The $\pm$ denotes a different helicity basis, i.e., the spin-index being either parallel or anti-parallel to the wave vector $\mathbf{k}$. As illustrated in Fig. 2.4(b), the ground state is in the negative helicity branch $\varepsilon_-(\mathbf{k})$. We notice a ring of states that represent the minima in momentum space, typically referred to as Rashba ring, with k_x, k_y that satisfy the condition $k_{\perp} = \lambda_R/(\hbar^2/M)$ to be degenerate. Hence, the single-

particle state is infinitely degenerate with allowed momenta in the Rashba ring*. These conclusions are based entirely on single-particle physics, as we see that the particle statistics play no role. This implies that the dispersion plots in Fig. 2.4 are as well applicable for fermions.

2.3.3 Trapped non-interacting gas with arbitrary SO coupling

Let† us now proceed to discuss the natural follow-up of the limiting case considered above, i.e., to include the effects of a harmonic trapping potential. However, we continue to assume that interatomic interactions are absent. Hence, the discussion in this section corresponds to the scenario of a trapped non-interacting spinor Bose gas with arbitrary strength of Rashba SO coupling. We proceed to solve the model Hamiltonian $\mathcal{H}_0$ and obtain the single-particle solutions. Rewriting the $\mathcal{H}_0$ component in Eqn. (2.1), the single-particle wavefunction $\phi(\mathbf{r}) = [\phi_\uparrow(\mathbf{r}), \phi_\downarrow(\mathbf{r})]^T$ with energy ϵ is given by

$$\begin{bmatrix} \mathcal{H}_{osc} & -i\lambda_R(\partial_y + i\partial_x) \\ -i\lambda_R(\partial_y - i\partial_x) & \mathcal{H}_{osc} \end{bmatrix} \begin{bmatrix} \phi_\uparrow \\ \phi_\downarrow \end{bmatrix} = \epsilon \begin{bmatrix} \phi_\uparrow \\ \phi_\downarrow \end{bmatrix}, \tag{2.4}$$

where $\mathcal{H}_{\rm osc} \equiv -\hbar^2\nabla^2/(2M) + V(\rho)$ [2]. In polar coordinates (ρ, φ), we have $-i(\partial_y \pm i\partial_x) = e^{\mp i\varphi}[\pm\partial/\partial\rho - (i/\rho)\partial/\partial\varphi]$. We define two characteristic lengths, $a_\perp = \sqrt{\hbar/(M\omega_\perp)}$ for the harmonic trap and $a_\lambda = \hbar^2/(M\lambda_R)$ for the SO coupling. The dimensionless SO coupling strength can be then defined as $\lambda_{SO} = \tilde{\lambda} = a_\perp/a_\lambda = \sqrt{(M/\hbar^3)}\lambda_R/\sqrt{\omega_\perp}$ [1]. Because of the isotropic harmonic potential $V(\rho)$, the single-particle wave-function

*This is in contrast with the more conventional case of spinor BECs, which include two or more spin states, but do not alter the energy-momentum dispersion relation.

†The following section 2.3.3 is taken largely from our publications in Refs. [2, 3].

has a well-defined azimuthal angular momentum $l_z = m$, and takes the form

$$\phi_m(\mathbf{r}) = \begin{bmatrix} \phi_\uparrow(\rho) \\ \phi_\downarrow(\rho)e^{i\varphi} \end{bmatrix} \frac{e^{im\varphi}}{\sqrt{2\pi}}. \tag{2.5}$$

This state also has a well-defined total angular momentum $j_z = l_z + s_z = m + 1/2$ [2]. In general, we may denote the energy spectrum as ϵ_{nm}, where $n = (0, 1, 2...)$ is the quantum number for the transverse (radial) direction. There is an interesting two-fold degeneracy of the energy spectrum: any eigenstate $\phi(\mathbf{r}) = [\phi_\uparrow(\mathbf{r}), \phi_\downarrow(\mathbf{r})]^T$ is degenerate with its time-reversal partner $\mathcal{T}\phi(\mathbf{r}) \equiv (i\sigma_y\mathcal{C})\phi(\mathbf{r}) = [\phi^*_\downarrow(\mathbf{r}), -\phi^*_\uparrow(\mathbf{r})]^T$. Here $\mathcal{C}$ is the complex conjugate operation. This Kramers doublet is the direct consequence of the time-reversal symmetry satisfied by the model Hamiltonian [2]. This symmetry is even preserved in the presence of interatomic interactions. As a result, we may restrict the quantum numbers m to be non-negative integers, since a negative m can always be regarded as the time-reversal partner for a state with $m \geq 0$ [2].

To numerically solve the single-particle spectrum, we adopt a basis-expansion method. To this end, we first expand,

$$\phi_\uparrow(\rho) = \sum_k A_k R_{km}(\rho), \tag{2.6}$$

$$\phi_\downarrow(\rho) = \sum_k B_k R_{km+1}(\rho), \tag{2.7}$$

where

$$R_{km} = \frac{1}{a_\perp}\sqrt{\frac{2k!}{(k+|m|)!}}\left(\frac{\rho}{a_\perp}\right)^{|m|} e^{-\frac{\rho^2}{2a_\perp^2}} \mathcal{L}_k^{|m|}(\frac{\rho^2}{a_\perp^2}) \tag{2.8}$$

is the radial wave-function of a 2D harmonic oscillator $\mathcal{H}_{osc}$ with energy $(2k + |m| + 1)\hbar\omega_\perp$, and $\mathcal{L}_k^{|m|}$ is the associated Legendre polynomial [2]. Then we have the following

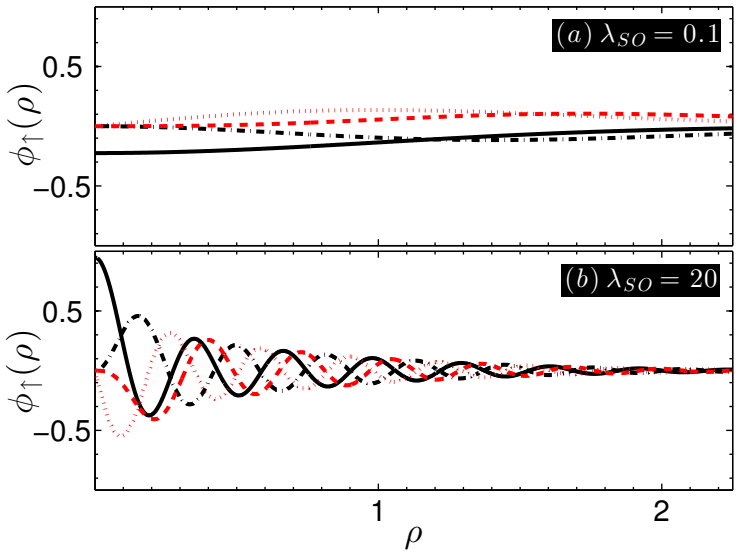

Figure 2.5 : Plots (a) and (b) show wavefunctions $\phi_\uparrow(\rho)$ of single-particle states in the $n = 0$ manifold at small, and large SO coupling strengths respectively. $m = 0$ (solid black), $m = 1$ (dotted red), $m = 2$ (dash-dotted black) and $m = 3$ (dashed red). Image from Ref. [3].

secular matrix,

$$\begin{bmatrix} \mathcal{H}_{\text{osc}\uparrow} & \mathcal{M}^T \\ \mathcal{M} & \mathcal{H}_{\text{osc}\downarrow} \end{bmatrix} \begin{bmatrix} A_k \\ B_k \end{bmatrix} = \epsilon \begin{bmatrix} A_k \\ B_k \end{bmatrix}, \tag{2.9}$$

where the matrix elements are given by (for $m \geq 0$)

$$\begin{aligned} \mathcal{H}_{\text{osc}\uparrow,\text{kk}'} &= \hbar\omega_\perp \left[2k + m + 1\right] \delta_{kk'}, \\ \mathcal{H}_{\text{osc}\downarrow,\text{kk}'} &= \hbar\omega_\perp \left[2k + (m+1) + 1\right] \delta_{kk'}, \\ \mathcal{M}_{kk'} &= \hbar\omega_\perp \lambda_{SO} \left[\sqrt{k' + m + 1}\delta_{kk'} + \sqrt{k'}\delta_{kk'-1}\right]. \end{aligned}$$

Diagonalization of the secular matrix Eq. (2.9) leads to the single-particle spectrum and single-particle wave-functions [2]. In numerical calculations, it is necessary to impose a cut-off k_{max} for the radial quantum number k of the 2D harmonic oscillator.

For $\lambda_{SO} \leq 20$, we find that $k_{\max} = 256$ is sufficiently large to have an accurate energy spectrum. With this cut-off, the dimension of the secular matrix in Eq. (2.9) is $2k_{\max} = 512$ [2].

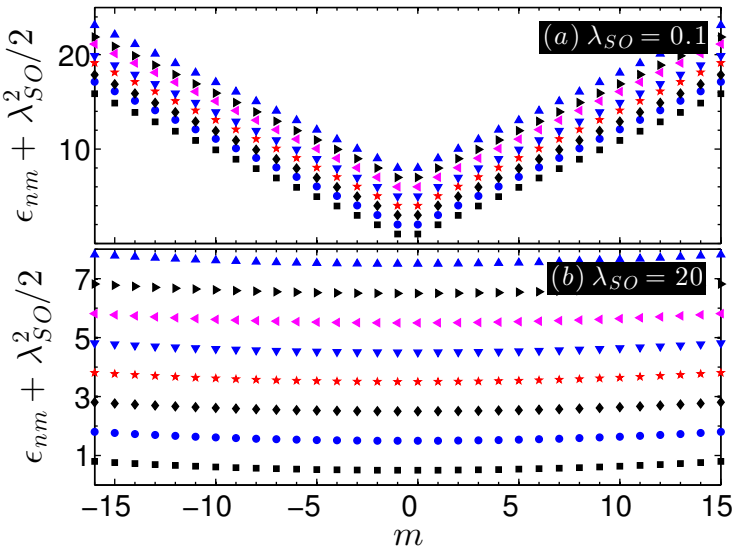

Figure 2.6 : Plots (a) and (b) show energy spectrum of single-particle states at small and large SO coupling strengths respectively: $n = 0 \rightarrow 7$ (bottom→top) and $m = -16 \rightarrow +15$. While energies of states within each n are represented by a specific symbol, it is evident that states with higher n have progressively higher energies. Image from Ref. [3].

In Fig. 2.5, we show wavefunctions of single-particle eigenstates at representative values of small and large SO coupling strengths [2]. It is evident that a larger SO coupling strength leads to increased oscillations and increased localization at radii determined by $|m|$ in the radial direction. Corresponding wavefunctions $\phi_{\downarrow}(\rho)$ also have similar characteristics [2]. In Fig. 2.6, we show the energy spectrum for single-particle states at small and large SO coupling strengths. From Fig. 2.6(a), it is evident that the energy spectrum is strongly dispersive in m at small SO coupling strengths, with a large overlap between the energies of single-particle states with different radial quantum number n [2]. Qualitatively, the energy spectrum at small

SO coupling strengths may be understood as a weak perturbation of the harmonic oscillator energy levels of the two pseudo-spin components. On the other hand, we observe from Fig. 2.6(b) that the energy spectrum is weakly dispersive or *nearly* flat in m at large SO coupling strengths. For the range of m shown here, there is no overlap between the energies of single-particle states belonging to different radial quantum numbers n, i.e., each n manifold represents single-particle states labelled by their azimuthal angular momenta m with no overlap with adjacent n manifolds [2]. Furthermore, the harmonic trapping potential may be qualitatively understood as a weak perturbation to the energy spectrum at large SO coupling strengths of the corresponding translationally invariant system [2].

At large SO coupling (i.e., $\lambda_{SO} > 5$), to a good approximation we numerically find that the low-lying spectrum forms discrete manifolds with spacing $\hbar\omega_\perp$(indexed by an integer $n \geq 0$),

$$\epsilon_{nm} \simeq \left[-\tilde{\lambda}^2 + (2n+1) + m\,(m+1)/\tilde{\lambda}^2\right] \hbar\omega_\perp/2\,. \tag{2.10}$$

There are about $2\sqrt{2}\tilde{\lambda}$ levels within each manifold with the smallest level spacing $\Delta E = \hbar\omega_\perp/\tilde{\lambda}^2$ [1]. The discrete manifolds of spectrum are similar to the well-known Landau levels, formed when a charged particle moves in magnetic fields. However, the reasons for their formation are very different [1]. In our case of large SO coupling, without trap the spectrum is characterized by a continuous momentum $\mathbf{k}$ and is given by $\epsilon_{\mathbf{k}} = [-\tilde{\lambda}^2/2 + (k \pm \tilde{\lambda})^2/2]\hbar\omega_\perp$, with infinite degeneracy along the azimuthal direction [1]. The inclusion of trapping potential quantizes the radial motion for $\mathbf{k}$ and the azimuthal motion, giving the standard quantization contribution of $(n+1/2)\hbar\omega_\perp$ and $(m+1/2)^2/(2\tilde{\lambda}^2)\hbar\omega_\perp$ to the energy, respectively [1].

In summary, we identify from Figs. 2.5 and 2.6 that the nature of solutions is fundamentally different at small and large SO coupling strengths. In the forthcoming chapter, we present a detailed discussion of the mean-field theoretical study of weakly correlated ground state phases of the interacting many-particle system at small and large SO coupling strengths.

Chapter 3

Mean-field theoretical study of weakly correlated phases*

We study an interacting many-body system of two-component Bose gases confined in a 2D isotropic harmonic trapping potential with Rashba SO coupling. As outlined in Sec. 2.3, the degenerate ground states of a Rashba SO coupled Hamiltonian offers an interesting platform for exploring novel condensed phases of matter. Based on the model Rashba SO coupling Hamiltonian in Eqn. (2.2), we discussed the non-interacting limit and derived single-particle solutions at small and large SO coupling strengths in Sec. 2.3. We illustrated that the nature of solutions is fundamentally different at small and large SO coupling strengths. In this chapter, we present a detailed discussion of ground state phases at system parameters that correspond to the weakly correlated regime. Mean-field theory provides a suitable approach to analyze this scenario. Firstly, we present a detailed discussion of the phase diagram of interacting gases at small SO coupling strengths in the weakly correlated regime. Subsequently, we present an analogous discussion at large SO coupling strengths.

In Sec. 1.4.2, we discussed that in a dilute and cold gas, only binary collisions at low energy are relevant. These collisions are characterized by a single parameter, the s-wave scattering length a, independent of the details of the two-body potential. The inter-atomic interaction strength g between identical spin states in 3D space takes the form: $g = 4\pi\hbar^2 a/M$ (for example, see Ref. [16]). In the present scenario

*Chapter 3 taken largely from our publications in Refs. [1, 2].

of two-component Bose gases confined in a 2D isotropic harmonic trapping potential, we perform dimensional-reduction to derive interaction strengths in 2-dimensions: $g = \sqrt{8\pi}(\hbar^2/M)(a/a_z)$ and $g_{\uparrow\downarrow} = \sqrt{8\pi}(\hbar^2/M)(a_{\uparrow\downarrow}/a_z)$. Here $a_z = \sqrt{\hbar/(M\omega_z)}$ is the characteristic oscillator length in the z-direction, a is the intra-component scattering length, and $a_{\uparrow\downarrow}$ is the inter-component scattering length [2]. Note that here we consider a weakly interacting regime with $a_z \gg a, a_{\uparrow\downarrow}$ [2]. In the strongly interacting regime where $a_z \sim a, a_{\uparrow\downarrow}$, one needs to include the confinement induced resonance in the calculation of 2D interaction paraemeters g and $g_{\uparrow\downarrow}$ [78].

3.1 Theory formalism

For a weakly interacting trapped Bose gas at zero temperature, we assume that all the bosons condense into a single quantum state $\Phi(\mathbf{r}) = [\Phi_\uparrow(\mathbf{r}), \Phi_\downarrow(\mathbf{r})]^T$. Following the standard mean-field theory approach [79–81], we separate the field operator into a condensate and a fluctuation part, $\Psi_\sigma(\mathbf{r}) = \Phi_\sigma(\mathbf{r}) + \tilde{\Psi}_\sigma(\mathbf{r})$. Keeping up to quadratic terms in $\tilde{\Psi}_\sigma(\mathbf{r})$, this separation leads to an approximate Hamiltonian $\mathcal{H} = \int d\mathbf{r}[\mathcal{H}_{\rm GP} + \mathcal{H}_T]$. Here, the condensate part is given by,

$$\begin{aligned} \mathcal{H}_{\rm GP} &= \Phi^\dagger \left[\mathcal{H}_{\rm osc} + \mathcal{V}_{SO} - \mu\right] \Phi \\ &\quad + \frac{g}{2}\left(|\Phi_\uparrow|^4 + |\Phi_\downarrow|^4\right) + g_{\uparrow\downarrow}\,|\Phi_\uparrow \Phi_\downarrow|^2\,, \end{aligned} \tag{3.1}$$

where $\mathcal{H}_{\rm osc} \equiv -\hbar^2\nabla^2/(2M) + V(\rho)$, and $V_{\rm so} \equiv -i\lambda_R(\partial_y + i\partial_x)$ [2]. The fluctuation part is $\mathcal{H}_T = \tilde{\Psi}^\dagger \mathcal{H}_{\rm Bog} \tilde{\Psi}$, where $\mathcal{H}_{\rm Bog}$ is the Bogoliubov matrix and we have introduced a 4×1 Nambu spinor $\tilde{\Psi} = [\tilde{\Psi}_\uparrow(\mathbf{r}), \tilde{\Psi}_\downarrow(\mathbf{r}), \tilde{\Psi}^\dagger_\uparrow(\mathbf{r}), \tilde{\Psi}^\dagger_\downarrow(\mathbf{r})]^T$. We postpone the discussion of the Bogoliubov formalism and the associated solutions until Ch. 4. However, the information about the nature of condensed ground state phases can be obtained by

exclusively analyzing the $\mathcal{H}_{\rm GP}$ part of the Hamiltonian.

The condensate wave-function can be obtained from the mean-field GP equations $\delta\mathcal{H}_{\rm GP}/\delta\Phi(\mathbf{r}) = 0$ [79–81], or explicitly,

$$\begin{bmatrix} \mathcal{H}_{s_\uparrow} & -i\lambda_R(\partial_y + i\partial_x) \\ -i\lambda_R(\partial_y - i\partial_x) & \mathcal{H}_{s_\downarrow} \end{bmatrix} \begin{bmatrix} \Phi_\uparrow(\mathbf{r}) \\ \Phi_\downarrow(\mathbf{r}) \end{bmatrix} = 0. \tag{3.2}$$

Here, $\mathcal{H}_{s_\uparrow} \equiv \mathcal{H}_{\rm osc} + g|\Phi_\uparrow|^2 + g_{\uparrow\downarrow}|\Phi_\downarrow|^2 - \mu$, and $\mathcal{H}_{s_\downarrow} \equiv \mathcal{H}_{\rm osc} + g_{\uparrow\downarrow}|\Phi_\uparrow|^2 + g|\Phi_\downarrow|^2 - \mu$. At zero temperature, we assume a single condensate state with *zero* quantum depletion, so that the condensate wave-function is normalized by $\int d\mathbf{r}[|\Phi_\uparrow|^2 + |\Phi_\downarrow|^2] = N$, where N is the total number of bosons. The equation is simplified if we write $\Phi_\uparrow = N^{1/2}\phi_\uparrow$ and $\Phi_\downarrow = N^{1/2}\phi_\downarrow$ and use corresponding interaction strengths $g(N-1)$ and $g_{\uparrow\downarrow}(N-1)$ [2]. The normalization condition becomes $\int d\mathbf{r}\,[|\phi_\uparrow|^2 + |\phi_\downarrow|^2] = 1$. In harmonic traps, it is natural to use trap units, i.e. to take $\hbar\omega_\perp$ as the unit for energy and the harmonic oscillator length $a_\perp = \sqrt{\hbar/(M\omega_\perp)}$ as the unit for length. This is equivalent to setting $\hbar = k_B = M = \omega_\perp = 1$. The unit of interaction strength $g(N-1)$ or $g_{\uparrow\downarrow}(N-1)$ is then $\hbar\omega_\perp a_\perp^2 = \hbar^2/M$ [2]. Analogously, we introduce an SO coupling length $a_\lambda = \hbar^2/(M\lambda_R)$ and consequently define a dimensionless SO coupling strength $\lambda_{SO} = a_\perp/a_\lambda = \sqrt{(M/\hbar^3)}\lambda_R/\sqrt{\omega_\perp}$. In an SO coupled spin-1/2 BEC of ^{87}Rb atoms as realized recently by the NIST group [59], λ_{SO} is about 10. In the typical experiment for 2D spin-1/2 ^{87}Rb BECs [29], the interatomic interaction strengths are about $g(N-1) \approx g_{\uparrow\downarrow}(N-1) = 10^2 \sim 10^3(\hbar\omega_\perp a_\perp^2)$ [2]. These coupling strengths, however, can be tuned by changing the number of trapped atoms or by properly choosing the parameters of the laser fields that lead to the harmonic confinement and the SO coupling.

3.2 Interacting Bose gas with small SO coupling

Bosonic* atoms in a weakly interacting spin-1/2 Bose gas in a 2D harmonic trap would condense into a non-trivial half-integer angular momentum state with a *skyrmion*-type spin texture. For convenience purposes, the half-integer angular momentum condensed state is referred to as a half-quantum vortex state. In this section, we solve the mean-field GP equation for the density distributions and spin textures. The condensation of an SO coupled spin-1/2 Bose gas into a half-quantum vortex configuration was first suggested by Congjun Wu *et al.* in Ref. [82], and its existence was discussed under the condition that the interaction is SU(2) symmetric, i.e., $g = g_{\uparrow\downarrow}$. Here, we explore systematically the parameter space for the half-quantum vortex state and analyze its stability qualitatively [2]. We postpone the discussion of a detailed quantitative stability analysis and the ground state phase diagram to Chapter 4. In general, we observe that at small SO coupling strengths, the half-quantum vortex state is stable and thrives in a much larger phase space.

3.2.1 Appearance of the half-quantum vortex state

In Fig. 3.1(a), we show the single-particle energy spectrum at $\lambda_{SO} = 1$. For an arbitrary SO interaction strength, we find numerically that the doublet single-particle ground state always occurs at $m = 0$ (or $m = -1$ for its time-reversal partner state) [2]. The single-particle state with $m = 0$, $\phi_0(\mathbf{r}) = [\phi_\uparrow(\rho), \phi_\downarrow(\rho)e^{i\varphi}]^T/\sqrt{2\pi}$, has a half-quantum vortex configuration [82, 83], as the spin-up component stays in the s-state while the spin-down component is in the p-state. In the absence of interactions, however, there is a degenerate time-reversed state, $\mathcal{T}\phi_0(\mathbf{r}) = [\phi_\downarrow(\rho)e^{-i\varphi}, -\phi_\uparrow(\rho)]^T/\sqrt{2\pi}$,

*Contents of section 3.2 is taken largely from our publication in Ref. [2].

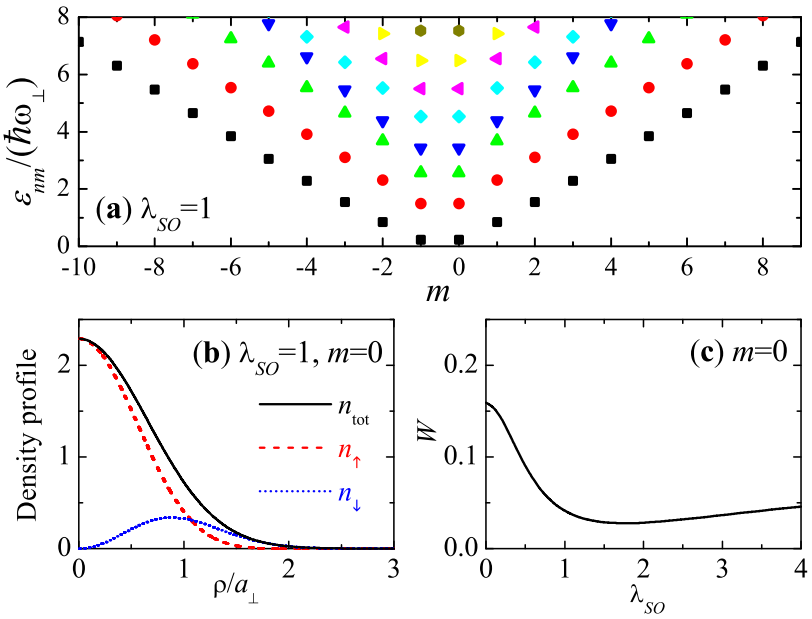

Figure 3.1 : (color online). (a) Single-particle energy spectrum at $\lambda_{SO} = 1$. (b) The density profiles for the single-particle state with $m = 0$ at $\lambda_{SO} = 1$. (c) The W-function for the $m = 0$ single-particle state as a function of SO coupling strength. It is always positive at arbitrary SO coupling strength. Image from Ref. [2].

which is also a half-quantum vortex state [2]. Therefore, in general, the ground single-particle state is a superposition of two degenerate half-quantum vortex states, $\phi_0(\mathbf{r})$ and $\mathcal{T}\phi_0(\mathbf{r})$, which takes the form $\phi_s(\mathbf{r}) = \alpha\phi_0(\mathbf{r}) + \beta\mathcal{T}\phi_0(\mathbf{r})$, or explicitly,

$$\phi_s(\mathbf{r}) = \frac{1}{\sqrt{2\pi}} \begin{bmatrix} \alpha\phi_\uparrow(\rho) + \beta\phi_\downarrow(\rho)e^{-i\varphi} \\ \alpha\phi_\downarrow(\rho)e^{i\varphi} - \beta\phi_\uparrow(\rho) \end{bmatrix}. \tag{3.3}$$

Here α and β are two arbitrary complex numbers satisfying $|\alpha|^2 + |\beta|^2 = 1$ [2].

In the presence of very weak interatomic interactions such that $g(N-1), g_{\uparrow\downarrow}(N-1) \ll \Delta\epsilon a_\perp^2$, where $\Delta\epsilon$ is the energy difference between the single-particle ground state $\phi_0(\mathbf{r})$ and the first excited state $\phi_1(\mathbf{r})$, we may determine the superposition coefficients α and β by minimizing the GP energy, $E_{\rm GP}[\phi_s(\mathbf{r})] = \int d\mathbf{r}\, \mathcal{H}_{\rm GP}[\phi_s(\mathbf{r})]$ [2].

After simple algebra, we find that,

$$\Delta E = E_{\rm GP}[\phi_s(\mathbf{r})] - E_{\rm GP}[\phi_0(\mathbf{r})], \tag{3.4}$$

$$= (g_{\uparrow\downarrow} - g)\,(N-1)\,|\alpha\beta|^2\,W[\phi_0(\mathbf{r})], \tag{3.5}$$

where the W-function is given by,

$$W[\phi(\mathbf{r})] = \int d\mathbf{r}[(|\phi_\uparrow|^2 - |\phi_\downarrow|^2)^2 - 2\phi_\uparrow^2\phi_\downarrow^2]. \tag{3.6}$$

Therefore, a half-quantum vortex state is preferable if $(g_{\uparrow\downarrow} - g)W > 0$ [2]. Otherwise, an equal-weight superposition of two degenerate half-quantum vortex states with $|\alpha| = |\beta| = 1/\sqrt{2}$ will be the ground state. As shown in Fig. 3.1(c), the W-function for $\phi_0(\mathbf{r})$ is positive for *arbitrary* SO coupling. We thus conclude that a half-quantum vortex state should appear for weak interatomic interactions provided that the inter-species interaction is larger than the intra-species interaction ($g_{\uparrow\downarrow} > g$) [2].

The afore-mentioned qualitative stability analysis gives an approximate indication of the phase space available for the half-quantum vortex state. To obtain a more accurate phase diagram, it would be useful to include quantitative discussions about the critical interaction strengths at which various instabilities relevant to half-quantum vortex state would occur. We postpone this detailed quantitative discussion of the phase diagram to Chapter 4.

3.2.2 Density distributions

Let us now consider finite interatomic interactions, by solving the GP equation for density distributions and spin-textures. For the half-quantum vortex condensate state

with $m = 0$, the GP equation becomes $\mathcal{L}_{GP}[\phi_\uparrow(\rho), \phi_\downarrow(\rho)] = 0$, where

$$\mathcal{L}_{GP} = \begin{bmatrix} \mathcal{H}_{s,0} + \bar{g}\phi_\uparrow^2 + \bar{g}_{\uparrow\downarrow}\phi_\downarrow^2 & \lambda_R(\partial_\rho + 1/\rho) \\ \lambda_R(-\partial_\rho) & \mathcal{H}_{s,1} + \bar{g}_{\uparrow\downarrow}\phi_\uparrow^2 + \bar{g}\phi_\downarrow^2 \end{bmatrix}. \tag{3.7}$$

Here $\bar{g} \equiv g(N-1)/(2\pi)$ and $\bar{g}_{\uparrow\downarrow} \equiv g_{\uparrow\downarrow}(N-1)/(2\pi)$, while the single-particle Hamiltonian operator is:

$$\mathcal{H}_{s,m} \equiv -\frac{\hbar^2}{2M}\left[\frac{\partial^2}{\partial\rho^2} + \frac{1}{\rho}\frac{\partial^2}{\partial\rho^2}\partial_\rho - \frac{m^2}{\rho^2}\right] + V(\rho) - \mu\,. \tag{3.8}$$

The numerical procedure for solving GP equation is very similar to that for single-particle states in Eqn. (2.9) [2]. We expand $\phi_\uparrow(\rho) = \sum_k A_k R_{k0}(\rho)$ and $\phi_\downarrow(\rho) = \sum_k B_k R_{k1}(\rho)$, and obtain the secular matrix (with $m = 0$),

$$\begin{bmatrix} \mathcal{H}_{osc\uparrow} + \mathcal{I}_\uparrow & \mathcal{M}^T \\ \mathcal{M} & \mathcal{H}_{osc\downarrow} + \mathcal{I}_\downarrow \end{bmatrix} \begin{bmatrix} A_k \\ B_k \end{bmatrix} = \mu \begin{bmatrix} A_k \\ B_k \end{bmatrix}, \tag{3.9}$$

where

$$\mathcal{I}_{\uparrow,kk'} = \int_0^\infty \rho d\rho R_{k0}(\rho)\left(\bar{g}\phi_\uparrow^2 + \bar{g}_{\uparrow\downarrow}\phi_\downarrow^2\right) R_{k'0}(\rho)\,, \tag{3.10}$$

$$\mathcal{I}_{\downarrow,kk'} = \int_0^\infty \rho d\rho R_{k1}(\rho)\left(\bar{g}_{\uparrow\downarrow}\phi_\uparrow^2 + \bar{g}\phi_\downarrow^2\right) R_{k'1}(\rho)\,. \tag{3.11}$$

The chemical potential is given by the lowest eigenvalue of the secular matrix. Due to the non-linear terms $\mathcal{I}_{\uparrow,kk'}$ and $\mathcal{I}_{\uparrow,kk'}$, we have to update the condensate wave-functions and densities iteratively [2]. To overcome the large non-linearity, we use a simple mixing scheme by setting a small parameter $0 < \gamma < 1$ and replacing the previous density $\phi_{\sigma,old}^2$ by $(1-\gamma)\,\phi_{\sigma,old}^2 + \gamma\phi_\sigma^2$, where ϕ_σ^2 is the density calculated in the current

step [84]. The choice of γ depends on the interaction strength. It becomes smaller for larger $\bar{g}$ and $\bar{g}_{\uparrow\downarrow}$ [2]. We run this iteration until convergence is achieved within a set tolerance. We have checked that this procedure of solving GP equation is stable for interaction strengths up to $g(N-1), g_{\uparrow\downarrow}(N-1) < 10^3(\hbar\omega_\perp a_\perp^2)$ [2]. For even larger nonlinearity, it seems to be impractical to expand the condensate wave-function using the 2D harmonic oscillator basis. Therefore for large interaction strengths, we use a time-splitting spectral method (TSSP) technique to solve the coupled GP equations and obtain the ground state by imaginary-time propagation [85–87]. For small interaction strengths, results obtained from TSSP are identical to those obtained from the basis-expansion method [2].

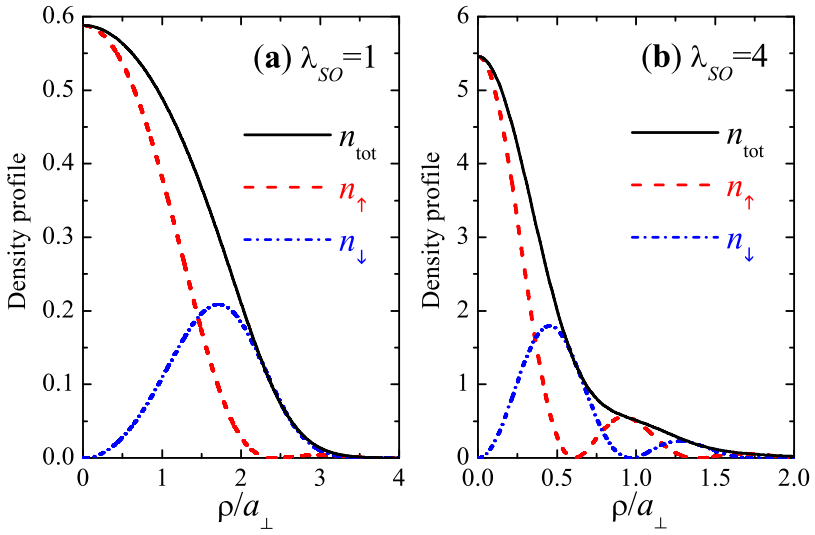

Figure 3.2 : (color online). Density distributions at $\lambda_{SO} = 1$ and $g(N-1) = 40(\hbar\omega_\perp a_\perp^2)$ (a) and at $\lambda_{SO} = 4$ and $g(N-1) = \hbar\omega_\perp a_\perp^2$ (b). Here, the ratio $g_{\uparrow\downarrow}/g = 1.1$. Image from Ref. [2].

In Fig. 3.2, we present the radial density distributions of the half-quantum vortex condensate state at two SO coupling strengths: $\lambda_{SO} = 1$ and $\lambda_{SO} = 4$. The increased SO coupling leads to more oscillations in the radial direction. By compar-

ing Fig. 3.2(a) with Fig. 3.1(b), one finds that the density distributions are flattened significantly by interatomic interactions, as anticipated [2].

3.2.3 Spin textures

To gain more insight into the half-quantum vortex state, it is useful to calculate the spin vector

$$\mathbf{S}(\mathbf{r}) = \frac{1}{2}\frac{\Phi^{\dagger}\sigma\Phi}{|\Phi|^2} = \frac{1}{2}\mathbf{n}(\mathbf{r}) \tag{3.12}$$

and the skyrmion density

$$n_{\text{skyrmion}}(\mathbf{r}) = \frac{1}{4\pi}\mathbf{n}\cdot\left[\partial_x\mathbf{n}\times\partial_y\mathbf{n}\right]. \tag{3.13}$$

The skyrmion density is a measure of the winding of the spin profile [2]. If it integrates to 1 or -1, a topological knot exists in the spin texture [88,89]. In Fig. 3.3, we graph the three components of the spin vector at $\lambda_{SO} = 1$, $g(N-1) = 40(\hbar\omega_{\perp}a_{\perp}^2)$ and $g_{\uparrow\downarrow}/g = 1.1$. The transverse spin texture is shown in Figs. 3.4(a) and 3.4(b) by arrows, with length representing the magnitude of the transverse spin vector (S_x,S_y) or (S_x,S_z).

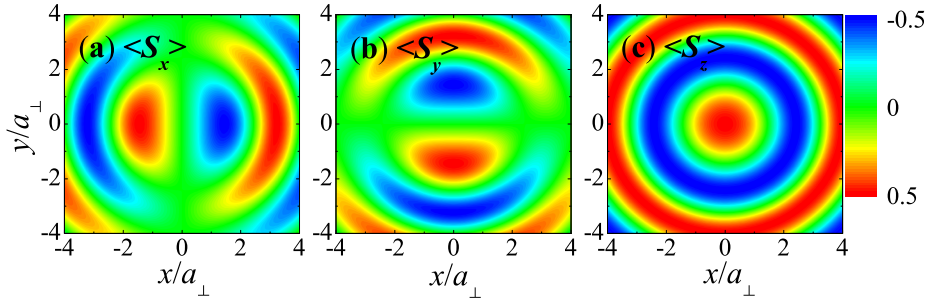

Figure 3.3 : (color online). Contour plots of the three components of the spin vector $\mathbf{S}(\mathbf{r})$ at $\lambda_{SO} = 1$, $g(N-1) = 40(\hbar\omega_{\perp}a_{\perp}^2)$ and $g_{\uparrow\downarrow}/g = 1.1$. Image from Ref. [2].

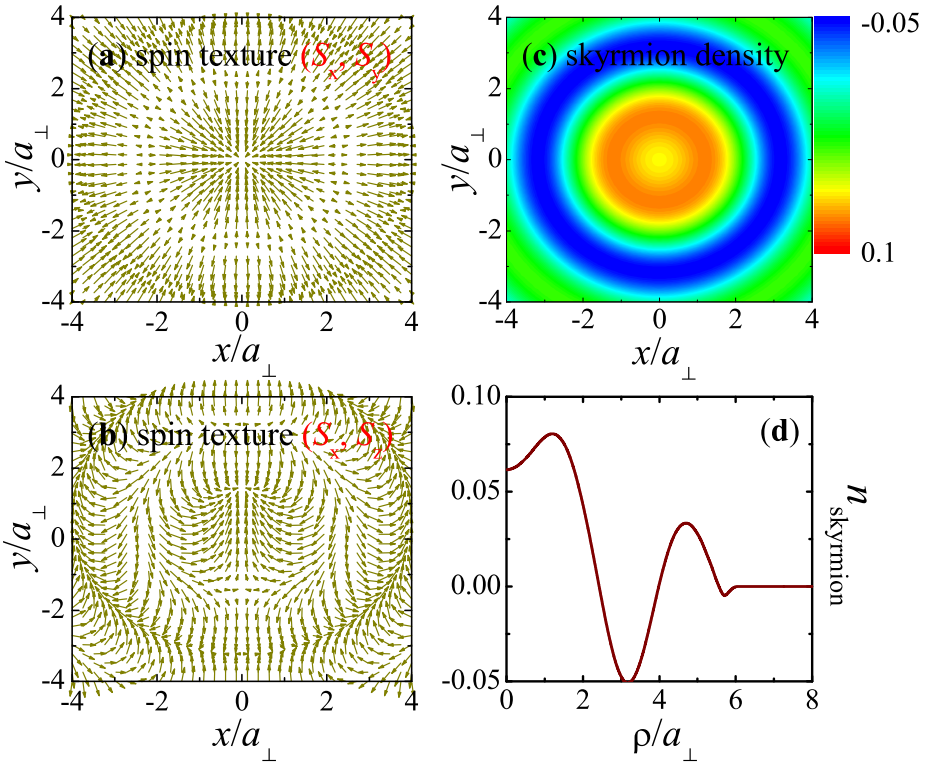

Figure 3.4 : (color online) (a) and (b), Two-dimensional vector plot of the transverse spin vector (S_x,S_y) and (S_x,S_z) at $\lambda_{SO} = 1$, $g(N-1) = 40(\hbar\omega_\perp a_\perp^2)$ and $g_{\uparrow\downarrow}/g = 1.1$. The length of the arrows gives the magnitude of (S_x,S_y) or (S_x,S_z). The corresponding skyrmion density $n_{\text{skyrmion}}(\mathbf{r})$ is plotted in (c) and (d). Image from Ref. [2].

Let us highlight key attributes of this interesting spin texture. "The spins are locally parallel and produces a smooth topological defect in the spin orientation" [90]. This topological defect is known as *skyrmion* by analogy with related objects in the Skyrme model of nuclear physics [91]. As stated by Girvin in Ref. [90], for instance, rather than having a single spin suddenly flip over, this object gradually turns over the spin as the center is approached. As shown in Fig. 3.4(a) and (b), the spin is down (up) at the origin and gradually turns up (down) at a finite radius. It is readily seen that the spin vector spirals in space to form a skyrmion-type texture. At intermediate distances, the spin components exhibit a vortex-like configuration.

However, unlike a $U(1)$ vortex, there is no singularity at the origin because the spins are able to rotate downwards out of the xy plane [90]. Quantitatively, this is most clearly illustrated in Figs. 3.4(c) and 3.4(d), where we plot the 2D contour and 1D radial distribution of skyrmion density. The nonzero skyrmion density oscillates between positive and negative. Moreover, the skyrmion number $\Phi = \int n_{skyrmion}(\mathbf{r})d\mathbf{r}$ is quantized to $+1$. We note that for the time-reversal half-quantum vortex condensate state with $m = -1$, the skyrmion number is -1 [2].

3.3 Interacting Bose gas with large SO coupling

Over* the past few years there have been great theoretical efforts to determine quantum states of an SO coupled spinor BEC [92–99] in this parameter regime. In a recent work by Wang *et al.* [95], two distinct phases are identified for a 'homogeneous' 2D spin-1/2 BEC. Depending on the relative magnitude of intra-species (g) and inter-species ($g_{\uparrow\downarrow}$) interactions, all bosons can condense into either a single plane-wave state ($g < g_{\uparrow\downarrow}$) or a density-stripe state ($g > g_{\uparrow\downarrow}$). In this section, we show that the presence of a harmonic trap can change dramatically the phase diagram of SO coupled BECs [1]. As shown in Fig. 2.6, at large SO coupling, the single-particle spectrum decomposes into discrete manifolds, analogous to discrete Landau levels, separated by $\hbar\omega_\perp$, where $\omega_\perp$ is the trapping frequency. Non-trivial quantum states with skyrmion lattices emerge when all bosons occupy into the lowest manifold (LM) [1]. For a weakly interacting gas, quantum states with skyrmion lattice patterns emerge spontaneously and preserve either parity symmetry or combined parity-time-reversal symmetry. While these properties are fundamentally different from that of a

*Contents of section 3.3 is taken largely from our publication in Ref. [1].

homogeneous system, these phases can potentially be observed in a SO coupled gas of ^{87}Rb atoms in a highly oblate trap [1].

3.3.1 Significance of lowest Landau level manifold

We consider N-bosons in a 2D harmonic trap $V(\rho) = M\omega_\perp^2\rho^2/2$ with a Rashba SO coupling $\mathcal{V}_{so} = -i\lambda_R(\partial_y\hat{\sigma}_x - \partial_x\hat{\sigma}_y)$, where $\hat{\sigma}_{x,y,z}$ are the Pauli matrices. The model Hamiltonian in Eqn. (2.2) may be re-written as $\mathcal{H} = \mathcal{H}_0 + \mathcal{H}_{int}$, where

$$\mathcal{H}_0 = \int d\mathbf{r}\Psi^+\left[-\hbar^2\nabla^2/(2M) + V(\rho) + \mathcal{V}_{so}\right]\Psi, \tag{3.14a}$$

$$\mathcal{H}_{\rm int} = \int d\mathbf{r}\left[(g+g_{\uparrow\downarrow})\hat{n}^2 + (g-g_{\uparrow\downarrow})\hat{S}_z^2\right]/4\,, \tag{3.14b}$$

$\Psi = [\Psi_\uparrow(\mathbf{r}), \Psi_\downarrow(\mathbf{r})]^T$ denotes collectively the spinor Bose field operators, and $\hat{n}, \hat{S}_z = \Psi_\uparrow^+\Psi_\uparrow \pm \Psi_\downarrow^+\Psi_\downarrow$ [1]. We define two characteristic lengths, $a_\perp = \sqrt{\hbar/(M\omega_\perp)}$ for the harmonic trap and $a_\lambda = \hbar^2/(M\lambda_R)$ for the SO coupling. The dimensionless SO coupling strength can be then defined as $\lambda_{SO} = \tilde{\lambda} = a_\perp/a_\lambda = \sqrt{(M/\hbar^3)}\lambda_R/\sqrt{\omega_\perp}$ [1]. The Hamiltonian is invariant under two symmetry operations, associated respectively with the anti-unitary time-reversal operator $\mathcal{T} = i\sigma_y\mathcal{C}$, where $\mathcal{C}$ takes the complex conjugate, and the unitary parity operator $\mathcal{P} = \sigma_z\mathcal{I}$, where $\mathcal{I}$ is the spatial inversion operator. The Hamiltonian is also invariant under the combined $\mathcal{PT}$ operator, which is unitary since $\mathcal{P}$ and $\mathcal{T}$ anti-commute with each other, i.e., $\{\mathcal{P}, \mathcal{T}\} = 0$ [1].

In polar coordinates (ρ, φ), the single-particle eigen-wavefunctions of $\mathcal{H}_0$ may be written in the form, $\Phi_m(\mathbf{r}) = [\phi_\uparrow(\rho)e^{im\varphi}, \phi_\downarrow(\rho)e^{i(m+1)\varphi}]^T$, which is energetically degenerate with its time reversed partner $\mathcal{T}\Phi_m(\mathbf{r}) = [\phi_\downarrow(\rho)e^{-i(m+1)\varphi}, -\phi_\uparrow(\rho)e^{-im\varphi}]^T$ [1]. This degeneracy is a direct consequence of the Kramers' Theorem. Here we may restrict m to be non-negative integers, as a negative m state can be regarded as the

time reversal partner for a state with $m \geq 0$. In this construction, Φ_m and $\mathcal{T}\Phi_m$ are both parity eigenstates with corresponding eigenvalues $(-1)^m$ and $(-1)^{m+1}$, respectively. However, they break the $\mathcal{PT}$ symmetry [1]. As discussed in Sec. 3.2, the lowest single-particle state occurs at $m = 0$ and has a half-quantum vortex configuration. Due to the degeneracy, any linear superposition of Φ_m and $\mathcal{T}\Phi_m$ — which breaks the parity symmetry — is also an eigenstate of the system. In particular, we may choose the equal-weight superposition as $(\Phi_m + \mathcal{T}\Phi_m)/\sqrt{2}$ which can be easily shown to be eigenstates of $\mathcal{PT}$ [1].

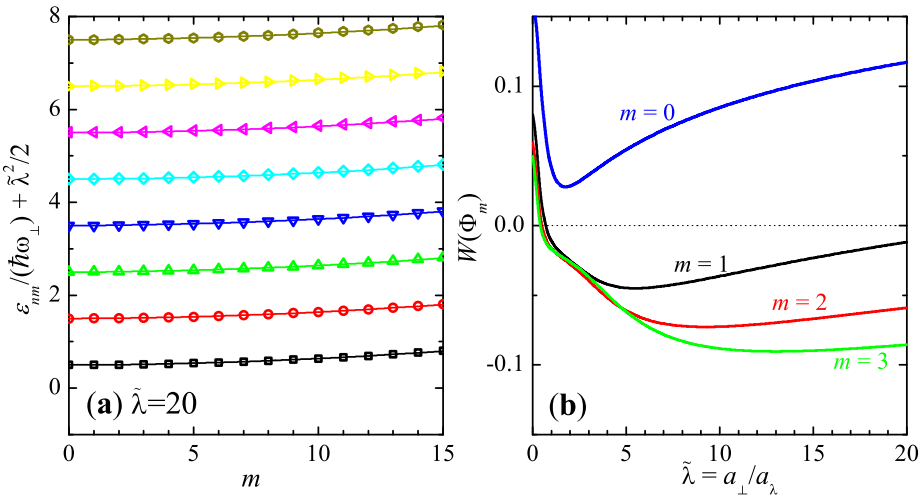

Figure 3.5 : (color online). (a) Single-particle energy spectrum. The lines show the empirical Eq. (3.15). (b) The W-function for the lowest four single-particle states in the LM. Image from Ref. [1].

The wavefunctions and the corresponding eigenenergies can be found numerically. At large SO coupling (i.e., $\lambda_{SO} > 5$), to a good approximation we find numerically that the low-lying spectrum forms discrete manifolds with spacing $\hbar\omega_\perp$(indexed by an integer $n \geq 0$),

$$\epsilon_{nm} \simeq \left[-\tilde{\lambda}^2 + (2n+1) + m\,(m+1)/\tilde{\lambda}^2\right] \hbar\omega_\perp/2\,. \tag{3.15}$$

As discussed in Sec. 2.3.3, the discrete manifolds of spectrum are similar to the well-known Landau levels, formed when a charged particle moves in magnetic fields. However, the reasons for their formation are very different [1].

3.3.2 Density distributions and spin textures

For a weakly interacting BEC with gN, $g_{\uparrow\downarrow}N \ll \hbar\omega_\perp$, only the LM is occupied. It is thus convenient to expand the field operator $\Psi = \sum_m \Phi_m(\mathbf{r})a_m$, where $\Phi_m(\mathbf{r})$ is the single-particle wavefunctions at the LM with energy ϵ_m [1]. The many-body Hamiltonian may then be rewritten as,

$$\mathcal{H} = \sum_m \epsilon_m a_m^+ a_m + \sum_{ijkl} V_{ijkl} a_i^+ a_j^+ a_k a_l, \tag{3.16}$$

where the interaction elements V_{ijkl} can be calculated straightforwardly for the contact interatomic interactions. We solve Eq. (3.16) numerically by using both mean-field theory [100] and exact diagonalization [101], for a conserved total angular momentum $\sum_m (m + 1/2)a_m^+ a_m = N m_{tot}$. Within mean-field, we replace a_m by a complex number $N^{1/2}c_m$ and minimize the GP energy $E_{GP}/N = \sum_m \epsilon_m |c_m|^2 + (N - 1)\sum_{ijkl} V_{ijkl} c_i^* c_j^* c_k c_l$, under the constraints $\sum_m |c_m|^2 = 1$ and $\sum_m (m + 1/2)|c_m|^2 = m_{tot}$. In practice, we truncate the angular momentum to $|m| \leq m_c$ (up to $m_c = 16$) [1].

Symmetry of condensate states: In the presence of the interaction represented by Eq. (3.14b), the many-body Hamiltonian still possesses both $\mathcal{P}$ and $\mathcal{PT}$ symmetries. As we have shown above, for a non-interacting system, we may choose the single-particle ground state to be an eigenstate of $\mathcal{P}$, or of $\mathcal{PT}$, or of neither operator [1]. In the mean-field level, this freedom of choosing different symmetry eigenstates may be

removed by inter-atomic interactions. In other words, the symmetry of condensate states would be determined *spontaneously* by interaction [1]. We have found that in the weakly interacting limit we are interested in here, the ground state is either an eigenstate of $\mathcal{P}$, or that of $\mathcal{PT}$. Which symmetry the ground state will possess can be determined in the following way. Let us consider an eigenstate of $\mathcal{P}$ with wavefunction $\Phi_{\mathcal{P}} = [\phi_\uparrow(\mathbf{r}), \phi_\downarrow(\mathbf{r})]^T$. The corresponding eigenstate of $\mathcal{PT}$ can be constructed as $\Phi_{\mathcal{PT}} = (\Phi_{\mathcal{P}} \pm \mathcal{T}\Phi_{\mathcal{P}})/\sqrt{2}$ [1]. The mean-field energy difference between these two states is determined by the S_z^2 term in Eq. (3.14b) which breaks the spin rotational symmetry in the interaction Hamiltonian:

$$\Delta E_{sp}(\Phi) = E(\Phi_{\mathcal{PT}}) - E(\Phi_{\mathcal{P}}) = (g_{\uparrow\downarrow} - g)W(\Phi)/4, \tag{3.17}$$

where $W(\Phi) \equiv \int d\mathbf{r}[(|\phi_\uparrow|^2 - |\phi_\downarrow|^2)^2 - (\phi_\uparrow\phi_\downarrow + \phi_\uparrow^*\phi_\downarrow^*)^2]$ [1]. The ground state will be a $\mathcal{P}$-eigenstate if $\Delta E_{sp}(\Phi) > 0$ for which we have $n_\sigma(\mathbf{r}) = n_\sigma(-\mathbf{r})$, or a $\mathcal{PT}$-eigenstate if $\Delta E_{sp}(\Phi) < 0$ for which we have $n_\uparrow(\mathbf{r}) = n_\downarrow(-\mathbf{r})$. The W-functions of several parity eigenstates are shown in Fig. 3.5(b). Equation (3.17) also shows that the symmetry of the ground state is sensitive to the relative magnitude of the interaction parameters g and $g_{\uparrow\downarrow}$ [1].

3.3.3 Ground state phase diagram

Phase diagram in the LM: Our symmetry argument suggests that all the condensate states could be classified by its $\mathcal{P}$ or $\mathcal{PT}$ symmetry, to be referred to respectively as phases I and II hereafter. We now check numerically this argument in the quantum Hall like regime with all bosons occupying into the LM, as shown in Fig. 3.8(a) for $\tilde{\lambda} = 20$ [1]. The characteristic density distributions for spin-up bosons in each phase

are shown in Fig. 3.6.

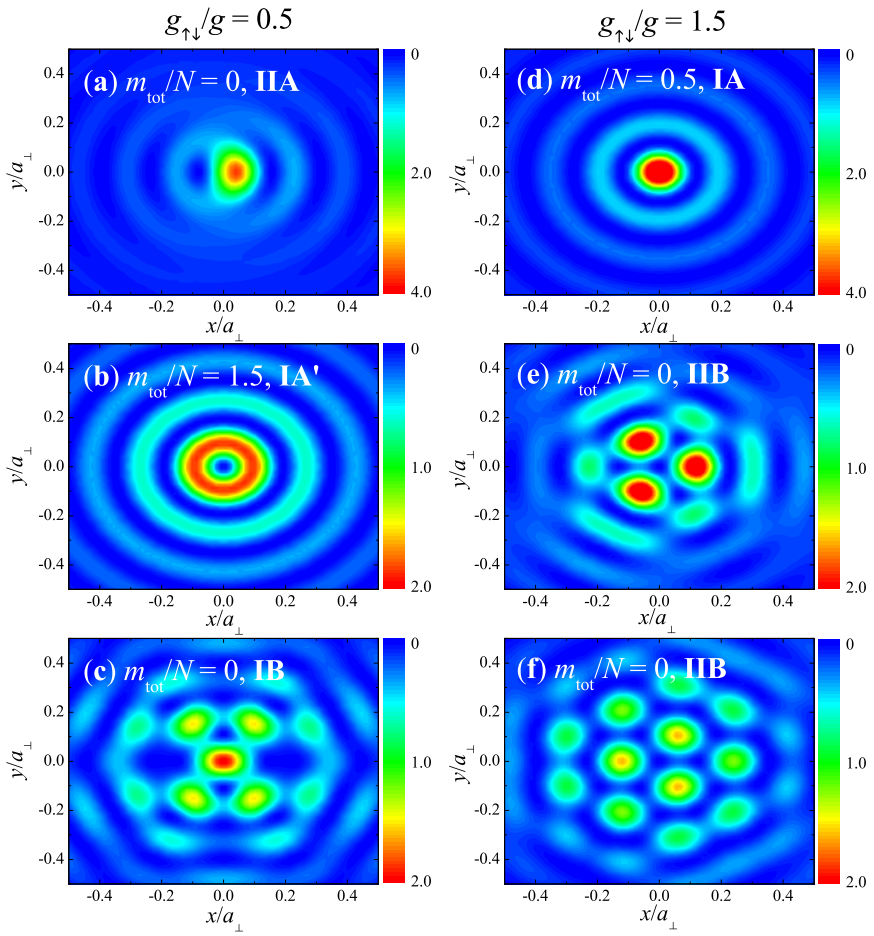

Figure 3.6 : (color online). Density patterns of spin-up bosons in the different ground states at three intra-species interactions $g(N-1)a_\perp^2$: (a,d) $0.02\hbar\omega_\perp$, (b,e) $0.1\hbar\omega_\perp$, and (c,f) $0.2\hbar\omega_\perp$. Image from Ref. [1].

At sufficiently weak interactions, where the characteristic interaction energy $g(N-1)a_\perp^2$ is smaller than the lowest intra-manifold spacing $\Delta E = \hbar\omega_\perp/\tilde{\lambda}^2$, only the ground single-particle state is occupied. The condensate state is thus either half-quantum vortex states of Φ_0 (or $\mathcal{T}\Phi_0$) or their superposition [1]. As $W(\Phi_0) > 0$ as shown in Fig. 3.5(b), we conclude that the ground state is a $\mathcal{PT}$-eigenstate for $g > g_{\uparrow\downarrow}$ (IIA) and it is a half-quantum vortex state (a $\mathcal{P}$-eigenstate) for $g < g_{\uparrow\downarrow}$ (IA). Their spin-up

density patterns are shown in Figs. 3.6(a) and (d), respectively [1].

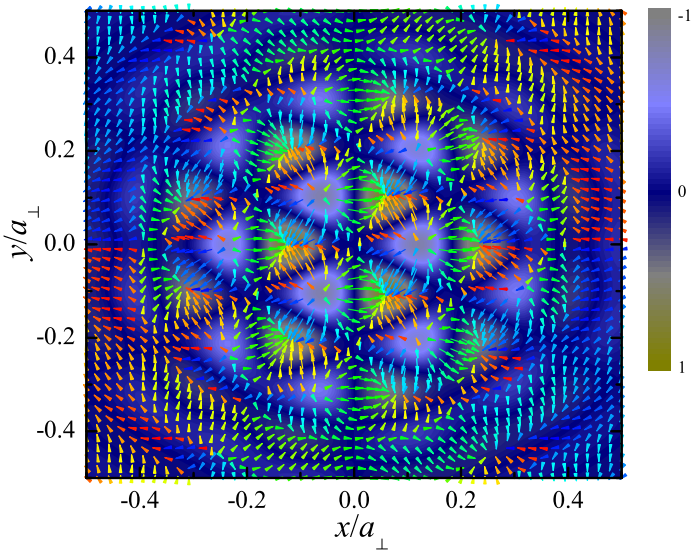

Figure 3.7 : (color online). Spin texture $\mathbf{S} = (1/2)\Phi^{+}\sigma\Phi$ corresponding to the state represented in Fig. 3.6(f). The arrows represent the transverse spin vector (S_x, S_y) with color and length representing the orientation and the magnitude of the transverse spin. The contour plot shows the axial spin $S_z = (1/2)\left(\phi_\uparrow^2 - \phi_\downarrow^2\right)$. Image from Ref. [1].

When the interaction becomes larger, more and more single-particle states are occupied. The occupation of the first excited single-particle state (Φ_1 and $\mathcal{T}\Phi_1$) occurs at $g_c(N-1)a_\perp^2 \simeq 0.0367\hbar\omega_\perp$, where the critical interaction strength g_c is determined from the equation $\epsilon_0 + (N-1)V_{0000} = \epsilon_1 + (N-1)V_{1111}$ [1]. As $W(\Phi_m) < 0$ for $m \geq 1$, we find an interesting reversal of the phase diagram when $g > g_c$: the $\mathcal{P}$-preserving phase (IA) changes into a $\mathcal{PT}$-preserving phase (IIB) at $g < g_{\uparrow\downarrow}$, while the $\mathcal{PT}$-preserving phase (IIA) changes into a $\mathcal{P}$-preserving phase (IA$'$ and IB) if $g > 0.2g_{\uparrow\downarrow}$. The phases IA$'$ and IB differ in the total angular momentum m_{tot} and density distribution [1]. In Phase IB, m_{tot} is suppressed to zero by large interatomic interactions. Note that in the phases (IIB) and (IB), we observe regular lattice patterns. In particular, a hexagonal lattice form gradually in the phase IIB, as shown

clearly in Figs. 3.6(e) and (f). In Fig. 3.7, we show the corresponding spin texture of the state, from which one can see that the system represents a lattice of skyrmions. Skyrmion lattice can be generated by rotating a spinor condensate [102, 103]. Here the skyrmion texture is induced by the SO coupling without rotation [1].

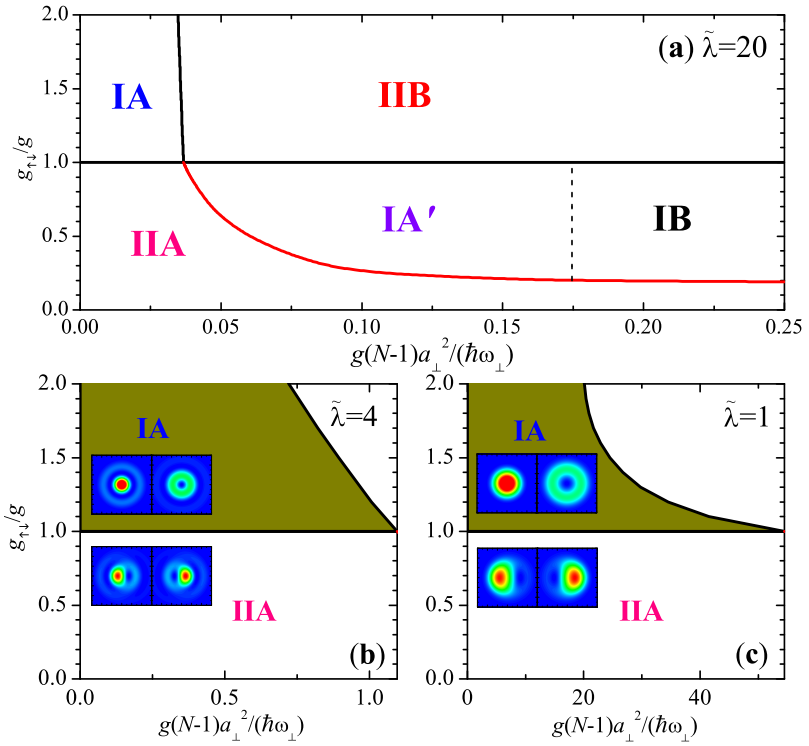

Figure 3.8 : (color online). (**a**) Phase diagram of a trapped 2D BEC with a large SO coupling $\tilde{\lambda} = 20$, where the single-particle spectrum forms discrete manifolds. For the weak interaction considered here, only the LM is occupied. The phases I and II preserve, respectively, the parity and parity-time-reversal symmetries. There are several sub-phases indicated by A, A′ and B, which differ in the density profile and/or angular momentum. The mean-field density patterns in different phases of spin-up bosons are shown in Fig. 3.6. (**b**) and (**c**) Phase diagram at weak SO coupling. Here the phases are determined without the restriction to the LM approximation. The insets illustrate the density profiles of the two spin components in phases IA and IIA. Image from Ref. [1].

The symmetry of the ground state at $g = g_{\uparrow\downarrow}$ cannot be determined within mean-field theory, since in this case $\Delta E_{sp}(\Phi) = 0$ [see Eq. (3.17)] and the energy becomes

invariant for different m_{tot}. However, it can be ordered by quantum fluctuations [82], which are well captured by exact diagonalization [1]. We have calculated the energy as a function of m_{tot} at $g(N-1)a_\perp^2/(\hbar\omega_\perp) = 0.02$ and 0.1 for $N = 4$, 8, and 12. With increasing N, the exact diagonalization result approaches the mean-field prediction. We find that the ground state at $g(N-1)a_\perp^2 = 0.02\hbar\omega_\perp$ has a spontaneous angular momentum $m_{tot} = -1/2$ or $+1/2$, while the ground state at $g(N-1)a_\perp^2 = 0.1\hbar\omega_\perp$ occurs at $m_{tot} = 0$ [1]. Therefore, we identify that the phases at $g = g_{\uparrow\downarrow}$ follow those at $g < g_{\uparrow\downarrow}$. This is in agreement with the result of Ref. [82], which employs a different "order from disorder" argument.

Summary: Our main results are summarized in Fig. 3.8, which shows the ground state as a function of interatomic interaction at a specific dimensionless SO coupling strength $\tilde{\lambda}$ [1]. By using mean-field theory and exact diagonalization, we find that: (**i**) The ground state falls into two classes of quantum phases, I and II, preserving respectively the parity ($\mathcal{P}$) and parity-time-reversal ($\mathcal{PT}$) symmetries. Both symmetries are satisfied by the model Hamiltonian [see Eqs. (3.14)]. (**ii**) In each class, there are several sub-phases (IA, IA$'$, IB and IIA, IIB) differing in the density distribution and/or total angular momentum [1]. (**iii**) The transition between different phases depends on interatomic interactions. At weak intra-species interactions below a critical value, $g < g_c$, the ground state is a half-quantum vortex state (IA) if $g < g_{\uparrow\downarrow}$ and a superposition of two degenerate half-quantum vortex states (IIA) otherwise. The phases IA and IIA vanish in the limit of large SO coupling, but dominate the phase diagram in the opposite [1]. When the intra-species interactions becomes larger ($g > g_c$), there is an interesting reversal of the symmetry class, i.e., interactions change the phase IA into IIB and the phase IIA into IA$'$ and then IB. In the phases IIB and IB, skyrmion lattices emerge spontaneously without rotation [1]. (**iv**) At $g = g_{\uparrow\downarrow}$, the phases are or-

dered by quantum fluctuations. Using exact diagonalization, we find that the phases follow those at $g < g_{\uparrow\downarrow}$ [1].

Phase diagram beyond LM: So far we have clarified the phase diagram at a particular SO coupling $\tilde{\lambda} = 20$ in the *weakly-interacting* LM regime [1]. However, the qualitative picture of diagram may persist beyond the regime of LM, as far as our symmetry argument holds. To check this, we performed a direct numerical calculation based on the full GP equation using the TSSP technique derived from Eqs. (3.14) without making the LM assumption [1]. In the regime as shown in Fig. 3.8(a), the results are in good agreement with the LM calculation. At larger interaction strength when higher manifolds get mixed in the ground state, we have found from the GP calculation that Phase IIB in Fig. 3.8(a) will change to a density-stripe phase with $\mathcal{P}$ symmetry, while Phase IB will change to a plane-wave phase with $\mathcal{PT}$ symmetry [1]. The density-stripe and the plane-wave phases have earlier been shown to be the mean-field ground state for a *homogeneous* system [95]. For the trapped system as studied here, at large interaction strength, the effect of the trap becomes less important and our results are therefore consistent with those reported in Ref. [95]. With decreasing $\tilde{\lambda}$, the phases IA and IIA will gradually become dominant in the diagram, as we find numerically that $g_c \propto 1/\tilde{\lambda}^2$ increases very rapidly. The skyrmion lattice phase, related to the LM formation, would disappear. This is confirmed by the GP calculation for smaller SO coupling and the results are represented in Fig. 3.8 (b) and (c). The half-quantum vortex state and its superposition dominate over a much larger parameter space as compared to the large SO coupling case [1]. A more detailed study of the complete phase diagram and the properties of different phases will be presented in Chapter 4.

Experimental relevance: We finally consider the experimental feasibility. A Rashba SO coupling can be induced in spinor ^{87}Rb gases [59]. The interaction strengths of ^{87}Rb atoms may be tuned by properly choosing the parameters of the laser fields that induce the SO coupling [97]. The two-dimensionality in such system has now been routinely realized by imposing a large harmonic confinement $V(z) = M\omega_z^2 z^2/2$ along the z-direction with $\omega_z \gg \omega_\perp$. The critical temperature for an ideal 2D SO BEC is given by $T_c = (c_\lambda/\pi)\sqrt{3N}\hbar\omega_\perp/k_B$, where the pre-factor $c_\lambda < 1$ takes into account the suppression due to the SO coupling [1]. Taking parameters from a recent experiment [29] with $\omega_\perp = 2\pi \times 20.6$ Hz and $N \sim 10^5$, we find at $\tilde{\lambda} = 10$, $c_\lambda \sim 0.6$ and $k_B T_c \simeq 120$ nK. Experimentally, a BEC temperature below 0.5 nK has been recorded [104], which is also lower than $\hbar\omega_\perp/k_B$. The mean-field LLL regime is therefore potentially attainable in future experiments [1].

Several technical challenges remain to be overcome as summarized, for example, by Mueller in Ref. [105]. As shown in Fig. 2.2, lasers are employed to couple atomic motion and hyperfine states (atomic pseudo-spin states). Thus, to allow the transition between the chosen atomic pseudo-spin states, experimentalists must tune the lasers near a multiplet of excited states. As discussed by Mueller in Ref. [105], the laser detuning from resonant frequency between the chosen pseudo-spin states must be the same order of magnitude as the fine structure splitting of that multiplet. However, there is a finite probability that an optically allowed transition may occur, which in-turn causes resonant absorption and eventual heating of the quantum gas. An important parameter that determines this heating, often referred to as Raman heating, is the ratio of the linewidth of the resonance to the fine structure splitting of the multiplet [105]. As the ratio is larger for lighter atoms, ^{87}Rb atoms are more

suitable than ^{40}K atoms, which in-turn are more suitable than ^{6}Li atoms. Furthermore, it is likely that the pair of laser-dressed pseudo-spin states are not the lowest energy states. Hence, collisional deexcitation can rapidly transfer population into the actual ground state [75]. In addition, to realize pure Rashba SO coupling, continuous rotational symmetry must be preserved. Several interesting experimental proposals have been put forward to overcome these challenges and to realize SO coupling [76]. In specific, Campbell *et al.* put forward a scheme to overcome (albeit partially) the limitations of Raman heating, collisional decay, and lack of rotational symmetry by introducing a cyclic 4-state topology [75].

In summary, we have investigated the phase diagram of a spin-orbit coupled spinor BEC in harmonic traps, by using mean-field theory and exact diagonalization method. We have predicted that the condensate states preserve the parity or parity-time-reversal symmetry and exhibit spontaneous vortex and skyrmion lattice structure in the lowest energy manifold which is induced by large spin-orbit coupling. Our results are valid for weak correlations with large number of bosons. Strongly correlated states would emerge with small number of bosons [106]. We address this potential possibility using exact diagonalization scheme in Chapter 5.

Chapter 4

Bogoliubov theory and dynamical simulation of collective excitations*

Collective excitations constitute one of the main sources of information for understanding the physics of many-body systems [107]. Measurement of low-lying collective oscillations in response to perturbations of the trap potential acts as an important experimental probe for the many-body physics of ultracold gases (for example, see Refs. [107, 108]). At the moment, the collective oscillations of trapped BECs [26] and two-component atomic gases with s-wave interactions in three dimensions [109] are both understood fairly well. For instance, experimental data from the study of low energy excitations of trapped Bose gases are found to be very good agreement with the ones derived from a simple linearization of the time-dependent GP equation [107, 110–112]. Therefore, it is only natural that we expect to learn more about the many-body physics of Rashba SO coupled Bose gases through a discussion of its collective excitations.

In Chapter 3, we discussed the mean-field GP equation to understand the ground state density distributions and spin textures of a Rashba SO coupled Bose gas in a 2D isotropic trapping potential. Furthermore, we discussed the condensation into a half-quantum vortex state that was qualitatively shown to occupy a large part of the phase space at small SO coupling strengths. Now, we proceed to systematically explore the parameter space for the half-quantum vortex state and analyze its stability. We

*Chapter 4 taken largely from our publication in Ref. [2].

present the phase diagram as a function of the SO coupling and the interatomic interaction strengths. We do this by solving the Bogoliubov equations and computing the collective excitation spectrum. Upon presenting this computational procedure in detail, we analyze the stability of the half-quantum vortex state by monitoring the softening of collective mode frequencies and by comparing the energy with that of competing states. We also investigate the dynamical properties of the half-quantum vortex state by directly simulating the corresponding time-dependent GP equation via the real-time propagation of the mean-field ground state under perturbations. The collective excitation spectrum obtained from the Bogoliubov equation is then compared to the results from direct simulation. Finally, the stability of the half-quantum vortex state against both trap anisotropy and anisotropy in the SO coupling term is examined.

4.1 Theory formalism

The theory of collective excitations in a one-component Bose gas with no SO coupling is described, for example, in the seminal review article by Dalfovo et al. in Ref. [26]. In this section, we elaborate on the analogous theory on Bogoliubov formalism for SO coupled two-component Bose gas*. For a weakly interacting trapped Bose gas at zero temperature, we assume that all the bosons condense into a single quantum state $\Phi(\mathbf{r}) = [\Phi_\uparrow(\mathbf{r}), \Phi_\downarrow(\mathbf{r})]^T$. Following the standard mean-field theory approach, we separate the field operator into a condensate and a fluctuation part, $\Psi_\sigma(\mathbf{r}) = \Phi_\sigma(\mathbf{r}) + \tilde{\Psi}_\sigma(\mathbf{r})$ [2]. Keeping up to quadratic terms in $\tilde{\Psi}_\sigma(\mathbf{r})$, this separation leads to an approximate Hamiltonian $\mathcal{H} = \int d\mathbf{r}[\mathcal{H}_{\rm GP} + \mathcal{H}_T]$, where the condensate

*The remainder of this chapter is taken largely from our publication in Ref. [2].

part is given by,

$$\begin{aligned}\mathcal{H}_{\rm GP} &= \Phi^\dagger\left[\mathcal{H}_{\rm osc}+\mathcal{V}_{SO}-\mu\right]\Phi \\ &\quad +\frac{g}{2}\left(|\Phi_\uparrow|^4+|\Phi_\downarrow|^4\right)+g_{\uparrow\downarrow}\left|\Phi_\uparrow\Phi_\downarrow\right|^2, \end{aligned} \tag{4.1}$$

and the fluctuation part is $\mathcal{H}_T=\tilde{\Psi}^\dagger\mathcal{H}_{\rm Bog}\tilde{\Psi}$ with

$$\mathcal{H}_{\rm Bog}=\begin{bmatrix} \mathcal{H}_{s_\uparrow}+g\left|\Phi_\uparrow\right|^2 & V_{\rm so}+g_{\uparrow\downarrow}\Phi_\uparrow\Phi_\downarrow^* & g\Phi_\uparrow^2 & g_{\uparrow\downarrow}\Phi_\uparrow\Phi_\downarrow \\ V_{\rm so}^\dagger+g_{\uparrow\downarrow}\Phi_\uparrow^*\Phi_\downarrow & \mathcal{H}_{s_\downarrow}+g\left|\Phi_\downarrow\right|^2 & g_{\uparrow\downarrow}\Phi_\uparrow\Phi_\downarrow & g\Phi_\downarrow^2 \\ g\left(\Phi_\uparrow^*\right)^2 & g_{\uparrow\downarrow}\Phi_\uparrow^*\Phi_\downarrow^* & \mathcal{H}_{s_\uparrow}+g\left|\Phi_\uparrow\right|^2 & -V_{\rm so}^\dagger+g_{\uparrow\downarrow}\Phi_\uparrow^*\Phi_\downarrow \\ g_{\uparrow\downarrow}\Phi_\uparrow^*\Phi_\downarrow^* & g\left(\Phi_\downarrow^*\right)^2 & -V_{\rm so}+g_{\uparrow\downarrow}\Phi_\uparrow\Phi_\downarrow^* & \mathcal{H}_{s_\downarrow}+g\left|\Phi_\downarrow\right|^2 \end{bmatrix}. \tag{4.2}$$

Here $\mathcal{H}_{\rm osc}\equiv-\hbar^2\nabla^2/(2M)+V(\rho)$, $\mathcal{H}_{s_\uparrow}\equiv\mathcal{H}_{\rm osc}+g\left|\Phi_\uparrow\right|^2+g_{\uparrow\downarrow}\left|\Phi_\downarrow\right|^2-\mu$, $\mathcal{H}_{s_\downarrow}\equiv\mathcal{H}_{\rm osc}+g_{\uparrow\downarrow}\left|\Phi_\uparrow\right|^2+g\left|\Phi_\downarrow\right|^2-\mu$, $V_{\rm so}\equiv-i\lambda_R(\partial_y+i\partial_x)$ and $V_{\rm so}^\dagger\equiv-i\lambda_R(\partial_y-i\partial_x)$, and we have introduced a 4×4 Nambu spinor $\tilde{\Psi}=[\tilde{\Psi}_\uparrow(\mathbf{r}),\tilde{\Psi}_\downarrow(\mathbf{r}),\tilde{\Psi}_\uparrow^\dagger(\mathbf{r}),\tilde{\Psi}_\downarrow^\dagger(\mathbf{r})]^T$ [2].

While the condensate wave-function can be obtained from the GP equations $\delta\mathcal{H}_{\rm GP}/\delta\Phi(\mathbf{r})=0$, the quasi-particle wave-functions with energy $\hbar\omega$ satisfy the Bogoliubov equations [79–81],

$$\mathcal{H}_{Bog}\begin{bmatrix} u_\uparrow(\mathbf{r}) \\ u_\downarrow(\mathbf{r}) \\ v_\uparrow(\mathbf{r}) \\ v_\downarrow(\mathbf{r}) \end{bmatrix}=\hbar\omega\begin{bmatrix} +u_\uparrow(\mathbf{r}) \\ +u_\downarrow(\mathbf{r}) \\ -v_\uparrow(\mathbf{r}) \\ -v_\downarrow(\mathbf{r}) \end{bmatrix}, \tag{4.3}$$

and are normalized by $\int d\mathbf{r}\left[|u_\uparrow|^2+|u_\downarrow|^2-|v_\uparrow|^2-|v_\downarrow|^2\right]=1$. These Bogoliubov quasi-particles correspond to collective density oscillation modes around the condensate

with frequency ω [113]. It is easy to see that the wave-function $[v_\uparrow^*(\mathbf{r}), v_\downarrow^*(\mathbf{r}), u_\uparrow^*(\mathbf{r}), u_\downarrow^*(\mathbf{r})]^T$ is also a solution of Eq. (4.3), but with energy $-\hbar\omega$ [2]. This is an unphysical solution, due to the Bogoliubov transformation which enlarges the Hilbert space for quasiparticles. Physically, we should restrict to a non-negative mode frequency, $\omega \geq 0$. For the fermionic Bogoliubov transformation, we have exactly the same situation [2]. The fermionic Bogoliubov equation has the same "particle-hole" symmetry or duality [114–116]. In that case, one needs to remove the particle-hole redundancy by multiplying a factor of $1/2$ in the calculation of physical quantities such as density and order parameter [114–116].

4.2 Solutions of Bogoliubov equations

Given the wave-function of the half-quantum vortex state, $[\phi_\uparrow(\rho), \phi_\downarrow(\rho)\, e^{i\varphi}]^T/\sqrt{2\pi}$, we now turn to consider its collective excitations, as described by the coupled Bogoliubov equations (4.3). As a result of rotational symmetry, it is easy to see that the Bogoliubov wave-functions have a good azimuthal quantum number m and hence can be written as, $[u_\uparrow(\rho), u_\downarrow(\rho)\, e^{i\varphi}, v_\uparrow(\rho), v_\downarrow(\rho)\, e^{-i\varphi}]^T e^{im\varphi}/\sqrt{2\pi}$ [2]. Therefore, we have

$$\mathcal{H}_{\mathrm{Bog}} \begin{bmatrix} u_\uparrow(\rho) \\ u_\downarrow(\rho) \\ v_\uparrow(\rho) \\ v_\downarrow(\rho) \end{bmatrix} = \hbar\omega \begin{bmatrix} +u_\uparrow(\rho) \\ +u_\downarrow(\rho) \\ -v_\uparrow(\rho) \\ -v_\downarrow(\rho) \end{bmatrix}, \tag{4.4}$$

where

$$\mathcal{H}_{\mathrm{Bog}} = \begin{bmatrix} \mathcal{L}_m + \mathcal{U} & \mathcal{U} \\ \mathcal{U} & \mathcal{L}_{-m} + \mathcal{U} \end{bmatrix}, \tag{4.5}$$

with

$$\mathcal{L}_m = \begin{bmatrix} \mathcal{H}_{s,m} + \bar{g}\phi_\uparrow^2 + \bar{g}_{\uparrow\downarrow}\phi_\downarrow^2 & \lambda_R\left[\partial_\rho + (m+1)/\rho\right] \\ \lambda_R\left(-\partial_\rho + m/\rho\right) & \mathcal{H}_{s,m+1} + \bar{g}_{\uparrow\downarrow}\phi_\uparrow^2 + \bar{g}\phi_\downarrow^2 \end{bmatrix}, \tag{4.6}$$

and

$$\mathcal{U} = \begin{bmatrix} \bar{g}\phi_\uparrow^2 & \bar{g}_{\uparrow\downarrow}\phi_\uparrow\phi_\downarrow \\ \bar{g}_{\uparrow\downarrow}\phi_\uparrow\phi_\downarrow & \bar{g}\phi_\downarrow^2 \end{bmatrix}. \tag{4.7}$$

Following the prescription described in Secs. 3.1 and 3.2, various parameters are made dimensionless for computational convenience.

To solve the Bogoliubov equations, as before we expand the wave-functions using a 2D harmonic oscillator basis,

$$u_\uparrow(\rho) = \sum_k a_k R_{km}(\rho), \tag{4.8}$$

$$u_\downarrow(\rho) = \sum_k b_k R_{km+1}(\rho), \tag{4.9}$$

$$v_\uparrow(\rho) = \sum_k c_k R_{km}(\rho), \tag{4.10}$$

$$v_\downarrow(\rho) = \sum_k d_k R_{km-1}(\rho). \tag{4.11}$$

This leads to a secular matrix of $\mathcal{H}_{\rm Bog}$, whose elements can be calculated directly using the 2D harmonic oscillator basis [2]. We note that to obtain the Bogoliubov quasiparticles we cannot diagonalize the secular matrix directly, because of the minus sign before $v_\uparrow(\rho)$ and $v_\downarrow(\rho)$ on the right-hand side of Eq. (4.4) [2]. To remove the minus sign, we may multiply a matrix Diag$\{+1,+1,-1,-1\}$ on both sides of Eq. (4.4). Therefore, we should diagonalize a *non-symmetric* matrix Diag$\{+1,+1,-1,-1\}\mathcal{H}_{\rm Bog}$ and normalize the quasi-particle wave-functions according to

$$\int_0^\infty \rho d\rho [u_\uparrow^2 + u_\downarrow^2 - v_\uparrow^2 - v_\downarrow^2] = 1. \tag{4.12}$$

The number of resulting eigenvalues is two times the number that we want, since the Bogoliubov transformation enlarges the Hilbert space for quasiparticles. As we mentioned earlier, there are two branches of eigenvalues, one positive and the other negative, as a result of the "particle-hole" duality between the solution $[u_\uparrow(\mathbf{r}), u_\downarrow(\mathbf{r}), v_\uparrow(\mathbf{r}), v_\downarrow(\mathbf{r})]^T$ (with energy $+\hbar\omega$) and $[v_\uparrow^*(\mathbf{r}), v_\downarrow^*(\mathbf{r}), u_\uparrow^*(\mathbf{r}), u_\downarrow^*(\mathbf{r})]^T$ (with energy $-\hbar\omega$) [2]. We should take the positive branch, since the Bogoliubov quasiparticle corresponds to the collective oscillation of the cloud and should have the positive oscillation frequency. Note that, because of the "particle-hole" duality, in our case with rotational symmetry the Bogoliubov quasiparticles at negative azimuthal quantum number m may be obtained from the negative energy branch of the solution with $m > 0$ [2].

4.2.1 Monopole and dipole modes

In the case of *monopole* mode ($m = 0$), also referred to as *breathing* mode, where the matrix takes the form:

$$\mathcal{H}_{\text{Bog}} = \begin{bmatrix} \mathcal{L}_{\text{GP}} + \mathcal{U} & \mathcal{U} \\ \mathcal{U} & \mathcal{L}_{\text{GP}} + \mathcal{U} \end{bmatrix}, \tag{4.13}$$

there is an alternative way to solve the Bogoliubov equation, following Hutchinson, Zaremba, and Griffin (HZG) [117]. By denoting collectively $u = [u_\uparrow(\rho), u_\downarrow(\rho)]$ and $v = [v_\uparrow(\rho), v_\downarrow(\rho)]$, we have,

$$(\mathcal{L}_{\text{GP}} + 2\mathcal{U})(u + v) = \hbar\omega(u - v), \tag{4.14}$$

$$\mathcal{L}_{\text{GP}}(u - v) = \hbar\omega(u + v). \tag{4.15}$$

Let us now expand the wave-functions $u \pm v$ in terms of the eigenfunctions ψ_α of $\mathcal{L}_{\rm GP}$ with energy ϵ_α (i.e., $\mathcal{L}_{\rm GP}\psi_\alpha = \epsilon_\alpha \psi_\alpha$),

$$u - v = \sum_{\alpha \neq 0} \frac{c_\alpha}{\epsilon_\alpha^{1/2}} \psi_\alpha, \tag{4.16}$$

$$u + v = \sum_{\alpha \neq 0} \frac{\epsilon_\alpha^{1/2} c_\alpha}{\hbar\omega} \psi_\alpha. \tag{4.17}$$

Here, the lowest eigenstate of $\mathcal{L}_{\rm GP}$ with zero energy should be removed, as it simply corresponds to the condensate mode. It is easy to see that $(\mathcal{L}_{\rm GP} + 2\mathcal{U})\mathcal{L}_{GP}(u-v) = (\hbar\omega)^2(u-v)$ and $\mathcal{L}_{\rm GP}(\mathcal{L}_{\rm GP} + 2\mathcal{U})(u+v) = (\hbar\omega)^2(u+v)$. Inserting the expansion of $u - v$ or $u + v$, one finds the secular equation,

$$\sum_\beta \left\{ \epsilon_\alpha^2 \delta_{\alpha\beta} + 2\epsilon_\alpha^{1/2} \mathcal{U}_{\alpha\beta} \epsilon_\beta^{1/2} \right\} c_\beta = (\hbar\omega)^2 c_\alpha, \tag{4.18}$$

where

$$\mathcal{U}_{\alpha\beta} = \int_0^\infty \rho d\rho \, \psi_\alpha^\dagger(\rho) \mathcal{U} \psi_\beta(\rho). \tag{4.19}$$

By diagonalizing the secular matrix, one obtains the mode frequency ω and the coefficients c_α. The latter should be normalized as $\sum_\alpha c_\alpha^2 = \hbar\omega$, in accord with the normalization condition for u and v. We have numerically checked that the HZG solution leads to exactly the same result as the direct diagonalization of the non-symmetric matrix $\mathrm{Diag}\{+1,+1,-1,-1\}\mathcal{H}_{\rm Bog}$, if we discard the zero-frequency condensate mode in the latter method.

In Fig. 4.1, we graph the monopole ($m = 0$) and the dipole mode ($m = \pm 1$) frequencies as a function of the interaction strength. With increasing interaction, the mode frequency decreases and appears to saturate at sufficiently large interactions [2].

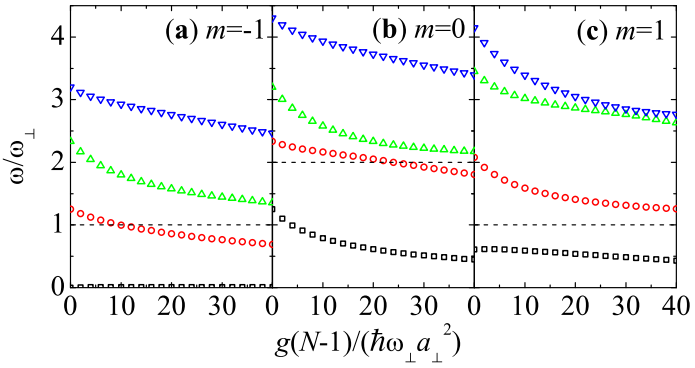

Figure 4.1 : (color online). The mode frequency of monopole ($m = 0$) and dipole ($m = \pm 1$) modes as a function of interaction strength at a fixed SO coupling $\lambda_{SO} = 1$ and at $g_{\uparrow\downarrow} = 1.1g$. Image from Ref. [2].

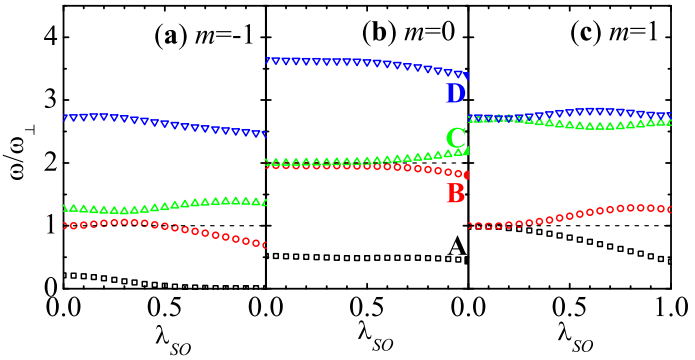

Figure 4.2 : (color online). The mode frequency of monopole ($m = 0$) and dipole ($m = \pm 1$) modes as a function of SO coupling at a fixed interaction strength $g(N - 1) = 40(\hbar\omega_\perp a_\perp^2)$ and at $g_{\uparrow\downarrow} = 1.1g$. Image from Ref. [2].

This may be anticipated from the point of view of two-fluid hydrodynamic behavior in the Thomas-Fermi regime. In Fig. 4.2, we report the dependence of the mode frequencies on SO coupling. In the absence of SO coupling, the monopole mode with $\omega = 2\omega_\perp$ and the dipole mode with $\omega = \omega_\perp$ are the exact solutions of quantum many-body systems in a harmonic trap [2]. At a finite SO coupling we find that these two solutions are no longer exact. The relative deviations of the monopole mode and dipole mode at $\lambda_{SO} = 1$ are about 10% and 30%, respectively, from the exact solution

of $\omega = 2\omega_\perp$ and $\omega = \omega_\perp$ in the absence of SO coupling [2].

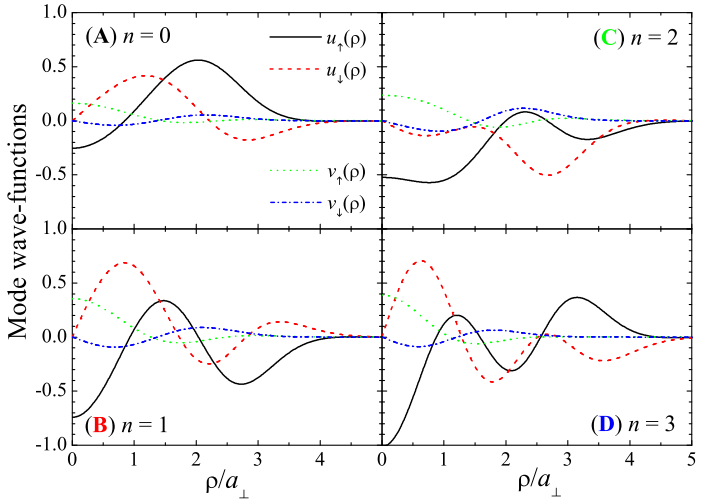

Figure 4.3 : (color online). Bogoliubov wave-functions of the lowest four monopole modes at $\lambda_{SO} = 1$, $g(N-1) = 40(\hbar\omega_\perp a_\perp^2)$ and $g_{\uparrow\downarrow} = 1.1g$. The mode frequencies are indicated in Fig. 7b by solid symbols. Image from Ref. [2].

In Fig. 4.3, we plot the Bogoliubov wave-functions of the lowest four monopole modes at $\lambda_{SO} = 1$, $g(N-1) = 40(\hbar\omega_\perp a_\perp^2)$ and $g_{\uparrow\downarrow} = 1.1g$. We find that the density response is mainly carried by $u_\uparrow(\rho)$ and $u_\downarrow(\rho)$ components. With increasing mode frequency, more nodes appear in $u_\uparrow(\rho)$ and $u_\downarrow(\rho)$. In contrast, the response in $v_\uparrow(\rho)$ and $v_\downarrow(\rho)$ is relatively weak, and the curve shape is nearly unchanged as the mode frequency increases [2].

4.3 Instability analysis and phase diagram

We are now ready to analyze the parameter space for the existence of half-quantum vortex state. We observe that it becomes unstable with respect to increasing interaction strength or decreasing coupling ratio, $g_{\uparrow\downarrow}/g$. We explain the instability either by energy considerations and by the softening of collective density modes.

4.3.1 Dipole instability

As mentioned earlier, for any half-quantum vortex state, $\phi(\mathbf{r}) = [\phi_\uparrow(\rho), \phi_\downarrow(\rho)e^{i\varphi}]^T/\sqrt{2\pi}$, there is a degenerate time-reversal partner state, $\mathcal{T}\phi(\mathbf{r}) = [\phi_\downarrow(\rho)e^{-i\varphi}, -\phi_\uparrow(\rho)]^T/\sqrt{2\pi}$ [2]. This leads to an instability for the half-quantum vortex state with respect to a superposition state, which with equal weight takes the form,

$$\phi_s(\mathbf{r}) = \frac{1}{\sqrt{4\pi}} \begin{bmatrix} \phi_\uparrow(\rho) + \phi_\downarrow(\rho)e^{-i(\varphi-\varphi_0)} \\ \phi_\downarrow(\rho)e^{i(\varphi-\varphi_0)} - \phi_\uparrow(\rho) \end{bmatrix}. \tag{4.20}$$

Here φ_0 is an arbitrary azimuthal angle. The energy difference between the superposition state and the half-quantum vortex state is given by

$$\Delta E_{\mathrm{GP}} = \frac{(g_{\uparrow\downarrow} - g)(N-1)}{4} W[\phi(\mathbf{r})]. \tag{4.21}$$

Therefore, if $W[\phi(\mathbf{r})] > 0$, the half-quantum vortex state is stable only when $g < g_{\uparrow\downarrow}$ [2].

In Figs. 4.4(a) and (b), we check the W-function of the half-quantum vortex state in the presence of interatomic interactions. It always appears to be positive, though the interactions tend to decrease its absolute magnitude. Hence, there must be a quantum phase transition occurring at the isotropic point $g = g_{\uparrow\downarrow}$. Once $g > g_{\uparrow\downarrow}$, a superposition state with density pattern,

$$n_{\uparrow,\downarrow} = \frac{1}{2\pi}\left[\frac{\phi_\uparrow^2 + \phi_\downarrow^2}{2} \pm \phi_\uparrow\phi_\downarrow\cos(\varphi - \varphi_0)\right], \tag{4.22}$$

becomes preferable. The 2D contour plot of this density pattern with $\varphi_0 = 0$ is schematically shown in the inset of Fig. 4.7 (in the phase IIA) [2].

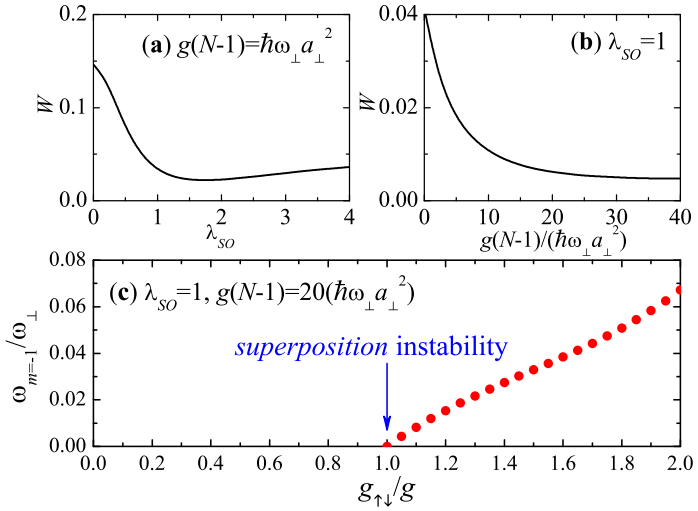

Figure 4.4 : (color online). (a) The W-function as a function of SO coupling at $g(N-1) = \hbar\omega_\perp a_\perp^2$ and $g_{\uparrow\downarrow} = 1.1g$. (b) The W-function as a function of interaction strength at $\lambda_{SO} = 1$ and $g_{\uparrow\downarrow} = 1.1g$. (c) The instability of the lowest dipole mode frequency $\omega_{m=-1}$ with decreasing $g_{\uparrow\downarrow}/g$ at $\lambda_{SO} = 1$ and $g(N-1) = 20(\hbar\omega_\perp a_\perp^2)$. Image from Ref. [2].

In general, in passing through the quantum phase transition point, we observe the softening of a particular mode frequency. As the superposition state involves a time-reversed state with angular momentum $m = -1$, the lowest dipole mode with $m = -1$ can become unstable [2]. In Fig. 4.4(c), we plot the lowest dipole mode frequency $\omega_{m=-1}$ as a function of $g_{\uparrow\downarrow}/g$ at $\lambda_{SO} = 1$ and $g(N-1) = 20(\hbar\omega_\perp a_\perp^2)$. Indeed, with decreasing $g_{\uparrow\downarrow}/g$, the mode frequency $\omega_{m=-1}$ decreases and approaches to zero exactly at the phase transition point [2].

4.3.2 Quadrupole instability

There is another instability for the half-quantum vortex state, occurring with increasing interatomic interaction strength. With sufficiently large interactions, we anticipate that the state with high-order azimuthal angular momentum will energet-

ically become favorable [2]. For example, let us consider a condensate state with an azimuthal angular momentum $m = 1$ (the 3/2-quantum vortex state), which has the form,

$$\phi_{m=1}(\mathbf{r}) = \frac{1}{\sqrt{2\pi}} \begin{bmatrix} \phi_{\uparrow}(\rho)e^{i\varphi} \\ \phi_{\downarrow}(\rho)e^{i2\varphi} \end{bmatrix}. \tag{4.23}$$

The mean-field energy of this state can be obtained by solving the GP equation as before, except that we need to take $R_{k1}(\rho)$ and $R_{k2}(\rho)$ as the expansion functions for $\phi_{\uparrow}(\rho)$ and $\phi_{\downarrow}(\rho)$, respectively. Its degenerate time-reversal partner state has an azimuthal angular momentum $m = -2$ [2].

It is easy to see from Fig. 4.5(a) that beyond a critical interaction strength the condensate state with $m = 1$, $\phi_{m=1}(\mathbf{r})$, is lower in energy than the half-quantum vortex state, $\phi_{m=0}(\mathbf{r})$. We note, however, that the critical interaction strength determined in this way is not accurate, as a superposition state of $\phi_{m=0}(\mathbf{r})$ and $\phi_{m=1}(\mathbf{r})$ may already become energetically more preferable than $\phi_{m=1}(\mathbf{r})$ at a smaller interaction strength [2].

An accurate determination of the threshold could be obtained by monitoring the instability in a particular collective mode. As the condensate state has a well-defined parity, we find that the instability occurs in the lowest quadrupole mode with $m = -2$. In Fig. 4.5(b), we graph the lowest quadrupole mode frequency $\omega_{m=-2}$ as a function of the interaction strength [2]. As the interaction increases, the real part of mode frequency decreases to zero and the imaginary part becomes positive, indicating clearly that this mode will exponentially grow if the condensate is initially in the half-quantum vortex configuration. The condensate then starts to involve high-order angular momentum components [2]. The critical interaction strength g_c can be simply determined from the softening of the mode frequency, i.e., $\omega_{m=-2}(g = g_c) = 0$.

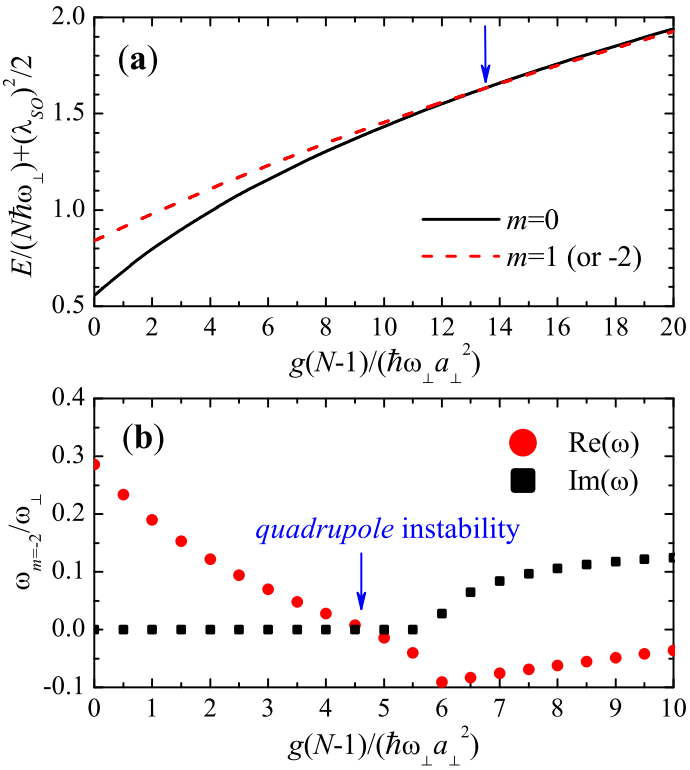

Figure 4.5 : (color online). (a) GP energy of the 3/2-quantum vortex state $\phi_{m=1}(\mathbf{r})$ and of the half-quantum vortex state $\phi_{m=0}(\mathbf{r})$ as a function of interaction strength at $\lambda_{SO} = 2$ and $g_{\uparrow\downarrow}/g = 1.1$. Beyond a critical interaction strength as indicated by an arrow, $\phi_{m=1}(\mathbf{r})$ becomes energetically favorable. (b) The corresponding lowest quadrupole mode frequency $\omega_{m=-2}$. It becomes unstable beyond a threshold g_c. Image from Ref. [2].

In Fig. 4.6, we graph the critical interacting strength as a function of SO coupling at $g_{\uparrow\downarrow} = g$ and $g_{\uparrow\downarrow} = 2g$. The solid line at the isotropic point $g_{\uparrow\downarrow}/g$ has been recently calculated by Zhou *et al.* by using an imaginary time evolution method [82, 93]. Our results are in excellent agreement with theirs. We find that at smaller SO couplings the critical interaction strength decreases rapidly with increasing $g_{\uparrow\downarrow}/g$.

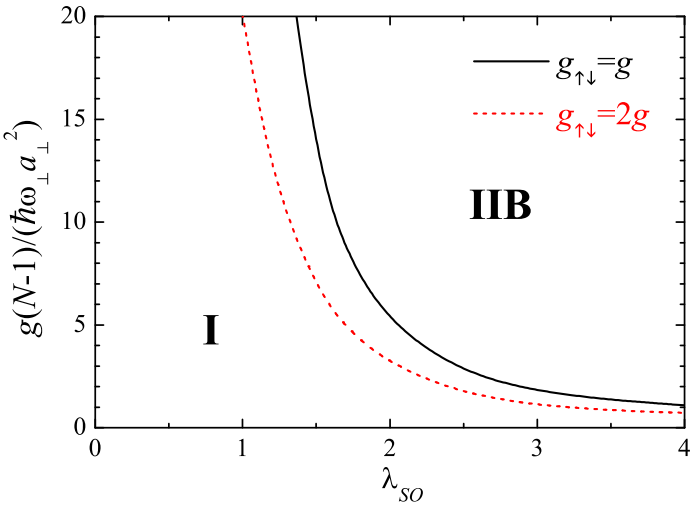

Figure 4.6 : (color online). Phase diagram at $g_{\uparrow\downarrow} = g$ and $g_{\uparrow\downarrow} = 2g$. The critical interaction strength has been shown as a function of SO coupling. Image from Ref. [2].

4.3.3 Phase diagram

We have systematically investigated the ground condensate state of a spin-orbit coupled spin-1/2 Bose gas confined by a two-dimensional harmonic trap. The density distributions and collective density excitations have been obtained respectively by solving the GP equation and the Bogoliubov equation, which are generalized to include SO coupling [2]. Our main results are summarized in Fig. 4.7. The half-quantum vortex state (the phase I) is the ground state if the intra-species interaction is smaller than the inter-species interaction ($g < g_{\uparrow\downarrow}$) and if the interaction strength is below a threshold ($g < g_c$), where g_c depends on the ratio of $g_{\uparrow\downarrow}/g$ [2]. Otherwise, it becomes energetically unstable towards a superposition state of two degenerate half-quantum vortex states (phase IIA), or a state involving higher-order angular momentum components (phase IIB). With decreasing dimensionless SO coupling strength λ_{SO}, the threshold g_c becomes exponentially large, leading to a large parameter space for the half-quantum vortex state (see Fig. 4.6) [2]. It is therefore feasible to observe this in

current experiments with ultracold SO coupled spinor Bose gases of ^{87}Rb atoms.

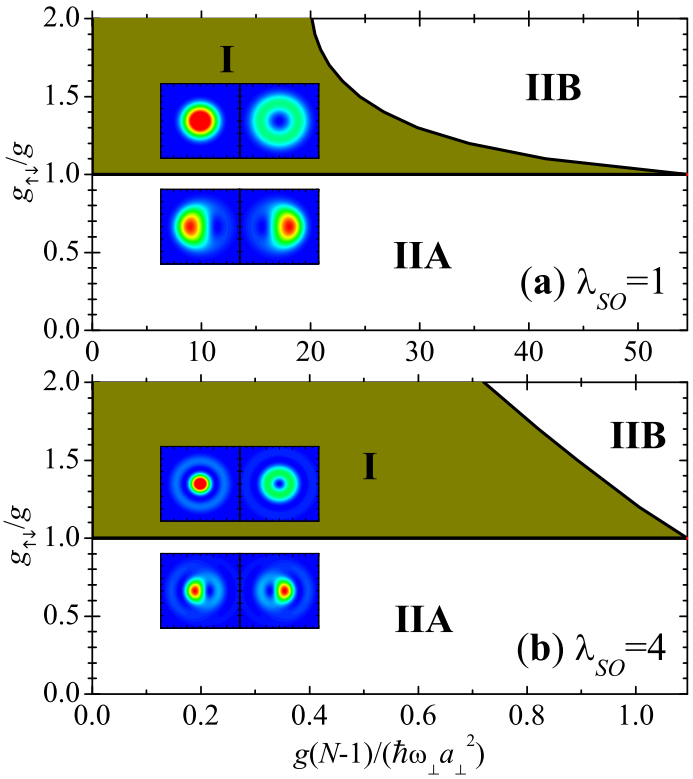

Figure 4.7 : (color online). Phase diagram at two dimensionless SO coupling strengths, $\lambda_{SO} = 1$ (a) and $\lambda_{SO} = 4$ (b). The half-quantum vortex state (phase I) becomes unstable when the intra-species interaction is larger than the inter-species interaction ($g > g_{\uparrow\downarrow}$, phase IIA) or when the interatomic interactions are sufficiently strong ($g > g_c$, phase IIB). The insets show the density patterns of spin-up and spin-down bosons in phases I and IIA. We note that the critical interaction strength g_c increases rapidly with decreasing SO coupling strength λ_{SO}. Image from Ref. [2].

We shall now to summarize various findings from our analysis: (**1**) The condensate is in a half-quantum vortex state if the intra-species interaction g is smaller than inter-species interaction $g_{\uparrow\downarrow}$, and if the interaction strength is below a threshold g_c. We have calculated the threshold by monitoring the unstable quadrupole mode with an azimuthal angular momentum $m = -2$. A phase diagram for the half-quantum vortex state is therefore determined, as given in Figs. 4.6 and 4.7 [2]. (**2**) The

half-quantum vortex state (phase I) will turn into a superposition of two degenerate half-quantum vortex states (phase IIA) if $g > g_{\uparrow\downarrow}$ and will start to involve high-order angular momentum components (phase IIB) if $g > g_c$, where g_c depends on the ratio $g_{\uparrow\downarrow}/g$ [2]. (**3**) In the presence of spin-orbit coupling, the behavior of collective density modes becomes complicated. In particular, the monopole mode with $\omega = 2\omega_\perp$ and the dipole mode with $\omega = \omega_\perp$ are no longer exact solutions of the many-body system [2]. (**4**) The condensate wave-functions in the phases IIA and IIB break the rotational symmetry. Interesting density patterns will emerge in the limit of very large interatomic interactions. The phase IIB in Fig. 4.7 will change to a density-stripe phase, while the IIA will ultimately change to a plane-wave phase (not shown). The density-stripe and the plane-wave phases have been shown to be the mean-field ground state of a homogeneous spin-orbit coupled Bose gas [95]. For the trapped system considered here, at large interaction strength, the effect of the trap becomes less important and our result therefore is consistent with that of a homogeneous system [2].

4.4 Dynamical simulation

As discussed in the introductory part of this chapter, measurement of collective oscillations of trapped gases in response to perturbations of the trap potential acts as an important experimental probe for the many-body physics of ultracold gases [108]. To theoretically investigate the corresponding dynamical properties of the system, we perform direct numerical simulations by real-time propagation of the ground state under perturbation. To do this, firstly we obtain the ground state by solving the coupled GP equations in Eqn. (4.1) using TSSP method. For illustration and analysis purposes, we focus on the half-quantum vortex ground state and perturb it in

two ways – excite the monopole and dipole modes – and determine the collective excitation spectrum.

4.4.1 Monopole or breathing mode analysis

To begin with, let us briefly explain the scheme to excite monopole modes in a conventional trapped atom experiment. For instance, with a magnetic trap, the trapping frequency may be adjusted by varying the bias field at the center of the trap. Therefore, the monopole (breathing) mode may be excited by modifying the bias field, which changes the trapping frequency. If after a finite time, the bias field is set back to its original value, the atomic gas cloud oscillates freely in the magnetic trap for an adjustable time [107]. One could then measure the density profile of the gas after a period of free expansion. Measurements of the density profile of atomic cloud would provide crucial insights about the underlying physics of the trapped many-body system.

In an analogous fashion, in our dynamical simulation, we excite the monopole mode by weak relaxation of the trapping frequency at time $t = 0$, and letting the system propagate in time [2]. As the monopole mode excitation is isotropic in x-y space, it is sufficient to observe the dynamic response of the collective coordinate along one direction, say, the x-axis. Here, we pick the mean square of the center-of-mass coordinate as the quantity of interest:

$$\langle x^2 \rangle_\sigma = \frac{\int |\phi_\sigma|^2 x^2 dx\, dy}{\int |\phi_\sigma|^2 dx\, dy}\,,$$

where $\sigma = \uparrow, \downarrow$-spin components. In Figs. 4.8(a) and (b), we plot the time response of $\langle x^2(t) \rangle_\sigma$ for a typical parameter set [2]. In Figs. 4.8(c) and (d), we show the

corresponding frequency response by plotting the single-sided amplitude spectrum $|\langle x^2(\omega)\rangle|_\sigma$, which are just the Fourier transforms of $\langle x^2(t)\rangle_\sigma$ [2]. We observe frequency peaks at $\omega/\omega_\perp \simeq 0.46, 1.8, 2.18$ and at 3.40 (not shown). We note that these values exactly match the mode frequencies obtained for this parameter set by solving the Bogoliubov equations, shown in Fig. 4.1(b).

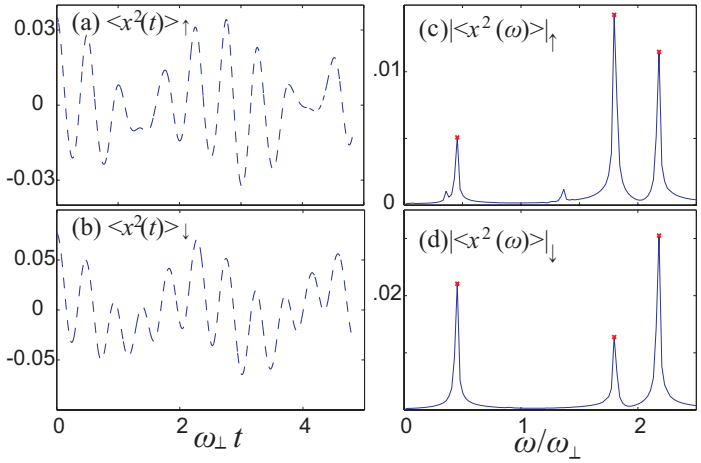

Figure 4.8 : (color online). (a),(b): Dynamic response of the mean square of the center-of-mass coordinate in x-direction of $\uparrow$- and $\downarrow$- spin components respectively. We have shifted the curves by subtracting the time-averaged $\langle x^2(t)\rangle_\sigma$. Without this shift, the Fourier spectrum as shown in (c) and (d) is dominated by a large peak at $\omega = 0$. (c),(d): Corresponding single-sided amplitude spectrum of the collective coordinate. Parameters used: $\lambda_{SO} = 1.0, g(N-1) = 40(\hbar\omega_\perp a_\perp^2), g_{\uparrow\downarrow}/g = 1.1$. Image from Ref. [2].

Dynamical calculations also reveal the coupling between the center-of-mass motion and the internal spin degrees of freedom, a trademark signature of SO coupled systems [2]. We shall now discuss the dynamic response of the population difference $\Delta n = \int d\mathbf{r}\,(|\phi_\uparrow|^2 - |\phi_\downarrow|^2)$. In Fig. 4.9(a), we plot the time response of $\Delta n(t)$ for the same parameter set mentioned in Fig. 4.8. In Fig. 4.9(b), we show the corresponding frequency response by plotting the single-sided amplitude spectrum $|\Delta n(\omega)|$. We observe frequency peaks at $\omega/\omega_\perp \simeq 0.46, 1.8, 2.18$ and at 3.40 (not shown), exactly

matching the mode frequencies obtained in Fig. 4.8 [2]. This analysis clearly shows that the population transfer between the two spin components shares a similar dynamic response with the collective motional coordinate. In this aspect, the response of Δn in a SO coupled spinor BEC (shown here) is similar to the effects observed in multi-component condensates, in the presence of internal Josephson coupling [118].

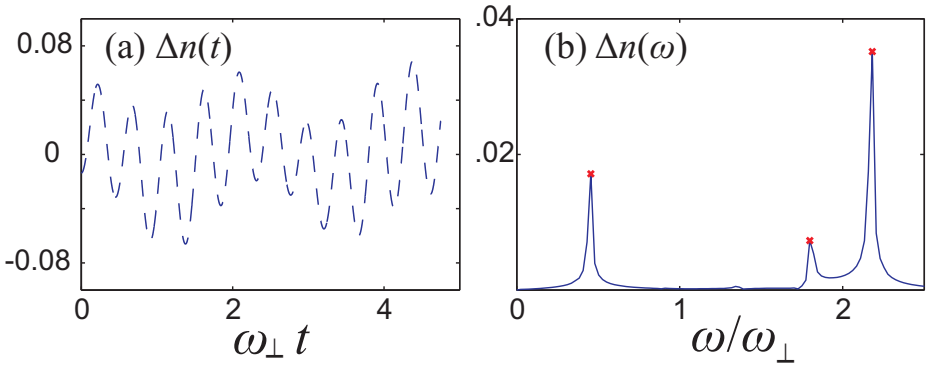

Figure 4.9 : (color online). (a) Dynamic response and (b) single-sided amplitude spectrum of population difference Δn for the same parameter set used in Fig. 4.8. Image from Ref. [2].

4.4.2 Dipole or sloshing mode analysis

Collective dipole oscillation is a center-of-mass motion of all atoms. For a conventional BEC, dipole oscillation is trivial: from the Kohn theorem, we understand that the frequency is just the harmonic-trap frequency, independent of oscillation amplitude and inter-atomic interaction [26]. Let us now analyze the dipole mode oscillations in a SO coupled trapped spinor Bose gas.

We excite the dipole modes by displacing the trap in the x-direction by a small amount at time $t = 0$, and letting the system propagate in time [2]. Let us now elaborate on how this approach is appropriate to begin with. As discussed in Sec. 1.3.2, in a trapped atomic system the Bose condensate shows up not only in momentum

space, but also in coordinate space. This implies that apart from being a macroscopic occupation of atoms in the zero-momentum state, the condensate may be considered as a macroscopic object physically present in the center of the trap. Owing to the coherent motion of the macroscopic number of atoms in the condensate, the center of mass motion is an appropriate observable. As a classical analogue, the Bose condensate acts as a continuum elastic medium and the trap displacement serves to excite the collective modes in this medium.

Upon excitation of the dipole mode and letting the system propagate in time, we observe the dynamic response of the center-of-mass coordinate in the x-direction:

$$\langle x \rangle_\sigma = \frac{\int |\phi_\sigma|^2 \, x \, dx \, dy}{\int |\phi_\sigma|^2 dx \, dy} \, .$$

In Fig. 4.10 (a),(b), we plot the time response of this collective coordinate in the x-direction of $\uparrow$- and $\downarrow$- spin components for a typical parameter set [2]. In Fig. 4.10 (c),(d), we show the corresponding frequency response by plotting the single-sided amplitude spectrum $|\langle x(\omega) \rangle|_\sigma$. We observe frequency peaks at $\omega/\omega_\perp \simeq 0.05, 0.43, 0.70, 1.25, 1.34,$ (shown) and at 2.5, 2.64, 2.76 (not shown). We note that these values also agree with the mode frequencies obtained for this parameter set by solving the Bogoliubov equations, shown in Fig. 4.1(a),(c).

In the inset of Fig. 4.10(a), we show the dynamics of the center-of-mass coordinate. It is important to note that even though the trap is displaced only in the x-direction, we also observe a similar dynamic response in the y-direction of both spin components (only $\uparrow$-spin component shown). This behavior occurs due to the vorticity induced by the spin-orbit coupling: the vortex state experiences a Magnus force that is perpendicular to its motion [2]. Hence a displacement in the x-direction

induces a motion along the y-direction. Furthermore, the trace of the center-of-mass and its magnitude are affected by the strength of the inter-particle interactions and the spin-orbit coupling induced population transfer, as observed in the case of the monopole mode excitation, between the ↑- and ↓- spin components [2].

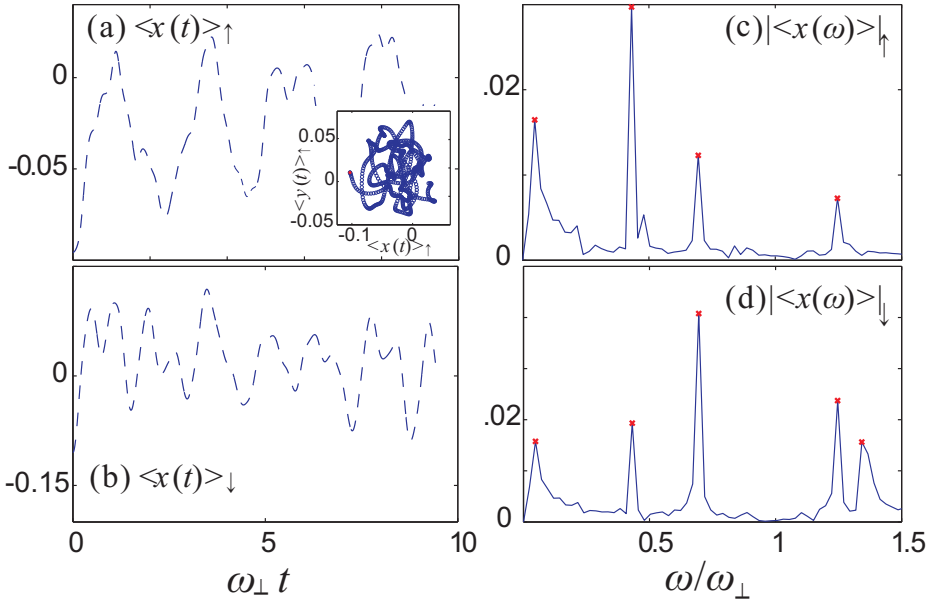

Figure 4.10 : (color online). Parameters used: $\lambda_{SO} = 1.0, g(N-1) = 40(\hbar\omega_\perp a_\perp^2), g_{\uparrow\downarrow} = 1.1\,g$. (a),(b): Dynamic response of the center-of-mass coordinate in x-direction of ↑- and ↓- spin components respectively. The inset in (a) shows the dynamics of the center-of-mass coordinate over 12 trap periods. The filled (red) marker denotes the initial position. (c),(d): Corresponding single-sided amplitude spectrum of the collective coordinate. Image from Ref. [2].

The induced population transfer and the corresponding oscillation spectrum reflects the locking between the spin and momentum in the SO coupled Hamiltonian. In Ref. [119], Zhang *et al.* discuss this phenomenon theoretically using a variational approach and explain the observation from the absence of Galilean invariance. Consider a BEC that moves with a velocity v along $\hat{x}$; in the co-moving frame, the single-particle Hamiltonian acquires an additional term vk_x. In a conventional BEC,

this term can be gauged away by a gauge transformation $\psi \rightarrow e^{imvx}\psi$ [119]. In an SO coupled system, however, such a procedure will introduce a velocity dependent Zeeman-energy term $-mvk_r\hat{\sigma}_z$. Hence, once the condensate moves, a population transfer has to be induced [119].

4.4.3 Instability against anisotropy in SO coupling

So far we have focused our attention on the half-quantum vortex state in an isotropic 2D harmonic trap subject to an isotropic Rashba SO coupling. Here we discuss the effect of anisotropy in the SO coupling strength λ_R on the stability of the half-quantum vortex state. The effect of *trap* anisotropy will be discussed subsequently. In the context of ultracold gases, anisotropic Rashba SO coupling was first discussed by Stanescu *et al.* in Ref. [92]. The coupled GP equations were solved for a many-body system in the absence of the trap and in the restricted scenario where $g_{\uparrow\downarrow} = g$ [2].

Here, we move beyond these restrictions and discuss the ground state of the system. We write the SO coupling term in the form $\mathcal{V}_{SO} = -i(\lambda_y\hat{\sigma}_x\partial_y - \lambda_x\hat{\sigma}_y\partial_x)$, where λ_x, λ_y are SO coupling strengths in the two perpendicular directions. By including this modified SO coupling term and solving the coupled GP equations under the Hamiltonian as given in Eq. (4.1), we obtain the ground state wavefunction at various values of anisotropy in SO coupling represented by λ_x/λ_y [2].

In Fig. 4.11, we plot the corresponding ground state density profiles of $\downarrow$-spin component for a fixed SO coupling strength ($\lambda_x = 4.0$), and for various values of λ_x/λ_y.We see from Fig. 4.11(a) that the half-quantum vortex state is indeed the ground state (already mentioned in Fig. 4.7(b)) for the parameter set: $g(N-1) = 0.1(\hbar\omega_\perp a_\perp^2)$, $g_{\uparrow\downarrow}/g = 1.1$, $\lambda_x = 4.0$ and $\lambda_x/\lambda_y = 1.0$ [2]. We shall now analyze the pattern of density profile changes, as the anisotropy in SO coupling strength is

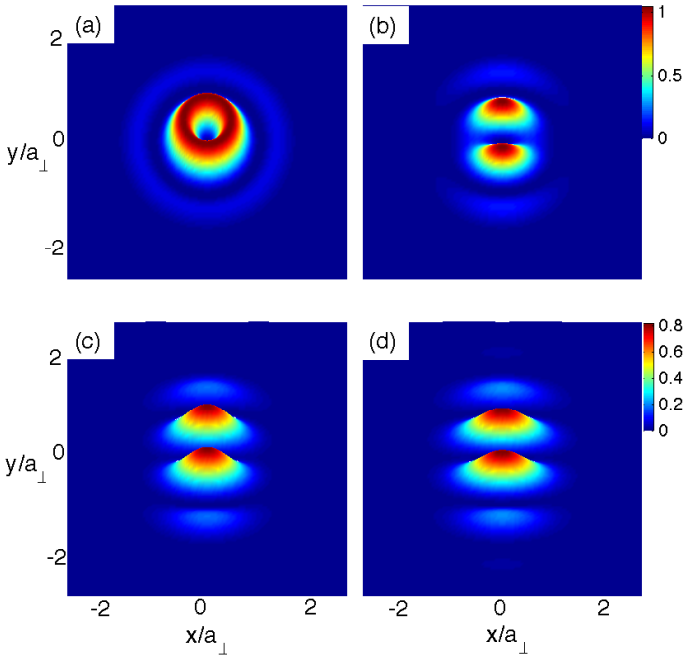

Figure 4.11 : (Color online) Plot of the ground state density profiles of ↓-spin component for the parameter set: $g(N-1) = 0.1(\hbar\omega_\perp a_\perp^2)$, $g_{\uparrow\downarrow}/g = 1.1$, $\lambda_x = 4.0$, with varying ratios of λ_x/λ_y. (a) Isotropic case: $\lambda_x/\lambda_y = 1.0$, (b) $\lambda_x/\lambda_y = 1.01$, (c) $\lambda_x/\lambda_y = 1.05$, (d) $\lambda_x/\lambda_y = 1.1$. Viewing angle is slightly tilted for aesthetic purposes. Image from Ref. [2].

varied. This is shown in Fig. 4.11(b)-(d). It is evident from the density distributions that the half-quantum vortex state is unstable even against a small anisotropy in the SO coupling strength. Adopting a similar method to that presented in Ref. [120], we analyze this systematically by expanding the wavefunction of the down-spin ↓-component in an orthogonal basis set of the form: $\Phi_\downarrow(\rho) = \Sigma_n\, f_n(\rho)\, e^{i\,(2n+1)\,\varphi}$, where n measures the vorticity, and $f_n(\rho)$ absorbs the nth mode's contribution in the radial direction. We quantify the weights of the wavefunction in the nth mode by computing $a_n = \int d\rho\, |f_n(\rho)|^2$ [2]. In Fig. 4.12, we plot the weights a_n relative to a_0, as computed for a half-quantum vortex state with $\lambda_x/\lambda_y = 1.0$. As we would expect, for this

isotropic case, $a_0 = 1$ and $a_n = 0$ for $n \neq 0$. As the anisotropy in the SO coupling strength increases, more and more $n \neq 0$ components become mixed into the ground state [2].

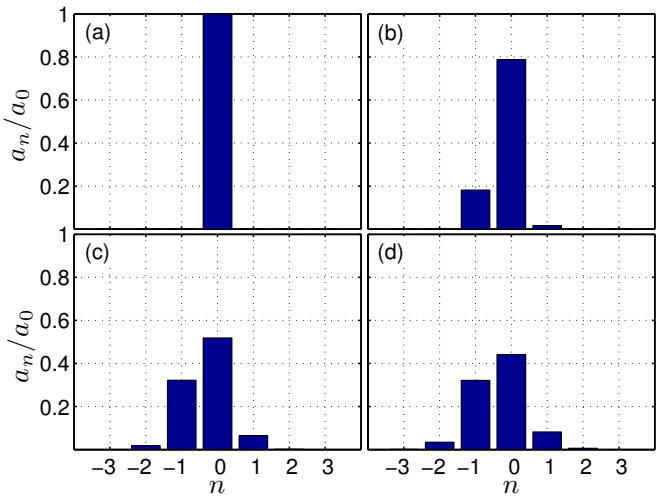

Figure 4.12 : (Color online) Plot of the weights of the ground-state wavefunction of $\downarrow$-spin component - corresponding to the density profiles in Fig. 4.11 - in the nth mode. The weights are normalized with respect to a_0 computed for a half-quantum vortex state with $\lambda_x/\lambda_y = 1.0$. (a) Isotropic case: $\lambda_x/\lambda_y = 1.0$, (b) $\lambda_x/\lambda_y = 1.01$, (c) $\lambda_x/\lambda_y = 1.05$, (d) $\lambda_x/\lambda_y = 1.1$. Image from Ref. [2].

We note that due to the sensitivity of the half-quantum vortex state with respect to the anisotropy in the SO coupling strength, to observe such a state therefore requires a highly symmetric Rashba spin-orbit coupling in experiments.

4.4.4 Instability against anisotropy in trap potential

Now we examine the effect of anisotropy in the trapping potential, but with isotropic SO coupling, on the stability of half-quantum vortex state. We write the trapping potential in the form $V(x,y) = M(\omega_x^2 x^2 + \omega_y^2 y^2)/2 = M\omega_\perp^2(x^2 + f_y^2 y^2)/2$, where $\omega_x = \omega_\perp, \omega_y = f_y\omega_\perp$ are trapping frequencies in x- and y-directions respectively [2].

We again obtain the ground state wavefunctions at various values of f_y by solving the coupled GP equations. In Fig. 4.13, we plot the corresponding ground state density profiles of the $\downarrow$-spin component for an SO coupling strength of $\lambda_{SO} = 4.0$, and for various values of trap anisotropy ranging from 0 to 10% [2].

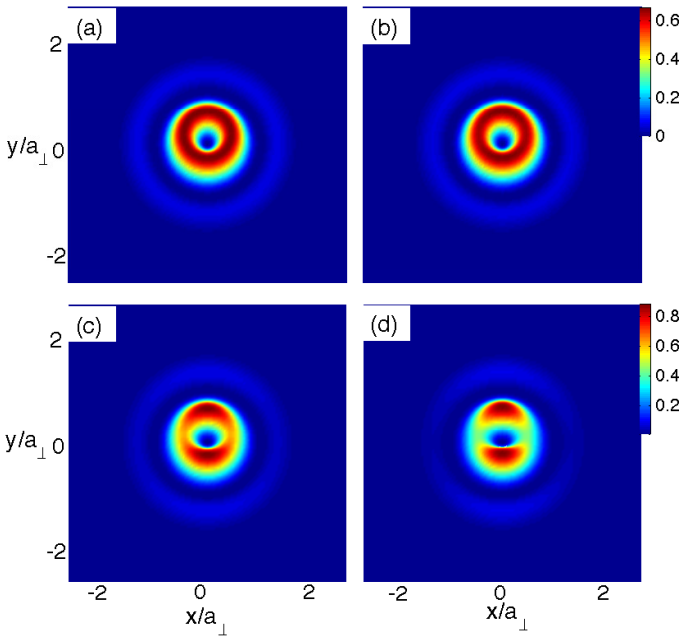

Figure 4.13 : (Color online) Plot of the ground state density profiles of $\downarrow$-spin component for the parameter set: $\lambda_{SO} = 4.0$, $g(N-1) = 0.1(\hbar\omega_\perp a_\perp^2)$, $g_{\uparrow\downarrow}/g = 1.1$, but with varying ratios of $f_y = \omega_y/\omega_x$. (a) Isotropic case: $f_y = 1.0$, (b) $f_y = 1.01$, (c) $f_y = 1.05$, (d) $f_y = 1.1$. Viewing angle is slightly tilted for aesthetic purposes. Image from Ref. [2].

We see from Fig. 4.13(a) that the half-quantum vortex state is indeed the ground state (already mentioned in Fig. 4.11(a)) for the parameter set: $\lambda_{SO} = 4.0$, $g(N-1) = 0.1(\hbar\omega_\perp a_\perp^2)$, $g_{\uparrow\downarrow}/g = 1.1$ [2]. We shall now analyze the pattern in which the density profile changes depending on the trap anisotropy, as shown in Fig. 4.13(b)-(d). It is evident from the density distributions that the vortex core becomes increas-

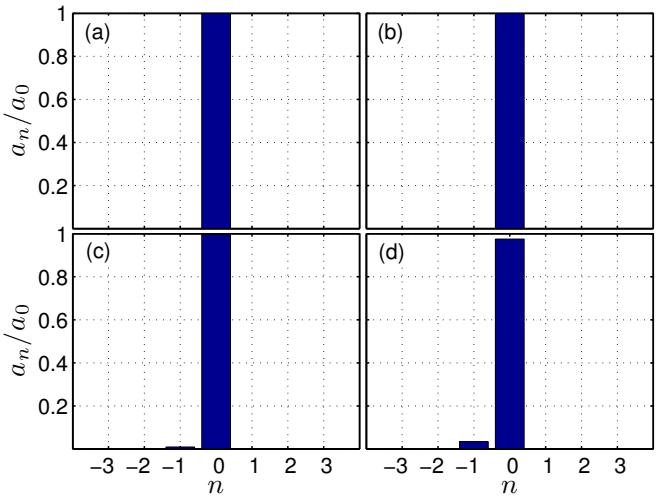

Figure 4.14 : (Color online) Plot of the weights of ground-state wavefunction of ↓-spin component - corresponding to the density profiles in Fig. 4.13 - in the nth mode. The weights are normalized with respect to a_0 computed for half-quantum vortex state with $f_y = 1.0$. (a) Isotropic case: $f_y = 1.0$, (b) $f_y = 1.01$, (c) $f_y = 1.05$, (d) $f_y = 1.1$. Image from Ref. [2].

ingly anisotropic with increasing f_y [2]. We analyze this systematically by expanding the wavefunction of the ↓-component in an orthogonal basis set and quantifying the weights in the nth mode by a_n, as mentioned in Sec. 4.4.3. In Fig. 4.14, we plot the weights a_n relative to a_0 computed for a half-quantum vortex state with $f_y = 1.0$. As we would expect, for the isotropic case with $f_y = 1.0$, $a_0 = 1$ and $a_n = 0$ for $n \neq 0$ [2]. As the trap anisotropy increases, we observe that the ground state is a mixture of $n \neq 0$ components as well. Nevertheless, we see that the trap anisotropy has a much smaller effect on the half-quantum vortex state than the anisotropy in the SO coupling strength [2].

In summary, the half-quantum vortex state is unstable against small anisotropies in the SO coupling strength and large anisotropies in the trapping potential. The state tends to be a superposition of higher angular momentum states.

Chapter 5

Exact diagonalization study of strongly correlated phases*

In the presence of synthetic gauge fields in trapped ultracold bosonic systems, experimental evidence for SO coupling with equal Rashba and Dresselhaus type strengths was reported in a seminal paper by NIST group [59]. Recently, commendable experimental progress has also been achieved towards simulating SO coupling in ultracold fermionic systems [60, 61], a phenomenon critical to the simulation of certain topologically insulating states in condensed-matter systems [121, 122]. The introduction of *synthetic* gauge fields in ultracold neutral atomic systems has thus opened the possibility of exploring a whole new set of phenomena that would manifest in the presence of abelian and non-abelian vector potentials [76]. In a previous work, the NIST group has experimentally realized an artificial Abelian gauge field which leads to the observation of vortex lattice in a non-rotating ^{87}Rb Bose condensate [57]. The work presented in this chapter represents an important extension into the regime of non-Abelian gauge field† in which the spin degrees of freedom play an essential role [3].

In Chapter 3, we discussed in detail the emergence of weakly correlated phases at large SO coupling strengths and presented the phase diagram. However, these results are valid for weak correlations with large number of bosons. Strongly correlated

*Chapter 5 taken largely from our publication in Ref. [3].

†As stated by Galitski *et al.* in Ref. [53], for instance, a gauge field A is non-Abelian when the components of the vector $A = (A_x, A_y, A_z)$ are non-commuting operators, for example $A_x A_y \neq A_y A_x$. Such non-Abelian gauge potentials are generic in a wide range of problems in physics [53].

states would emerge with small number of bosons [106]. In this Chapter, we address this potential possibility using exact diagonalization (ED) scheme. We emphasize that understanding the physics of few-body systems is not anymore a mere theoretical fantasy. With tremendous experimental progress, it is now possible to experimentally study few-body phenomena in trapped atomic and molecular systems with unprecedented control. As stated by Blume in Ref. [123], for instance, trapped few-particle systems can be realized by loading *micro-traps* with just a few particles [123–126].

In the presence of SO coupling, a generic Hamiltonian may be broadly classified in two classes: (a) one that breaks $\mathcal{T}$ (time-reversal) symmetry, and which can be shown to be gauge-equivalent to a Hamiltonian in the combined presence of abelian and non-abelian vector potentials [3]. For example in Refs. [127, 128], the authors consider an SO coupling Hamiltonian in the presence of a real (abelian) magnetic field and attempt to simulate the physics of traditional quantum Hall systems; (b) one that preserves $\mathcal{T}$ symmetry, and which can be shown to be gauge-equivalent to a Hamiltonian in a pure non-abelian vector potential [3]. In this chapter, we study an SO coupling Hamiltonian of the latter class, and discuss the emergence of ground states with unique topological and correlation properties [3].

The chapter is organized as follows: In Sec. 5.1, we begin by re-iterating the model Rashba SO coupling Hamiltonian introduced in Sec. 2.3.1 and discuss various symmetries. We show that the Hamiltonian is gauge-equivalent to particles subject to a pure non-abelian vector potential that preserves $\mathcal{T}$ symmetry. Then, we consider the non-interacting limit of this Hamiltonian, and revisit the characteristic features of the single-particle solutions at small and large SO coupling strengths discussed in Sec. 2.3.3. We proceed to discuss the implementation of ED scheme to obtain the low-energy eigenstates of the interacting Hamiltonian in the regime of large SO coupling

strengths. Then, we introduce various analysis techniques namely, energy spectrum, density distribution, single-particle density matrix, pair-correlation function, reduced wavefunction, entanglement spectrum, and entanglement entropy. Each technique would offer its unique perspective to the overall understanding of the ground state properties [3].

In Sec. 5.2, we discuss the phase diagram and analyze the ground state properties of the interacting Hamiltonian at different particle numbers N, and at varied inter-atomic interaction strengths. At small particle numbers with $N = 2$, we illustrate the unique topological and symmetry properties of ground states. In the relatively large particle number scenario with $N = 8$, we observe that the ground states fall into two distinct regimes: (a) at weak interaction strengths (*mean-field-like regime*), we observe ground states with topological and symmetry properties that are also obtained via mean-field theory computations; (b) at intermediate to strong interaction strengths (*strongly correlated regime*), we report the emergence of strongly correlated ground states. We proceed to illustrate the topological, symmetry and strong correlation properties of these ground states. Finally in Sec. 5.3, we summarize and present concluding remarks [3].

5.1 Theoretical framework

5.1.1 System under study

As discussed earlier in Sec. 2.3.1, we study a two-component Bose gas confined in a 2D isotropic harmonic trapping potential: $V(\rho) = M\omega_\perp^2(x^2 + y^2)/2 = M\omega_\perp^2\rho^2/2$. For convenient reference, we re-iterate the model system under study here. We consider the isotropic Rashba SO coupling term, that couples pseudo-spin-1/2 degree

of freedom and linear momentum: $\mathcal{V}_{SO} = -i\lambda_R(\hat{\sigma}_x\partial_y - \hat{\sigma}_y\partial_x)$, where λ_R is the SO coupling strength and $\hat{\sigma}_{x,y,z}$ are 2×2 Pauli matrices. The model Hamiltonian for the interacting system is then given by: $\mathcal{H} = \int d\mathbf{r}[\mathcal{H}_0 + \mathcal{H}_{\rm int}]$,

$$\mathcal{H}_0 = \Psi^\dagger\left[-\frac{\hbar^2\nabla^2}{2M} + V(\rho) + \mathcal{V}_{SO} - \mu\right]\Psi, \tag{5.1}$$

$$\mathcal{H}_{\rm int} = (g/2)\sum_{\sigma=\uparrow,\downarrow}\Psi^\dagger_\sigma\Psi^\dagger_\sigma\Psi_\sigma\Psi_\sigma + g_{\uparrow\downarrow}\Psi^\dagger_\uparrow\Psi_\uparrow\Psi^\dagger_\downarrow\Psi_\downarrow, \tag{5.2}$$

where $\mathbf{r} = (x, y)$ and $\Psi = [\Psi_\uparrow(\mathbf{r}), \Psi_\downarrow(\mathbf{r})]^T$ denotes the spinor Bose field operators. The chemical potential μ is to be determined by the total number of bosons N (i.e., $\int d\mathbf{r}\Psi^\dagger\Psi = N$). For simplicity, we have assumed that the intra-component interaction strengths are equal, so that $g_{\uparrow\uparrow} = g_{\downarrow\downarrow} = g$ [3]. The Hamiltonian is invariant under symmetry operations associated with the anti-unitary time-reversal operator $\mathcal{T} = i\hat{\sigma}_y\mathcal{C}$, and the unitary parity operator $\mathcal{P} = \hat{\sigma}_z\mathcal{I}$, where $\mathcal{C}$ and $\mathcal{I}$ perform complex conjugation and spatial inversion operations respectively. The Hamiltonian is also invariant under the combined $\mathcal{PT}$ operator, which is unitary since operators $\mathcal{P}$ and $\mathcal{T}$ anti-commute, i.e., since $[\mathcal{P}, \mathcal{T}]_+ = 0$ [3]. As can be readily seen, Rashba SO coupling term in Eqn. (5.1) breaks inversion symmetry.

5.1.2 Gauge-equivalent form of $\mathcal{H}_0$

A generic single-particle Hamiltonian may be written in the form $\mathcal{H}_g = (\mathbf{p}-\mathbf{A})^2/2M$, where $\mathbf{p} = \hbar\mathbf{k}$ is the particle momentum and $\mathbf{k}$ is the wave-vector. The vector potential $\mathbf{A}$ may possibly have components in both physical space and spin space. Depending upon the commutation properties of the components of $\mathbf{A}$, we may hence have an abelian or non-abelian type vector potential [3]. The primary motivation behind deriving a gauge-equivalent form is to map our model Hamiltonian $\mathcal{H}_0$ onto

$\mathcal{H}_g$, and hence derive the nature of $\mathbf{A}$. It is conceivable that depending upon the nature of $\mathcal{H}_0$, $\mathbf{A}$ could comprise of purely abelian components, or purely non-abelian components, or a combination of both [3].

In order to map $\mathcal{H}_0$ onto $\mathcal{H}_g$, it suffices to compare $\mathcal{H}_g$ with the terms $-\hbar^2\nabla^2/2M - i\lambda_R(\hat{\sigma}_x\partial_y - \hat{\sigma}_y\partial_x)$ in $\mathcal{H}_0$. The latter terms may actually be rewritten as $|\mathbf{p}|^2/2M + \lambda_R(\hat{k}_y\hat{\sigma}_x - \hat{k}_x\hat{\sigma}_y)$. For a two-component Bose gas confined in a 2D isotropic harmonic trap, we have a two-component vector potential $\mathbf{A}$, with A_x, A_y being 2×2 matrices [3]. Comparing $\mathcal{H}_0$ with $\mathcal{H}_g$, we expect $A_x \propto \hat{\sigma}_y$ and $A_y \propto -\hat{\sigma}_x$. Specifically, it can be shown that the vector potential is $\mathbf{A} = (A_x, A_y, 0) = (\hbar M\omega_\perp)^{1/2}\lambda_{SO}(\hat{\sigma}_y, -\hat{\sigma}_x, 0)$. In trap units, we then simply have $\mathbf{A} = \lambda_{SO}(\hat{\sigma}_y, -\hat{\sigma}_x, 0)$. The term involving $|\mathbf{A}|^2$ is a constant, and can be gauged out without loss of generality. Therefore, the strength of the non-abelian vector potential proportionally determines the strength of SO coupling [3]. It is further evident that $[A_x, A_y] \neq 0$, and that $\mathbf{A}$ is a pure non-abelian vector potential. Furthermore, the $\mathcal{T}$ operator commutes with the SO coupling term $\lambda_R(\hat{k}_y\hat{\sigma}_x - \hat{k}_x\hat{\sigma}_y)$. In essence, the model Rashba SO coupling Hamiltonian in Eqn. (5.1) is gauge-equivalent to particles subject to a pure non-abelian vector potential that preserves $\mathcal{T}$ symmetry [3]. As discussed in Sec. 2.2, proposals to realize vector potentials of similar forms have been addressed by multiple groups [76, 129–131].

5.1.3 Single-particle solutions

We solve the model Hamiltonian $\mathcal{H}$ in the absence of interatomic interactions and obtain the single-particle solutions, as discussed earlier in Sec. 2.3.3. Rewriting the $\mathcal{H}_0$ component in Eqn. (5.1), the single-particle wavefunction $\phi(\mathbf{r}) = [\phi_\uparrow(\mathbf{r}), \phi_\downarrow(\mathbf{r})]^T$

with energy ϵ is given by

$$\begin{bmatrix} \mathcal{H}_{osc} & -i\lambda_R(\partial_y + i\partial_x) \\ -i\lambda_R(\partial_y - i\partial_x) & \mathcal{H}_{osc} \end{bmatrix} \begin{bmatrix} \phi_\uparrow \\ \phi_\downarrow \end{bmatrix} = \epsilon \begin{bmatrix} \phi_\uparrow \\ \phi_\downarrow \end{bmatrix}, \tag{5.3}$$

where $\mathcal{H}_{\text{osc}} \equiv -\hbar^2\nabla^2/(2M) + V(\rho)$. In polar coordinates (ρ, φ), we have $-i(\partial_y \pm i\partial_x) = e^{\mp i\varphi}[\pm\partial/\partial\rho - (i/\rho)\partial/\partial\varphi]$. The single-particle wavefunction takes the form

$$\phi_m(\mathbf{r}) = \begin{bmatrix} \phi_\uparrow(\rho) \\ \phi_\downarrow(\rho)e^{i\varphi} \end{bmatrix} \frac{e^{im\varphi}}{\sqrt{2\pi}}, \tag{5.4}$$

with well-defined total angular momentum j_z, that is a sum of orbital and spin angular momenta. In general, we may denote the energy spectrum as ϵ_{nm}, where $n = (0, 1, 2...)$ is the quantum number for the transverse (radial) direction [3].

The single-particle wavefunction $\phi_m(\mathbf{r})$ is an eigenstate of the unitary $\mathcal{P}$ operator:

$$\mathcal{P}\phi_m(\mathbf{r}) = \sigma_z(-1)^m \begin{bmatrix} \phi_\uparrow(\rho) \\ -\phi_\downarrow(\rho)e^{i\varphi} \end{bmatrix} \frac{e^{im\varphi}}{\sqrt{2\pi}} = (-1)^m\phi_m(\mathbf{r}).$$

The $\mathcal{T}$ symmetry preserved by the Hamiltonian results in a two-fold degeneracy (Kramer doublet) of the energy spectrum: any eigenstate $\phi(\mathbf{r}) = [\phi_\uparrow(\mathbf{r}), \phi_\downarrow(\mathbf{r})]^T$ is degenerate with its time-reversal partner $\mathcal{T}\phi(\mathbf{r}) = [\phi^*_\downarrow(\mathbf{r}), -\phi^*_\uparrow(\mathbf{r})]^T$. This symmetry is preserved even in the presence of interatomic interactions, as the terms in interacting Hamiltonian $\mathcal{H}_{\text{int}}$ are $\mathcal{T}$-invariant [3]. The superposition state, of $\phi_m(\mathbf{r})$ and its time-reversal partner state, is an eigenstate of the unitary $\mathcal{PT}$ operator:

$$\mathcal{PT}[\phi_m(\mathbf{r}) + \mathcal{T}\phi_m(\mathbf{r})] = (-1)^{m+1}[\phi_m(\mathbf{r}) + \mathcal{T}\phi_m(\mathbf{r})].$$

Following our detailed discussion in Sec. 2.3.3, we identified from Figs. 2.5 and 2.6 that the nature of solutions is fundamentally different at small and large SO coupling strengths. Let us now focus exclusively on the characteristic solutions at large SO coupling strengths. The localized nature of the wavefunctions in Fig. 2.5(b) and the weakly dispersive nature of the single-particle energy spectrum in Fig. 2.6(b) are characteristics that justify a comparison of the single-particle basis states at large SO coupling strengths with 2D Landau Level (LL) structures in magnetic fields. In Ref. [130], Li *et al.* discuss the mapping between $\mathcal{H}_0$ and 2D LL Hamiltonian in a rigorous fashion and generalize the terminology of LLs as '*topological* single-particle level structures labeled by angular momentum quantum numbers with flat or *nearly flat* spectra' [130]. Making use of this generalization, we term the $n = 0$ manifold as the lowest LL structure (LLL), $n = 1$ manifold as the next highest LL, and so on [3]. As seen in Fig. 2.6(b), the radial quantization generates energy gaps between adjacent LLs of the order of trap energy $\hbar\omega_\perp$, i.e., of order *unity* in trap units.

To summarize, we emphasize that the generalized LLs discussed here are created by a truly non-abelian vector potential, i.e., in the absence of any real (abelian) magnetic fields. The strength of Rashba SO coupling strength, and in-turn the *flatness* of the single-particle energy spectra can be experimentally controlled by using laser fields. At large SO coupling strengths, as shown for $\lambda_{SO} = 20$ in Fig. 2.6, we obtain a *nearly flat* single-particle energy spectra. In a non-interacting two-component Bose gas, quantum statistics obviates the occurrence of correlated states in a spectra that is not *perfectly flat*, due to potential condensation of all the particles in the lowest energy single-particle states, identified by $j_z = \pm 0.5$, of the LLL ($n = 0$ manifold) [3]. However, in the presence of inter-particle interactions, *nearly flat* energy spectra is sufficiently abled to act as an interesting playground to allow for the emergence of

strongly correlated ground states [3]. We now proceed to introduce the ED scheme to solve the interacting Rashba SO coupled Hamiltonian at large SO coupling strengths.

5.1.4 Exact diagonalization scheme

We solve the interacting Rashba SO coupled Hamiltonian $\mathcal{H}$ in Eqns. (5.1) and (5.2) within the Configuration Interaction alias exact diagonalization (ED) scheme. In this scheme, we expand the interacting many-body Hamiltonian in an appropriate single-particle basis (configuration) to obtain the solution. The solution becomes exact when we consider an infinite number of single-particle states. With N bosons and M single-particle states in the basis, the dimension of Hilbert space is $D = (N + M - 1)!/N!(M - 1)!$. With $M = 24$, for example, $D = 300$ for $N = 2$, and $D = 7888725$ for $N = 8$ [3]. The dimension of Hilbert space grows dramatically with system size and hence, for practical purposes, we limit our configuration to a finite size. We observe that the solution becomes *essentially* exact when we consider a *sufficient* number of single-particle states [3]. To solve the problem at hand, it is convenient to work with the SO single-particle basis:

$$\Phi(\mathbf{r}) = \sum_{nm} \begin{bmatrix} \phi_{\uparrow nm}(\mathbf{r}) \\ \phi_{\downarrow nm}(\mathbf{r}) \end{bmatrix} a_{nm} \equiv \sum_{i \equiv nm} \begin{bmatrix} \phi_{\uparrow i}(\mathbf{r}) \\ \phi_{\downarrow i}(\mathbf{r}) \end{bmatrix} a_i, \tag{5.5}$$

where the field operator a_i is related to the single-particle state $[\phi_{\uparrow nm}(\mathbf{r}), \phi_{\downarrow nm}(\mathbf{r})]^T$. Then, Eqns. (5.1) and (5.2) simply become

$$\mathcal{H} = \sum_i \epsilon_i a_i^\dagger a_i + \sum_{ijkl} V_{ijkl} a_i^\dagger a_j^\dagger a_k a_l, \tag{5.6}$$

where (i,j,k,l) collectively denotes (n,m), and $V_{ijkl} = (g/2)[V^{\uparrow\uparrow}_{ijkl} + V^{\downarrow\downarrow}_{ijkl}] + g_{\uparrow\downarrow}V^{\uparrow\downarrow}_{ijkl}$, with

$$\begin{aligned} V^{\uparrow\uparrow}_{ijkl} &= \int d\mathbf{r}\phi^*_{\uparrow i}(\mathbf{r})\phi^*_{\uparrow j}(\mathbf{r})\phi_{\uparrow k}(\mathbf{r})\phi_{\uparrow l}(\mathbf{r}) \\ V^{\downarrow\downarrow}_{ijkl} &= \int d\mathbf{r}\phi^*_{\downarrow i}(\mathbf{r})\phi^*_{\downarrow j}(\mathbf{r})\phi_{\downarrow k}(\mathbf{r})\phi_{\downarrow l}(\mathbf{r}) \\ V^{\uparrow\downarrow}_{ijkl} &= \int d\mathbf{r}\phi^*_{\uparrow i}(\mathbf{r})\phi^*_{\downarrow j}(\mathbf{r})\phi_{\uparrow k}(\mathbf{r})\phi_{\downarrow l}(\mathbf{r}). \end{aligned} \tag{5.7}$$

We perform the ED calculation in Fock space and the Hamiltonian $\mathcal{H}$ can be written as a matrix of dimension D^2, naively accounting for the possibility of inter-coupling every Fock state [132]. It is clear from the single particle solutions discussed in Eqn. (5.3), that the single-particle term $\epsilon_i a^\dagger_i a_i$ contributes only to diagonal entries of the Hamiltonian matrix, while the interaction term $V_{ijkl}a^\dagger_i a^\dagger_j a_k a_l$ contributes to off-diagonal entries as well [3]. The enumeration of off-diagonal entries can be enormously simplified by accounting for a symmetry preserved by $\mathcal{H}$: conservation of total angular momentum $J_z = \sum_N j_z$, as readily seen from Eqn. (5.6). If an entry V_{ijkl} is to be nonzero, we must have $m_i + m_j = m_k + m_l$ in Eqn. (5.7). Using only the radial wavefunction, we have (provided $m_i + m_j = m_k + m_l$),

$$\begin{aligned} V^{\uparrow\uparrow}_{ijkl} &= \frac{1}{2\pi}\int_0^\infty \rho d\rho\, \phi_{\uparrow i}(\rho)\phi_{\uparrow j}(\rho)\phi_{\uparrow k}(\rho)\phi_{\uparrow l}(\rho) \\ V^{\downarrow\downarrow}_{ijkl} &= \frac{1}{2\pi}\int_0^\infty \rho d\rho\, \phi_{\downarrow i}(\rho)\phi_{\downarrow j}(\rho)\phi_{\downarrow k}(\rho)\phi_{\downarrow l}(\rho) \\ V^{\uparrow\downarrow}_{ijkl} &= \frac{1}{2\pi}\int_0^\infty \rho d\rho\, \phi_{\uparrow i}(\rho)\phi_{\downarrow j}(\rho)\phi_{\uparrow k}(\rho)\phi_{\downarrow l}(\rho). \end{aligned} \tag{5.8}$$

This enables one to visualize the Hamiltonian in *block-diagonal* form, i.e., each *block* is a manifold comprising of Fock states with a fixed J_z. Hence, the term $V_{ijkl}a^\dagger_i a^\dagger_j a_k a_l$ can only couple states within the same manifold, therefore resulting in a sparse Hamil-

tonian matrix. We solve this sparse matrix to identify the low energy states of the system [3].

As discussed in Sec. 5.1.1, the Hamiltonian $\mathcal{H}$ preserves $\mathcal{T}$ symmetry. In a certain LL, the energies of states labelled j_z and $-j_z$ are equal and hence, we need to consider both positive and negative angular momentum states in the single-particle configuration [3]. This has two major implications: (a) computational intensity increases tremendously, and (b) a given configuration would never be sufficient to obtain a *complete* J_z manifold, where all contributing single-particle states are included. We note here that the latter issue does not arise when the Hamiltonian breaks $\mathcal{T}$ symmetry, as in studies of rotating trapped gases or gases subject to real magnetic fields [133–135]. In these studies, it was sufficient to consider only positive j_z states and hence obtain *complete* J_z manifolds. In the limit of large SO coupling strengths, if the interaction strengths are such that the energy contribution from H_{int} is less than unity (in trap units), we may restrict ourselves to the lowest $n = 0$ manifold. Within this LLL approximation, we may consider a *sufficient* number of single-particle eigenstates to obtain *essentially exact* low energy eigenstates [3].

5.1.5 Analysis techniques

ED scheme enables us to solve the Rashba SO coupled Hamiltonian $\mathcal{H}$ and obtain the ground state phase diagram at various interaction strengths and particle numbers. The ground states have interesting topological, symmetry and strong correlation properties. Here, we outline the details of various techniques that we use to analyze these properties.

5.1.5.1 Energy spectrum

First step in our analysis is to identify the total angular momentum manifold J_z to which the ground state belongs. As discussed earlier, the Hamiltonian matrix has a block-diagonal form, with each block identified by its unique J_z value. It is evident that each of these blocks can essentially be diagonalized independently. The energy spectrum comprises of energy eigenvalues from each block, and the lowest eigenvalue and its corresponding J_z may be readily associated with the ground state. Degeneracies in the energy spectrum naturally reflect the degeneracies in the ground state. For example, a typical energy spectrum plot is shown in Fig. 5.1.

Dimension of Fock space in the ground state J_z manifold will be much smaller when compared to the Hilbert space dimension D. For a given parameter set, once we identify the ground state J_z manifold, we can extract the coefficients of all Fock states from the corresponding eigenvector. In essence, we may then represent the ground state wavefunction as a sum of all contributing Fock states: $\Psi_G = \sum_{p=1}^{n_d} \alpha_p \Phi_p$, where n_d is the dimension of ground state J_z manifold and α_p is the coefficient of the Fock state Φ_p. As discussed in Sec. 5.1.1, the interacting Hamiltonian $\mathcal{H}$ is invariant under two *unitary* symmetry operations, $\mathcal{P}$ and $\mathcal{PT}$. With the knowledge of ground state wavefunction Ψ_G, we are now equipped to determine if the ground state is an eigenstate of $\mathcal{P}$ or $\mathcal{PT}$ operator [3].

5.1.5.2 Density distribution and single-particle density matrix

With the knowledge of Ψ_G, we are equipped to extract various properties of the ground state. We derive density distribution from the expectation value of single-

particle density operator, written in second-quantized form as

$$\hat{\rho}(\mathbf{r}) = \sum_{ij} \langle \phi_i(\mathbf{r'}) \mid \delta(\mathbf{r} - \mathbf{r'}) \mid \phi_j(\mathbf{r}) \rangle a_i^\dagger a_j, \tag{5.9}$$

where $|\phi_i(\mathbf{r})\rangle$ is the single-particle state identified by index j_z in the LLL [135]. In our case, we also have an additional index to denote up- and down- spin components. Since J_z is a good quantum number, the operator $a_i^\dagger a_j$ selects only one single-particle state within LLL approximation. As a consequence, it does not contain information about products of different amplitudes and loses information about interference pattern [135]. Hence, the density distribution solely preserves the information on individual densities:

$$n(\mathbf{r}) = \langle \Psi_G \mid \hat{\rho}(\mathbf{r}) \mid \Psi_G \rangle = \sum_{i=1}^{M} \mid \phi_i(\mathbf{r}) \mid^2 O_i \, , \tag{5.10}$$

where O_i is the total ground state occupation of the single-particle state $|\phi_i(\mathbf{r})\rangle$ [135]. Within the LLL approximation, O_i are essentially eigenvalues of the diagonal single-particle density matrix. Since single-particle states in Eqn. (5.4) are eigenstates of $\mathcal{P}$ operator, it is evident that the density distributions $n(\mathbf{r})$ would be cylindrically symmetric. For example, representative plots of O_i as a function of j_z, and plots of density distributions are shown in Figs. 5.4 and 5.7 [3].

5.1.5.3 Pair-correlation function

Pair-correlation functions help us analyze the internal structure of the ground states. We write the pair-correlation operator (not normalized) in second-quantized form

[135],

$$\hat{\rho}(\mathbf{r},\mathbf{r}_0) = \sum_{ijkl} \phi_i^*(\mathbf{r})\phi_j^*(\mathbf{r}_0)\phi_k(\mathbf{r})\phi_l(\mathbf{r}_0)a_i^\dagger a_j^\dagger a_l a_k. \tag{5.11}$$

In our case, we also have an additional index to denote up- and down-spin components. For instance, we may compute pair-correlation functions that determine the conditional probability to find an up-spin or a down-spin, when an up-spin component is assumed to be present at a fixed point $\mathbf{r}_0$, i.e., $\langle n_\uparrow(\mathbf{r}_0)n_\uparrow(\mathbf{r})\rangle$ or $\langle n_\uparrow(\mathbf{r}_0)n_\downarrow(\mathbf{r})\rangle$ respectively. We may choose $\mathbf{r}_0$ to be away from the origin, but with a substantial amplitude of $n(\mathbf{r})$. Due to angular momentum conservation, the condition $i+j = k+l$ must further be fulfilled. Computing the expectation value of $\hat{\rho}(\mathbf{r},\mathbf{r}_0)$ with respect to Ψ_G, we obtain the pair-correlation function as

$$\rho(\mathbf{r},\mathbf{r}_0) = \sum_{ijkl}\sum_{pp'} \alpha_p^*\alpha_{p'}\phi_i^*(\mathbf{r})\phi_j^*(\mathbf{r}_0)\phi_k(\mathbf{r})\phi_l(\mathbf{r}_0) \langle \Phi_p \mid a_i^\dagger a_j^\dagger a_l a_k \mid \Phi_{p'}\rangle. \tag{5.12}$$

When the wavefunction Ψ_G is an eigenstate of $\mathcal{PT}$ operator, pair-correlation function illustrate the ground state symmetry properties. Furthermore, they reveal the correlations between up- and down-spin components in real-space. Pair-correlation functions at representative interaction strengths are shown in Figs. 5.4 and 5.7 [3].

5.1.5.4 Reduced wavefunction

We shall now discuss techniques to analyze if the ground states possess vortex structures with distinct topological properties. One identifying property is the presence of quantized values of *skyrmion* number, as discussed in Chapter. 3. However, this requires the computation of ground state wavefunction in real-space, a computationally prohibitive task for the bosonic few-particle system under study. Here, we discuss a

viable approach to identify the topological nature of the ground state by computing the reduced wavefunction [136]:

$$\psi_{\mathrm{rwf}}(\mathbf{r}) = \frac{\Psi(\mathbf{r}, \mathbf{r_2^*}, ..., \mathbf{r_N^*})}{\Psi(\mathbf{r_1^*}, \mathbf{r_2^*}, ..., \mathbf{r_N^*})}. \tag{5.13}$$

Reduced wavefunction $\psi_{\mathrm{rwf}}(\mathbf{r})$ is computed with respect to one particle, here particle with index 1, while the remaining $N-1$ particles are placed at their most probable locations $\mathbf{r_i^*}$ [136,137]. In our case, we also have an additional index to denote up- and down-spin components. With $\psi_{\mathrm{rwf},\uparrow}(\mathbf{r})$ and $\psi_{\mathrm{rwf},\downarrow}(\mathbf{r})$ known, we can now extract phase information and compute a distinct topological quantity, *vorticity*, i.e., the number of phase slips from $+\pi$ to $-\pi$ along a closed contour. An integer-valued vorticity is an unambiguous way of establishing that the ground state is topological in nature with a distinct vortex structure. For example, typical phase plots revealing different vorticities are shown in Figs. 5.4 and 5.7 [3].

5.1.5.5 Entanglement measures

We compute entanglement measures to analyze correlation properties of various ground states. In particular, we intend to probe the ground state correlation properties that specifically stem from the presence of inter-particle interactions. To achieve this goal, we take cues from seminal papers in Ref. [138, 139]. We choose a *proper* single-particle basis comprising of the set of eigenstates in Eqn. (5.4) of the single-particle Hamiltonian $\mathcal{H}_0$. In such a single-particle basis, entanglement in the ground state, or any non-degenerate energy eigenstate, occurs specifically due to the presence of interactions [138, 139].

The first step in discussing any entanglement measure is to partition the system

and compute entanglement properties between different subsystems. As discussed in Sec. 5.1.3, similar to 2D LL orbitals, the single-particle eigenstates at large SO coupling strengths are fairly localized in nature. This warrants us to consider partitioning the system in *orbital space* [140]. The $\mathcal{T}$ symmetry preserved by the Hamiltonian $\mathcal{H}$ naturally prompts us to partition the orbitals into two subsystems: positive j_z states (subsystem A) and negative j_z states (subsystem B). We write the ground state wavefunction in Fock space as $\Psi_G = \sum_{p=1}^{n_d} \alpha_p \Phi_p$, where Φ_p is represented as $\mid n_{-j_c} n_{-(j_c-1)} .... n_{j_c-1} n_{j_c} \rangle$. Here, n_{j_z} represents the occupation number of the single-particle eigenstate j_z, and as discussed in Sec. 5.1.4, a finite size cut-off is made at a certain value $j_c \equiv j_{z,c}$ for computational feasibility. Now, we proceed to compute the bipartite entanglement properties between subsystems A and B, i.e., between the positive and negative j_z states respectively [3].

Orbital entanglement spectrum:- With the knowledge of Ψ_G, we compute the entries of the density matrix $\hat{\rho}$ for the ground state as

$$\langle n'_{-j_c} .... n'_{j_c} \mid \hat{\rho} \mid n_{-j_c} .... n_{j_c} \rangle = \alpha_p \alpha_p^*, \tag{5.14}$$

where the generic density operator is $\hat{\rho} = \mid \Psi_G \rangle \langle \Psi_G \mid$.

Now, we compute the reduced density matrix (RDM) $\hat{\rho}_A$ by tracing out the degrees of freedom of subsystem B, meaning $\hat{\rho}_A = \mathrm{Tr}_B \, \hat{\rho}$. As shown in Refs. [138, 139], occupation numbers act as distinguishable degrees of freedom in characterizing entanglement in a finite system of identical quantum particles. Hence in our study, RDM is computed by tracing out the occupation of all the negative j_z states from

the density matrix:

$$\langle n^{'}_{1/2}....n^{'}_{j_c} \mid \hat{\rho}_{j_c}(1/2,..,j_c) \mid n_{1/2}....n_{j_c}\rangle = \sum_{n_{-j_c}..n_{-1/2}} \langle n_{-j_c}..n_{-1/2}n^{'}_{1/2}..n^{'}_{j_c} \mid \hat{\rho} \mid n_{-j_c}..n_{-1/2}n_{1/2}..n_{j_c}\rangle \tag{5.15}$$

The RDM $\hat{\rho}_A$ has a block-diagonal structure, with each block characterized by the total angular momentum J_z^A that corresponds only to particles in subsystem A. The block-diagonal structure allows us to compute all the eigenvalues of the RDM using full-diagonalization techniques. Orbital entanglement spectrum (OES), termed so because the partition is defined in orbital space, is the plot of entanglement pseudo-energies ξ_i as a function of J_z^A. Here, $\xi_i = -\ln \rho_i^A$, with ρ_i^A being the eigenvalues of RDM $\hat{\rho}_A$ [141]. It is evident that ξ_i with smaller magnitudes maximally contribute to the ground state properties [3].

Plots of OES reveal information about the occupation of various Fock states in a given ground state manifold, and in-turn the correlation properties of the ground state. If various Fock states Φ_p in the ground state J_z manifold have similar magnitudes of α_p, it results in similar RDM eigenvalues of ρ_i^A, and in-turn, similar magnitudes of ξ_i. Thus, if an OES plot reveals that ξ_i values are degenerate or *nearly* degenerate, this is a clear manifestation of the correlated nature of the ground state. On the other hand, if the OES plot reveals that the values of ξ_i are distinctly non-degenerate, the ground state is clearly *not* correlated. For example, representative OES plots are shown in Figs. 5.4, and 5.7.

Entanglement entropy:- Plots of OES reveal the whole spectrum of eigenvalues of the RDM and help us understand the correlation properties of the ground state. However, it is sometimes useful to extract just a single representative quantity from

the RDM [142]. Entanglement entropy (EE) is such a measure that can be readily obtained from the set of eigenvalues ρ_i^A of the RDM $\hat{\rho}_A$, and is defined as $S_A = -\mathrm{tr}[\hat{\rho}_A \ln\hat{\rho}_A] = -\sum_i \rho_i^A \ln\rho_i^A$. A higher entropy value means that the ground state is more homogeneously spread in Fock space, i.e., a larger number of Fock states Φ_p make substantial contributions towards the ground state. A distinct advantage of an EE plot is that we are able to look at entropy values for a whole range of interaction strengths in a single plot, and thereby, understand correlation properties of various phases. For example, representative EE plots are shown in Figs. 5.2, 5.3, 5.5, and 5.6 [3].

In summary, density distribution, eigenvalues of single-particle density matrix, pair-correlation function and reduced wavefunction would help us identify various symmetry and topological properties of the ground states. Computation of RDM from *proper* single-particle basis enables us to extract various entanglement measures and allow us to analyze correlation properties that specifically stem from inter-particle interactions.

5.2 Results and discussion

As discussed in Sec. 5.1.3, in the absence of interactions, all particles would simply condense into the two lowest energy single-particle eigenstates in the LLL identified by quantum numbers $j_z = \pm 0.5$. This is due to the weak, but finite, dispersion in j_z present in the single-particle energy spectrum shown in Fig. 2.6(b). The $\mathcal{P}$-eigenstate, identified by $j_z = +0.5$, is represented by wavefunction $\Phi_{\mathcal{P}} = [\phi_\uparrow(\rho), \phi_\downarrow(\rho)e^{i\varphi}]^T/\sqrt{2\pi}$. It has a half-quantum vortex configuration, as the spin-up component stays in the s-state and the spin-down component is in the p-state [2, 82, 83]. The resulting spin texture of this topological state is of skyrmion type [2].

The degenerate time-reversed $\mathcal{P}$-eigenstate, identified by $j_z = -0.5$ and represented by $\mathcal{T}\Phi_{\mathcal{P}} = [\phi_\downarrow(\rho)e^{-i\varphi}, -\phi_\uparrow(\rho)]^T/\sqrt{2\pi}$, also has a half-quantum vortex configuration. We may as well construct a zero angular momentum $\mathcal{PT}$-eigenstate, from an equal superposition of opposite angular momentum $\mathcal{P}$-eigenstates: $\Phi_{\mathcal{PT},j_z=0} = (\Phi_{\mathcal{P}} \pm \mathcal{T}\,\Phi_{\mathcal{P}})/\sqrt{2}$. In the absence of interactions, either of the $\mathcal{P}$-eigenstates or the superposition $\mathcal{PT}$-eigenstate are degenerate. In addition, any arbitrary superposition of the degenerate $\mathcal{P}$-eigenstates, which in principle need not be a $\mathcal{PT}$-eigenstate, will also be a degenerate ground state [3].

In the presence of inter-particle interactions, the ground state is not anymore determined solely by the energy contribution of the non-interacting part of the Hamiltonian $\mathcal{H}_0$. Depending upon the strengths of g and $g_{\uparrow\downarrow}$, the energy contribution from the interacting part of the Hamiltonian $\mathcal{H}_{\rm int}$ also plays a crucial role. This competition can be better understood, especially at large SO coupling strengths, by analyzing the single-particle wavefunctions and energy. As shown in Fig. 2.6(b), energy contributions due to $\mathcal{H}_0$ tries to keep the particles in states with lower value of angular momenta j_z. However, for repulsive interaction strengths, energy considerations due to $\mathcal{H}_{\rm int}$ tries to keep the particles as far away from each other as possible. This in-turn means that the particles tend to occupy states with larger value of angular momenta, since they have a larger localization radii as shown in Fig. 2.5(b). In essence, the ground state of the interacting many-body Hamiltonian is determined by the competition between the $\mathcal{H}_0$ and $\mathcal{H}_{\rm int}$ terms [3].

The simplest scenario where the competition between the $\mathcal{H}_0$ and $\mathcal{H}_{\rm int}$ terms, in-turn the effect of inter-particle interactions, clearly manifests is in an interacting problem with $N = 2$ particles. For this reason, we discuss the results for $N = 2$ particles and analyze the ground state properties in greater detail, before proceed-

ing to larger particle numbers. We solve the interacting few-body Hamiltonian $\mathcal{H}$ at large SO coupling strengths using ED scheme within LLL approximation. The computational intensity, especially at large interaction strengths, limits the feasibility of this scheme to the order of $N = 8$ particles [137, 143]. In an earlier mean-field study on *homogeneous* two-component Bose gas [95], it was shown that the particles condense into either a single plane-wave state (for $g > g_{\uparrow\downarrow}$) or a density-stripe state (for $g < g_{\uparrow\downarrow}$). Similarly, in the earlier related work presented in Sec. 3.3, depending on the relative magnitudes of g and $g_{\uparrow\downarrow}$, we show that states with distinct topological and symmetry properties emerge in the mean-field phase diagram. Taking cues from these results, in this study, we solve for the ground state wavefunction at various interaction strengths, however fixing the relative magnitude $g_{\uparrow\downarrow}/g$ at 0.5 or 1.5. In this section, we present the results at different particle numbers N, and analyze the topological, symmetry and correlation properties of the ground states using various techniques elaborated in Sec. 5.1.5 [3].

5.2.1 $N = 2$

As discussed in Sec. 5.1.5.1, we analyze the energy spectrum to identify the ground state angular momentum manifold J_z, or equivalently, J_z/N. In Fig. 5.1(a), we notice that the ground state belongs to $J_z/N = 0$ manifold. We further determine that the ground state wavefunction Ψ_G is an eigenstate of $\mathcal{PT}$ operator. On the other hand, we observe from Fig. 5.1(b) that the ground state is degenerate in $J_z/N = \pm 0.5$ manifolds. In either scenario, in Fig. 5.1(b), we determine that Ψ_G is an eigenstate of $\mathcal{P}$ operator. It is evident that, even in the presence of extremely weak interaction strengths, the interacting Hamiltonian picks either a $\mathcal{P}$-eigenstate or a $\mathcal{PT}$-eigenstate to be the ground state. Furthermore, it is clear that the ground state is sensitive to

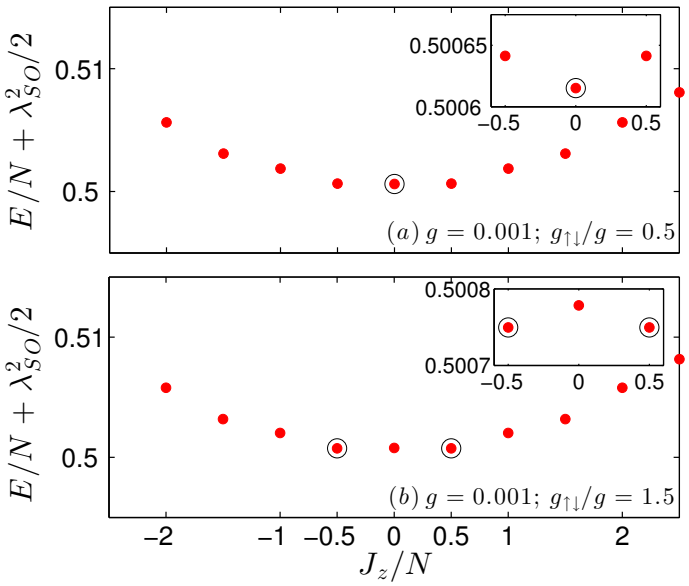

Figure 5.1 : (color online). Energy spectrum for extremely weak interaction strengths with $\lambda_{SO} = 20$ and $N = 2$. Here, each marker (red) represents the lowest energy eigenvalue of a specific *block diagonal* with a fixed value of J_z. Since energy eigenvalues are very close, we identify the ground state energies by circled (black) markers and further, show the zoomed-in plots in the inset. Image from Ref. [3].

the relative magnitudes of $g_{\uparrow\downarrow}$ and g [3].

Figs. 5.2(a), 5.3(a): We solve the interacting Hamiltonian $\mathcal{H}$ at various interaction strengths and identify corresponding ground state manifolds J_z/N in Figs. 5.2(a) and 5.3(a). It is evident from the phase diagram that depending on g and $g_{\uparrow\downarrow}$, the ground states belong to different J_z/N manifolds. Furthermore, we determine if the ground state wavefunction Ψ_G is an eigenstate of $\mathcal{PT}$ operator, and thereby identify whether the state belongs to $\mathcal{P}$ or $\mathcal{PT}$ symmetry phase. In a broader sense, it is evident that a ground state in $\mathcal{PT}$ symmetry phase belongs to $J_z/N = 0$ manifold, while ground states in various $J_z/N \neq 0$ manifolds belong to $\mathcal{P}$ symmetry phase. EE plots in Figs. 5.2(b) and 5.3(b) reveal correlation properties in various phases. For pedagogical purposes, before we explain the features in EE plots, we first discuss the

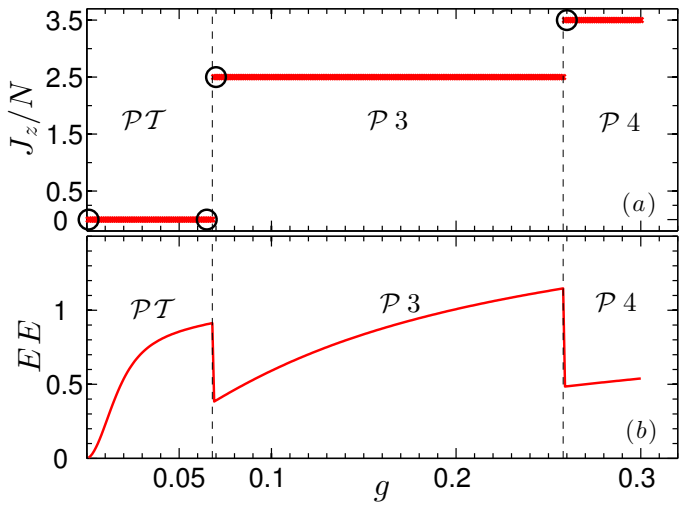

Figure 5.2 : (color online). Plots of (a) ground state J_z/N manifolds and (b) entanglement entropy, as a function of interaction strength g with $\lambda_{SO} = 20, N = 2, g_{\uparrow\downarrow}/g = 0.5$. For representative interaction strengths denoted by circled (black) markers, we illustrate the ground state properties in Fig. 5.4. Image from Ref. [3].

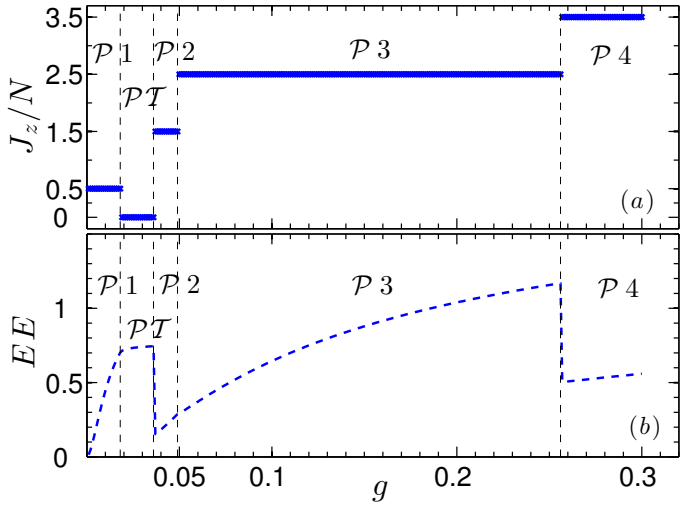

Figure 5.3 : (color online). Plots of (a) ground state J_z/N manifolds and (b) entanglement entropy, as a function of interaction strength g with $\lambda_{SO} = 20, N = 2, g_{\uparrow\downarrow}/g = 1.5$. Image from Ref. [3].

symmetry, topological and correlation properties of ground states [3].

In Fig. 5.4, we illustrate density distributions, eigenvalues of single-particle den-

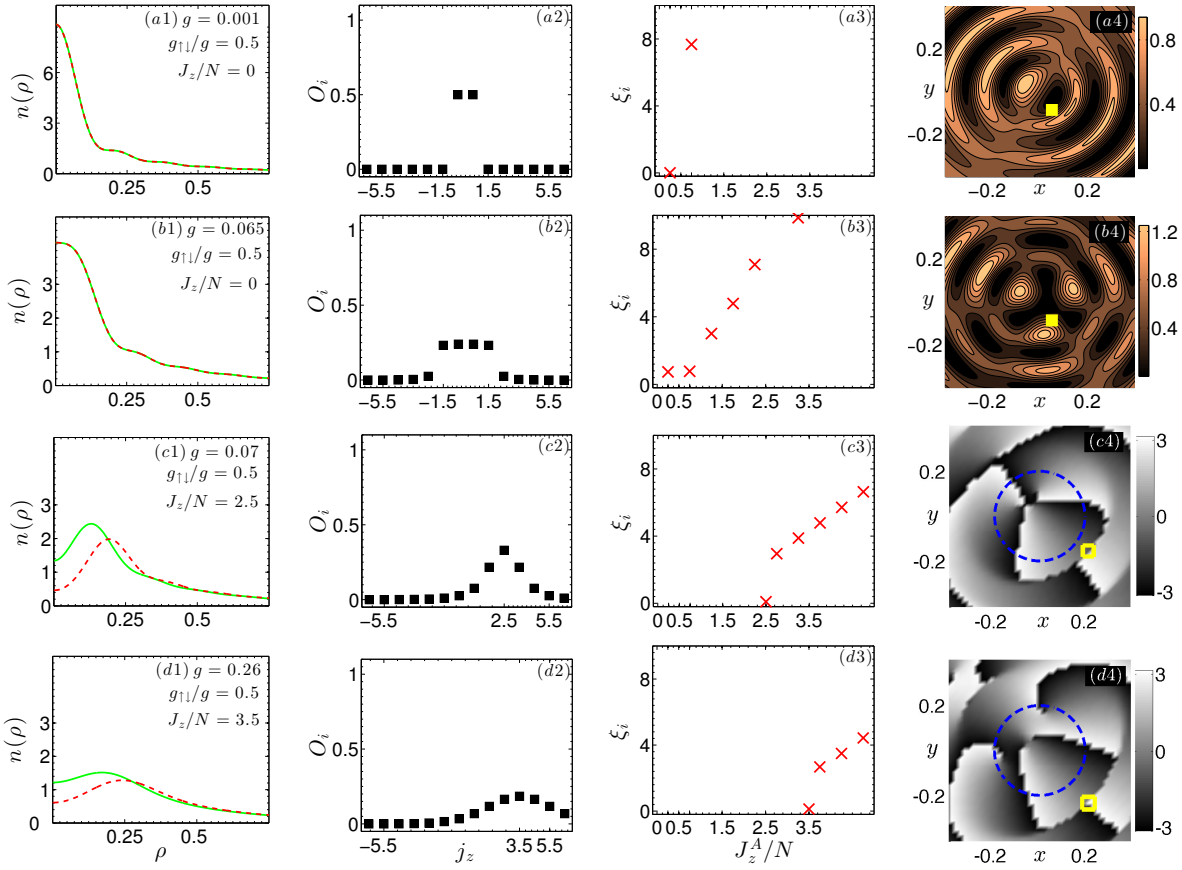

Figure 5.4 : (color online). Plots in each row illustrate the ground state properties at a representative interaction strength of Fig. 5.2(a). In the first column (from left), we show density distributions of spin-up component $n_{\uparrow}(\rho)$ (solid green) and of spin-down component $n_{\downarrow}(\rho)$ (dashed red). In the second column, we show eigenvalues O_i of single-particle density matrix as a function of angular momentum j_z of the single-particle states $|\phi_i(\mathbf{r})\rangle$. In the third column, we show corresponding OES plots of entanglement pseudo-energies ξ_i as a function of J_z^A/N, the average angular momentum of subsystem A. In the last column, we show contour plots ($a4$) and ($b4$) that are normalized pair-correlation functions $\langle n_{\uparrow}(\mathbf{r}_0)n_{\downarrow}(\mathbf{r})\rangle$, with $\mathbf{r}_0$ denoted by a (yellow) marker. Phase plots ($c4$) and ($d4$) are derived from reduced wavefunction $\psi_{c,\downarrow}(\mathbf{r})$, which is computed by fixing one of the two particles at their most probable locations and their corresponding radii are indicated by (yellow) markers. The closed dashed (blue) contour is a guide to the eye, that allows us to count the number of phase slips. Image from Ref. [3].

sity matrix, orbital entanglement spectrum, pair-correlation functions and reduced wavefunctions at representative interaction strengths within various J_z/N manifolds of Fig. 5.2(a). Using a similar line of reasoning, we may understand the properties of ground states in Fig. 5.2(b). Let us now proceed to discuss various plots shown in Fig. 5.4 [3].

Figs. 5.4($a1$) $\rightarrow$ 5.4($a4$): In this top row, we discuss the ground state properties of the $\mathcal{PT}$ eigenstate in $J_z/N = 0$ manifold at $g = 0.001$ of Fig. 5.2(a). As shown in Fig. 5.4($a1$), the cylindrically symmetric density distributions $n_\uparrow(\rho)$ and $n_\downarrow(\rho)$ overlap. Being a $\mathcal{PT}$ eigenstate, it is evident from Fig. 5.4($a2$) that the positive and negative angular momentum states are equally occupied. Furthermore, the time-reversal partner states identified by quantum numbers $j_z = \pm 0.5$ are predominantly occupied. As expected, from the corresponding OES plot in Fig. 5.4($a3$), we observe that the predominant contribution to the ground state is from the entanglement pseudo-energy ξ_i at $J_z^A/N = +0.25$. From Figs. 5.4($a2$) and 5.4($a3$), it is clear that the the maximally contributing Fock state is $\Phi_{\mathcal{PT}} =\mid n_{j_z=-0.5} = 1, n_{j_z=+0.5} = 1\rangle$, which explains the overlapping density distributions of $n_\uparrow(\rho)$ and $n_\downarrow(\rho)$ in Fig. 5.4($a1$). In Fig. 5.4($a4$), we plot the (normalized) pair-correlation function $\langle n_\uparrow(\mathbf{r}_0) n_\downarrow(\mathbf{r})\rangle$ of this $\mathcal{PT}$ eigenstate. This plot illustrates the conditional probability to find a down-spin, when an up-spin component is assumed to be at a fixed point $\mathbf{r}_0$, and reveals the presence of correlated regions (magnitude closer to 1) and anti-correlated regions (magnitude closer to 0). This plot illustrates the correlations present between up-spin and down-spin components that are not revealed by the cylindrically symmetric density distributions [3].

Figs. 5.4($b1$) $\rightarrow$ 5.4($b4$): In this second row, we discuss the ground state properties of the $\mathcal{PT}$ eigenstate in $J_z/N = 0$ manifold at $g = 0.065$ of Fig. 5.2(a). As

discussed with reference to Fig. 5.4($a1$), the density distributions $n_\uparrow(\rho)$ and $n_\downarrow(\rho)$ overlap in Fig. 5.4($b1$). It is evident from Fig. 5.4($b2$) that the time-reversal partner states identified by $j_z = \pm 0.5$ and $j_z = \pm 1.5$ are almost equally occupied. From the corresponding OES plot in Fig. 5.4($b3$), we observe that the ground state is equally occupied by ξ_i at $J_z^A/N = +0.25$ and $+0.75$. From Figs. 5.4($b2$) and 5.4($b3$), it is clear that the the maximally contributing Fock states are $\Phi_{\mathcal{PT}} =\mid n_{j_z=-0.5} = 1, n_{j_z=+0.5} = 1\rangle$ and $\Phi_{\mathcal{PT}} =\mid n_{j_z=-1.5} = 1, n_{j_z=+1.5} = 1\rangle$. To illustrate the internal structure of this $\mathcal{PT}$ eigenstate and the correlations between up-spin and down-spin components, we show the pair-correlation function in Fig. 5.4($b4$) [3].

Figs. 5.4($c1$) $\rightarrow$ 5.4($c4$): In this third row, we discuss the ground state properties of the $\mathcal{P}$ eigenstate in $J_z/N = +2.5$ manifold at $g = 0.07$ of Fig. 5.2(a). While the corresponding ground state is degenerate in $J_z/N = \pm 2.5$ manifolds, we restrict our discussion to $J_z/N = +2.5$ manifold without loss of generality. The cylindrically symmetric density distributions $n_\uparrow(\rho)$ and $n_\downarrow(\rho)$ are distinct, as shown in Fig. 5.4($c1$). In this $\mathcal{P}$ eigenstate, there is an inherent asymmetry in the occupation of positive and negative angular momentum states. This is evident from the plot of single-particle density matrix eigenvalues O_i in Fig. 5.4($c2$). This explains the presence of distinct density distributions in Fig. 5.4($c1$). Furthermore, we observe a peak in the occupation of eigenstate identified by $j_z = +2.5$ in Fig. 5.4($c2$). From the corresponding OES plot in Fig. 5.4($c3$), we observe that the ground state is predominantly occupied by ξ_i at $J_z^A/N = 2.5$. To illustrate the internal structure of this $\mathcal{P}$ eigenstate, we show the phase plot derived from the reduced wavefunction $\psi_{c,\downarrow}(\mathbf{r})$ in Fig. 5.4($c4$). To better understand this phase plot, we take cues from plots in Figs. 5.4($c2$) and 5.4($c3$). Though we observe from Fig. 5.4($c3$) that the ground state is predominantly occupied by ξ_i at $J_z^A/N = 2.5$, it may be conceived from Fig. 5.4($c2$) that the ground

state has contributions from various Fock states, for example: $\Phi_{\mathcal{P}} =\mid n_{j_z=+2.5} = 2\rangle$ or $\Phi_{\mathcal{P}} =\mid n_{j_z=+1.5} = 1, n_{j_z=+3.5} = 1\rangle$ or $\Phi_{\mathcal{P}} =\mid n_{j_z=+0.5} = 1, n_{j_z=+4.5} = 1\rangle$. From the representation of single-particle eigenstates in Eqn. (5.4), it is evident that the net orbital angular momentum of spin-up component in the ground state is $+2$ and that of spin-down component is $+3$. Correspondingly, the phase plot of the down-spin component in Fig. 5.4($c4$) reveals a vorticity of 3. We note here that the vorticity is the number of phase slips from $+\pi$ to $-\pi$, i.e., when the shadowing changes from white to black. For convenience, we identify this $\mathcal{P}$ eigenstate as $\mathcal{P}3$, where 3 is the vorticity of the down-spin component [3].

Figs. 5.4($d1$) $\rightarrow$ 5.4($d4$): In this last row, we discuss the ground state properties of the $\mathcal{P}$ eigenstate in $J_z/N = +3.5$ manifold at $g = 0.26$ of Fig. 5.2(a). The corresponding ground state is degenerate in $J_z/N = \pm 3.5$ manifolds, while we restrict our discussion to $J_z/N = +3.5$ manifold. As expected for a $\mathcal{P}$ eigenstate, the density distributions $n_\uparrow(\rho)$ and $n_\downarrow(\rho)$ shown in Fig. 5.4($d1$) are distinct. In addition to the asymmetric occupation of positive and negative angular momentum states in Fig. 5.4($d2$), we observe a peak occupation of eigenstate identified by $j_z = +3.5$. From the corresponding OES plot in Fig. 5.4($d3$), we observe that the ground state is predominantly occupied by ξ_i at $J_z^A/N = 3.5$. However, it may be conceived from Fig. 5.4($d2$) that the ground state has contributions from various Fock states, for example: $\Phi_{\mathcal{P}} =\mid n_{j_z=+3.5} = 2\rangle$ or $\Phi_{\mathcal{P}} =\mid n_{j_z=+1.5} = 1, n_{j_z=+5.5} = 1\rangle$ or $\Phi_{\mathcal{P}} =\mid n_{j_z=+2.5} = 1, n_{j_z=+4.5} = 1\rangle$. It is clear that with increasing inter-particle interaction strengths, the particles distribute themselves in higher angular momentum manifolds. Furthermore, it is evident that the net orbital angular momentum of spin-up component in the ground state is $+3$ and that of spin-down component is $+4$. Correspondingly, the phase plot of down-spin component in Fig. 5.4($d4$) reveals

a vorticity of 4. For convenience, we identify this $\mathcal{P}$ eigenstate as $\mathcal{P}4$. We further note that the phase plots of down-spin components derived for $\mathcal{P}1$ and $\mathcal{P}2$ eigenstates in Fig. 5.3(a) exhibit a vorticity of 1 and 2 respectively [3].

Figs. 5.2(b), 5.3(b): As noted earlier, OES preserves the whole spectrum of eigenvalues of the RDM, and hence allows us to extract information about the occupation of Fock states with different subsystem angular momenta J_z^A. With our understanding of OES plots in Figs. 5.4, we now proceed to explain various features observed in EE plots of Figs. 5.2(b) and 5.3(b). (**i**) The presence of distinctly different slopes suggests the presence of distinct correlation properties in ground states within various phases. (**ii**) Within each phase, EE increases monotonously with increasing g. As discussed in Sec. 5.1.5.5, this results from an increasingly homogeneous distribution of Fock states in the ground state J_z/N manifold, and in-turn an increased correlation. For example, to illustrate this feature within the $\mathcal{PT}$ symmetric phase in Fig. 5.2(b), we may compare OES plots in Fig. 5.4($a3$) and 5.4($b3$) and observe an increased homogeneity in distribution of Fock states. (**iii**) The presence of nearly degenerate ξ_i values results in a reduction in the *slope* of EE. While this feature is observed at larger interaction strengths within the $\mathcal{PT}$ symmetric phase of Fig. 5.2(b), the OES plot in Fig. 5.4($b3$) helps us understand this. (**iv**) Transition to a $\mathcal{P}$ symmetric phase is marked by a sharp reduction in the *value* of EE*. To better understand this feature, we compare OES plots in Fig. 5.4($b3$) and 5.4($c3$) and observe a sharp reduction in homogeneity of ξ_i values, accompanied by a substantial

*In Fig. 5.3(b), $\mathcal{P}2 \to \mathcal{P}3$ transition neither exhibits a change in slope nor a noticeable drop in EE value. From an analysis of OES plots across this transition (not shown), we observe that the maximally contributing entanglement pseudo-energies ξ_i at $J_z^A = 1.5$ ($\mathcal{P}2$) and $J_z^A = 2.5$ ($\mathcal{P}3$) are nearly degenerate, and hence we observe this anomaly. In a broader sense, we conclude that the ground states with $\mathcal{P}2$ symmetry in Fig. 5.3(b) may merely occupy a small *crossover* region between $\mathcal{PT}$ and $\mathcal{P}3$ phases.

drop in the minimum value of ξ_i. In summary, we emphasize that the knowledge of OES helps us understand various features exhibited by EE plots [3].

In summary, it is evident that the interacting Hamiltonian picks either a $\mathcal{P}$-eigenstate or a $\mathcal{PT}$-eigenstate to be the ground state. The ground state is sensitive to the relative magnitudes of $g_{\uparrow\downarrow}$ and g. J_z/N plots allow us to identify various $\mathcal{P}$ and $\mathcal{PT}$ symmetry phases in the interacting system. With the analysis of density distributions, single-particle density matrix and reduced wavefunctions, we illustrate ground state symmetry and topological properties. We assert that the bosons condense into an array of $\mathcal{P}$-symmetric topological ground states that have $n + 1/2$ -quantum angular momentum vortex configuration, with $n = 0, 1, 2, 3$. With the analysis of single-particle density matrix, OES and pair-correlation functions, we illustrate the internal structure of different ground states in the $\mathcal{PT}$ symmetry phase. We analyze the correlation properties of the ground states with the help of OES and EE plots [3].

5.2.2 $N = 8$

The detailed analysis presented above for the relatively simple, but rich, scenario of $N = 2$ particles shall be useful when discussing results at larger particle numbers. Even with a small increase in particle number from $N = 2$ to $N = 4$ (not shown), we observe the non-occurrence of ground states in $\mathcal{P}4$ phase. As discussed in the introduction of Sec. 5.2, this can be understood as a manifestation of the competition between energy contributions from $\mathcal{H}_0$ and $\mathcal{H}_{\rm int}$. A higher particle number increases the probability distribution into single-particle states with smaller angular momenta, when compared to larger angular momenta eigenstates. We shall now proceed to consider the few-body system with $N = 8$ particles, discuss the occurrence of various

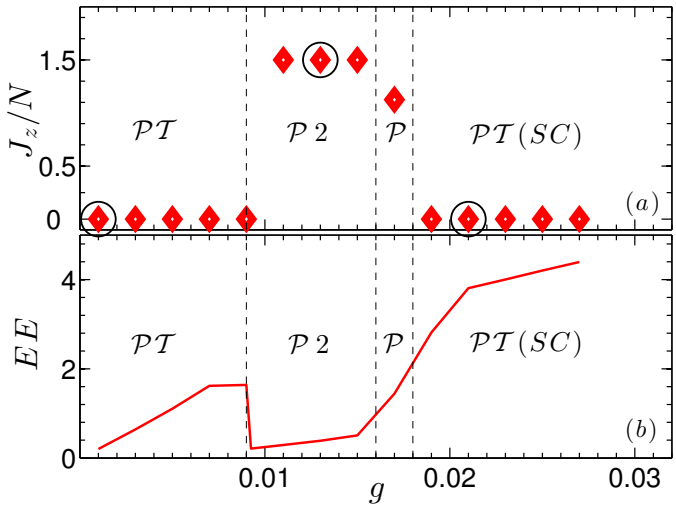

Figure 5.5 : (color online). Plots of (a) ground state J_z/N manifolds and (b) entanglement entropy, as a function of interaction strength g with $\lambda_{SO} = 20, N = 8, g_{\uparrow\downarrow}/g = 0.5$. For representative interaction strengths denoted by circled (black) markers, we illustrate the ground state properties in Fig. 5.7. Image from Ref. [3].

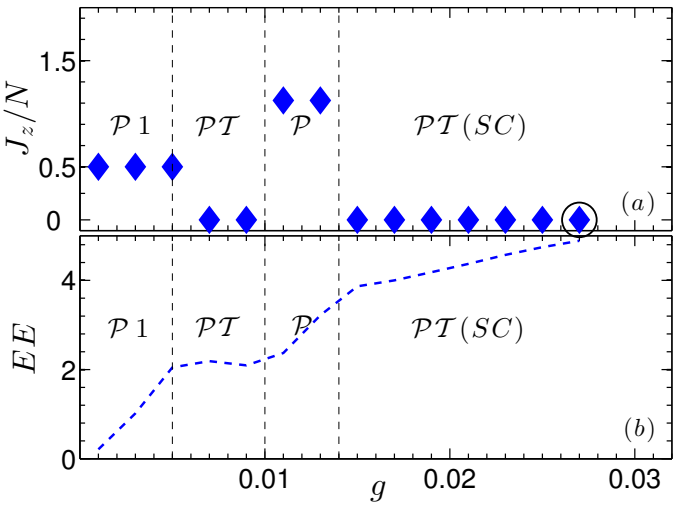

Figure 5.6 : (color online). Plots of (a) ground state J_z/N manifolds and (b) entanglement entropy, as a function of interaction strength g with $\lambda_{SO} = 20, N = 8, g_{\uparrow\downarrow}/g = 1.5$. For the representative interaction strength denoted by a circled (black) marker, we illustrate the ground state properties in Fig. 5.7. Image from Ref. [3].

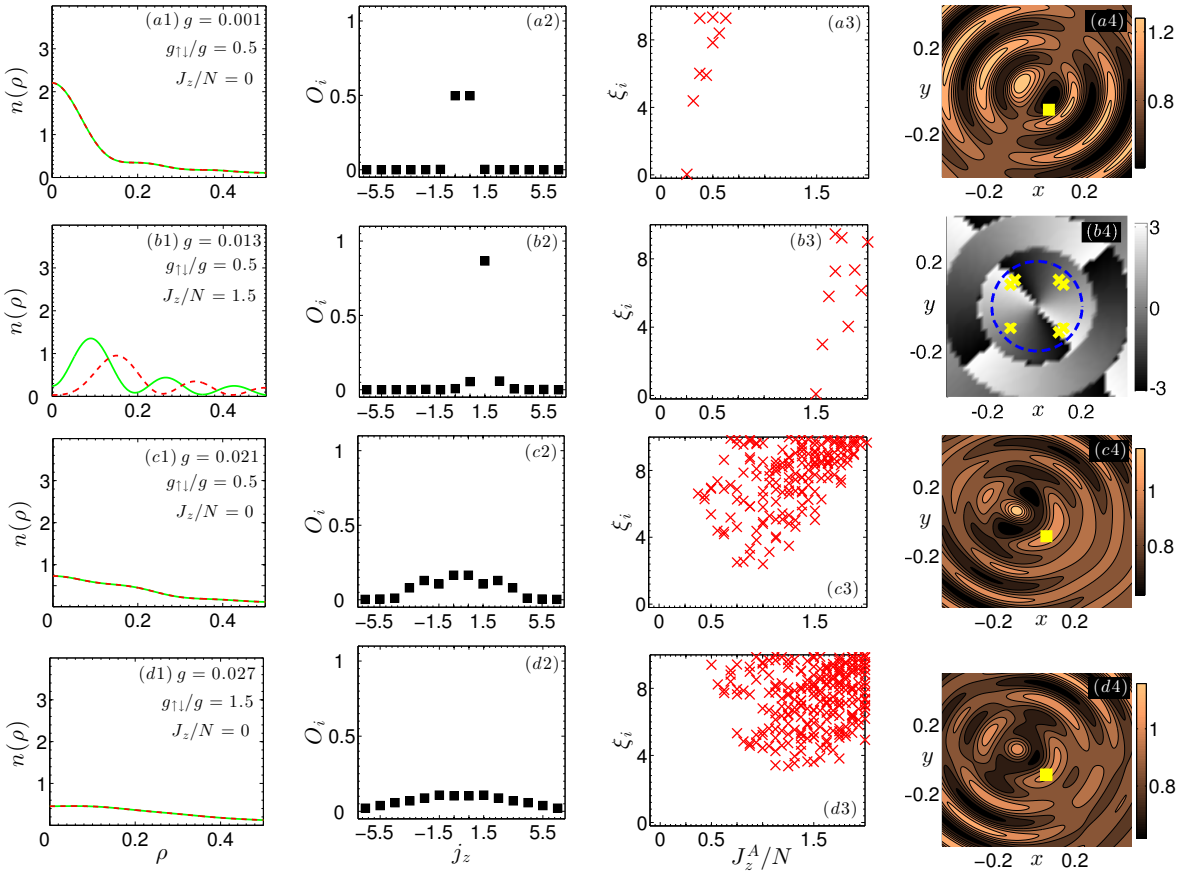

Figure 5.7 : (color online). Plots in each row illustrate the ground state properties at a representative interaction strength in Fig. 5.5(a) or 5.6(a). In the first column (from left), we show density distributions of spin-up component $n_\uparrow(\rho)$ (solid green) and of spin-down component $n_\downarrow(\rho)$ (dashed red). In the second column, we show eigenvalues O_i of single-particle density matrix as a function of angular momentum j_z of the single-particle states $|\phi_i(\mathbf{r})\rangle$. In the third column, we show corresponding OES plots of entanglement pseudo-energies ξ_i as a function of J_z^A/N, the average angular momentum of subsystem A. In the last column, we show contour plots ($a4$), ($c4$), and ($d4$) that are normalized pair-correlation functions $\langle n_\uparrow(\mathbf{r}_0)n_\downarrow(\mathbf{r})\rangle$, with $\mathbf{r}_0$ denoted by a (yellow) marker. Phase plot ($b4$) is derived from reduced wavefunction $\psi_{c,\downarrow}(\mathbf{r})$, which is computed by fixing 7 of the 8 particles at their most probable locations and their corresponding radii are indicated by (yellow) markers. Closed dashed (blue) contour is a guide to the eye, that allows us to count the number of phase slips. Image from Ref. [3].

phases, and analyze the ground state properties at representative interaction strengths using various techniques outlined in Sec. 5.1.5 [3].

Figs. 5.5(a), 5.6(a): We solve the interacting Hamiltonian $\mathcal{H}$ at various interaction strengths and identify corresponding ground state manifolds J_z/N in Figs. 5.5(a) and 5.6(a). As discussed with reference to Figs. 5.2(a) and 5.3(a), it is evident that depending on g and $g_{\uparrow\downarrow}$, the ground states belong to different J_z/N manifolds, and in-turn to $\mathcal{PT}$ or $\mathcal{P}$ symmetry phases. In this relatively larger particle number scenario, we observe that the ground states fall into two distinct regimes: (a) at weak interaction strengths (*mean-field-like regime*), we observe ground states with topological and symmetry properties that are consistent with mean-field theory computations [1]; (b) at intermediate to strong interaction strengths (*strongly correlated regime*), we report the emergence of strong correlations in ground states. The strongly correlated ground states are eigenstates of $\mathcal{PT}$ operator, and we additionally identify them with the label 'SC'. In Fig. 5.7, we illustrate the ground state properties at representative interaction strengths in these two regimes [3].

***Mean-field-like regime:-* Figs. 5.7($a1$) $\rightarrow$ 5.7($a4$), 5.7($b1$) $\rightarrow$ 5.7($b4$):** In the top row, we illustrate the ground state properties of the $\mathcal{PT}$ eigenstate in $J_z/N = 0$ manifold at $g = 0.001$ of Fig. 5.5(a). It is evident that the properties in Figs. 5.7($a1$) $\rightarrow$ 5.7($a4$) are qualitatively identical to their counterparts in Figs. 5.4($a1$) $\rightarrow$ 5.4($a4$). In the second row, we discuss the ground state properties of the $\mathcal{P}$ eigenstate in $J_z/N = +1.5$ manifold at $g = 0.013$ of Fig. 5.5(a). The corresponding ground state is degenerate in $J_z/N = \pm 1.5$ manifolds, while we restrict our discussion to $J_z/N = +1.5$ manifold. As expected for a $\mathcal{P}$ eigenstate, the density distributions $n_\uparrow(\rho)$ and $n_\downarrow(\rho)$ shown in Fig. 5.7($b1$) are distinct. It is evident from the single-particle density matrix eigenvalues in Fig. 5.7($b2$) that there is a peak in the occupation of eigenstate identified

by $j_z = +1.5$. From the corresponding OES plot in Fig. 5.7(b3), we observe that the ground state is predominantly occupied by ξ_i at $J_z^A/N = 1.5$. To illustrate the internal structure of this $\mathcal{P}$ eigenstate, we show the phase plot derived from the reduced wavefunction $\psi_{c,\downarrow}(\mathbf{r})$ in Fig. 5.7(b4). It is evident from the representation in Eqn. (5.4) that the orbital angular momentum of spin-up component in the ground state is $+1$ and that of spin-down component is $+2$. Correspondingly, the phase plot of the down-spin component shown in Fig. 5.7(b4) exhibits a vorticity of 2, and hence we identify this $\mathcal{P}$ eigenstate as $\mathcal{P}2$ [3].

***Strongly correlated regime:-* Figs. 5.7(c1) $\rightarrow$ 5.7(c4), 5.7(d1) $\rightarrow$ 5.7(d4):** In the third and fourth rows, we illustrate the ground state properties of the $\mathcal{PT}$ eigenstates in the strongly correlated regime at $g = 0.021$ of Fig. 5.5(a) and $g = 0.027$ of Fig. 5.6(a) respectively. At intermediate to strong interaction strengths, as shown in Figs. 5.5(a) and Fig. 5.6(a), all the ground states in this regime are eigenstates of $\mathcal{PT}$ operator in $J_z/N = 0$ manifold. As expected, the density distributions $n_\uparrow(\rho)$ and $n_\downarrow(\rho)$ overlap in Figs. 5.7(c1) and 5.7(d1). We observe that the density distributions become increasingly flat with increasing magnitude of interaction strengths, g and $g_{\uparrow\downarrow}$. The interaction-induced correlations present in the ground states are revealed by the eigenvalues of single-particle density matrix and OES plots. From the plots in Figs. 5.7(c2) and 5.7(d2), it is evident that the particles are nearly uniformly distributed across many single-particle eigenstates, with an equal distribution among time-reversal partner states. This distribution is qualitatively in the opposite limit to the corresponding plots in the mean-field-like regime illustrated in Figs. 5.7(a2) and 5.7(b2). This feature is further substantiated in the OES plots of Figs. 5.7(c3) and 5.7(d3), where a large number of entanglement pseudo-energies ξ_i are degenerate or *nearly* degenerate. As discussed in Sec. 5.1.5.5, the presence of a large degeneracy

in entanglement pseudo-energies is a clear manifestation of the strongly correlated nature of the ground states. We further observe that with increasing interaction strengths, the minima of the entanglement pseudo-energies ξ_i shifts to larger J_z^A/N values. To illustrate the internal structure and the correlations between up-spin and down-spin components of these $\mathcal{PT}$ eigenstates, we show the pair-correlation functions in Figs. 5.7($c4$) and 5.7($d4$) [3].

With our understanding of OES plots in Figs. 5.7, we may now explain various features observed in EE plots that help us understand the correlation properties of the ground states in the mean-field-like and strongly correlated regimes. As discussed with reference to Figs. 5.2(b) and 5.3(b), we observe qualitatively similar features in $N = 8$ particle case as well. The presence of distinctly different slopes in Figs. 5.5(b) and 5.6(b) suggests the presence of distinct correlation properties in different ground states within various phases. Within each phase, EE increases monotonously with increasing g due to the presence of increased correlations in the ground state. For example, to illustrate this feature within the $\mathcal{PT}(SC)$ phase, we may compare OES plots in Figs. 5.7($c3$) and 5.7($d3$) and observe an increased homogeneity in Fock states. As a side note, we observe a small region of $\mathcal{P}$-symmetric states before the transition to strongly correlated regime. These states do not possess distinct topological or correlation properties. Without loss of generality, we assert that these ground states merely occupy a *crossover* region prior to the transition to strongly correlated regime [3].

In summary, we emphasize that the ground states in the weakly interacting regime illustrated in the top two rows of Fig. 5.7 are mean-field-like states. Their density distributions, pair-correlation functions and reduced wavefunctions may be readily related to the results from mean-field theory computations discussed in our earlier

publication [1]. Within the ED scheme, we even reproduce the reversal of phase symmetry between $\mathcal{P}$ and $\mathcal{PT}$ eigenstates that is observed with an increasing value of g, but with a fixed value of $g_{\uparrow\downarrow}/g$ in our earlier mean-field study [1]. Such a correspondence between ED results and mean-field theory results is anticipated only when the ground state is predominantly occupied by one single-particle eigenstate (and/or its time-reversal partner), as revealed in Figs. 5.7(a2) and 5.7(b2). As illustrated in the bottom two rows of Fig. 5.7, the presence of a large degeneracy in entanglement pseudo-energies and the distribution of particles across many single-particle eigenstates, are clear manifestations of the strongly correlated nature of the ground states. Furthermore, we observe from Figs. 5.7, that the transition from mean-field-like regime to a strongly correlated regime is attained with only small variations in the magnitudes of inter-particle interaction strengths. We emphasize here that the pivotal reason behind this feature is the presence of *nearly flat* single-particle energy spectrum at large SO coupling strengths [3].

5.3 Conclusions

We systematically study an interacting few-body system of two-component Bose gases with 2D isotropic Rashba SO coupling in a 2D isotropic harmonic trap. We show that the model Hamiltonian is gauge-equivalent to particles subject to a $\mathcal{T}$-symmetry preserving pure non-abelian vector potential, whose magnitude proportionally determines the strength of Rashba SO coupling. It is experimentally feasible to device a scheme in which tunable parameters, such as laser fields, can be used to control the magnitude of non-abelian vector potential, and hence simulate large SO coupling strengths. In this limit of large SO coupling strengths, we show that the single-particle energy spectrum is *nearly flat*. In the recent past, several research groups

have made proposals to engineer quantum systems in which interactions would play a dominant role and the ground states would in-turn be strongly correlated. For example, recent proposals suggest schemes that would engineer *nearly flat* Chern bands to study strongly correlated fractional quantum Hall states in the lattice limit [144–147]. Though we study few-body Bose gases in traps, we emphasize that the intention with which we have identified the existence of *nearly flat* energy spectra at large SO coupling strengths is not too dissimilar from the afore-mentioned line of thought [3].

In our model system with *nearly flat* energy spectra, we observe that the presence of inter-particle interactions allows for the emergence of ground states with distinct topological, symmetry and correlation properties. We solve the interacting Hamiltonian in different particle number scenarios and analyze the ground state properties with the help of energy spectrum, single-particle density matrix, pair-correlation functions, reduced wavefunctions, and entanglement measures. At small particle numbers, we show the phase diagram in Figs. 5.2 and 5.3, with ground states being eigenstates of either $\mathcal{P}$ or $\mathcal{PT}$ operator. In Fig. 5.4, we illustrate the ground state properties at representative interaction strengths in various phases. We further assert that the bosons condense to an array of topological $\mathcal{P}$ eigenstates with $n + 1/2$ quantum angular momentum vortex configuration, with $n = 0, 1, 2, 3,$. At large particle numbers, we illustrate the phase diagram in Figs. 5.5 and 5.6. We observe the presence of two distinct regimes: (a) at weak interaction strengths (mean-field-like regime), we obtain ground states with topological and symmetry properties that are also obtained via mean-field theory computations. We justify this correspondence and illustrate the ground state properties in detail in Fig. 5.7. (b) at intermediate to strong interaction strengths (strongly correlated regime), we report the emergence of strongly correlated ground states. The properties illustrated in Fig. 5.7 demonstrate the correlated

nature of the ground states [3].

Chapter 6

Summary

In summary, we have discussed artificially induced SO coupling in ultracold dilute atomic gases. Combined with an unprecedented controllability of interactions and geometry in ultracold atoms, this manipulation of SO coupling has opened an entirely new paradigm for studying strong correlations of quantum many-body systems under Abelian and non-Abelian gauge fields. In this thesis, we theoretically investigated the ground state and collective excitations of a two-component Bose gas in a two-dimensional harmonic trap, subject to Rashba SO coupling. Our work represents an important extension into the regime of non-Abelian gauge field in which the spin degrees of freedom play an essential role.

In Chapter 1, we presented an introduction to quantum gases and a broad motivation to do research in ultracold dilute atomic Bose and Fermi gases. In Chapter 2, we introduced the system under study and discussed the single-particle physics in the presence of Rashba SO coupling in a homogeneous system and in the presence of a harmonic trapping potential. We illustrated that the nature of solutions is fundamentally different in the two limits of small and large SO coupling strengths. In Chapter 3, we presented a detailed discussion of ground state phases in the presence of inter-atomic interactions, at parameters that correspond to weak correlations with large number of bosons. We analyzed the weakly correlated interaction regime at small and large SO coupling strengths with the mean-field theoretical approach.

In Chapter 4, we systematically derived the mean-field phase diagram as a function

of SO coupling and interatomic interaction strengths. We did this by solving the Bogoliubov equations and computing the collective excitation spectrum, since they constitute one of the main sources of information for understanding the physics of many-body systems. We also investigated the dynamical properties of the mean-field ground state and understood instabilities against both trap anisotropy and anisotropy in the SO coupling term.

In Chapter 5, we presented the ground state phase diagram in the regime of strong interatomic interaction strengths and large SO coupling strengths using Exact Diagonalization scheme. We identified that the energy spectra is *nearly flat* at large SO coupling strengths. In such a scenario, the presence of inter-particle interactions allows for the emergence of ground states with distinct topological, symmetry and correlation properties. We analyzed the ground state properties using various techniques namely – energy spectrum, density distribution, single-particle density matrix, pair-correlation function, reduced wavefunction, entanglement spectrum, and entanglement entropy. Each technique was shown to offer its unique perspective to the overall understanding of the ground state properties. At small particle numbers, we illustrated the topological and symmetry properties of ground states. In the relatively large particle number scenario, we observed that the ground states fell into two distinct regimes: (a) at weak interaction strengths (*mean-field-like* regime), we observed ground states with topological and symmetry properties that are also obtained via mean-field theory computations; (b) at intermediate to strong interaction strengths (*strongly correlated* regime), we reported the emergence of strongly correlated ground states.

Looking ahead, it would be interesting to inquire if the strongly correlated ground states that emerge in the *nearly flat* energy spectra would eventually allow for the

manifestation of bosonic analogues of topological insulators predicted to occur in traditional condensed matter systems. We emphasize that in our system of trapped bosons, quantum statistics makes it impossible to fill up the lowest generalized Landau level. This results in the absence of 'sharp boundaries', which in-turn obviates the occurrence of states with topological order [3]. However, this fundamental roadblock may be circumvented when we consider a system of SO coupled bosons or fermions in specially engineered optical lattices [148]*. Furthermore, several challenges remain in the experimental realization of various SO coupling schemes in ultracold quantum gases.

Taking cues from history, we can be optimistic that the theoretical and experimental challenges will be overcome as we march ahead. In scientific pursuits, as in several major endeavors, collaborations will remain the key to success!

*In Ref. [148], the authors propose to realize topological phases emerging from single-particle Hamiltonian in optical lattices.

Part

Appendix

Appendix A

Mixture of Bose and Fermi superfluids*

Ultracold atom experiments offer the unique opportunity to study mixing of different types of superfluid states. Our interest is in superfluid mixtures comprising particles with different statistics – Bose and Fermi. Such scenarios occur naturally, for example, in dense QCD matter. Interestingly, cold atomic experiments are performed in traps with finite spatial extent, thus critically destabilizing the occurrence of various homogeneous phases. Critical to this analysis is the understanding that the trapped system can undergo phase separation, resulting in a unique situation where phase transition in either species (bosons or fermions) can overlap with the phase separation between possible phases. Here, we illustrate how this intriguing interplay manifests in an interacting 2-species atomic mixture – one bosonic and another fermionic with two spin components – within a realistic trap configuration. We further show that such interplay of transitions can render the nature of the ground state to be highly sensitive to the experimental parameters and the dimensionality of the system.

A.1 Introduction

Ultracold trapped-atom experiments offer the unique possibility to understand many-body physics beyond what can be explored in typical condensed matter settings [27]. Essentially, they provide clean many-body systems in which attributes like den-

*Appendix A taken largely from our publication in Ref. [4].

sity, dimensionality and interactions, may be controlled with commendable precision [5, 16, 17, 149–152]. As a result, from a theoretical perspective, there are broadly two kinds of challenges: (**1**) investigate configurations appropriate for emulating many-body theory models, thereby allowing for a systematic verification of claims made in the condensed matter context, and (**2**) investigate new configurations extremely difficult to realize in material settings. While the former program has proved quite successful with demonstrations of, for example, Mott insulator to superfluid transition with ultracold ^{87}Rb atoms in an optical lattice [67], the latter is just beginning to attract attention with several new experiments comprising degenerate mixtures of bosons and fermions, of same or different species being set up [153–156]. A potentially rich scenario in this context is provided by an atomic mixture comprising superfluids of two kinds- bosonic and fermionic. Studying this system may also have strong implications for, say nuclear physics, as a recent proposal investigates the intriguing possibility of simulating dense QCD matter with superfluid atomic mixtures [157]. Further, considering that in condensed matter setting, the analogous ^{3}He - ^{4}He superfluid mixture is difficult to realize*, achieving Bose-Fermi superfluid mixtures with ultracold atoms maybe an important step towards understanding corresponding occurrences in a broader context.

In analyzing experiments with ultracold Bose-Fermi mixtures, it is important to understand the effects of inhomogeneity due to traps. These effects are at the heart of determining the stability of possible thermodynamic phases in a given experiment. To this end, we construct the finite-temperature phase diagram of an interacting 3-dimensional (3D) mixture comprising of two fermions (spin $\uparrow$ & $\downarrow$) of one species and

*Experimental realization has not been possible due to extremely low superfluid transition temperature of ^{3}He.

a bosons of another. To draw such a phase diagram, it is important to understand the interplay between the following two phenomena: (**1**) phase transition that occurs near a critical temperature where suddenly an order parameter corresponding to one of the species nucleates. In fact, the critical temperature of such a transition may itself depend intricately on the state of the second species. Moreover, the already nucleated phase may subsequently be drastically affected in a certain region of trap due to the nucleation of a new phase, corresponding to the second species, as the system is further cooled and crosses below a lower critical temperature. (**2**) phase separation between possible phases, a phenomenon unique to trapped configurations. It also implies that the trap potential can simultaneously accommodate one or more of the phases as determined by the experimental parameters. Thus, remarkably what phase/phases will be observed will critically depend on the trap geometry. This, in fact is a very important observation implying the possibility of tuning the trap parameters such that a desired density profile is observed only if a certain phase has nucleated. On top of all this, the dimensionality of the trapped system, whether we consider a 3D or a 1D trap, will also largely determine what phase is energetically favorable for phase separation.

While various possibilities discussed above exist and some insight may be borrowed from previous studies on pure Bose and Fermi superfluids, the intrinsically new nature of Bose-Fermi superfluid mixtures strongly motivates us to derive a framework within which an elaborate finite temperature phase diagram can be generated. Also, such finite temperature studies comprising interacting fermions have never been performed in the past. The chapter is organized as follows. In Sec. A.2, we first review the theory for analyzing the thermodynamic instabilities of the Bose-Fermi mixture. While the technique is quite standard and maybe found elsewhere, to our knowledge this is

the first instance where it has been applied for deriving the finite temperature phase diagram of the inhomogeneous mixture comprising of bosons and fermions, both in the superfluid phase. As discussed in the previous paragraphs, the trap introduces multiple scenarios that are new to these systems making the analysis complicated. Therefore as a warmup, in Sec. A.3.1 we illustrate our method by first considering the simplest case of the $T = 0$ superfluid mixture in 3D. The finite temperature phase diagram for the 3D Bose Fermi mixture will be derived in Sec. A.3.2. Finally, in Sec. A.4, we will discuss the implication of the phase diagram for a *trapped* Bose-Fermi mixture by introducing a spatially varying chemical potential in the spirit of a Local Density Approximation (LDA), followed by brief discussion of the dependance on dimensionality in Sec. A.5.

A.2 Theory

We begin by writing the Hamiltonian for the interacting Bose-Fermi mixture in the form

$$\hat{H} = \underbrace{\hat{H}_b - \mu_b \hat{N}_b}_{\hat{\mathcal{H}}_b} + \underbrace{\hat{H}_f - \mu_f \hat{N}_f + U_{bf} \hat{N}_b \hat{N}_f}_{\hat{\mathcal{H}}_{bf}}, \tag{A.1}$$

where the subscript b (f) stands for bosons (fermions), μ's represent corresponding chemical potentials, $\hat{N}$'s the corresponding number operators and U_{bf} denotes the interaction energy between bosons and fermions. Our interest is in studying this interacting Bose-Fermi mixture in the vicinity of the superfluid critical temperature T_c of the fermions. Of course, it is true that the T_c itself will be modified due to the presence of Bose component. Further, the phase of fermions may modify the critical temperature for the condensation of the Bose component, T_{BEC}. Thus, while the general problem is indeed complicated, we focus our attention on the situation when

T_{BEC} is much greater than T_c, typically the case in most trapped experiments*. This allows us to work in the Thomas-Fermi limit of the Bose component by neglecting its kinetic energy. We represent the contact interaction strength between a pair of bosons as $\lambda_b = U_b V = 4\pi\hbar^2 a_b/m$, where U_b is the interaction energy of bosons, V is the volume, a_b is the s-wave boson-boson scattering length, assumed to be positive implying repulsive interactions, and m is the mass of bosonic atom. For large boson number N_b, total pairs of bosons is approximately $N_b^2/2$ and hence, $\hat{H}_b$ is simply a constant given by $U_b N_b^2/2$. Thus, the contribution to the free energy density arising from just the bosonic component is

$$f_b = \langle \hat{\mathcal{H}}_b \rangle = \lambda_b \frac{n_b^2}{2} - \mu_b n_b, \tag{A.2}$$

where $n_b = N_b/V$ is the boson density.

Now, we focus on the $\hat{\mathcal{H}}_{bf}$ part of the Hamiltonian and write it explicitly in second quantized form as

$$\hat{\mathcal{H}}_{bf} = \sum_{k,\sigma} (\varepsilon_k - \mu_f)\, c^\dagger_{k,\sigma} c_{k,\sigma} + \lambda_f \sum_{k,k',q} c^\dagger_{k+q,\uparrow}\, c^\dagger_{-k,\downarrow} c_{-k'+q,\downarrow}\, c_{k',\uparrow} + \lambda_{bf}\, n_b \sum_{k,\sigma} c^\dagger_{k,\sigma} c_{k,\sigma}. \tag{A.3}$$

Here $\varepsilon_k = \hbar^2 k^2/2m$ and $c^\dagger_{k,\sigma}(c_{k,\sigma})$ is the creation (annihilation) operator for a fermion with momentum k and spin σ. Further, the boson-fermion interaction, which is typically short range, is described by a δ-potential contact interaction with strength given by $\lambda_{bf} = 2\pi\hbar^2 a_{bf}/\mu_m$, where a_{bf} is the corresponding s-wave scattering length and μ_m is the reduced mass of the boson-fermion system. Here we will confine our analysis to the repulsive regime with $a_{bf} > 0$. Similarly, we describe the fermion-

*An interesting proposal to make $T_c > T_{BEC}$ is considered by Onofrio *et al.* in Ref. [158].

fermion interaction by the contact interaction strength $\lambda_f = 4\pi\hbar^2 a_f/m$, where a_f is the corresponding s-wave scattering length. Here, since the interaction is s-wave, only unequal-spin fermions interact. Also, we are interested in the superfluid regime, which occurs for attractive interactions, thus we assume $a_f < 0$. Now, in the superfluid state with Bardeen-Cooper-Schrieffer (BCS)-type pairing (for instance, see Refs. [9, 159, 160]), the center-of-mass momentum, q, of the Cooper pair is set to zero allowing $\hat{\mathcal{H}}_{bf}$ to be simply

$$\hat{\mathcal{H}}_{bf} = \sum_{k,\sigma} \xi_k \, c^\dagger_{k,\sigma} c_{k,\sigma} - |\lambda_f| \sum_{k,k'} c^\dagger_{k,\uparrow} \, c^\dagger_{-k,\downarrow} c_{-k',\downarrow} \, c_{k',\uparrow}, \tag{A.4}$$

with $\xi_k = \varepsilon_k - \mu_f + \lambda_{bf} n_b$. One can immediately notice that this is just the usual BCS Hamiltonian with a modified chemical potential, hence can be diagonalized with the usual Bogoliubov transformation*. Firstly, defining the mean-field order parameter $\Delta = |\lambda_f| \sum_{k'} \langle c_{-k',\downarrow} \, c_{k',\uparrow} \rangle$ and its complex conjugate Δ^*, we write $\hat{\mathcal{H}}_{bf}$ as

$$\hat{\mathcal{H}}_{bf} \overset{M.F}{=} \sum_k \xi_k \big(c^\dagger_{k,\uparrow} c_{k,\uparrow} + c^\dagger_{k,\downarrow} c_{k,\downarrow} \big) + \frac{|\Delta|^2}{|\lambda_f|} - \big(\Delta^* \sum_{k'} c_{-k',\downarrow} \, c_{k',\uparrow} + \Delta \sum_k c^\dagger_{k,\uparrow} \, c^\dagger_{-k,\downarrow} \big) \tag{A.5}$$

Re-writing the above in terms of the *Nambu spinor* $\Psi^\dagger_k = (c^\dagger_{k,\uparrow}, c_{-k,\downarrow})$ and its hermitian conjugate Ψ_k, we have

$$\hat{\mathcal{H}}_{bf} = \sum_k \Psi^\dagger_k \begin{pmatrix} \xi_k & -\Delta \\ -\Delta^* & -\xi_k \end{pmatrix} \Psi_k + \sum_k \xi_k + \frac{|\Delta|^2}{|\lambda_f|} \, . \tag{A.6}$$

*For diagonalizing the mean-field Hamiltonian, we closely follow the arguments presented by Altland *et al.* in Ref. [161].

Now the Bogoliubov transformation immediately gives

$$\begin{aligned}\hat{\mathcal{H}}_{bf} &= \sum_k \left(\alpha^\dagger_{k,\uparrow}, \alpha_{-k,\downarrow}\right) \begin{pmatrix} E_k^+ & 0 \\ 0 & E_k^- \end{pmatrix} \begin{pmatrix} \alpha_{k,\uparrow} \\ \alpha^\dagger_{-k,\downarrow} \end{pmatrix} \\ &+ \sum_k \xi_k + \frac{\Delta^2}{|\lambda_f|}, \end{aligned} \tag{A.7}$$

where the eigenenergies are $E_k^\pm = \pm\sqrt{\xi_k^2 + \Delta^2}$ and Δ is assumed real*. The operator $\alpha^\dagger_{k,\uparrow}$ ($\alpha_{k,\uparrow}$) creates (annihilates) Bogoliubov quasiparticles that are distributed according to the Fermi-Dirac distribution $f_k = 1/(1 + e^{\beta E_k})$ with $\beta = 1/k_B\,T$. Thus the relevant thermodynamic potential is given by

$$\langle \hat{\mathcal{H}}_{bf} \rangle - TS = \sum_k (\xi_k - E_k) + \frac{\Delta^2}{|\lambda_f|} - \frac{2}{\beta}\sum_k \ln\left(1 + e^{-\beta\, E_k}\right) \tag{A.8}$$

where S is the entropy. The derivations and mean-field analysis presented henceforth is quantitatively exact only when the interactions are weak. Our analysis is only qualitatively correct in the strong interaction limit, where a strong-coupling theory presented along the lines of Ref. [162] would be quantitatively more accurate.

A.2.1 Free energy, equilibrium and dynamical stability conditions

Free energy density of the interacting mixture comprising of bosons and fermions, both in the superfluid state, can now be written from Eqns. (A.2) and (A.8):

$$f = \frac{\lambda_b n_b^2}{2} - \mu_b\, n_b + \sum_k (\xi_k - E_k) + \frac{\Delta^2}{|\lambda_f|} - \frac{2}{\beta}\sum_k \ln\left(1 + e^{-\beta\, E_k}\right).$$

*Even if Δ is not real and $\Delta = |\Delta| e^{i\phi}$, it can always be made real by the global gauge transformation [161].

As one can immediately notice, f depends on numerous parameters: interaction strengths $\lambda_{\{b,f,bf\}}$ (in-turn, the scattering lengths $a_{\{b,f,bf\}}$), particle densities $n_{\{b,f\}}$, chemical potentials $\mu_{\{b,f\}}$, BCS superfluid order parameter Δ and temperature T. It is quite evident that the phase space of this interacting mixture is huge and thus an exhaustive study is impossible. However, noticing the fact that not all of these parameters are independent, we adopt the following scheme that was first introduced by Bhongale *et al.* in Ref. [163], allowing us to investigate the experimentally relevant region of the phase space: (1) fix parameters λ_b, λ_{bf} and μ_f and perform our analysis at fixed values of T^*; (2) we project the multi-dimensional phase diagram in the $\{n_b, \Delta\}$ phase space; (3) the remaining dependent parameters μ_b, n_f and λ_f are determined by the equilibrium stability conditions to be derived below.

(1) First derivative conditions: First of these is the Gap equation obtained as the extremum of f with respect to Δ and provides the self-consistent value of the interaction strength parameter λ_f:

$$\frac{\partial f}{\partial \Delta} = 0 \implies \frac{1}{|\lambda_f|} = \sum_k \frac{1}{2\,E_k} \tanh\left(\frac{\beta E_k}{2}\right).$$

However, in three dimensions, the momentum sum in the above expression diverges, an artifact of the contact interaction approximation. This unphysical effect is easily eliminated by an appropriate regularizing prescription. One of the easiest and

*This choice is especially useful if we consider the bosons to be in a tight trap enclosed by the fermions in a larger trap.

convenient methods is to subtract the diverging piece:

$$\frac{1}{|\lambda_f|} = \frac{m}{4\pi\hbar^2|a_f|} = \sum_k \frac{1}{2\,E_k}\tanh\left(\frac{\beta E_k}{2}\right) - \frac{1}{2\,\varepsilon_k}. \tag{A.9}$$

Correspondingly, we upgrade the free energy f to the regularized $f_{\rm reg}$ such that the extremum condition automatically reproduces the regularized version of the Gap equation*

$$\begin{aligned} f_{\rm reg}(n_b,\Delta) &= \lambda_b\,\frac{n_b^2}{2} - \mu_b\,n_b + \sum_k(\xi_k - E_k + \frac{\Delta^2}{2\,\varepsilon_k}) \\ &\quad + \frac{\Delta^2}{|\lambda_f|} - \frac{2}{\beta}\sum_k \ln\left(1+e^{-\beta\,E_k}\right). \end{aligned} \tag{A.10}$$

The above step is essential for our case since we will be eventually interested not only in the stability of the Fermi system but that of the combined Bose-Fermi system. The presence of bosons affects the self-consistent value of λ_f, through the combination $\lambda_{bf}\,n_b$. Next we consider the variation with respect to the fermion chemical potential μ_f. This produces the familiar equation determining the fermion number density n_f:

$$\frac{\partial(f_{\rm reg} + \mu_f\,n_f)}{\partial\mu_f} = 0 \implies n_f = \sum_k 1 - \frac{\xi_k}{E_k}\tanh\left(\frac{\beta E_k}{2}\right). \tag{A.11}$$

Finally, the last of dependent parameters, the boson chemical potential μ_b is determined by minimizing $f_{\rm reg}$ with respect to the boson density. This leads to the modified Thomas-Fermi equation given by

$$\partial f_{\rm reg}/\partial n_b = 0 \implies \mu_b = \lambda_b n_b + \lambda_{bf} n_f. \tag{A.12}$$

*In 3D, the term $\sum_k(\xi_k - E_k)$ itself diverges and hence it is useful to add the term $\sum_k \Delta^2/2\,\varepsilon_k$. At equilibrium, the absolute value of free energy f remains unchanged due to regularization, since we have simply included terms $+\sum_k \Delta^2/2\,\varepsilon_k$ in $\sum_k(\xi_k - E_k)$ and $-\sum_k \Delta^2/2\,\varepsilon_k$ in $\Delta^2/|\lambda_f|$.

(2) Second derivative conditions: The second derivatives at the extremum points derived above provide the dynamical stability criterion for the mixture via positive definiteness of the Hessian matrix $\mathcal{M}$. The relevant Hessian matrix elements are:

$$\begin{aligned}
\mathcal{M}_{11} &= \frac{\partial^2 f_{\rm reg}}{\partial n_b^2} = \lambda_b - \lambda_{bf}^2 \sum_k \frac{\Delta^2}{E_k^3} \tanh(\frac{\beta E_k}{2}) - \frac{\beta}{2} \frac{\xi_k^2}{E_k^2} \,\mathrm{sech}(\frac{\beta E_k}{2})^2; \\
\mathcal{M}_{22} &= \frac{\partial^2 f_{\rm reg}}{\partial \Delta^2} = \sum_k \frac{\Delta^2}{E_k^3} \tanh(\frac{\beta E_k}{2}) - \frac{\beta}{2} \frac{\Delta^2}{E_k^2} \,\mathrm{sech}(\frac{\beta E_k}{2})^2; \\
\mathcal{M}_{12} &= \mathcal{M}_{21} = \frac{\partial^2 f_{\rm reg}}{\partial \Delta \, \partial n_b} = \lambda_{bf} \sum_k \frac{\Delta \, \xi_k}{E_k^3} \tanh(\frac{\beta E_k}{2}) - \frac{\beta}{2} \frac{\Delta \, \xi_k}{E_k^2} \,\mathrm{sech}(\frac{\beta E_k}{2})^2.
\end{aligned} \tag{A.13}$$

A.3 Finite temperature phase diagram

For illustrative purposes, we start with a brief discussion of the zero-temperature phase diagram. Throughout, we follow the scheme outlined in Sec. A.2.1 to construct all the phase diagrams.

A.3.1 Zero-temperature limit

This is simply derived by taking the $T = 0$ limit of Eqns. (A.9)-(A.13). In the phase diagram shown in Fig. A.1(a), the solid (green) curve represents the boundary of the dynamically stable region above it, separating the unstable region below. However, it is important to note that, in the phase diagram the interaction parameter λ_f is determined self-consistently from the Gap equation. Thus in any single experimental realization, only a small portion, corresponding to a fixed λ_f, of the above phase space is accessible. In our analysis, we choose a value of λ_f (corresponding to

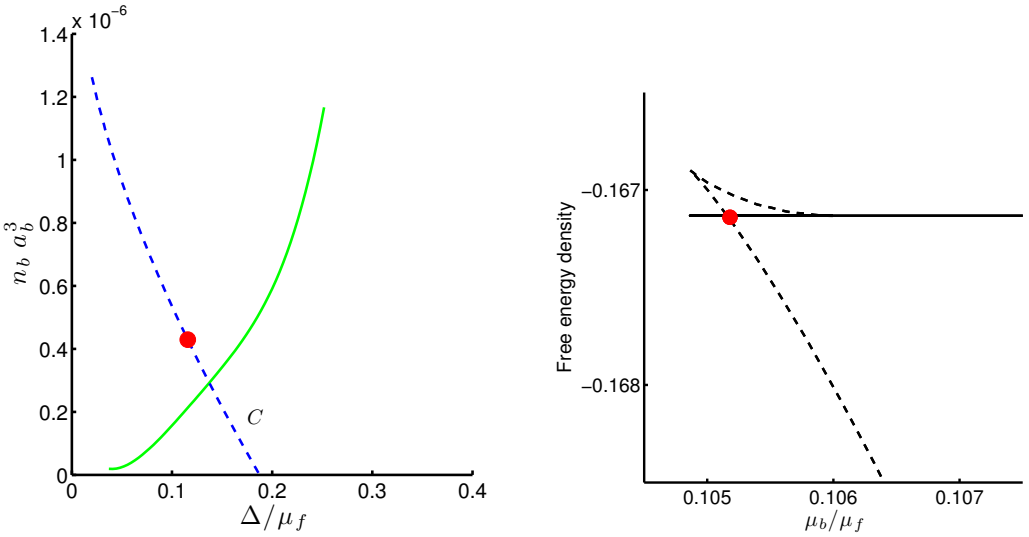

Figure A.1 : (Color online) (a)-(left): Phase diagram of the Bose-Fermi superfluid mixture at $T = 0^*$. Solid (green) curve is the dynamical stability contour while the dashed (blue) contour C denotes points in phase space with a fixed value of λ_f such that $T_c = 0.11\, T_f$. The filled (red) circle represents the critical point, for this specific experimental realization, at which the homogeneous mixture enters the dynamically and mechanically stable region. (b)-(right): Plot of the free energy densities of pure fermions (solid) and the homogeneous mixture (dashed) against $\mu_b[C]$. Free energy of homogeneous mixture is lower than that of pure fermions only beyond the critical point represented by the filled (red) circle. Here, free energy density is a dimensionless quantity[†]. Image from Ref. [4].

$1/k_f\, a_f = -1.10$) such that pure fermions are in the BCS superfluid regime. This corresponds to a BCS superfluid critical temperature of $T_c = 0.11\, T_f$, with T_f being the Fermi temperature[‡]. It is however important to note that $T_{c,\mathrm{mix}}$, the BCS transition temperature of fermions in the presence of bosons, is modified by the presence of

[†]Free energy density is made dimensionless by scaling with respect to the energy density of a 3D non-interacting gas occupying a volume of $1/k_f^3$ with fermi-momentum $k_f = 1/3200\, a_0$ and $m = 6\, amu$. Corresponding vales in the 1D limit are computed using the results of Olshanii in Ref. [164].

[‡]For the given range of λ_f, mean-field treatment overestimates T_c by about a factor of 2 as shown in Refs. [165] and [166]. However, Shin *et al.* in Ref. [167] report achieving temperatures in the range $T < 0.05\, T_f$. For the given value of $1/k_f a = -1.1$, the actual critical temperature, T_c, is definitely greater than $0.05\, T_f$ and hence represents a scenario already realized in current experiments.

the factor $\lambda_{bf}\, n_b$ in the effective fermion chemical potential. Further, the dependence is such that $T_{c,\mathrm{mix}} \leq T_c$ and the equality is satisfied when $\lambda_{bf} n_b \to 0$.

Points in the phase space that correspond to this fixed value of λ_f is shown by the dashed (blue) contour C in Fig. A.1(a). The crossing of this contour with the dynamical stability contour indicates the phase space point at which the homogeneous mixture enters the dynamically stable region. However, for the homogeneous mixture to be the stable ground state, mechanical stability condition should also be satisfied on top of the dynamical stability condition. This additional criterion is exclusively present due to the spatial inhomogeneity intrinsic in trapped-atom setups. By mechanical stability, we mean that the free energy of the homogeneous mixture should be less than the free energy of the pure bosonic phase or the pure fermionic phase along the contour C. The value of the latter is a constant, since λ_f is fixed along C. Free energy of pure bosons along C is given by

$$f_b[C] = -\frac{\mu_b^2[C]}{2\,\lambda_b} \tag{A.14}$$

where, $\mu_b[C]$ is the boson chemical potential along C.

The plot of Fig. A.1(b) shows the comparison of free energies mentioned above. The free energy of the pure fermionic phase and that of the homogeneous Bose-Fermi mixture along C are represented by the solid and the dashed lines respectively. The free energy of pure bosons is much higher than the others and hence bosons do not phase separate out of the mixture. Actually this observation is a general property of the phase space of a 3D Bose-Fermi mixture. The filled circle (red) represents the critical point along contour C, at which the free energy of the homogeneous mixture is lower than that of pure fermions, i.e., the critical point at which the homogeneous

mixture enters a region of both dynamical and mechanical stability. This implies that, for the specific experimental realization considered here, up until this critical point pure fermions phase separate out of the mixture, while above the critical point the Bose-Fermi superfluid exists as a stable mixed phase.

A.3.2 Finite-temperature scenario

We begin the discussion of the finite temperature case by first emphasizing some of the generic aspects of such a phase diagram as depicted in the schematic of Fig. A.2.

A.3.2.1 Generic features

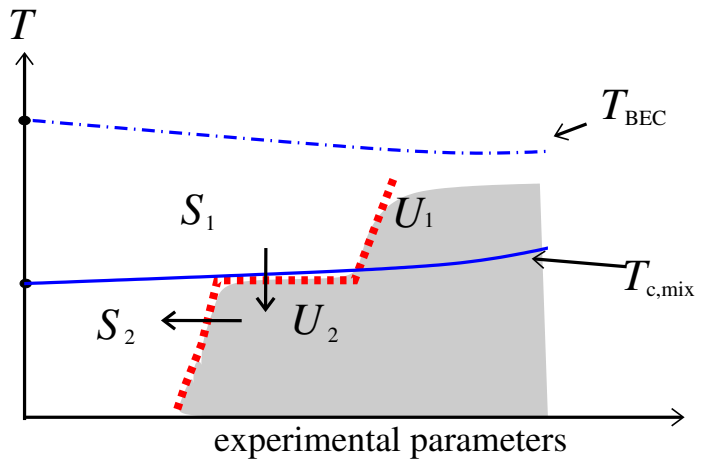

Figure A.2 : (Color online) Schematic depicting possible first-order transitions occurring in Bose-Fermi mixtures across $T_{c,\mathrm{mix}}$. Horizontal axis denotes the $\mathbb{R}^5$ phase space of experimental parameters defined by $\{\lambda_b, \lambda_{bf}, \mu_f, n_b, \Delta\}$. Image from Ref. [4].

Similar to the above illustration of the zero-temperature limit, we analyze the stability of the superfluid Bose-Fermi mixture in the vicinity of BCS critical temperature for a wide range of temperature and other parameter values. As mentioned earlier in Sec. A.2.1, the phase space is huge (5-dimensional) allowing for complicated

boundaries between stable (S_i) and unstable (U_i) regions of the homogeneous mixture. Before proceeding to the detailed quantitative finite temperature phase diagram in Fig. A.3, we therefore summarize our findings by pointing out the broad features, as depicted in Fig. A.2. In a certain projected subspace, the homogeneous Bose-Fermi mixture becomes dynamically and/or mechanically unstable towards phase separation through a first-order transition $S_1 \rightarrow U_2$, when cooled across $T_{c,\mathrm{mix}}$. The tunability of experimental parameters further allows us to access the $U_2 \rightarrow S_2$ transition at some fixed temperature below $T_{c,\mathrm{mix}}$. We also observe the existence of a parameter regime where the homogeneous mixture remains unstable across $T_{c,\mathrm{mix}}$ going from $U_1 \rightarrow U_2$. If fermions phase separate out of the unstable regions, then along the phase space boundary between U_1 and U_2, and that between U_2 and S_1, $T_{c,\mathrm{mix}}$ is essentially T_c. Thus, in short, the Bose-Fermi mixture exhibits rich mixing-demixing physics in the vicinity of the BCS critical temperature. Particularly interesting is the parameter regime exhibiting the first-order transitions $S_1 \rightarrow U_2 \rightarrow S_2$, which shows how the already condensed bosons affect the nucleation of fermions when cooled across the critical temperature, thereby clearly indicating direct implication for the observation of Fermi superfluidity in trapped mixtures. We therefore address this part of the phase space in more detail.

A.3.2.2 Quantitative features

For temperatures $T > T_{c,\mathrm{mix}}$ before the onset of BCS superfluidity, $\Delta = 0$ and hence we are confined to the n_b axis. Correspondingly, the free energy and the stability conditions of the homogeneous Bose-Fermi mixture are given by simply substituting $\Delta = 0$ in Eqns. (A.9)-(A.13). For the parameter space under investigation, we find that the homogeneous mixture is always the stable ground state in this temperature

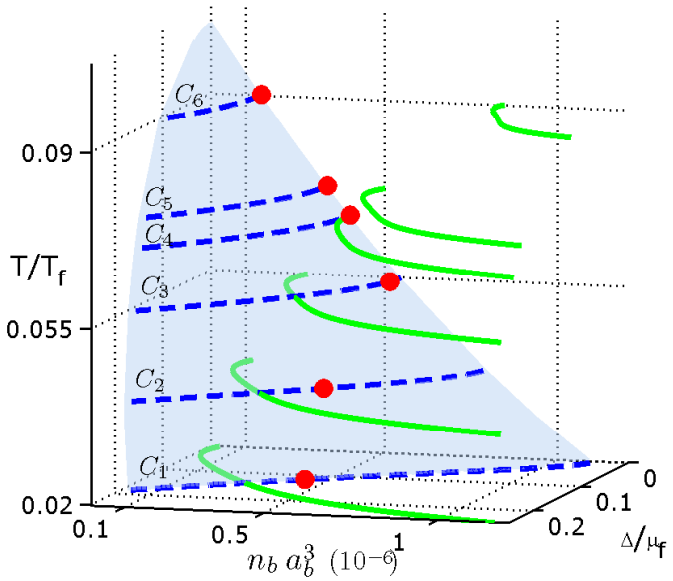

Figure A.3 : (Color online) Phase diagram of the Bose-Fermi superfluid mixture at temperatures $T_c > T$. Solid (green) curves show dynamical stability criteria and the (blue) surface represents points of fixed λ_f, such that $T_c = 0.11\ T_f$. Dashed (blue) curves C_i are contours of fixed temperature T_i along this surface and (red) circles indicate critical points at which the homogeneous mixture enters the region of both dynamical and mechanical stability. Image from Ref. [4].

regime. On the other hand, at temperatures $T < T_{c,\mathrm{mix}}$, the onset of BCS superfluidity in fermions is characterized by a non-zero value of Δ. In Fig. A.3, we plot the phase diagram for a wide range of temperatures below T_c to observe that the mixture is dynamically stable only above the solid (green) curves at a given temperature. Thus the presence of an all-stable homogeneous phase above $T_{c,\mathrm{mix}}$ and a mixture of unstable/stable phases below $T_{c,\mathrm{mix}}$, as seen in Fig. A.3, depicts the unambiguous manifestation of $S_1 \to U_2 \to S_2$ transitions.

Now we can immediately recognize the significance of this phase diagram for a realistic experimental situation. Again, just like the $T = 0$ case, only a small part of the stable phase space, corresponding to a fixed value of λ_f, is accessible in a

particular experimental realization. This we indicate by the two-dimensional surface shown in Fig. A.3, for our chosen value of λ_f such that the fermions are in the BCS superfluid regime. The dashed lines C_i's are contours connecting phase space points on this surface with fixed temperatures T_i's. The crossing of contours C_i's with dynamical stability contours indicates the phase space points at which the mixture enters the dynamically stable region. The filled circles represent critical points at which the homogeneous Bose-Fermi superfluid mixture becomes the stable ground state, i.e., both dynamically and mechanically stable. We observe their occurrence to transpire in two different ways: (1) In C_1-C_4, critical points occur in the dynamically stable region where the mixture also attains mechanical stability (as illustrated in Sec. A.3.1). (2) Along C_5 (C_6), the BCS transition temperature monotonously reduces with Δ by such an extent that when $\Delta \to 0$, $T_{c,\mathrm{mix}} < T_5$ (T_6). However as discussed before, the mixture is always the stable ground state for $T_{c,\mathrm{mix}} < T$. Hence in C_5-C_6, the critical points are given by their intersections with Δ=0 plane. Thus along each C_i, below these critical points the homogeneous mixture becomes dynamically and/or mechanically unstable. We further find that in the unstable regions, pure fermions phase separate from the mixture. Thus in Fig. A.3 we clearly demonstrate the occurrence of temperature-driven mixing-demixing transitions at fixed interaction strengths.

A.4 Trap profiles within LDA

We now show the direct experimental implications of the above phase stability analysis. This, we do by reliably translating this analysis to the inhomogeneous case via Local Density Approximation (LDA) by defining a position dependent chemical potential $\mu_b(\mathbf{r}) = \mu_b - V_{\mathrm{trap}}(\mathbf{r})$, where $\mu_b(\mathbf{r})$ is the local chemical potential and $V_{\mathrm{trap}}(\mathbf{r})$

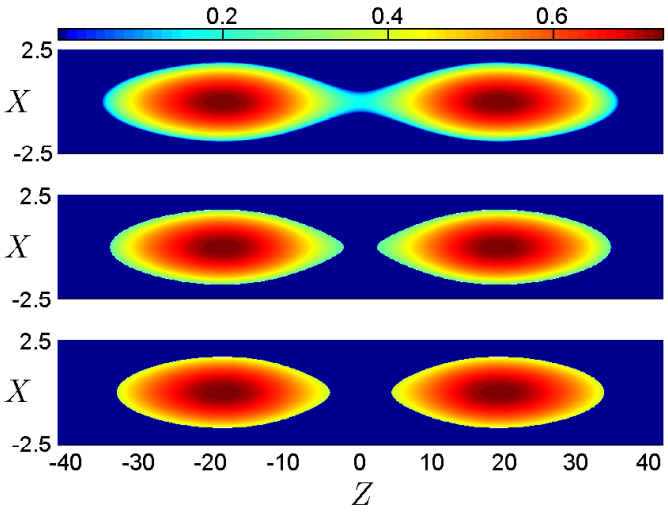

Figure A.4 : (Color online) Subplots top, middle and bottom show boson density profiles (slice along y=0 plane) computed within the LDA for temperatures T = 0.13, 0.072, 0.055 T_f respectively, with T_c=0.11 T_f. μ_b is adjusted to ensure number conservation (∼42000 atoms). X, Z are in μm. Color bar shows density variations in scale of $n_b a_b^3$ (10^{-6}). Chosen trap parameters V_0 (several mW), σ=12 μm and $\omega_z/\omega_\perp$=0.08. Image from Ref. [4].

is the trap potential for bosons [16]. While this approximation is known to be very efficient for large densities (typically the case in trapped-atom experiments), it also implies that the trap potential can simultaneously accommodate one or more of the phases discussed above. Thus, remarkably what phase/phases will be observed will critically depend on the trap geometry. This in fact, is a very important observation implying the possibility of tuning the trap parameters such that a desired density profile is observed only if a certain phase has nucleated.

To illustrate this program, let us consider bosons to be in a tightly confined trap surrounded by the Fermi gas in a larger trap*, a scenario that takes advantage of our framework to consider a homogeneous Fermi gas with fixed μ_f. Additionally, this

*The general idea of controlling trap geometries was highlighted in Sec. 2.2.

consideration is completely justified as the trapping potential for each species can be independently controlled [153, 154]. After careful analysis of the phase diagram in Fig. A.3, we find it advantageous to confine bosons in a trap with a finite barrier near the center. As this also helps to enhance the contrast in imaging the nucleated phases, we propose a double-well cigar shaped trap with a potential

$$V_{\rm trap}(\mathbf{r}) = \frac{1}{2}m\omega_{\perp}(x^2+y^2) + \frac{1}{2}m\omega_z z^2 + V_0 \exp(-\frac{z^2}{2\sigma^2})$$

to confine bosons, where $\omega_{\perp}$ (ω_z) is the trap frequency in the transverse (longitudinal) direction to the Gaussian beam creating the trapping potential. V_0 and σ, defining the barrier peak and beam-width respectively, are chosen to ensure a readily detectable overlap of boson density profiles from the two wells for $T = 0.13\,T_f$ (i.e., $T_c < T$), as shown in the top plot of Fig. A.4. At $T = 0.072\,T_f$ ($0.055\,T_f$), phase stability analysis along contour C_5 (C_3) in Fig. A.3 indicates the existence of a critical boson density (and correspondingly a critical boson chemical potential $\mu_b(r)$), only above which the Bose-Fermi mixture homogeneously co-exists as the stable ground state. Corresponding regions of the trap where this condition is not satisfied are devoid of bosons in a drastic fashion, as seen from the $\sim$4 μm (8 μm) gap between the separated bosonic islands in Fig. A.4. As these separation lengths are far greater than the healing length of the condensate, this illustration vividly shows how crucial aspects of the finite temperature phase diagram readily translate into detectable signatures in experiments. Furthermore, this particular signature in Fig. A.4 may be used as a signal indicating the onset of BCS superfluidity in the particular parameter regime of the attractive Fermi gas.

A.5 Effect of dimensionality on the phase diagram

As a final piece, we analyze how the phase diagram gets modified when only the trap geometry of the experimental setup is deformed (all other parameters kept constant) such that the confinement in two orthogonal directions is made much tighter compared to that in the third*. In effect, the system can be considered to be one-dimensional if the trapping frequency in the tight directions is such that $\hbar\,\omega_{\rm tight} \gg \mu_{b,f}$. For simplicity, we restrict ourselves to the $T = 0$ limit, where all the qualitative features can be comprehensively discussed† The effective 1D interaction strength can be written in terms of the 1D scattering length, which in turn can be easily related to the 3D scattering length‡ [164]. This mapping is critically dependent on the aspect ratio of the trap. We choose experimentally relevant values for $\omega_\perp$ and ω_z§. While we assume $\omega_\perp \simeq 2\,\pi\,10^5$ Hz for both bosons and fermions, we find it useful to consider $\omega_\perp/\omega_z \simeq 10^3$ for fermions but smaller values of $\omega_\perp/\omega_z$ for bosons. Apart from ensuring that we are indeed in the 1D regime, this choice guarantees a highly elongated trapping potential for fermions. From the parameter values used in deriving the 3D phase diagram of Fig. A.1(a), we obtain the corresponding values for the 1D scenario [164].

We thus construct the phase diagram of the interacting one dimensional superfluid mixture, by performing the 1D integrals instead of 3D in Eqns. (A.9)-(A.13). The phase diagram is shown in Fig. A.5(a), where the solid (green) curve represents the dynamical stability contour that separates the dynamically unstable region (inside

*The general idea of controlling trap dimensionality was highlighted in Sec. 2.2.

†Phase diagram of the Bose-Fermi superfluid mixture in 1D at $T = 0$ was already discussed by Bhongale *et al.* in Ref. [163].

‡Also, we assume here that the regularization performed in determining fermion-fermion interaction strength λ_f in 3D has no effect on the corresponding 1D effective strength $\lambda_{1d\,f}$.

§Say, as discussed by Liao *et al.* in Ref. [30].

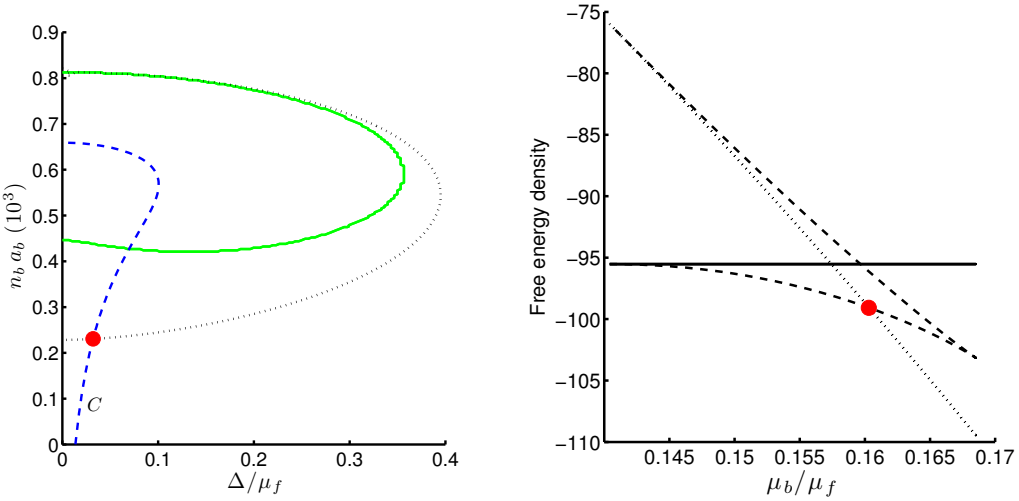

Figure A.5 : (Color online) (a)-(left): Phase diagram of the Bose-Fermi superfluid mixture in 1D at $T = 0$ (for the same parameters used in Fig. A.1(a)). Solid (green) curve is the dynamical stability contour, while the dashed (blue) contour C denotes phase space points with a fixed value of $\lambda_{1D\,f}$. The dotted (black) curve represents the region within which the homogeneous mixture is mechanically unstable. The filled circle (red) represents the critical point, for this specific experimental realization, at which the homogeneous mixture enters the mechanically unstable region. (b)-(right): Plot of the free energy densities of pure bosons (dotted), of pure fermions (solid) and the homogeneous mixture (dashed) against $\mu_b[C]$. Free energy density of homogeneous mixture becomes higher than that of pure bosons at the critical point represented by the filled (red) circle, resulting in the phase separation of pure bosons out of the mixture. Here, free energy density is a dimensionless quantity*. Image from Ref. [4].

the ellipse) from the dynamically stable region (outside the ellipse). Phase space points that correspond to the fixed value of $\lambda_{1d\,f}$, are shown by the dashed (blue) contour C. The crossing of C and the dynamical stability contours indicates the point at which the homogeneous mixture enters the dynamically unstable region. However, as discussed before in Sec. A.3.1, for the Bose-Fermi homogeneous mixture to be stable, it is necessary that the mechanical stability condition be simultaneously

*See footnote associated with Fig. A.1(b) and the work by Olshanii in Ref. [164].

satisfied. For this, we plot the relevant free energies in Fig. A.5(b), where the free energies of pure bosons, homogeneous mixture and pure fermions along C are given by dotted, dashed and solid lines respectively. We immediately note that pure fermions can never phase separate out of the mixture, a remarkably different result when compared to the 3D case [see Fig. A.1(b)]. The filled circle (red) represents the critical point along contour C, at which the free energy of the bosons becomes lower than that of the homogeneous mixture, i.e., the critical point at which the homogeneous mixture becomes mechanically unstable. This means that up until this critical point, homogeneous superfluid mixture coexists as the stable ground state. However, above this critical point pure bosons phase separate out of the mixture. The significance of this critical point is clear since we can now directly obtain the boson density profile in the boson trap by mapping the boson chemical potential $\mu_b[C]$ onto the spatial coordinate in the trap via LDA using $\mu_b[C] = \mu_b(r) = \mu_b - V(r[C])$, where $V(r)$ is the probe trapping potential for the bosons. It is evident from Figs. A.5(a) and A.5(b) that the pure bosons phase separate out of the homogeneous mixture in the trap above the critical value of boson chemical potential μ_b corresponding to the critical point (filled red circle).

A.6 Conclusions

In summary, we have discussed a consistent theoretical method for performing the finite temperature phase stability analysis of an ultracold mixture comprising of bosons and fermions, both in the superfluid regime. Based on our stability analysis in the vicinity of the Fermi superfluid temperature, we discussed two distinct scenarios where the homogeneous superfluid mixture becomes unstable (**1**) when the normal-superfluid phase transition (second-order) occurs in the fermionic component,

and (**2**) below the Fermi superfluid temperature via mechanical instability which is a first-order phase-separation phase transition. The latter scenario happens exclusively due to the trap inhomogeneity inherent in trapped-atom experiments, thereby allowing for the two phases to be simultaneously present. We have illustrated the emergence of these instabilities and the ensuing phase separation by considering a realistic experimental setting. We fine-tuned the trap geometry to enhance the effect of phase separation. Finally, we briefly discussed the effect of dimensionality on the stability of various phases. We reiterate that while our phase diagram analysis is quantitatively exact when the interactions are weak, our study is only qualitatively correct in the strong interaction limit.

We emphasize here that the interplay between the first and second order phase transitions, similar to that discussed in this paper, will have strong implications for analyzing experimental observations involving ultracold mixtures in general*. While our framework is also valid to study the regime of strong interactions near a broad Feshbach resonance, it can be easily extended within a two channel model for the case of a narrow Feshbach resonance. Further, while such a treatment will naturally allow for a molecular condensate of Fermi atoms [171], it is not hard to speculate emergence of rich physics due to occurrence of Efimov bound states in the Bose-molecule interaction channel [172,173]. Finally, an important extension of the current work would be to consider spin-dependent Bose-Fermi interactions. The presence of a small BEC can shift the chemical potential of a particular spin component relative to the other. This is analogous to the situation encountered in solid-state samples

*Theoretical work by Baksmaty *et al.* in Ref. [168] based on extensive numerical calculation has confirmed a crucial role played by condensate nucleation and the resulting phase separation in a polarized Fermi gas. In this paper, the authors attribute such non-homogeneous nucleation as an explanation to the controversy between the MIT and Rice polarized Fermi gas experiments reported in Refs. [169] and [170] respectively.

with magnetic impurities, thereby providing a new platform for studying the interplay between superfluidity and magnetism.

Appendix B

Modeling condensate collapse and expansion in optical Feshbach resonance*

B.1 Introduction

The ability to tune interactions in ultracold atomic gases makes these systems ideal for exploring many-body physics [27] and has enabled some of the most important recent advances in atomic physics, such as investigation of the Bose-Einstein condensate (BEC)-Bardeen-Cooper-Schrieffer (BCS) crossover regime [27] and creation of quantum degenerate molecules [171, 174]. As discussed in Sec. 2.2, magnetic Feshbach resonances are now the standard tool for changing atomic interactions and have proven incredibly powerful [28]. However, they are also limited because the methods for creating magnetic fields preclude high-frequency spatial and temporal modulation. Also, in atoms with non-degenerate ground states, such as alkaline-earth-metal atoms, magnetic Feshbach resonances do not exist. These limitations can be overcome by using an optical Feshbach resonance (OFR), which tunes interatomic interactions by coupling a colliding atom pair to a bound molecular level of an excited state potential with a laser tuned near a photoassociative resonance [175].

Early experiments on OFRs [176–178] used strong dipole-allowed transitions in alkali-metal atoms to alter atomic collision properties, but substantial change in the atom-atom scattering length was accompanied by rapid atom losses. Tuning of in-

*Appendix B taken largely from our publication in Ref. [5]. Associated experiments were performed by M. Yan, B. J. DeSalvo, and T. C. Killian.

teractions in alkali-metal atoms, but with smaller atom loss, was recently obtained with a magnetic Feshbach resonance using an AC Stark shift of the closed channel to modify the position of the resonance [179]. Recently, a multiple-laser optical method was proposed for wider modulation of the interaction strength near a magnetic Feshbach resonance [180]. Unfortunately, none of these hybrid variations are feasible for atoms lacking magnetic Feshbach resonances [5].

Ciurylo *et al.* [151, 181] predicted that an OFR induced by a laser tuned near a weakly allowed transition should tune the scattering length with significantly less induced losses. This can be done even with divalent atoms (that lack magnetic Feshbach resonance), such as strontium and ytterbium, by exciting near an intercombination transition from the singlet ground state to a metastable triplet level*. The improved OFR properties result from the long lifetime of the excited molecular state and relatively large overlap integral between excited molecular and ground collisional wave functions [5].

Intercombination-transition OFRs have been used to modify the photoassociation (PA) spectrum in a thermal gas of Yb [182], modulate the mean field energy in a Yb BEC in an OFR-laser standing wave [183], and modify thermalization and loss rates in a thermal gas of ^{88}Sr [184]. In the OFR work with an Yb BEC [183], small detunings from a molecular resonance were used ($|\Delta| < 10\,\Gamma_{\rm mol}$, where $\Gamma_{\rm mol}$ is the natural decay rate of the excited molecular level), which led to short sample lifetimes on the order of microseconds. Longer exposure times and detunings $|\Delta| < 50\,\Gamma_{\rm mol}$ were used in thermal Sr gases [184], but at much lower atomic density than typically found in a degenerate sample. There is great interest in intercombination-line OFRs

*Foot in Ref. [12] and Chin *et al.* in Ref. [28] provide useful introduction to inter-combination lines transition.

at much larger detuning in quantum degenerate gases of divalent atoms [24,185–187], with the goal of modifying the scattering length and still maintaining sample lifetimes on the order of dynamical timescales of quantum fluids [188, 189].

Optical Feshbach resonances may open new avenues of research in nonlinear matter waves [190–192] and quantum fluids [188, 189, 193], and could be very valuable for experiments with fermionic alkaline-earth atoms [24, 194] in lattices [195], which possess SU(N) symmetry with large N and have attracted great attention lately because of novel thermodynamics [196–198] and predictions of frustrated magnetism and topological ground states [199–202]. With this broad motivation in mind, here we discuss details of a combined experimental and modeling effort to understand OFR in an ^{88}Sr BEC [5]. The rest of this chapter is organized as follows. We briefly summarize the experimental aspects to control the collapse and expansion of an ^{88}Sr BEC with an OFR near the $^1S_0$-$^3P_1$ inter-combination transition. Then, we present details of a theoretical model based on time-dependent non-linear Gross-Pitaevskii (GP) equation to understand condensate dynamics in the presence of OFR. We proceed to analyze and discuss the experimental results in detail based on this model. Finally, we summarize and present a brief outlook.

B.2 Experiment

We demonstrate control of the collapse and expansion of an ^{88}Sr Bose-Einstein condensate during time-of-flight measurements, using an OFR near the $^1S_0$-$^3P_1$ inter-combination transition at 689 nm. ^{88}Sr has an s-wave background scattering length of $a_{\rm bg} = -2\,a_0$ [203,204], which allows convenient modification of the scattering length either positive or more negative. Changes in scattering length are monitored through changes in the size of the condensate after a time-of-flight measurement. Significant

changes in dynamics are caused by modifications of scattering length by up to $\pm 10\, a_{\rm bg}$. Because the background scattering length is close to zero, blue detuning of the OFR laser with respect to a photoassociative resonance leads to increased interaction energy and a faster condensate expansion, while red detuning triggers a collapse of the condensate [5].

To probe the change in scattering length and loss, we monitor expansion of an ^{88}Sr BEC after release from the optical dipole trap (ODT) with time-of-flight absorption imaging using the $^1S_0$-$^1P_1$ transition. Details of the formation of an ^{88}Sr BEC are given by Mickelson *et al.* in Ref. [187]. We create condensates with about 7000 atoms, size $\sigma_0 = 0.8\,\mu$m, and peak density $n_0 = 1 \times 10^{15}\,\mathrm{cm}^{-3}$. About 10% of the trapped atoms are in the condensate and this represents about 95% of the critical number for collapse with the background scattering length of ^{88}Sr for our ODT, which is close to spherically symmetric with the geometric mean of the trap oscillation frequency $\overline{\omega} = 2\pi \times (60 \pm 5)\,$Hz [205]. The 689 nm OFR laser beam is tuned near the photoassociative transition to the second least bound vibrational level on the $^1S_0$+$^3P_1$ molecular potential, which has the binding energy of $h \times 24\,$MHz [206]. The OFR laser, with a beam waist of $725\,\mu$m, is applied to the condensate $20\,\mu$s before extinguishing the ODT and left on for a variable time τ during expansion [5]. The exposure time in the ODT is short enough that the initial density distribution of the condensate reflects the ODT potential and the background scattering length, while the expansion dynamics is sensitive to the interaction energy determined by induced changes to the inherent scattering length. We explore detunings $|\Delta|$ as large as $667\,\Gamma_{\rm mol}$ (absolute value), and obtain sample lifetimes of milliseconds during application of the OFR beam [5].

B.3 Theory

Our theoretical model is essentially based on the time-dependent GP equation introduced in Sec. **??**. However, the presence of laser beams to study optical Feshbach resonance necessitates two major modifications: (**1**) the inherent two-body contact interaction is modified (a_{opt} term) and (**2**) inelastic decay processes and the associated loss in atom number (K term) have to be accounted for in the presence of OFR laser beam. According to the isolated resonance model [151, 181], a laser of wavelength λ detuned by Δ from a photoassociative transition to an excited molecular state $|n\rangle$ modifies the atomic scattering length according to $a = a_{\rm bg} + a_{\rm opt}$ and induces two-body inelastic collisional losses described by the loss rate constant $K_{\rm in}$, where

$$\begin{aligned} a_{\rm opt} &= \frac{\ell_{\rm opt}\Gamma_{\rm mol}\Delta}{\Delta^2 + \frac{(\eta\Gamma_{\rm mol})^2}{4}}; \\ K_{\rm in} &= \frac{2\pi\hbar}{\mu}\frac{\ell_{\rm opt}\eta\Gamma_{\rm mol}^2}{\Delta^2 + \frac{(\eta\Gamma_{\rm mol}+\Gamma_{\rm stim})^2}{4}}. \end{aligned} \tag{B.1}$$

$K_{\rm in}$ is defined such that it contributes to the evolution of density n as $\dot{n} = -K_{\rm in}n^2$ for a BEC. The optical length $\ell_{\rm opt}$, which characterizes the strength of the OFR, is defined as

$$\ell_{\rm opt} = \frac{\lambda^3|\langle n|\varepsilon_r\rangle|^2 I}{16\pi c k_r}, \tag{B.2}$$

where c is the speed of light, I is the intensity of the OFR beam, and k_r is the wavenumber for colliding atoms, given by $k_r = \sqrt{21/8}/(2R_{\rm TF})$ for a BEC with Thomas-Fermi radius $R_{\rm TF}$, and $k_r = \sqrt{2\mu\varepsilon_r}/\hbar$ for a thermal gas, where $\mu = m/2$ is the reduced mass for the atomic mass m, ε_r is the kinetic energy of the colliding atom pair, and $\hbar$ is the reduced Planck constant [5]. $|\langle n|\varepsilon_r\rangle|^2$ is the Franck-Condon factor per unit energy for the free-bound PA transition. Because $|\langle n|\varepsilon_r\rangle|^2 \sim k_r$ in

the ultracold regime [207], following the Wigner threshold law, $\ell_{\rm opt}$ is independent of the collision energy. $\Gamma_{\rm mol} = 2\pi \times 15\,{\rm kHz}$ is the natural linewidth of the excited molecular level, and $\Gamma_{\rm stim} = 2k_r\ell_{\rm opt}\Gamma_{\rm mol}$ is the laser-stimulated linewidth [5]. The parameter $\eta > 1$ accounts for enhanced molecular losses, as observed in previous OFR experiments [177, 184].

As shown through coupled channels calculations [184], the isolated-resonance-model expressions (Eq. B.1) break down at large detunings from photoassociative resonance. The induced scattering length $a_{\rm opt}$ crosses zero between resonances. Outside approximately 100 linewidths from photoassociative resonance, the two-body loss is expected to make a transition to a broad background value that varies as $1/\delta^2$, where δ is 2π times the detuning from atomic resonance [184]. A rigorous theoretical description for loss in this regime is lacking, but the underlying mechanism is collisions involving a ground state atom and an atom excited in the wings of the atomic line [5]. In the regime where molecular levels are unresolved, such as in light-assisted collisions in a magneto-optical trap, this loss is often described with the classical Gallagher-Pritchard model [208]. In a coupled channels description, the background loss rate is sensitive to a cutoff atom-atom distance inside of which radiative loss is turned on, which is introduced as an *ad hoc* parameter. Our measurements could provide some experimental input to determine this cutoff distance [5]. We find the isolated-resonance-model expressions (Eq. B.1) useful for describing our measurements with the modification that the total loss rate constant is given by $K_{\rm total} = K_{\rm in} + K_{\rm b}$, where the background loss is described phenomenologically in our regime as $K_{\rm b} = K_0[\Gamma_{\rm mol}/(2\delta)]^2$ [5].

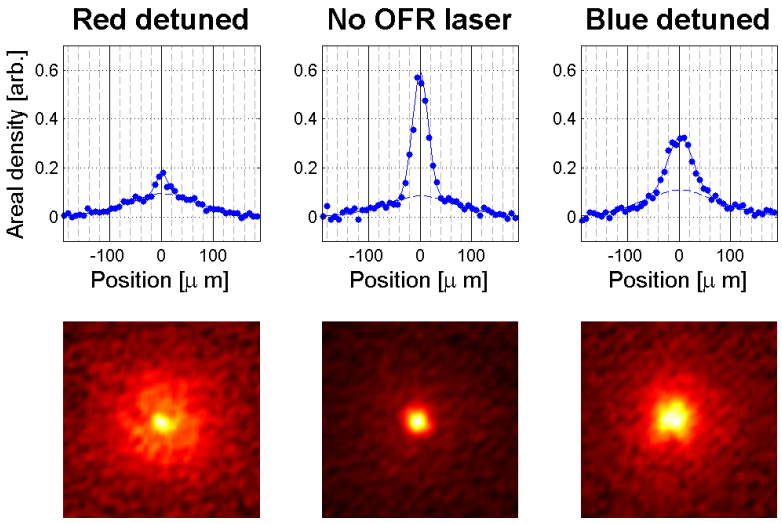

Figure B.1 : (color online) Line profiles through absorption images showing OFR-induced variation of BEC expansion. Data correspond to no OFR laser and an OFR laser blue and red detuned by 0.5 MHz with respect to the -24 MHz PA line [206] applied for $\tau = 1.2$ ms. Expansion times are 35 ms. Fits are a Bose distribution for the thermal atoms (- -) and a Gaussian density distribution for the BEC. Image from Ref. [5].

B.4 Results and discussion

Figure B.1 shows 1D slices through absorption images of atoms after a 35 ms time-of-flight with and without application of the OFR laser [5]. Absorption images measure the areal density, which is fit with a bimodal function including a Bose distribution for the thermal atoms and a narrow gaussian density distribution for the BEC, $n(r) = \frac{N_0}{2\pi\sigma^2} \exp\left[-\frac{r^2}{2\sigma^2}\right]$, to determine the number of atoms in the BEC N_0 and BEC size σ. (Quoted sizes reflect correction for imaging system resolution, which is modeled by a point spread function $L(r) = \frac{1}{2\pi s^2} \exp\left[-\frac{r^2}{2s^2}\right]$ with $s = 5 \pm 1\,\mu$m.) The condensate size after a long time of flight is a good probe of interactions because of the sensitivity to the initial interaction energy [5].

To obtain a qualitative understanding of the data, one can calculate the total energy immediately after the trap is extinguished using the condensate energy functional [26, 209] assuming a gaussian density for the BEC in the ODT with initial size σ_0 [5]. When atom losses are negligible, this energy can be equated to the total kinetic energy when the condensate has expanded to a low density to give,

$$N_0 \frac{3}{2} m\sigma_v^2 = N_0 \frac{3}{8} \frac{\hbar^2}{m\sigma_0^2} + N_0^2 \frac{g}{2(4\pi)^{3/2}\sigma_0^3}. \quad \text{(B.3)}$$

The first and second terms on the right-hand side are the kinetic energy and interaction energy in the trap before release, respectively, for $g = 4\pi\hbar^2 a/m$. σ_v is the rms velocity, which can be related to the BEC size after a long expansion time t through $\sigma = \sigma_v t$ [5]. A blue OFR laser detuning near the -24 MHz PA line [206] increases a, leading to more interaction energy and larger expansion velocity and BEC size. Red detuning produces the opposite behavior. When the the total energy becomes negative, this simple explanation breaks down, and one observes condensate collapse and significant loss of condensate atoms [5].

In Fig. B.2, we study the variation of the BEC size and number with the exposure time, τ, for several blue detunings of the OFR laser. We observe that several ms is required for full conversion of the interaction energy into kinetic, with larger detuning and smaller optically induced scattering length requiring longer τ. We can estimate the timescale for conversion with a hydrodynamic description of the condensate dynamics [26]. The acceleration of atoms during expansion arises from the interaction pressure $P = gn(r)^2/2$, and a characteristic acceleration $\tilde{a}$ can be approximated from $mn(r)\tilde{a} \approx -\nabla P \approx -n(r)\nabla[gn(r)]$ [5]. This yields $\tilde{a} = -\nabla[gn(r)]/m \sim gn_0/m\sigma_0$. In the large $N_0 a/a_{\rm ho}$ limit with $a_{\rm ho} = [\hbar/(m\overline{\omega})]^{1/2}$, one can neglect the kinetic-energy

term in Eq. B.3 to find the characteristic final velocity given by the conservation of energy, $v_f \sim \sigma_v \sim \sqrt{gn_0/m}$. This implies a conversion timescale, $v_f/\tilde{a} \sim \sigma_0\sqrt{m/(gn_0)}$, of 1 ms for $a_{\rm opt}$ of $10\,a_0$, which roughly matches observations [5]. Losses from single-atom light scattering preclude leaving the OFR beam on during the entire expansion time, and knowledge of the time required for close to full conversion is helpful for interpreting the results of experiments in which we apply the OFR laser for a fixed interaction time and vary the detuning, which will be discussed below [5].

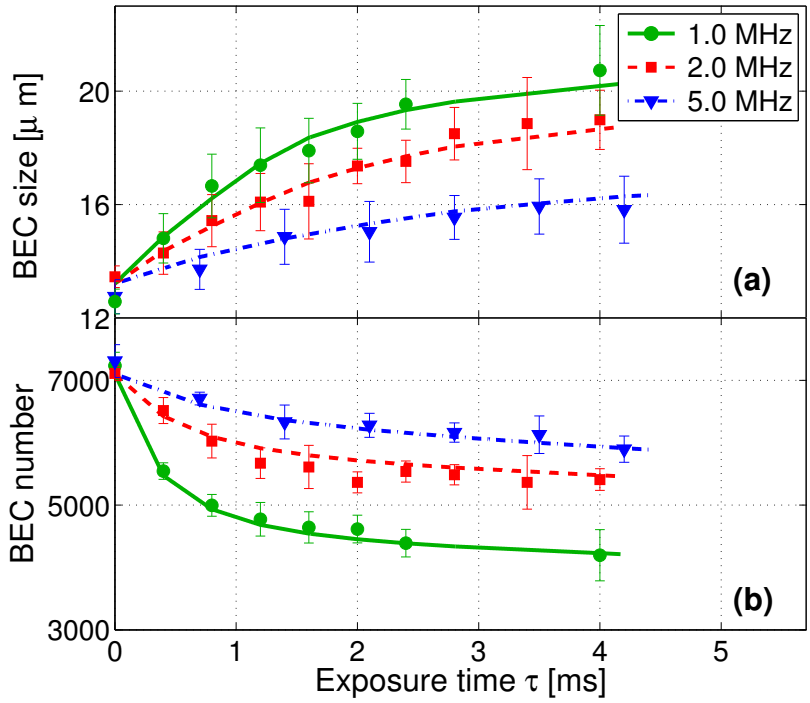

Figure B.2 : (color online) (a) BEC size after 35 ms of expansion versus the exposure time of the OFR laser with the intensity of $0.057\,\mathrm{W/cm^2}$ and three different detunings from the -24 MHz PA line. (b) Number of condensate atoms versus exposure time. Curves calculated by the Gross-Pitaevskii equation correspond to a combined fit of the data, yielding $\eta = 19.5$, $\ell_{\rm opt}/I = 2.2\times10^4\,a_0/(\mathrm{W/cm^2})$, and $K_0 = 5.8\times10^{-7}\,\mathrm{cm^3/s}$. Error bars represent the standard deviation of the mean from multiple measurements. Image from Ref. [5].

To quantitatively analyze the variation of size and atom number versus interaction time and extract OFR parameters, it is necessary to treat dynamics and atom loss with the time-dependent non-linear GP equation, including the effects of $a_{\rm opt}$, $K_{\rm total}$, and single atom light scattering, and neglecting effects of thermal atoms. The fit parameters are $\ell_{\rm opt}/I$, η, and K_0. The rate of atomic light scattering varies from 12 to $17\,{\rm s}^{-1}$, and is included in the simulation assuming every scattering event results in the loss of one atom [5].

The fits are shown in Fig. B.2. The data at largest detuning from photoassociative resonance strongly determine the background loss because loss from the OFR is small there [5]. The fit optical length is $\ell_{\rm opt}/I = (2.2 \pm 1.0) \times 10^4\, a_0/({\rm W/cm}^2)$, and the fit parameter $K_0 = (5.8 \pm 1.3) \times 10^{-7}\,{\rm cm}^3/{\rm s}$. Loss from the OFR is described by $\ell_{\rm opt}$ and $\eta = 19.5^{+8}_{-3}$, and there is strong anti-correlation between $\ell_{\rm opt}$ and η. The uncertainty is dominated by systematic uncertainty in the trap oscillation frequency and imaging resolution [5]. These results are in good agreement with the measured value $\ell_{\rm opt}/I = 1.58 \times 10^4\, a_0/({\rm W/cm}^2)$ and disagree slightly with $\ell_{\rm opt}/I = 8.3 \times 10^3\, a_0/({\rm W/cm}^2)$ calculated directly from knowledge of the molecular potentials [184].

Experiments with a thermal strontium gas [184] found larger losses associated with an OFR than described by theory, which was described by $\eta = 2.7$. These measurements probed the core of the photoassociative transition ($|\Delta| < 50\,\Gamma_{\rm mol}$). The additional loss is not well understood. We see a similar resonance width in a BEC when we significantly reduce the laser intensity and interaction time and take a photoassociative loss spectrum of this core region [5]. Our use of the OFR probes the distant wings ($50\,\Gamma_{\rm mol} < \Delta < 667\,\Gamma_{\rm mol}$), and a fit of the loss using the single resonance model requires an even larger value of η. We interpret the varying η values as meaning that the full spectrum of photoassociative loss, including the far wings,

is not well described by a Lorentzian [5].

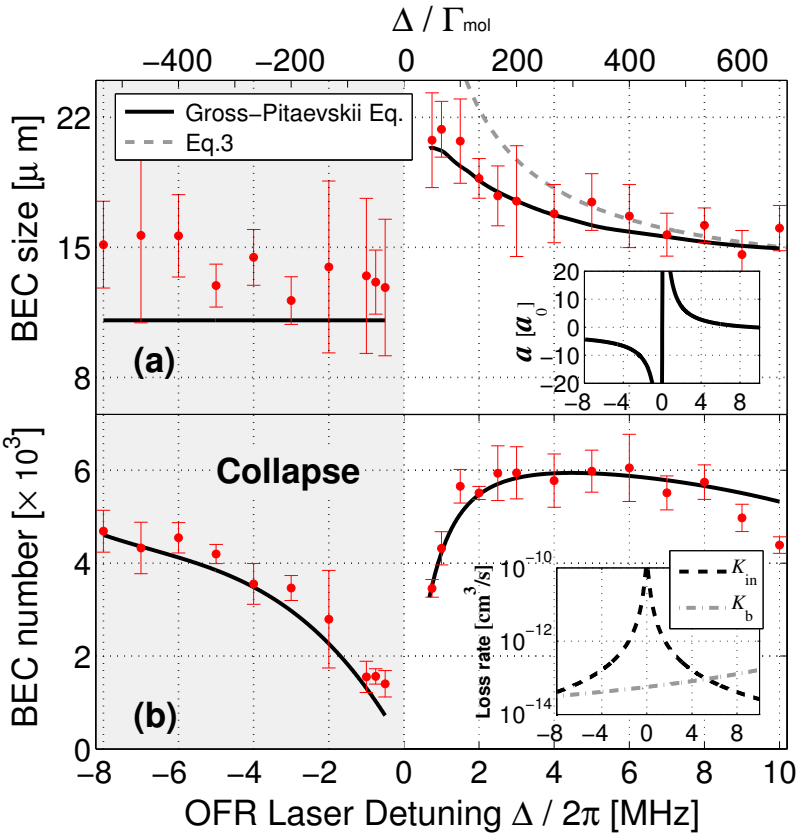

Figure B.3 : (color online) The BEC size(a) and number(b) versus the detuning with respect to the -24 MHz PA resonance for an intensity of $0.057\,\mathrm{W/cm^2}$. The OFR beam is applied for 4.0 ms, and the data are recorded after 35 ms of expansion. The insets give the total scattering length a and the loss rate constants. Image from Ref. [5].

The dependence of the BEC size and number on detuning from the -24 MHz PA line is shown in Fig. B.3 for a fixed intensity and interaction time $\tau = 4\,\mathrm{ms}$ [5]. The fit parameters from Fig. B.2 describe the data well over this range. Note that the number of atoms initially increases with blue detuning from PA resonance as the loss from the OFR (K_{in}) decreases. The number then slowly decreases because the background loss (K_{b}) increases approaching atomic resonance [5]. The BEC size data predicted

by Eq. B.3, which neglects atom loss and assumes that the OFR laser is applied long enough to fully convert interaction energy into kinetic, is also shown in Fig. B.3a. The difference between this curve and the data highlights that atom loss is significant during the conversion process at smaller detunings, and the Gross-Pitaevskii equation simulation is required to describe the data. A typical total scattering length (Fig. B.3a inset) is $a = 20\,a_0$ for $\Delta = 2\pi \times 1\,\mathrm{MHz} \simeq 67\,\Gamma_{\mathrm{mol}}$ [5].

For red detuning, the OFR laser makes the scattering length more negative and triggers a collapse of the condensate, which is evident as large loss in the plot of condensate number remaining after expansion (Fig. B.3b). The dramatic asymmetry of loss with respect to detuning from resonance shows that the loss must reflect condensate dynamics [210–212], not photoassociative loss directly caused by the OFR laser [5]. The GP equation provides a good description of the BEC number data for red detuning in spite of the fact that the collapse dynamics may contain beyond-mean-field effects [213] not taken into account in the GP formalism [5].

A variational calculation of the condensate energy functional as a function of condensate size [26, 209] for the parameters of Fig. B.3 predicts that the condensate expands initially after the trap is extinguished if $a > -3.8 \pm 0.2\,a_0$. For more negative a ($-10 \pm 3\,\mathrm{MHz} < \Delta/2\pi < 0\,\mathrm{MHz}$), there is no repulsive energy barrier on the effective potential for the system and collapse results [5]. Numerical simulation of the GP equation supports this interpretation. Simulations show that collapse can be very non-uniform, as predicted in [210], with significant density increase only near the condensate center for a only moderately more negative than the threshold [5].

B.5 Summary

In summary, we have demonstrated control of collapse and expansion of an ^{88}Sr BEC using an intercombination-transition OFR. At large detuning from PA resonance ($\lesssim 667, \Gamma_{\rm mol}$), we obtain sample lifetimes on the order of 1 ms while changing the scattering length by 10's of a_0 [5]. While this is a moderate change compared to the mean scattering length [214] for Sr, $\bar{a} = [4\pi/\Gamma(1/4)^2](1/2)(2\mu C_6/\hbar^2)^{1/4} = 75.06\, a_0$, it is an extremely large relative change for ^{88}Sr ($a_{\rm opt}/a_{\rm bg} = \pm 10$) because of the small $a_{\rm bg}$. The OFR can thus drastically change the dynamics. Here, $\Gamma(x)$ is the gamma function, and $C_6 = 3170\,$a.u. is the van der Waals coefficient for the interaction between two ground state Sr atoms [215] in atomic units [5].

Our work probes collisions of atoms in a light field in a previously unexplored region of large detuning from photoassociative resonance. The isolated resonance model [151,181] provides a good description of the optically induced scattering length (Eq. B.1) out to a detuning of $|\Delta| \simeq 667\,\Gamma_{\rm mol}$ for this photoassociative transition. This is not surprising because the detuning from the PA resonance is still much less than the spacing between excited molecular states [5]. A coupled channels numerical calculation [184] shows the breakdown of the isolated resonance approximation and absence of a significant OFR effect at comparable detuning from two PA lines. The isolated resonance model is valid over a much smaller range for describing the loss induced by the OFR laser because of the background loss and the enhanced loss parameterized by a large value of η in the far wings of the line [5].

The original peak density of the condensate is extremely high in our experiment because of the attractive interactions. Increased lifetime or larger OFR effect should be obtainable for densities commensurate with single-site loading of an optical lattice [5]. Improvements could also be made by working at larger detuning from PA resonance

and larger laser intensities. Working with a more deeply bound excited molecular state such as the PA line at $-1.08\,\mathrm{GHz}$ [206] may offer advantages in this direction, such as greater suppression of atomic light scattering and reduced background two-body loss. This holds promise to bring many possible experiments involving optical Feshbach resonances and quantum fluids into reach [5].

Bibliography

[1] H. Hu, B. Ramachandhran, H. Pu, and X.-J. Liu, "Spin-orbit coupled weakly interacting bose-einstein condensates in harmonic traps," *Phys. Rev. Lett.*, vol. 108, p. 010402, Jan 2012.

[2] B. Ramachandhran, B. Opanchuk, X.-J. Liu, H. Pu, P. D. Drummond, and H. Hu, "Half-quantum vortex state in a spin-orbit-coupled bose-einstein condensate," *Phys. Rev. A*, vol. 85, p. 023606, Feb 2012.

[3] B. Ramachandhran, H. Hu, and H. Pu, "Emergence of topological and strongly correlated ground states in trapped rashba spin-orbit-coupled bose gases," *Phys. Rev. A*, vol. 87, p. 033627, Mar 2013.

[4] B. Ramachandhran, S. G. Bhongale, and H. Pu, "Finite-temperature study of bose-fermi superfluid mixtures," *Phys. Rev. A*, vol. 83, p. 033607, Mar 2011.

[5] M. Yan, B. J. DeSalvo, B. Ramachandhran, H. Pu, and T. C. Killian, "Controlling condensate collapse and expansion with an optical feshbach resonance," *Phys. Rev. Lett.*, vol. 110, p. 123201, Mar 2013.

[6] H. K. Onnes, "Award ceremony speech." `"http://www.nobelprize.org/nobel_prizes/physics/laureates/1913/press.html"`, 1913.

[7] W. Ketterle, D. S. Durfee, and D. M. Stamper-Kurn, "Making, probing and understanding bose-einstein condensates," in *Bose-Einstein condensation in atomic gases, Proceedings of the International School of Physics 'Enrico Fermi', Course CXL; Edited by M. Inguscio, S. Stringari and C.E. Wieman*, pp. 67–176, IOS Press Amsterdam, 1999.

[8] `"http://people.ccmr.cornell.edu/~emueller/coldgases.html"`.

[9] A. J. Leggett, *Quantum Liquids: Bose condensation and Cooper pairing in condensed-matter systems.* Oxford: Oxford University Press, 2006.

[10] `"http://en.wikipedia.org/wiki/Maxwell-Boltzmann_statistics"`.

[11] `"http://en.wikipedia.org/wiki/Fermi-Dirac_statistics"`.

[12] C. J. Foot, *Atomic Physics (Oxford Master Series in Atomic, Optical and Laser Physics).* Oxford University Press, USA, 1 ed., Feb. 2005.

[13] W. D. Phillips, "Nobel lecture: Laser cooling and trapping of neutral atoms," *Rev. Mod. Phys.*, vol. 70, pp. 721–741, Jul 1998.

[14] "http://en.wikipedia.org/wiki/Doppler_cooling".

[15] "http://www.physics.otago.ac.nz/nx/jdc/experimental-aspects-of-bec.html".

[16] C. J. Pethick and H. Smith, *Bose-Einstein Condensation in Dilute Gases*. Cambridge University Press, Cambridge, 2 ed., Oct. 2008.

[17] M. Inguscio, W. Ketterle, and C. Salomon, "Making, probing and understanding ultracold fermi gases," in *Ultracold Fermi Gases , Proceedings of the International School of Physics "Enrico Fermi", Course CLXIV, Varenna, 20 - 30 June 2006; Edited by M. Inguscio, W. Ketterle, and C. Salomon*, pp. 247–422, IOS Press Amsterdam, Jul 2008.

[18] B. DeMarco and D. S. Jin, "Onset of fermi degeneracy in a trapped atomic gas," *Science*, vol. 285, no. 5434, pp. 1703–1706, 1999.

[19] A. G. Truscott, K. E. Strecker, W. I. McAlexander, G. B. Partridge, and R. G. Hulet, "Observation of fermi pressure in a gas of trapped atoms," *Science*, vol. 291, no. 5513, pp. 2570–2572, 2001.

[20] C. C. Bradley, C. A. Sackett, and R. G. Hulet, "Bose-einstein condensation of lithium: Observation of limited condensate number," *Phys. Rev. Lett.*, vol. 78, pp. 985–989, Feb 1997.

[21] M. H. Anderson, J. R. Ensher, M. R. Matthews, C. E. Wieman, and E. A. Cornell, "Observation of bose-einstein condensation in a dilute atomic vapor," *Science*, vol. 269, no. 5221, pp. 198–201, 1995.

[22] K. B. Davis, M. O. Mewes, M. R. Andrews, N. J. van Druten, D. S. Durfee, D. M. Kurn, and W. Ketterle, "Bose-einstein condensation in a gas of sodium atoms," *Phys. Rev. Lett.*, vol. 75, pp. 3969–3973, Nov 1995.

[23] T. Fukuhara, Y. Takasu, M. Kumakura, and Y. Takahashi, "Degenerate fermi gases of ytterbium," *Phys. Rev. Lett.*, vol. 98, p. 030401, Jan 2007.

[24] B. J. DeSalvo, M. Yan, P. G. Mickelson, Y. N. Martinez de Escobar, and T. C. Killian, "Degenerate fermi gas of ^{87}Sr," *Phys. Rev. Lett.*, vol. 105, p. 030402, Jul 2010.

[25] P. G. Mickelson, Y. N. Martinez de Escobar, M. Yan, B. J. DeSalvo, and T. C. Killian, "Bose-einstein condensation of ^{88}Sr through sympathetic cooling with ^{87}Sr," *Phys. Rev. A*, vol. 81, p. 051601, May 2010.

[26] F. Dalfovo, S. Giorgini, L. P. Pitaevskii, and S. Stringari, "Theory of bose-einstein condensation in trapped gases," *Reviews of Modern Physics*, vol. 71, pp. 463–512, Apr. 1999.

[27] I. Bloch, J. Dalibard, and W. Zwerger, "Many-body physics with ultracold gases," *Rev. Mod. Phys.*, vol. 80, pp. 885–964, Jul 2008.

[28] C. Chin, R. Grimm, P. Julienne, and E. Tiesinga, "Feshbach resonances in ultracold gases," *Reviews of Modern Physics*, vol. 82, pp. 1225–1286, Apr. 2010.

[29] T. Yefsah, R. Desbuquois, L. Chomaz, K. J. Günter, and J. Dalibard, "Exploring the thermodynamics of a two-dimensional bose gas," *Phys. Rev. Lett.*, vol. 107, p. 130401, Sep 2011.

[30] Y.-a. Liao, A. S. C. Rittner, T. Paprotta, W. Li, G. B. Partridge, R. G. Hulet, S. K. Baur, and E. J. Mueller, "Spin-imbalance in a one-dimensional fermi gas," *Nature*, vol. 467, pp. 567–569, Sep 2010. 10.1038/nature09393.

[31] C.-H. Cheng and S.-K. Yip, "Anisotropic fermi superfluid via p-wave feshbach resonance," *Phys. Rev. Lett.*, vol. 95, p. 070404, Aug 2005.

[32] "http://www.colorado.edu/physics/2000/bec/what_its_good_for.html".

[33] "http://en.wikipedia.org/wiki/Quantum_metrology".

[34] K. Bongs, "Quantum leaps," in *InnovOil*^{TM}, p. 20, Published by NewsBase, January 2013.

[35] "http://mpa.ac.uk/muarc/research.html".

[36] "http://www.nasa.gov/topics/technology/features/atom-optics_prt.htm".

[37] J. Hogan. "http://www-conf.slac.stanford.edu/ssi/2011/Hogan_080311.pdf".

[38] J. Hogan. "http://scpnt.stanford.edu/pnt/PNT08/Posters/SCPNT-EPposter2008.pdf".

[39] S. Dimopoulos, P. W. Graham, J. M. Hogan, and M. A. Kasevich, "Testing general relativity with atom interferometry," *Phys. Rev. Lett.*, vol. 98, p. 111102, Mar 2007.

[40] S. Dimopoulos, P. W. Graham, J. M. Hogan, M. A. Kasevich, and S. Rajendran, "Atomic gravitational wave interferometric sensor," *Phys. Rev. D*, vol. 78, p. 122002, Dec 2008.

[41] S.-w. Chiow, T. Kovachy, H.-C. Chien, and M. A. Kasevich, "102$\hbar k$ large area atom interferometers," *Phys. Rev. Lett.*, vol. 107, p. 130403, Sep 2011.

[42] "http://www.nasa.gov/centers/glenn/shuttlestation/station/microgex.html".

[43] M. Arndt, "Free-falling interferometry," *Physics*, vol. 6, p. 23, Feb 2013.

[44] H. Müntinga and et al., "Interferometry with bose-einstein condensates in microgravity," *Phys. Rev. Lett.*, vol. 110, p. 093602, Feb 2013.

[45] J. Stajic, "The future of quantum information processing," *Science*, vol. 339, no. 6124, p. 1163, 2013.

[46] "http://www.zmescience.com/science/physics/first-universal-two-qubit-quantum-processor-created/".

[47] "http://qo.pitt.edu/research_qc.html".

[48] "http://en.wikipedia.org/wiki/Optical_lattice".

[49] R. Feynman, "Simulating physics with computers," *International Journal of Theoretical Physics*, vol. 21, no. 6-7, pp. 467–488, 1982.

[50] A. Trabesinger, "Quantum simulation," *Nat Phys*, vol. 8, pp. 263–263, Apr 2012. 10.1038/nphys2258.

[51] I. Bloch, J. Dalibard, and S. Nascimbene, "Quantum simulations with ultracold quantum gases," *Nat Phys*, vol. 8, pp. 267–276, Apr 2012. 10.1038/nphys2259.

[52] J. Tuoriniemi, K. Juntunen-Nurmilaukas, J. Uusvuori, E. Pentti, A. Salmela, and A. Sebedash, "Superconductivity in lithium below 0.4 millikelvin at ambient pressure," *Nature*, vol. 447, pp. 187–189, May 2007. 10.1038/nature05820.

[53] V. Galitski and I. B. Spielman, "Spin-orbit coupling in quantum gases," *Nature*, vol. 494, pp. 49–54, Feb 2013. 10.1038/nature11841.

[54] M. Lewenstein, A. Sanpera, V. Ahufinger, B. Damski, A. Sen(De), and U. Sen, "Ultracold atomic gases in optical lattices: mimicking condensed matter physics and beyond," *Advances in Physics*, vol. 56, no. 2, pp. 243–379, 2007.

[55] D. Greif, T. Uehlinger, G. Jotzu, L. Tarruell, and T. Esslinger, "Short-range quantum magnetism of ultracold fermions in an optical lattice," *Science*, vol. 340, no. 6138, pp. 1307–1310, 2013.

[56] "http://www.ethlife.ethz.ch/archive_articles/130524_quantenmagnetismus_at/index_EN".

[57] Y. J. Lin, R. L. Compton, K. Jimenez-Garcia, J. V. Porto, and I. B. Spielman, "Synthetic magnetic fields for ultracold neutral atoms," *Nature*, vol. 462, pp. 628–632, Dec 2009. 10.1038/nature08609.

[58] Y. J. Lin, R. L. Compton, K. Jimenez-Garcia, W. D. Phillips, J. V. Porto, and I. B. Spielman, "A synthetic electric force acting on neutral atoms," *Nat Phys*, vol. 7, pp. 531–534, Jul 2011. 10.1038/nphys1954.

[59] Y. J. Lin, K. Jimenez-Garcia, and I. B. Spielman, "Spin-orbit-coupled bose-einstein condensates," *Nature*, vol. 471, pp. 83–86, Mar 2011. 10.1038/nature09887.

[60] P. Wang, Z.-Q. Yu, Z. Fu, J. Miao, L. Huang, S. Chai, H. Zhai, and J. Zhang, "Spin-orbit coupled degenerate fermi gases," *Phys. Rev. Lett.*, vol. 109, p. 095301, Aug 2012.

[61] L. W. Cheuk, A. T. Sommer, Z. Hadzibabic, T. Yefsah, W. S. Bakr, and M. W. Zwierlein, "Spin-injection spectroscopy of a spin-orbit coupled fermi gas," *Phys. Rev. Lett.*, vol. 109, p. 095302, Aug 2012.

[62] X.-L. Qi and S.-C. Zhang, "The quantum spin Hall effect and topological insulators," *Physics Today*, vol. 63, pp. 33+, Jan. 2010.

[63] R. Onofrio, C. Raman, J. M. Vogels, J. R. Abo-Shaeer, A. P. Chikkatur, and W. Ketterle, "Observation of superfluid flow in a bose-einstein condensed gas," *Phys. Rev. Lett.*, vol. 85, pp. 2228–2231, Sep 2000.

[64] R. Desbuquois, L. Chomaz, T. Yefsah, J. Leonard, J. Beugnon, C. Weitenberg, and J. Dalibard, "Superfluid behaviour of a two-dimensional bose gas," *Nat Phys*, vol. 8, pp. 645–648, Sep 2012. 10.1038/nphys2378.

[65] S. E. Pollack, D. Dries, and R. G. Hulet, "Universality in three- and four-body bound states of ultracold atoms," *Science*, vol. 326, no. 5960, pp. 1683–1685, 2009.

[66] J. R. Williams, E. L. Hazlett, J. H. Huckans, R. W. Stites, Y. Zhang, and K. M. O'Hara, "Evidence for an excited-state efimov trimer in a three-component fermi gas," *Phys. Rev. Lett.*, vol. 103, p. 130404, Sep 2009.

[67] M. Greiner, O. Mandel, T. Esslinger, T. W. Hansch, and I. Bloch, "Quantum phase transition from a superfluid to a mott insulator in a gas of ultracold atoms," *Nature*, vol. 415, pp. 39–44, Jan 2002. 10.1038/415039a.

[68] R. Jordens, N. Strohmaier, K. Gunter, H. Moritz, and T. Esslinger, "A mott insulator of fermionic atoms in an optical lattice," *Nature*, vol. 455, pp. 204–207, Sep 2008. 10.1038/nature07244.

[69] U. Schneider, L. Hackermüeller, S. Will, T. Best, I. Bloch, T. A. Costi, R. W. Helmes, D. Rasch, and A. Rosch, "Metallic and insulating phases of repulsively interacting fermions in a 3d optical lattice," *Science*, vol. 322, no. 5907, pp. 1520–1525, 2008.

[70] T. A. Corcovilos, S. K. Baur, J. M. Hitchcock, E. J. Mueller, and R. G. Hulet, "Detecting antiferromagnetism of atoms in an optical lattice via optical bragg scattering," *Phys. Rev. A*, vol. 81, p. 013415, Jan 2010.

[71] J. Struck, C. Ölschläger, R. Le Targat, P. Soltan-Panahi, A. Eckardt, M. Lewenstein, P. Windpassinger, and K. Sengstock, "Quantum simulation of frustrated classical magnetism in triangular optical lattices," *Science*, vol. 333, no. 6045, pp. 996–999, 2011.

[72] I. Žutić, J. Fabian, and S. Das Sarma, "Spintronics: Fundamentals and applications," *Rev. Mod. Phys.*, vol. 76, pp. 323–410, Apr 2004.

[73] Y. A. Bychkov and E. I. Rashba, "Oscillatory effects and the magnetic susceptibility of carriers in inversion layers," *Journal of Physics C: Solid State Physics*, vol. 17, no. 33, p. 6039, 1984.

[74] J. Higbie and D. M. Stamper-Kurn, "Periodically dressed bose-einstein condensate: A superfluid with an anisotropic and variable critical velocity," *Phys. Rev. Lett.*, vol. 88, p. 090401, Feb 2002.

[75] D. L. Campbell, G. Juzeliūnas, and I. B. Spielman, "Realistic rashba and dresselhaus spin-orbit coupling for neutral atoms," *Phys. Rev. A*, vol. 84, p. 025602, Aug 2011.

[76] J. Dalibard, F. Gerbier, G. Juzeliūnas, and P. Öhberg, "*Colloquium*: Artificial gauge potentials for neutral atoms," *Rev. Mod. Phys.*, vol. 83, pp. 1523–1543, Nov 2011.

[77] Z. Hadzibabic, P. Krüger, M. Cheneau, S. P. Rath, and J. Dalibard, "The trapped two-dimensional bose gas: from bose-einstein condensation to berezinskii-kosterlitz-thouless physics," *New Journal of Physics*, vol. 10, p. 045006, 2008.

[78] D. S. Petrov, M. Holzmann, and G. V. Shlyapnikov, "Bose-einstein condensation in quasi-2d trapped gases," *Phys. Rev. Lett.*, vol. 84, pp. 2551–2555, Mar 2000.

[79] A. Griffin, "Conserving and gapless approximations for an inhomogeneous bose gas at finite temperatures," *Phys. Rev. B*, vol. 53, pp. 9341–9347, Apr 1996.

[80] P. A. Ruprecht, M. Edwards, K. Burnett, and C. W. Clark, "Probing the linear and nonlinear excitations of bose-condensed neutral atoms in a trap," *Phys. Rev. A*, vol. 54, pp. 4178–4187, Nov 1996.

[81] H. Pu and N. P. Bigelow, "Collective excitations, metastability, and nonlinear response of a trapped two-species bose-einstein condensate," *Phys. Rev. Lett.*, vol. 80, pp. 1134–1137, Feb 1998.

[82] W. Cong-Jun, I. Mondragon-Shem, and Z. Xiang-Fa, "Unconventional bose-einstein condensations from spin-orbit coupling," *Chinese Physics Letters*, vol. 28, no. 9, p. 097102, 2011.

[83] M. M. Salomaa and G. E. Volovik, "Half-quantum vortices in superfluid ^{3}he-a," *Phys. Rev. Lett.*, vol. 55, pp. 1184–1187, Sep 1985.

[84] H. Pu and N. P. Bigelow, "Properties of two-species bose condensates," *Phys. Rev. Lett.*, vol. 80, pp. 1130–1133, Feb 1998.

[85] W. Bao, D. Jaksch, and P. A. Markowich, "Numerical solution of the gross-pitaevskii equation for bose-einstein condensation," *Journal of Computational Physics*, vol. 187, no. 1, pp. 318 – 342, 2003.

[86] W. Bao, "Ground states and dynamics of multicomponent bose–einstein condensates," *Multiscale Modeling & Simulation*, vol. 2, no. 2, pp. 210–236, 2004.

[87] H. Wang, "A time-splitting spectral method for coupled gross-pitaevskii equations with applications to rotating bose-einstein condensates," *Journal of Computational and Applied Mathematics*, vol. 205, no. 1, pp. 88 – 104, 2007.

[88] B. Binz and A. Vishwanath, "Chirality induced anomalous-hall effect in helical spin crystals," *Physica B: Condensed Matter*, vol. 403, no. 5-9, pp. 1336 – 1340, 2008.

[89] S. Mühlbauer, B. Binz, F. Jonietz, C. Pfleiderer, A. Rosch, A. Neubauer, R. Georgii, and P. Böni, "Skyrmion lattice in a chiral magnet," *Science*, vol. 323, no. 5916, pp. 915–919, 2009.

[90] S. M. Girvin, "The quantum hall effect: Novel excitations and broken symmetries," in *Topological aspects of low dimensional systems, Les Houches 1998 Summer School; Edited by A. Comtet, T. Jolicceur, S. Ouvry and F. David*, pp. 53–176, EDP Sciences and Springer, 1998.

[91] T. Skyrme, "A unified field theory of mesons and baryons," *Nuclear Physics*, vol. 31, no. 0, pp. 556 – 569, 1962.

[92] T. D. Stanescu, B. Anderson, and V. Galitski, "Spin-orbit coupled bose-einstein condensates," *Phys. Rev. A*, vol. 78, p. 023616, Aug 2008.

[93] X.-F. Zhou, J. Zhou, and C. Wu, "Vortex structures of rotating spin-orbit-coupled bose-einstein condensates," *Phys. Rev. A*, vol. 84, p. 063624, Dec 2011.

[94] J. Larson and E. Sjöqvist, "Jahn-teller-induced berry phase in spin-orbit-coupled bose-einstein condensates," *Phys. Rev. A*, vol. 79, p. 043627, Apr 2009.

[95] C. Wang, C. Gao, C.-M. Jian, and H. Zhai, "Spin-orbit coupled spinor bose-einstein condensates," *Phys. Rev. Lett.*, vol. 105, p. 160403, Oct 2010.

[96] T.-L. Ho and S. Zhang, "Bose-einstein condensates with spin-orbit interaction," *Phys. Rev. Lett.*, vol. 107, p. 150403, Oct 2011.

[97] Y. Zhang, L. Mao, and C. Zhang, "Mean-field dynamics of spin-orbit coupled bose-einstein condensates," *Phys. Rev. Lett.*, vol. 108, p. 035302, Jan 2012.

[98] Z. F. Xu, R. Lü, and L. You, "Emergent patterns in a spin-orbit-coupled spin-2 bose-einstein condensate," *Phys. Rev. A*, vol. 83, p. 053602, May 2011.

[99] T. Kawakami, T. Mizushima, and K. Machida, "Textures of f=2 spinor bose-einstein condensates with spin-orbit coupling," *Phys. Rev. A*, vol. 84, p. 011607, Jul 2011.

[100] D. A. Butts and D. S. Rokhsar, "Predicted signatures of rotating bose-einstein condensates," *Nature*, vol. 397, pp. 327–329, Jan 1999. 10.1038/16865.

[101] X.-J. Liu, H. Hu, L. Chang, W. Zhang, S.-Q. Li, and Y.-Z. Wang, "Fragmented condensate ground state of trapped weakly interacting bosons in two dimensions," *Phys. Rev. Lett.*, vol. 87, p. 030404, Jul 2001.

[102] A.-C. Ji, W. M. Liu, J. L. Song, and F. Zhou, "Dynamical creation of fractionalized vortices and vortex lattices," *Phys. Rev. Lett.*, vol. 101, p. 010402, Jul 2008.

[103] S.-W. Su, C.-H. Hsueh, I.-K. Liu, T.-L. Horng, Y.-C. Tsai, S.-C. Gou, and W. M. Liu, "Spontaneous crystallization of skyrmions and fractional vortices in fast-rotating and rapidly quenched spin-1 bose-einstein condensates," *Phys. Rev. A*, vol. 84, p. 023601, Aug 2011.

[104] A. E. Leanhardt, T. A. Pasquini, M. Saba, A. Schirotzek, Y. Shin, D. Kielpinski, D. E. Pritchard, and W. Ketterle, "Cooling bose-einstein condensates below 500 picokelvin," *Science*, vol. 301, no. 5639, pp. 1513–1515, 2003.

[105] E. J. Mueller, "Spin-orbit coupling comes in from the cold," *Physics*, vol. 5, p. 96, Aug 2012.

[106] N. K. Wilkin and J. M. F. Gunn, "Condensation of "composite bosons" in a rotating bec," *Phys. Rev. Lett.*, vol. 84, pp. 6–9, Jan 2000.

[107] F. Chevy, V. Bretin, P. Rosenbusch, K. W. Madison, and J. Dalibard, "Transverse breathing mode of an elongated bose-einstein condensate," *Phys. Rev. Lett.*, vol. 88, p. 250402, Jun 2002.

[108] M. Babadi and E. Demler, "Collective excitations of quasi-two-dimensional trapped dipolar fermions: Transition from collisionless to hydrodynamic regime," *Phys. Rev. A*, vol. 86, p. 063638, Dec 2012.

[109] R. Grimm, "Ultracold fermi gases in the bec-bcs crossover: a review from the innsbruck perspective," in *Proceedings of the International School of Physics "Enrico Fermi", Ultra-cold Fermi Gases, edited by M. Inguscio, W. Ketterle, and C. Salomon*, pp. 53–176, IOS Press, Amsterdam, 2007.

[110] S. Stringari, "Collective excitations of a trapped bose-condensed gas," *Phys. Rev. Lett.*, vol. 77, pp. 2360–2363, Sep 1996.

[111] D. S. Jin, J. R. Ensher, M. R. Matthews, C. E. Wieman, and E. A. Cornell, "Collective excitations of a bose-einstein condensate in a dilute gas," *Phys. Rev. Lett.*, vol. 77, pp. 420–423, Jul 1996.

[112] M.-O. Mewes, M. R. Andrews, N. J. van Druten, D. M. Kurn, D. S. Durfee, C. G. Townsend, and W. Ketterle, "Collective excitations of a bose-einstein condensate in a magnetic trap," *Phys. Rev. Lett.*, vol. 77, pp. 988–991, Aug 1996.

[113] X.-J. Liu, H. Hu, A. Minguzzi, and M. P. Tosi, "Collective oscillations of a confined bose gas at finite temperature in the random-phase approximation," *Phys. Rev. A*, vol. 69, p. 043605, Apr 2004.

[114] X.-J. Liu, H. Hu, and P. D. Drummond, "Mean-field thermodynamics of a spin-polarized spherically trapped fermi gas at unitarity," *Phys. Rev. A*, vol. 75, p. 023614, Feb 2007.

[115] X.-J. Liu, H. Hu, and P. D. Drummond, "Fulde-ferrell-larkin-ovchinnikov states in one-dimensional spin-polarized ultracold atomic fermi gases," *Phys. Rev. A*, vol. 76, p. 043605, Oct 2007.

[116] X.-J. Liu, H. Hu, and P. D. Drummond, "Finite-temperature phase diagram of a spin-polarized ultracold fermi gas in a highly elongated harmonic trap," *Phys. Rev. A*, vol. 78, p. 023601, Aug 2008.

[117] D. A. W. Hutchinson, E. Zaremba, and A. Griffin, "Finite temperature excitations of a trapped bose gas," *Phys. Rev. Lett.*, vol. 78, pp. 1842–1845, Mar 1997.

[118] P. Öhberg and S. Stenholm, "Internal josephson effect in trapped double condensates," *Phys. Rev. A*, vol. 59, pp. 3890–3895, May 1999.

[119] J.-Y. Zhang, S.-C. Ji, Z. Chen, L. Zhang, Z.-D. Du, B. Yan, G.-S. Pan, B. Zhao, Y.-J. Deng, H. Zhai, S. Chen, and J.-W. Pan, "Collective dipole oscillations of a spin-orbit coupled bose-einstein condensate," *Phys. Rev. Lett.*, vol. 109, p. 115301, Sep 2012.

[120] S. Yi and H. Pu, "Vortex structures in dipolar condensates," *Phys. Rev. A*, vol. 73, p. 061602, Jun 2006.

[121] C. L. Kane and E. J. Mele, "Quantum spin hall effect in graphene," *Phys. Rev. Lett.*, vol. 95, p. 226801, Nov 2005.

[122] B. A. Bernevig and S.-C. Zhang, "Quantum spin hall effect," *Phys. Rev. Lett.*, vol. 96, p. 106802, Mar 2006.

[123] D. Blume, "Few-body physics with ultracold atomic and molecular systems in traps," *Reports on Progress in Physics*, vol. 75, no. 4, p. 046401, 2012.

[124] F. Serwane, G. Zürn, T. Lompe, T. B. Ottenstein, A. N. Wenz, and S. Jochim, "Deterministic preparation of a tunable few-fermion system," *Science*, vol. 332, no. 6027, pp. 336–338, 2011.

[125] M. Köhl, H. Moritz, T. Stöferle, K. Günter, and T. Esslinger, "Fermionic atoms in a three dimensional optical lattice: Observing fermi surfaces, dynamics, and interactions," *Phys. Rev. Lett.*, vol. 94, p. 080403, Mar 2005.

[126] G. Thalhammer, K. Winkler, F. Lang, S. Schmid, R. Grimm, and J. H. Denschlag, "Long-lived feshbach molecules in a three-dimensional optical lattice," *Phys. Rev. Lett.*, vol. 96, p. 050402, Feb 2006.

[127] M. Burrello and A. Trombettoni, "Ultracold atoms in $u(2)$ non-abelian gauge potentials preserving the landau levels," *Phys. Rev. A*, vol. 84, p. 043625, Oct 2011.

[128] B. Juliá-Díaz, T. Graß, N. Barberán, and M. Lewenstein, "Fractional quantum hall states of a few bosonic atoms in geometric gauge fields," *New Journal of Physics*, vol. 14, no. 5, p. 055003, 2012.

[129] M. Burrello and A. Trombettoni, "Non-abelian anyons from degenerate landau levels of ultracold atoms in artificial gauge potentials," *Phys. Rev. Lett.*, vol. 105, p. 125304, Sep 2010.

[130] Y. Li, X. Zhou, and C. Wu, "Two- and three-dimensional topological insulators with isotropic and parity-breaking landau levels," *Phys. Rev. B*, vol. 85, p. 125122, Mar 2012.

[131] Z. F. Xu and L. You, "Dynamical generation of arbitrary spin-orbit couplings for neutral atoms," *Phys. Rev. A*, vol. 85, p. 043605, Apr 2012.

[132] J. M. Zhang and R. X. Dong, "Exact diagonalization: the bose-hubbard model as an example," *European Journal of Physics*, vol. 31, no. 3, p. 591, 2010. Techniques illustrated in this paper were particularly useful during implementation.

[133] L. O. Baksmaty, C. Yannouleas, and U. Landman, "Rapidly rotating boson molecules with long- or short-range repulsion: An exact diagonalization study," *Phys. Rev. A*, vol. 75, p. 023620, Feb 2007.

[134] B. Juliá-Díaz, D. Dagnino, K. J. Günter, T. Graß, N. Barberán, M. Lewenstein, and J. Dalibard, "Strongly correlated states of a small cold-atom cloud from geometric gauge fields," *Phys. Rev. A*, vol. 84, p. 053605, Nov 2011.

[135] N. Barberán, M. Lewenstein, K. Osterloh, and D. Dagnino, "Ordered structures in rotating ultracold bose gases," *Phys. Rev. A*, vol. 73, p. 063623, Jun 2006.

[136] H. Saarikoski, A. Harju, J. C. Cremon, S. Bargi, M. Manninen, and S. M. Reimann, "Coreless vortices in rotating two-component quantum droplets," *EPL (Europhysics Letters)*, vol. 91, no. 3, p. 30006, 2010.

[137] H. Saarikoski, S. M. Reimann, A. Harju, and M. Manninen, "Vortices in quantum droplets: Analogies between boson and fermion systems," *Rev. Mod. Phys.*, vol. 82, pp. 2785–2834, Sep 2010.

[138] Y. Shi, "Quantum entanglement of identical particles," *Phys. Rev. A*, vol. 67, p. 024301, Feb 2003.

[139] Y. Shi, "Quantum entanglement in second-quantized condensed matter systems," *Journal of Physics A: Mathematical and General*, vol. 37, no. 26, p. 6807, 2004.

[140] A. Sterdyniak, B. A. Bernevig, N. Regnault, and F. D. M. Haldane, "The hierarchical structure in the orbital entanglement spectrum of fractional quantum hall systems," *New Journal of Physics*, vol. 13, no. 10, p. 105001, 2011.

[141] H. Li and F. D. M. Haldane, "Entanglement spectrum as a generalization of entanglement entropy: Identification of topological order in non-abelian fractional quantum hall effect states," *Phys. Rev. Lett.*, vol. 101, p. 010504, Jul 2008.

[142] O. S. Zozulya, M. Haque, and N. Regnault, "Entanglement signatures of quantum hall phase transitions," *Phys. Rev. B*, vol. 79, p. 045409, Jan 2009.

[143] N. Gemelke, E. Sarajlic, and S. Chu, "Rotating few-body atomic systems in the fractional quantum hall regime," *cond-mat, arXiv: 1007.2677*, 2010.

[144] R. Roy and S. L. Sondhi, "Fractional quantum hall effect without landau levels," *Physics*, vol. 4, p. 46, Jun 2011.

[145] T. Neupert, L. Santos, C. Chamon, and C. Mudry, "Fractional quantum hall states at zero magnetic field," *Phys. Rev. Lett.*, vol. 106, p. 236804, Jun 2011.

[146] E. Tang, J.-W. Mei, and X.-G. Wen, "High-temperature fractional quantum hall states," *Phys. Rev. Lett.*, vol. 106, p. 236802, Jun 2011.

[147] K. Sun, Z. Gu, H. Katsura, and S. Das Sarma, "Nearly flatbands with nontrivial topology," *Phys. Rev. Lett.*, vol. 106, p. 236803, Jun 2011.

[148] T. D. Stanescu, V. Galitski, J. Y. Vaishnav, C. W. Clark, and S. Das Sarma, "Topological insulators and metals in atomic optical lattices," *Phys. Rev. A*, vol. 79, p. 053639, May 2009.

[149] E. Wille, F. M. Spiegelhalder, G. Kerner, D. Naik, A. Trenkwalder, G. Hendl, F. Schreck, R. Grimm, T. G. Tiecke, J. T. M. Walraven, S. J. J. M. F. Kokkelmans, E. Tiesinga, and P. S. Julienne, "Exploring an ultracold fermi-fermi mixture: Interspecies feshbach resonances and scattering properties of ^{6}li and ^{40}k," *Phys. Rev. Lett.*, vol. 100, p. 053201, Feb 2008.

[150] K. Pilch, A. D. Lange, A. Prantner, G. Kerner, F. Ferlaino, H.-C. Nägerl, and R. Grimm, "Observation of interspecies feshbach resonances in an ultracold rb-cs mixture," *Phys. Rev. A*, vol. 79, p. 042718, Apr 2009.

[151] R. Ciuryło, E. Tiesinga, and P. S. Julienne, "Optical tuning of the scattering length of cold alkaline-earth-metal atoms," *Phys. Rev. A*, vol. 71, p. 030701, Mar 2005.

[152] K. Enomoto, K. Kasa, M. Kitagawa, and Y. Takahashi, "Optical feshbach resonance using the intercombination transition," *Phys. Rev. Lett.*, vol. 101, p. 203201, Nov 2008.

[153] Z. Hadzibabic, C. A. Stan, K. Dieckmann, S. Gupta, M. W. Zwierlein, A. Görlitz, and W. Ketterle, "Two-species mixture of quantum degenerate bose and fermi gases," *Phys. Rev. Lett.*, vol. 88, p. 160401, Apr 2002.

[154] Z. Hadzibabic, S. Gupta, C. A. Stan, C. H. Schunck, M. W. Zwierlein, K. Dieckmann, and W. Ketterle, "Fiftyfold improvement in the number of quantum degenerate fermionic atoms," *Phys. Rev. Lett.*, vol. 91, p. 160401, Oct 2003.

[155] S. Inouye, J. Goldwin, M. L. Olsen, C. Ticknor, J. L. Bohn, and D. S. Jin, "Observation of heteronuclear feshbach resonances in a mixture of bosons and fermions," *Phys. Rev. Lett.*, vol. 93, p. 183201, Oct 2004.

[156] M. Zaccanti, C. D'Errico, F. Ferlaino, G. Roati, M. Inguscio, and G. Modugno, "Control of the interaction in a fermi-bose mixture," *Phys. Rev. A*, vol. 74, p. 041605, Oct 2006.

[157] K. Maeda, G. Baym, and T. Hatsuda, "Simulating dense qcd matter with ultracold atomic boson-fermion mixtures," *Phys. Rev. Lett.*, vol. 103, p. 085301, Aug 2009.

[158] R. Onofrio and C. Presilla, "Reaching fermi degeneracy in two-species optical dipole traps," *Phys. Rev. Lett.*, vol. 89, p. 100401, Aug 2002.

[159] C. Chin, M. Bartenstein, A. Altmeyer, S. Riedl, S. Jochim, J. H. Denschlag, and R. Grimm, "Observation of the pairing gap in a strongly interacting fermi gas," *Science*, vol. 305, no. 5687, pp. 1128–1130, 2004.

[160] M. Holland, S. J. J. M. F. Kokkelmans, M. L. Chiofalo, and R. Walser, "Resonance superfluidity in a quantum degenerate fermi gas," *Phys. Rev. Lett.*, vol. 87, p. 120406, Aug 2001.

[161] A. Altland and B. Simons, *Condensed Matter Field Theory*. Cambridge University Press, Cambridge, 1 ed., June 2006.

[162] D.-W. Wang, "Strong-coupling theory for the superfluidity of bose-fermi mixtures," *Phys. Rev. Lett.*, vol. 96, p. 140404, Apr 2006.

[163] S. G. Bhongale and H. Pu, "Phase separation in a mixture of a bose-einstein condensate and a two-component fermi gas as a probe of fermi superfluidity," *Phys. Rev. A*, vol. 78, p. 061606, Dec 2008.

[164] M. Olshanii, "Atomic scattering in the presence of an external confinement and a gas of impenetrable bosons," *Phys. Rev. Lett.*, vol. 81, pp. 938–941, Aug 1998.

[165] R. Haussmann, W. Rantner, S. Cerrito, and W. Zwerger, "Thermodynamics of the bcs-bec crossover," *Phys. Rev. A*, vol. 75, p. 023610, Feb 2007.

[166] C. A. R. Sá de Melo, M. Randeria, and J. R. Engelbrecht, "Crossover from bcs to bose superconductivity: Transition temperature and time-dependent ginzburg-landau theory," *Phys. Rev. Lett.*, vol. 71, pp. 3202–3205, Nov 1993.

[167] Y.-i. Shin, A. Schirotzek, C. H. Schunck, and W. Ketterle, "Realization of a strongly interacting bose-fermi mixture from a two-component fermi gas," *Phys. Rev. Lett.*, vol. 101, p. 070404, Aug 2008.

[168] L. O. Baksmaty, H. Lu, C. J. Bolech, and H. Pu, "Concomitant modulated superfluidity in polarized fermi gases," *Phys. Rev. A*, vol. 83, p. 023604, Feb 2011.

[169] M. W. Zwierlein, A. Schirotzek, C. H. Schunck, and W. Ketterle, "Fermionic superfluidity with imbalanced spin populations," *Science*, vol. 311, no. 5760, pp. 492–496, 2006.

[170] G. B. Partridge, W. Li, R. I. Kamar, Y.-a. Liao, and R. G. Hulet, "Pairing and phase separation in a polarized fermi gas," *Science*, vol. 311, no. 5760, pp. 503–505, 2006.

[171] M. Greiner, C. A. Regal, and D. S. Jin, "Emergence of a molecular bose-einstein condensate from a fermi gas," *Nature*, vol. 426, pp. 537–540, Dec 2003. 10.1038/nature02199.

[172] T. Kraemer, M. Mark, P. Waldburger, J. G. Danzl, C. Chin, B. Engeser, A. D. Lange, K. Pilch, A. Jaakkola, H. C. Naegerl, and R. Grimm, "Evidence for efimov quantum states in an ultracold gas of caesium atoms," *Nature*, vol. 440, pp. 315–318, Mar 2006. 10.1038/nature04626.

[173] E. Braaten and H. W. Hammer, "Efimov physics in cold atoms," *Annals of Physics*, vol. 322, pp. 120–163, Jan. 2007.

[174] S. Jochim, M. Bartenstein, A. Altmeyer, G. Hendl, S. Riedl, C. Chin, J. Hecker Denschlag, and R. Grimm, "Bose-einstein condensation of molecules," *Science*, vol. 302, no. 5653, pp. 2101–2103, 2003.

[175] P. O. Fedichev, Y. Kagan, G. V. Shlyapnikov, and J. T. M. Walraven, "Influence of nearly resonant light on the scattering length in low-temperature atomic gases," *Phys. Rev. Lett.*, vol. 77, pp. 2913–2916, Sep 1996.

[176] F. K. Fatemi, K. M. Jones, and P. D. Lett, "Observation of optically induced feshbach resonances in collisions of cold atoms," *Phys. Rev. Lett.*, vol. 85, pp. 4462–4465, Nov 2000.

[177] M. Theis, G. Thalhammer, K. Winkler, M. Hellwig, G. Ruff, R. Grimm, and J. H. Denschlag, "Tuning the scattering length with an optically induced feshbach resonance," *Phys. Rev. Lett.*, vol. 93, p. 123001, Sep 2004.

[178] G. Thalhammer, M. Theis, K. Winkler, R. Grimm, and J. H. Denschlag, "Inducing an optical feshbach resonance via stimulated raman coupling," *Phys. Rev. A*, vol. 71, p. 033403, Mar 2005.

[179] D. M. Bauer, M. Lettner, C. Vo, G. Rempe, and S. Durr, "Control of a magnetic feshbach resonance with laser light," *Nat Phys*, vol. 5, pp. 339–342, May 2009. 10.1038/nphys1232.

[180] H. Wu and J. E. Thomas, "Optical control of feshbach resonances in fermi gases using molecular dark states," *Phys. Rev. Lett.*, vol. 108, p. 010401, Jan 2012.

[181] R. Ciuryło, E. Tiesinga, and P. S. Julienne, "Stationary phase approximation for the strength of optical feshbach resonances," *Phys. Rev. A*, vol. 74, p. 022710, Aug 2006.

[182] K. Enomoto, K. Kasa, M. Kitagawa, and Y. Takahashi, "Optical feshbach resonance using the intercombination transition," *Phys. Rev. Lett.*, vol. 101, p. 203201, Nov 2008.

[183] R. Yamazaki, S. Taie, S. Sugawa, and Y. Takahashi, "Submicron spatial modulation of an interatomic interaction in a bose-einstein condensate," *Phys. Rev. Lett.*, vol. 105, p. 050405, Jul 2010.

[184] S. Blatt, T. L. Nicholson, B. J. Bloom, J. R. Williams, J. W. Thomsen, P. S. Julienne, and J. Ye, "Measurement of optical feshbach resonances in an ideal gas," *Phys. Rev. Lett.*, vol. 107, p. 073202, Aug 2011.

[185] Y. N. M. de Escobar, P. G. Mickelson, M. Yan, B. J. DeSalvo, S. B. Nagel, and T. C. Killian, "Bose-einstein condensation of ^{84}sr," *Phys. Rev. Lett.*, vol. 103, p. 200402, Nov 2009.

[186] S. Stellmer, M. K. Tey, B. Huang, R. Grimm, and F. Schreck, "Bose-einstein condensation of strontium," *Phys. Rev. Lett.*, vol. 103, p. 200401, Nov 2009.

[187] P. G. Mickelson, Y. N. Martinez de Escobar, M. Yan, B. J. DeSalvo, and T. C. Killian, "Bose-einstein condensation of ^{88}sr through sympathetic cooling with ^{87}sr," *Phys. Rev. A*, vol. 81, p. 051601, May 2010.

[188] R. Qi and H. Zhai, "Bound states and scattering resonances induced by spatially modulated interactions," *Phys. Rev. Lett.*, vol. 106, p. 163201, Apr 2011.

[189] C.-C. Chien, "Spatially varying interactions induced in ultra-cold atoms by optical feshbach resonance," *Physics Letters A*, vol. 376, no. 5, pp. 729 – 732, 2012.

[190] H. Saito and M. Ueda, "Dynamically stabilized bright solitons in a two-dimensional bose-einstein condensate," *Phys. Rev. Lett.*, vol. 90, p. 040403, Jan 2003.

[191] M. I. Rodas-Verde, H. Michinel, and V. M. Pérez-García, "Controllable soliton emission from a bose-einstein condensate," *Phys. Rev. Lett.*, vol. 95, p. 153903, Oct 2005.

[192] Y. V. Kartashov, B. A. Malomed, and L. Torner, "Solitons in nonlinear lattices," *Rev. Mod. Phys.*, vol. 83, pp. 247–305, Apr 2011.

[193] M. P. A. Fisher, P. B. Weichman, G. Grinstein, and D. S. Fisher, "Boson localization and the superfluid-insulator transition," *Phys. Rev. B*, vol. 40, pp. 546–570, Jul 1989.

[194] M. K. Tey, S. Stellmer, R. Grimm, and F. Schreck, "Double-degenerate bose-fermi mixture of strontium," *Phys. Rev. A*, vol. 82, p. 011608, Jul 2010.

[195] S. Sugawa, K. Inaba, S. Taie, R. Yamazaki, M. Yamashita, and Y. Takahashi, "Interaction and filling-induced quantum phases of dual mott insulators of bosons and fermions," *Nat Phys*, vol. 7, pp. 642–648, Aug 2011. 10.1038/nphys2028.

[196] K. R. A. Hazzard, V. Gurarie, M. Hermele, and A. M. Rey, "High-temperature properties of fermionic alkaline-earth-metal atoms in optical lattices," *Phys. Rev. A*, vol. 85, p. 041604, Apr 2012.

[197] Z. Cai, H.-h. Hung, L. Wang, D. Zheng, and C. Wu, "Pomeranchuk cooling of su($2n$) ultracold fermions in optical lattices," *Phys. Rev. Lett.*, vol. 110, p. 220401, May 2013.

[198] S. Taie, R. Yamazaki, S. Sugawa, and Y. Takahashi, "An $su(6)$ mott insulator of an atomic fermi gas realized by large-spin pomeranchuk cooling," *Nat Phys*, vol. 8, pp. 825–830, Nov 2012. 10.1038/nphys2430.

[199] C. Wu, J.-p. Hu, and S.-c. Zhang, "Exact $so(5)$ symmetry in the spin-3/2 fermionic system," *Phys. Rev. Lett.*, vol. 91, p. 186402, Oct 2003.

[200] M. A. Cazalilla, A. F. Ho, and M. Ueda, "Ultracold gases of ytterbium: ferromagnetism and mott states in an $su(6)$ fermi system," *New Journal of Physics*, vol. 11, no. 10, p. 103033, 2009.

[201] C. Honerkamp and W. Hofstetter, "Ultracold fermions and the $su(n)$ hubbard model," *Phys. Rev. Lett.*, vol. 92, p. 170403, Apr 2004.

[202] M. Hermele, V. Gurarie, and A. M. Rey, "Mott insulators of ultracold fermionic alkaline earth atoms: Underconstrained magnetism and chiral spin liquid," *Phys. Rev. Lett.*, vol. 103, p. 135301, Sep 2009.

[203] Y. N. Martinez de Escobar, P. G. Mickelson, P. Pellegrini, S. B. Nagel, A. Traverso, M. Yan, R. Côté, and T. C. Killian, "Two-photon photoassociative spectroscopy of ultracold ^{88}sr," *Phys. Rev. A*, vol. 78, p. 062708, Dec 2008.

[204] A. Stein, H. Knöckel, and E. Tiemann, "The ^{1}s+^{1}s asymptote of sr_2 studied by fourier-transform spectroscopy," *The European Physical Journal D*, vol. 57, no. 2, pp. 171–177, 2010.

[205] M. Yan, R. Chakraborty, A. Mazurenko, P. G. Mickelson, Y. N. M. de Escobar, B. J. DeSalvo, and T. C. Killian, "Numerical modeling of collisional dynamics of sr in an optical dipole trap," *Phys. Rev. A*, vol. 83, p. 032705, Mar 2011.

[206] T. Zelevinsky, M. M. Boyd, A. D. Ludlow, T. Ido, J. Ye, R. Ciuryło, P. Naidon, and P. S. Julienne, "Narrow line photoassociation in an optical lattice," *Phys. Rev. Lett.*, vol. 96, p. 203201, May 2006.

[207] J. L. Bohn and P. S. Julienne, "Semi-analytic theory of laser-assisted resonant cold collisions," *Phys. Rev. A*, vol. 60, pp. 414–425, Jul 1999.

[208] J. Weiner, *Cold and Ultracold Collisions in Quantum Microscopic and Mesoscopic Systems*. Cambridge University Press, Cambridge, 1 ed., 2003.

[209] V. M. Pérez-García, H. Michinel, J. I. Cirac, M. Lewenstein, and P. Zoller, "Dynamics of bose-einstein condensates: Variational solutions of the gross-pitaevskii equations," *Phys. Rev. A*, vol. 56, pp. 1424–1432, Aug 1997.

[210] Y. Kagan, A. E. Muryshev, and G. V. Shlyapnikov, "Collapse and bose-einstein condensation in a trapped bose gas with negative scattering length," *Phys. Rev. Lett.*, vol. 81, pp. 933–937, Aug 1998.

[211] J. M. Gerton, D. Strekalov, I. Prodan, and R. G. Hulet, "Direct observation of growth and collapse of a bose-einstein condensate with attractive interactions," *Nature*, vol. 408, pp. 692–695, Dec 2000. 10.1038/35047030.

[212] E. A. Donley, N. R. Claussen, S. L. Cornish, J. L. Roberts, E. A. Cornell, and C. E. Wieman, "Dynamics of collapsing and exploding bose-einstein condensates," *Nature*, vol. 412, pp. 295–299, Jul 2001.

[213] R. J. Dodd, M. Edwards, C. J. Williams, C. W. Clark, M. J. Holland, P. A. Ruprecht, and K. Burnett, "Role of attractive interactions on bose-einstein condensation," *Phys. Rev. A*, vol. 54, pp. 661–664, Jul 1996.

[214] G. F. Gribakin and V. V. Flambaum, "Calculation of the scattering length in atomic collisions using the semiclassical approximation," *Phys. Rev. A*, vol. 48, pp. 546–553, Jul 1993.

[215] S. G. Porsev and A. Derevianko, "High-accuracy relativistic many-body calculations of van der waals coefficients c_6 for alkaline-earth-metal atoms," *Phys. Rev. A*, vol. 65, p. 020701, Jan 2002.